UiT
THE ARCTIC UNIVERSITY OF NORWAY

Faculty of Science and Technology

Sedimentological and geomorphological study of a postglacial, fjord-side landslide and fan-delta complex at Russenes, inner Balsfjord, Troms county

—

Helen Elizabeth Dulfer

Master Thesis in Geology GEO-3900 – May 2017

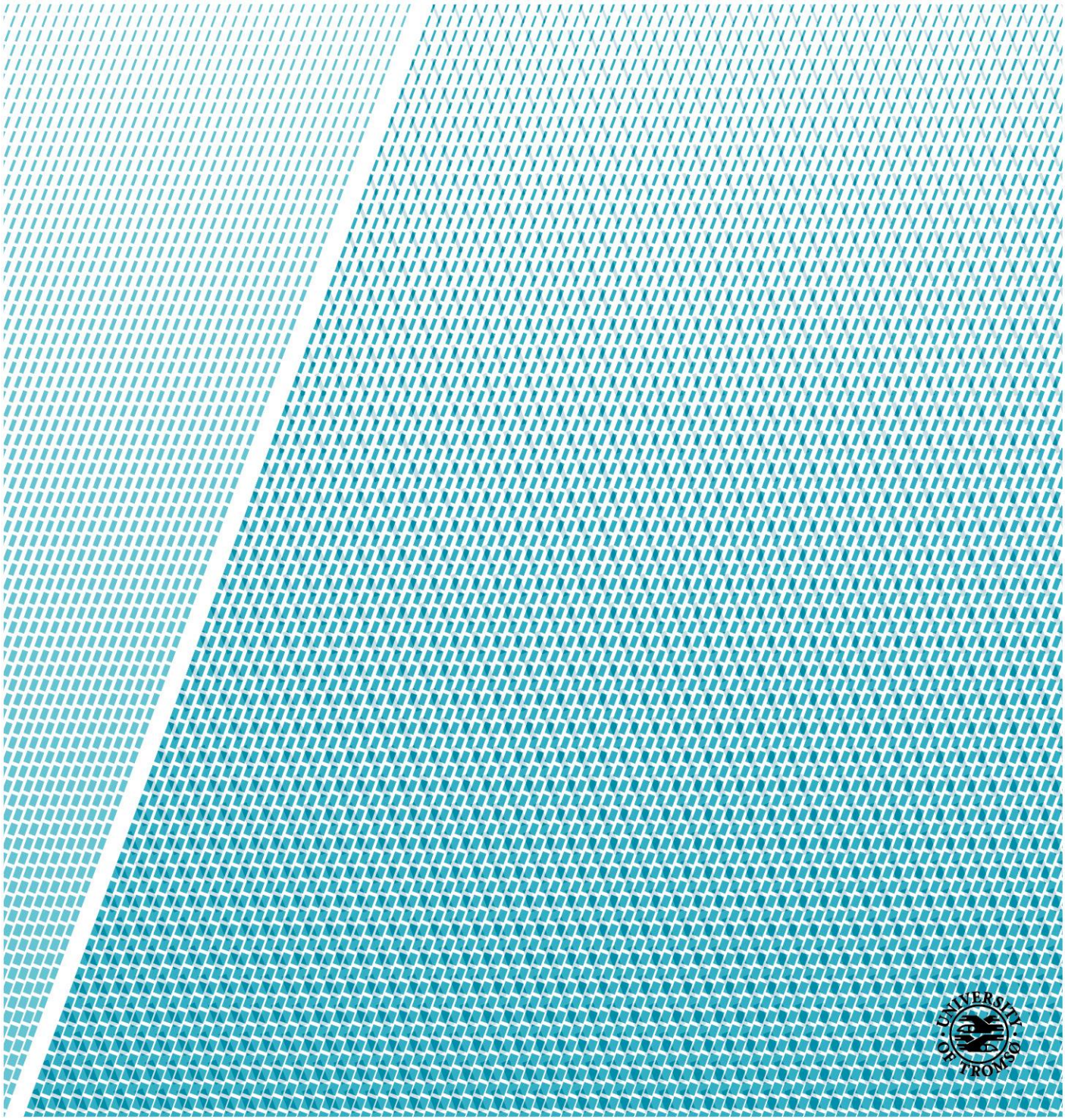

Table of Contents

Abstract 1
Acknowledgments 2
1 Introduction 3
1.1 Objectives 4
1.2 Setting 5
1.2.1 Climate 6
1.2.2 Bedrock Geology 7
1.2.3 Quaternary Geology 9
1.3 Previous Work 17
2 Fjord Geomorphology and Sedimentary Processes 19
2.1 Fjord Sedimentation 19
2.1.1 Glaciofluvial Deposits 21
2.1.2 Ice Front Accumulations 21
2.1.3 Glaciomarine Deposits 21
2.2 Deltas 22
2.2.1 Fjord-Head Deltas 23
2.2.2 Fan Deltas 24
2.3 Mass Movement Processes 25
2.3.1 Mass Movement Processes within Alluvial Fans 25
2.3.2 Mass Movement Processes within Deltas 27
2.3.3 Mass Movement Deposits at Russenes 28
2.4 Anthropogenic Activity 28
3 Methods and Materials 29
3.1 Quaternary Geological Map 29
3.1.1 Visual Interpretation of Aerial Photography 29
3.1.2 Field Mapping 30
3.1.3 Surface Sediment Analysis 31
3.1.4 Digital Terrain Models 33
3.1.5 Global Positioning Systems (GPS) 35
3.2 Subaqueous Morphology 35
3.2.1 Multibeam Bathymetry 35
3.3 Subsurface Composition and Structure 36
3.3.1 Sedimentary Logs 36

3.3.2 Ground Penetrating Radar 37
3.3.3 Radiocarbon Dating 42
4 Results 45
4.1 Quaternary Geological Map 45
4.2 Deglacial Sediment 47
4.2.1 Till 47
4.2.2 Glaciolacustrine Deposit 47
4.2.3 Ice Front Accumulation 50
4.2.4 Glaciofluvial and Rock-Avalanche Complex 55
4.2.5 Eastern Glaciofluvial Delta Complex 67
4.2.6 Colluvium 69
4.2.7 Headward Erosion 71
4.2.8 Raised Beach 73
4.3 Postglacial Fjord-Side Fan Delta 74
4.3.1 Subaerial Morphology 74
4.3.2 Subaqueous Morphology 86
4.3.3 Deltaic Subsurface Sediments 104
5 Discussion 119
5.1 Implications of the Ice-Contact Deglacial Landforms 119
5.1.1 Halt in the Retreat of the Balsfjord Glacier 119
5.1.2 Revised Deglacial History of Balsfjord 120
5.2 Implications of the Origin and Age of the Rock-Avalanche Complex 122
5.3 Evolution of the Postglacial Fjord-Side Fan Delta 123
5.3.1 Fan Delta Aggradation 123
5.3.2 Fan Delta Progradation 126
5.3.3 Russenes Fjord-Side Fan Delta Depositional Model 129
5.4 Reflections on the Factors Controlling Fan Delta Deposition 130
5.4.1 Is Russenes a true fan delta? 130
5.4.2 Other Examples of Holocene Fan Deltas 131
5.4.3 Comparison with Fjord-Head Deltas 132
5.4.4 Sea level, climate and sediment supply 134
6 Conclusions 137
7 References 139
Appendix 1: ArcGIS Methodology 147
Georeferencing field photographs 147

DTM visualization and interpretation 148
Georeferencing maps in ArcMap 150
Appendix 2: GPR Profiles 151
Appendix 3: Grainsize Data 159

List of Tables

Table 1: The aerial photographs used in this study. 30
Table 2: The Udden-Wentworth-Krumbein grainsize scale 32
Table 3: Lithofacies codes for the sorted sediments at Russenes 33
Table 4: Lithofacies codes for the different types of bedding at Russenes and their interpretation. 37
Table 5: List of the GPR lines collected in this study. 39
Table 6: Information about the samples prepared for AMS ^{14}C radiocarbon dating. 43
Table 7: Ages of material attached to the rock-avalanche boulders. 60
Table 8: List of the mollusca species identified in the study area. 114
Table 9: Radiocarbon dates obtained from shells within the bottomset sediment during this study. 114
Table 10: Summary of the lithofacies observed within the deltaic subsurface sediment. 116
Table 11: Summary of the radiocarbon dates that are avaliable for the study area. 127

List of Figures

Figure 1: A) Terrain map of Troms county. B) A topographic map of inner Balsfjord showing the location of the Russenes fan delta. 3
Figure 2: Oblique aerial view of the Russenes fjord-side fan delta and surrounding catchment area produced using Google Earth Pro. 5
Figure 3: A) Tide table for Storsteinnes, Balsfjord. B) Graph showing the monthly mean precipitation and temperature measured at the Storsteinnes weather station from 1961 to 1990. C) Graph showing the average monthly river discharge of the Lille Rostavatn river from 1960 to 2016. 6
Figure 4: A) Bedrock geological map (1:50 000 scale) of the study area. B) Photograph of the Store Russetinden and Rakeltinden mountains taken from across the fjord with the bedrock geology annotated. 7
Figure 5: A) A geological map showing the distribution of Precambrian and Caledonian rocks in Troms County B) Schematic west-east profile showing the geology between Kvaløya and Sweden/Finland. 8
Figure 6: A) Regional tectonic map of the SW Barents Sea margin B) Map of Troms county showing the lineaments identified using Landsat data 9
Figure 7: The extent of ice sheets in northern Europe during the Quaternary. 10
Figure 8: A) Map of the Troms county showing the location of the moraines. B) Time-distance deglaciation diagram of the Balsfjord glacier. 11
Figure 9: A) Isobases (in metres) showing the elevation of the postglacial marine limit across Scandinavia. B) Schematic showing how the marine limit is formed diachronously as the glacier retreats. 12
Figure 10: A) Isobases over Balsfjord for the extended S_0 (main shoreline) B) Shoreline emergence curve for inner Balsfjord, Troms county. C) Equidistant shore-line diagram for the Balsfjord area modified from Andersen (1968). 13

Figure 11: Quaternary geology map of the study area 14
Figure 12: Continuous temperature reconstructions of the Holocene across northern Scandinavia. ... 15
Figure 13: Mean Temperature-Precipitation-Wind Equilibrium Line Altitude of Lenangsbreene in Strupskardet, Lyngen, from 20,000 cal. yr BP to the present..... 16
Figure 14: Map of the skred danger zones for Russenes..... 17
Figure 15: Photograph of Ersfjord in northern Norway 19
Figure 16: Principle processes and deposits within fjords A) during the deglaciation stage and B) during the postglacial stage. 20
Figure 17: Process-based tripartite classification of delta morphology based on the relative influence of fluvial discharge and wave and tidal energy. 22
Figure 18: Sketch showing the dominant sedimentary processes that occur within a fjord environment..... 23
Figure 19: Idealized cross-section showing the different depositional environments and internal geometry of a prograding Gilbert-type delta. 24
Figure 20: Schematic of an ideal unconfined fan delta showing the different subaerial and subaqueous depositional environments..... 25
Figure 21: A) Outline map of Norway showing regions where a high number of rock slope failures have been recorded. B) Location of rock avalanches and rock slope failures in Troms county, Northern Norway.. 26
Figure 22: A schematic diagram showing four common types of subaqeuous mass movement processes..... 27
Figure 23: A) Aerial photograph WF_1133_F8 taken between 22 and 24 July 1960. This photograph was taken before the E6 highway was built. B) Aerial photograph Midt-troms 2013 taken on 11 August 2013. The red boxes highlight some of the areas that have changed between 1960 and 2013 due to construction of the main road. 30
Figure 24: Map of the study area showing the GPS tracks (blue) and waypoints (yellow) that were recorded during fieldwork. 31
Figure 25: Map showing the location of sediment grainsize data recorded during fieldwork 32
Figure 26: A hillshade image of the study area..... 34
Figure 27: Hillshade image of the DTM created from the Lidar data that is available over the study area. 34
Figure 28: Example of a lithological log created during this study. 36
Figure 29: Schematic showing the principles of ground penetrating radar (GPR). 37
Figure 30: Photograph of the PulseEKKO^{TM} IV GPR instrument used in this study. 38
Figure 31: Aerial photograph showing the location of the GPR lines collected during this study. 39
Figure 32: GPR line Russ5 (A) before topography information was added, and (B) after topography information was added to the line. 40
Figure 33: GPR profile Russ8 showing the profile is initially not located at timezero..... 41
Figure 34: GPR profiles Russ2, 3 and 4 (merged) (A) before migration and (B) after migration 41
Figure 35: Quaternary Geological Map produced during this study. The map shows the surficial sediment and geomorphological features of the postglacial Russenes fjord-side fan delta and associated deglacial sediment..... 46
Figure 36: Detailed map of the sorted silt sediment (glaciolacustrine deposit) located on the upper eastern side of the fan delta. 48

Figure 37: A) Photograph of the well sorted silt sediment located within an erosional scarp on the south-western side of the deposit. B) Photograph of the terrace-like surface located below the deposit of sorted silt. This surface occurs above the marine limit. 48
Figure 38: Schematic diagram of the interpreted depositional environment of the glaciolacustrine deposit. 49
Figure 39: A) Aerial photograph of the fan delta showing the location of the gravel pit on the western side of the Buktelva river. B) Photograph of part of the gravel pit showing the present-day grainsize distribution C) Photograph of the cobbly sandy gravel located at the edge of the gravel pit. 50
Figure 40: A) Aerial photograph WF_1133_F8 showing the landscape in 1960 before gravel pit operations commenced. B) Detailed map of the ridge. 51
Figure 41: Lidar-derived shaded-relief map of the present-day gravel pit 51
Figure 42: A) Uninterpreted GPR profile Russ2,3&4 (merged). B) Interpreted GPR profile Russ2,3&4 (merged). 52
Figure 43: A) Uninterpreted GPR profile Russ5. B) Interpretation of GPR profile Russ5. 53
Figure 44: Sketches of the interpreted depositional environment. A) Plan-view interpretation. B) Cross-section interpretation. 54
Figure 45: A) Detailed map of the rock-avalanche deposit (red) and glaciofluvial sediment (orange) created through field mapping and aerial photograph interpretation. B) Oblique aerial view photograph of the rock-avalanche deposit 56
Figure 46: A) Photograph of the front of the present-day glaciofluvial deposit. B) Photograph of the glaciofluvial sediment. 57
Figure 47: Detailed map of the front of the glaciofluvial and rock-avalanche complex 57
Figure 48: A) Photograph of a vertical sedimentary section of glaciofluvial sediment and rock-avalanche boulders taken shortly after the section was exposed by gravel pit operations. B) Lidar-derived shaded-relief map of the front of the rock-avalanche deposit 58
Figure 49: A) Photograph showing the vertical sedimentary section at the back of the gravel pit. B and C) Photographs of large rock-avalanche boulders located on the slope of the gravel pit. 59
Figure 50: Balanus shells observed on one of the large rock-avalanche boulders at the front of the deposit (65 m a.s.l).. 59
Figure 51: A and B) Photographs of the rock-avalanche boulders located above the gravel pit. C) Photograph of the terrace surface surrounding the rock-avalanche boulders. D) Photograph of the glaciofluvial sandy gravel. 60
Figure 52: A and B) Photographs of the rock-avalanche boulders located next to the Buktelva river. 61
Figure 53: A and B) Photographs showing the colluvial sediment that is located in the middle of the rock-avalanche complex. 62
Figure 54: A to C) Photographs of rock-avalanche boulders in the upper section of the deposit. 63
Figure 55: A) Oblique aerial view looking south of the upper section of the rock-avalanche deposit. B) Elevation profile across the rock-avalanche lobe 63
Figure 56: Map showing the bedrock geology above the Russenes rock-avalanche. The possible rock-avalanche source areas are indicated 64
Figure 57: Schematic model showing the depositional environment of the multiphase rock-avalanche and glaciofluvial complex. 66
Figure 58: Reconstruction of how the front-most rock-avalanche-boulders were buried by sediment from a side entry fluvial delta 66
Figure 59: A) Detailed map of the glaciofluvial sediment on the eastern side of the fan delta. B) Oblique aerial view image (looking south) of the upper eastern side of the fan delta 67

Figure 60: Schematic diagrams showing the interpreted depositional environment of the valley-side glaciofluvial delta 68
Figure 61: A) Photograph of part of the catchment area of the Russenes fjord-side fan delta taken from across the fjord by Rowan Romeyn. B) Panarama photograph of the Russetinden mountain taken from the middle of the rock-avalanche deposit. 69
Figure 62: A) Photograph of the colluvium sediment located adjacent to the rockslide deposit B) Photograph showing the surface morphology of colluvium sediment located immediately above the postglacial alluvial fan 70
Figure 63: A section of the Quaternary Geological map of the study area. The relict gullies (pink dashed lines) are shown within the red boxes. 71
Figure 64: A) Photograph of the small stream that is currently flowing through the western gully. B) Detailed map of the alluvial fan C) Cross-profile showing the elevation changes across the fan 72
Figure 65: Photograph of a 40 cm tall vertical sedimentary section containing raised beach sediment located just above the present day beach. 73
Figure 66: Map of the extent of the postglacial fjord-side fan delta (yellow). 74
Figure 67: Elevation profiles of the fan delta. A) Longitudinal profile of the fan delta B) A transverse profile across the fan delta 75
Figure 68: Slope map of the catchment area 76
Figure 69: Elevation profile of the Buktelva river. 77
Figure 70: A) Aerial photograph of the lower section of the Buktelva river. B) Photograph looking north of the lowest section of the Buktelva river before it enters the sea. C) Photograph looking south of the Buktelva river below the E6 highway. 77
Figure 71: Graph showing the daily river discharge of the Lille Rostavatn river in 2006. 78
Figure 72: A) Photograph of the Buktelva river with low water flow on 18 September 2016. B) Photograph of the same section of the Buktelva river in flood on 6 August 2004. 78
Figure 73: A and B) Photographs of the Buktelva river fan just below the fan apex. 79
Figure 74: Elevation profile of the Russedalselva river. 80
Figure 75: A) Aerial photogaph of the lower section of the Russedalselva river. 80
Figure 76: A and B) Photographs showing the surface morphology of some of the fluvial sediment within the study area 81
Figure 77: A) Locality map. B) Vertical cross-section of the fan delta. C) Lidar-derived shaded-relief map showing that fluvial sediment next to the Russedalselva river is characterised by elongate ridges and furrows. 82
Figure 78: A) Photograph of a thick accumulation of fluvial sediment that has been exposed along the Buktelva river. B and C) Photograph and graphical log of fluvial sediment exposed by the downcutting Buketlva river. 83
Figure 79: Photograph of a 70 cm high river bank located on the Russedalselva river. 84
Figure 80: A) Lidar-derived shaded relief map of the fluvial sediment below the eastern fan apex overlaied by the Quaternary Geological map. B) Elevation profile I-I' showing the fluvial terraces located beneath the eastern fan apex. 85
Figure 81: A) and B) Photographs of fluvial bars located in the present-day Buktelva river. 85
Figure 82: A) Locality map. B) Morphogenic profile of the modern Russenes fjord-side fan delta 86
Figure 83: Detailed map of the front-most section of the fan delta. The extent of the delta platform is shown by the red outline. 87
Figure 84: Photograph of a beach exposed at low tide on the western side of the Russenes delta platform. 88

Figure 85: Detailed map of the delta platform surrounding Area A 88
Figure 86: A and B) Photographs of some of the beaches in Area A. 89
Figure 87: A) Photograph of one of the beaches in Area A. B, C and D) Photographs of the sediment located at different places on the beach..... 89
Figure 88: Detailed map of the delta platfrom surrounding Area B..... 90
Figure 89: A and B) Photographs of beaches located in Area B..... 91
Figure 90: Photograph of one of the lagoons located within the study area 91
Figure 91: Detailed map of the delta platfrom surrounding Area C and D. 92
Figure 92: A) Photograph the eastern side of the Russenes fan delta taken from across the fjord. B) Photograph of high erosional scarp located immediately behind the beach in Area C 93
Figure 93: A) Photograph of the beach on the south-eastern part of the delta platform (Area D). B) Photograph of a bouldery beach ridge that is 100 cm high. 94
Figure 94: Detailed map of the fluvial dominated zone of the delta platform located at the top of the fan delta where the Russedalselva river discharges into the sea. 95
Figure 95: A and B) Photographs of the fluvial dominated delta platform located in front of the Russedalselva river..... 96
Figure 96: A and B) Photographs of a channel located near the delta lip 96
Figure 97: A to D) A series of orthophotographs over the fluvial dominated delta platform in front of the Russedalselva river mouth. The orthophotographs have been acquired over a 10 year period and show changes in the distribution of channels and bars on the delta platform over time. E) The channels observed in the orthophotographs shown in A to D have been digitised and are displayed together to show the changes in the position of channels over time..... 97
Figure 98: Detailed map of the fluvial dominated zone of the delta platform located where the Buktelva river enters the fjord..... 98
Figure 99: A) Panorama photograph of the fluvial-dominated delta platform where the Buktelva river discharges into the sea..... 98
Figure 100: A and B) Photographs of bars located in the upper section of the fluvial-dominated delta platform. 99
Figure 101: A) and B) Photographs of ripple marks on the sand-dominated bars of the lower fluvial-dominated delta platform beneath the Buktelva river mouth. 99
Figure 102: Map of the top of the Russenes fjord-side fan delta showing the present-day constructive and descructive areas of the delta platform.. 100
Figure 103: A) Aerial photograph overlaid by a shaded-relief multibeam bathymetry map of the subaqueous component of the fan delta 101
Figure 104: Slope map of the sea floor 102
Figure 105: Enlargement of the multibeam bathymetric map at the front of the Russenes fjord-side fan delta. 102
Figure 106: A ground penentrating radar profile collected in the study area showing the GPR facies architecture 104
Figure 107: Aerial photograph of the gravel pit. The location of the GPR profiles obtained near the gravel pit are shown. 106
Figure 108: A) Fluvial topset sediment exposed within the gravel pit. B) Uninterpreted GPR profile Russ10. C) Interpreted GPR profile Russ10..... 107
Figure 109: A) Photograph of the gravel pit showing the location of the two sedimentary sections. B) Photograph of the foreset beds located on the eastern side of the gravel pit..... 108

Figure 110: A) Photograph of the sand- and gravel-dominated delta foresets beds located on the south-eastern side of the gravel pit. B) Graphical log of the foreset beds..... 108
Figure 111: A) Photograph of the gravel-dominated delta foreset beds located on the north-western side of the gravel pit. B) Graphical log of these foreset beds..... 109
Figure 112: A) Photograph of the vertical sedimentary section located at the back of the gravel pit. B) Photograph of the boundary between Unit 1 and 2. 109
Figure 113: A) Uninterpreted GPR profile Russ 8. B) Interpreted GPR profile Russ 8. 110
Figure 114: A) Uninterpreted GPR profile Russ9. B) Interpreted GPR profile Russ9. 111
Figure 115: A) Aerial photograph showing the morphological and geological features mapped around the river cutting. B) Photograph of the river cutting 112
Figure 116: A) Graphical log of a sedimentary section located in the bank of the Buktelva river. B) Photograph of part of the logged vertical section showing the deltaic foreset and bottomset sediment. C) Wavy laminations observed within silty sand..... 113
Figure 117: A) Photograph of part of the foreset sediment identified within the river cutting. B) Graphical log of the foreset beds..... 114
Figure 118: A) Uninterpreted GPR profile Russ 7. B) Interpreted of GPR profile Russ 7. 115
Figure 119: Schematic model of the deposition of the submarine ice-contact landforms during a halt in the retreat of the Balsfjord glacier..... 119
Figure 120: Schematic model showing the response of a glacier to rock-avalanche debris covering the ablation zone. 120
Figure 121: A) Five distinct channel morphologies observed on alluvial fans related to different stages of the channel avulsion processes..... 124
Figure 122: A) Lidar-derived shaded relief map of the Buktelva river near the western fan apex B) Elevation profile across the upper Buktelva river 124
Figure 123: Map showing the morphology of the subaerial alluvial fan of the Russenes fjord-side fan delta.. 125
Figure 124: Reconstruction of fan delta progradation based on radiocarbon dated foreset and bottomset sediment, and the reconstruction of delta rim positions from deltaic terraces and foreset beds..... 128
Figure 125: Schematic diagram showing the different styles of delta progradation that have occured during the evolution of the Russenes fjord-side fan delta. 128
Figure 126: Schematic model of the two different stages of delta progradation under a regressive sea level regime. 129
Figure 127: 3D oblique aerial view of the Russenes fjord-side fan delta showing the the delta contains the distinctive geomorphological elements of a fan delta.. 131
Figure 128: A) Aerial photograph showing a large section of Troms county. B) Aerial photograph of a small fjord-side fan delta at Elsnes in Storfjord. C) Aerial photograph of the southern Lyngen alps. D) Aerial photograph of the northern Lyngen alps. 132
Figure 129: Profiles across (A) the Alta delta and (B) the Russenes fjord-side fan delta..... 133

Abstract

A comprehensive study of the Russenes postglacial fjord-side fan delta and landslide complex has been undertaken in inner Balsfjord, Troms county, northern Norway. High-resolution bathymetric data, digital terrain models, aerial photography, ground penetrating radar profiling, radiocarbon dating and field mapping have been used to determine the geometry, structure, lithofacies and evolution of the Russenes fjord-side fan delta. A 1:10 000 scale Quaternary Geological Map of the Russenes fjord-side fan delta and associated deglacial landforms has been produced during this study. Previously unrecognised deglacial ice-contact landforms have been mapped above the Russenes fjord-side fan delta. These landforms provide new insights into the deglaciation history of Balsfjord because they indicate that there was a halt in the retreat of the Balsfjord glacier at Russenes. Radiocarbon dating of *Balanus* shells located within these deglacial ice-contact landforms provides a minimum age for the glacier standstill of 10 884 ± 96 cal. yr BP (1σ).

Detailed field investigation of a distinctive rock-avalanche complex located immediately above the Russenes fjord-side fan delta suggests that it was deposited by multiple rock-avalanche events. The composition of the boulders in the lower section indicates that they have been sourced from outside the catchment area, transported on the Balsfjord glacier and subsequently, deposited along with the ice-contact landforms. The composition of the rock-avalanche boulders in the upper section of the rock-avalanche complex indicates another rock-avalanche event was triggered on the mountains located directly above the Russenes fjord-side fan delta.

Investigation of the present-day morphology and structure of the fjord-side fan delta indicates there are two distinct depositional environments within the postglacial fan delta: (1) a subaerial alluvial fan; and (2) a subaqueous Gilbert-type delta. Within both environments sediment transport occurs during episodic high-energy flood events. The subaerial alluvial fan contains two perennial river channels that migrate over the fan via channel back-filling and avulsion processes. Additionally, the subaqueous component of the fan delta can be further divided into three depositional environments: (1) a flatly lying intertidal delta platform; (2) a steeply dipping subaqueous delta slope; and (3) a deep, subaqueous, gently dipping prodelta region. Investigation of the deltaic subsurface reveals the delta has a Gilbert-type tripartite structure composed of bottomset, foreset and topset units and the relationship between the subsurface structure and the present-day fan delta morphology has been discussed. The surficial morphology and subsurface structure of the postglacial fjord-side fan delta has been used to determine the progradational and aggradational history of the fan delta. Finally, the response of the Russenes fjord-side fan delta to variations in climate, sea level and sediment supply over the Holocene has been investigated.

Acknowledgments

Firstly, I would like to acknowledge my supervisor, Prof. Geoffrey Corner, for his assistance and advice throughout my master's thesis. Geoff shared his wealth of knowledge in Quaternary geology and provided invaluable guidance during fieldwork. Additionally, he spent considerable time setting up, testing and fixing the GPR instrument and computer so that it could be used in the field and assisted with the collection of the GPR profiles. I would also like to thank Geoff for all the meetings and discussions we have had throughout the year, which helped to develop and advance my knowledge and understanding of the study area. And finally, I would like to thank Geoff for his detailed manuscript reviews. I appreciate all the knowledge and insights I have gained from working on this project.

I would also like to acknowledge Laura Swinkels for her assistance in the field and Trine for her assistance in the laboratory with the identification of the marine fossils. I would also like to thank my fallow master's students for their help and support throughout the year. I have enjoyed spending time with you all and facing the challenges our master's program together.

Finally, I would like to thank my friends and family back in Australia for their support and encouragement to pursue my studies and passions in Arctic Norway and Rowan Romeyn for moving to Norway with me and providing support, companionship and assistance over the last two years.

Helen Dulfer

13 May 2017

1 Introduction

This study investigates the Quaternary sedimentology and geomorphology of a fjord-side fan delta at Russenes (or Russenest). The study area is located at the head of Balsfjord, Troms county, northern Norway (Figure 1), which is approximately 60 km south-east of Tromsø. Balsfjord is a narrow, shallow fjord, with a length of 46 km, maximum width of 5 km and maximum depth of 190 m (Wassmann et al., 1996, Forwick and Vorren, 2002).

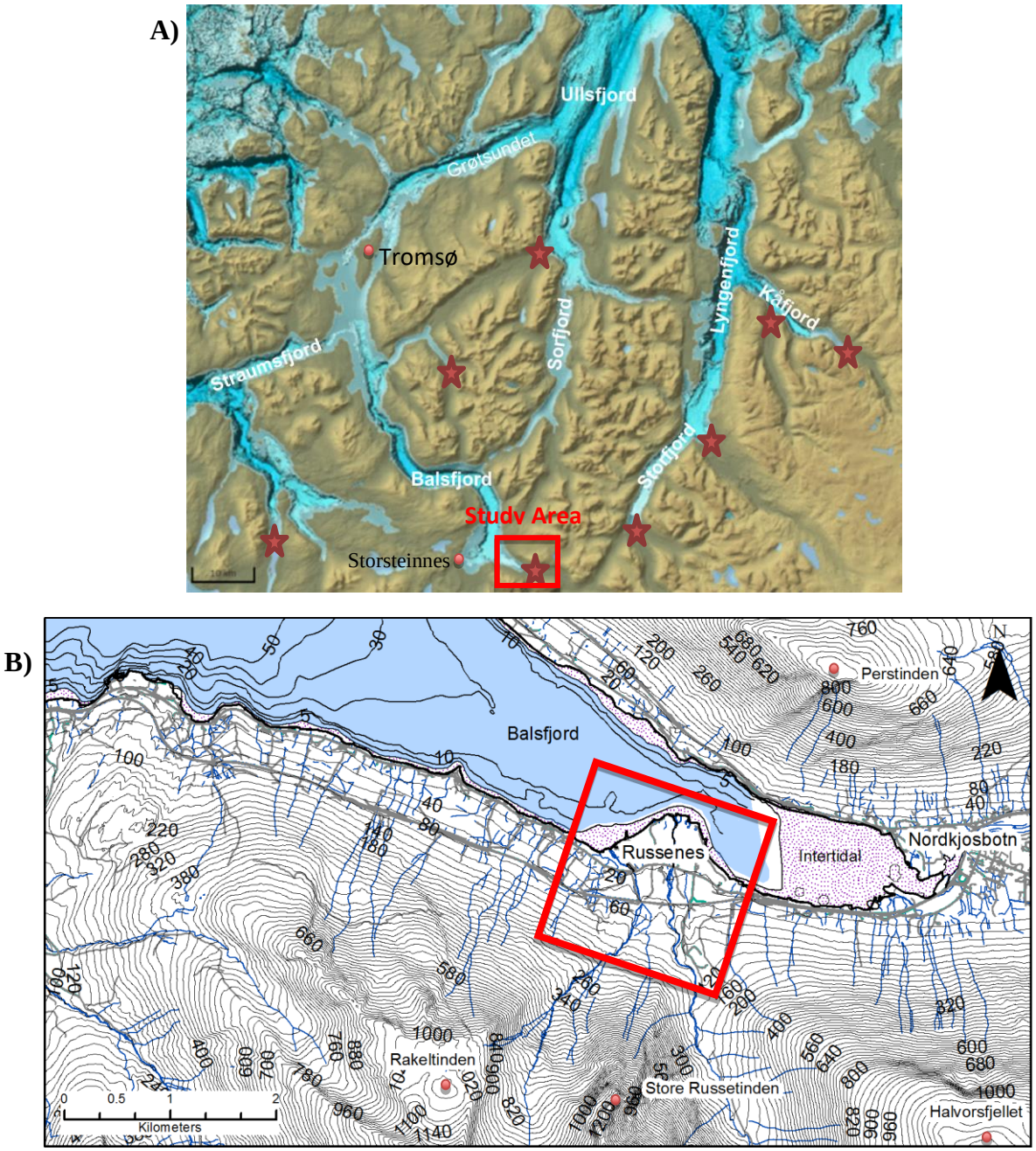

Figure 1: A) Terrain map of Troms county showing a distinctive mountainous landscape dissected by fjords. The stars show the location of fjord-head deltas. This map has been produced from www.norgeskart.no B) A topographic map of inner Balsfjord showing the location of the Russenes fan delta. This map has been produced from digital data available at www.kartverket.no.

Balsfjord has been repeatedly eroded by large ice sheets that formed during glacial-interglacial cycles throughout the Late Quaternary (Andersen, 1968, Forwick and Vorren, 2002, Stokes et al., 2014). Fjords occur at the interface between continents and the sea and the processes that occur within fjords are directly related to the movement of water and sediment and thus are dependent on the hydrological cycle (Syvitski et al., 1987). Rivers are the main source of fresh water into fjords and the majority of fluvial activity occurs at the head of the fjord whereby retreating glaciers or fjord-valley rivers deliver a large amount of fresh water and sediment. The deposition of this sediment into the fjord produces a fjord-head delta (Syvitski et al., 1987, Benn and Evans, 1998) and Balsfjord has a fjord-head delta located at Nordkjosbotn (Figure 1).

Consequently, fjord-head deltas are common across northern Norway (Figure 1A) and have been widely studied (Corner et al., 1990, Corner et al., 1996, Corner, 1998, Corner, 2006, Eilertsen et al., 2006), whilst fjord-side fan deltas are rare and poorly studied (Corner, 1977, Rose and Synge, 1979, Postma and Cruickshank, 1988). The protrusion at Russenes can be defined as a fan delta because it is a coarse-grained delta formed by an alluvial fan prograding directly into a standing body of water from an adjacent highland (Holmes, 1965, McPherson et al., 1987). However, the Russenes fan delta is unusual because it is fed by two distinct rivers systems and it has a very steep gradient. Additionally, it also contains a large partially buried rock-avalanche that provides information about the rock-avalanche history of Troms county (Blikra, 1998, Braathen et al., 2004, Blikra et al., 2006, Fenton et al., 2011).

1.1 Objectives

This study aims to use a diverse range of datasets to investigate different aspects of the Russenes fjord-side fan delta, including the modern subaqueous delta, the present-day surficial sediments and the subsurface sediments, to determine the deglacial depositional history of the fjord-side fan delta.

The specific aims of this study are:

(1) Produce a Quaternary Geological Map of the deglacial, postglacial and present-day surficial sediments of Russenes fan delta;
(2) Investigate the subaerial and subaqueous morphology of the modern fjord-side fan delta;
(3) Investigate the subsurface structure of the fjord-side fan delta; and
(4) Determine the depositional history of the postglacial fjord-side fan delta.

Finally, the data collected during this study will be used to determine how the fan delta has responded to changes in sea level, sediment supply and climate since the deglaciation of Balsfjord and determine why the occurrence of fjord-side fan deltas in unusual in Troms county.

1.2 Setting

The Russenes fjord-side fan delta protrudes into Balsfjord as a 1 km wide, fan shaped accumulation of predominately sandy gravel sediment (69°13'N, 19°29'E; Figure 1). This fan delta is located on the south side of the fjord and it is 500 m from the fjord-head delta at Nordkjosbotn. The two different river systems feeding the fan delta are called the Buktelva river and the Russdalselva river and they are 4 km and 6 km in length respectively (Figure 2). The combined catchment area is approximately 20.5 km^2.

Balsfjord is surrounded by large mountains that rise directly from the sea and the study area is located adjacent to three tall mountains; Store Russetinden (1405 m), Rakeltinden (1400 m) and Halvorsfjellet (1214 m) (Figure 2). These mountains host three small cirque glaciers that have a total area of 2.02 km^2. The Russetindbreen glacier is the largest with an area of 1 km^2 (Andreassen et al., 2012) (Figure 2). The glaciers all drain into rivers that feed the Russenes fjord-side fan delta. The high topography surrounding the fan delta causes the study area to be affected by mass movement processes. Sediment deposited in the fan delta is derived locally from deposits of colluvium and till as well as glaciofluvial and fluvial gravel, sand and occasional mud.

The sea in inner Balsfjord is protected and wave energy is low. Sea ice forms on the fjord surrounding the Russenes and Nordkjosbotn deltas during winter. The region has a semi-diurnal, mesotidal regime with a mean spring tidal range of 2.9 m (Kartverket, 2016) (Figure 3A). The Skjevelnes moraine divides the Balsfjord into an inner and outer basin and restricts deep water circulation (Forwick and Vorren, 2002). Balsfjord is connected to the open ocean by a number of inlets, such as Straumsfjord and Grøtsundet, and has relatively high water temperatures (Figure 1A) (Wassmann et al., 1996).

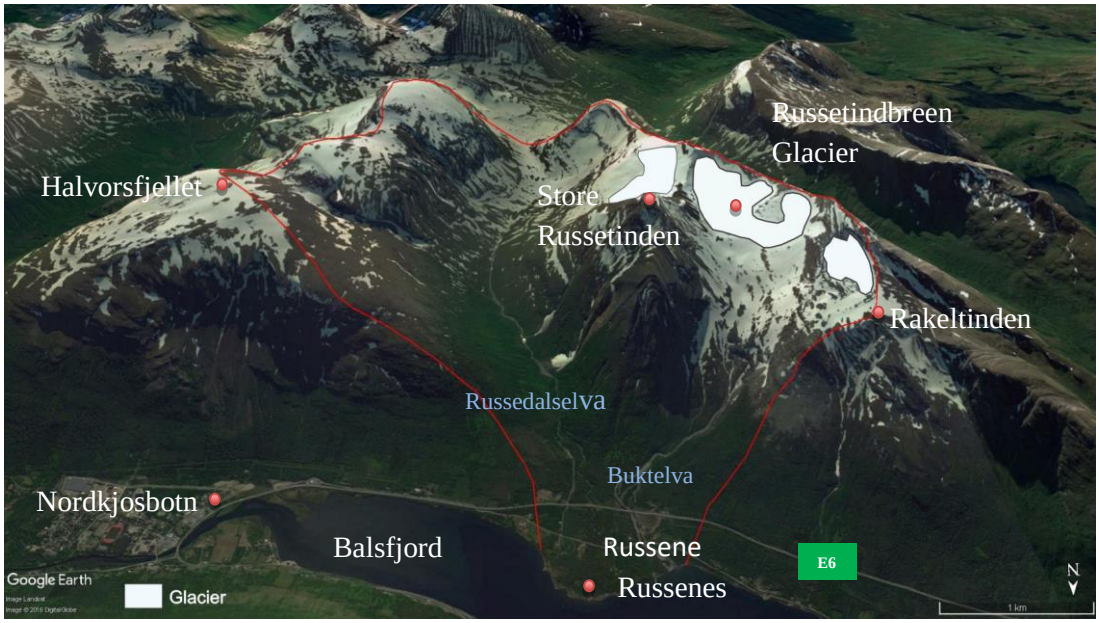

Figure 2: Oblique aerial view of the Russenes fjord-side fan delta and surrounding catchment area (red line) produced using Google Earth Pro.

1.2.1 Climate

A large temperature anomaly occurs along the coast of northern Norway whereby the mean January temperature is approximately 24°C warmer than the worldwide mean temperatures for the same latitude (Bakke et al., 2005). This temperature anomaly is created by the heat advection of warm air and water masses from the Norwegian Current and consequently, Balsfjord has a subartic climate with a mean annual precipitation of 768 mm (Norwegian Meteorogisk Institutt). Figure 3B shows that the amount of precipitation in Balsfjord has a seasonal cyclicity with the highest precipitation occurring in autumn and winter whilst the month of May has the lowest mean precipitation. River discharge is also highly seasonal. The maximum river discharge occurs in early summer (May and June) due to snow and ice melt, whilst minimum river discharge values occur during winter (Figure 3C). The rivers can also have an increased discharge during periods of heavy rain in autumn (Wassmann et al., 1996). The wind in the fjord is affected by the high topography, which causes the wind direction to often align with the fjord (Wassmann et al., 1996). The air temperature varies between a January mean of -6.5°C and a July mean of 12.8°C with a yearly average of 2.4°C (Norwegian Meteorogisk Institutt) (Figure 3B).

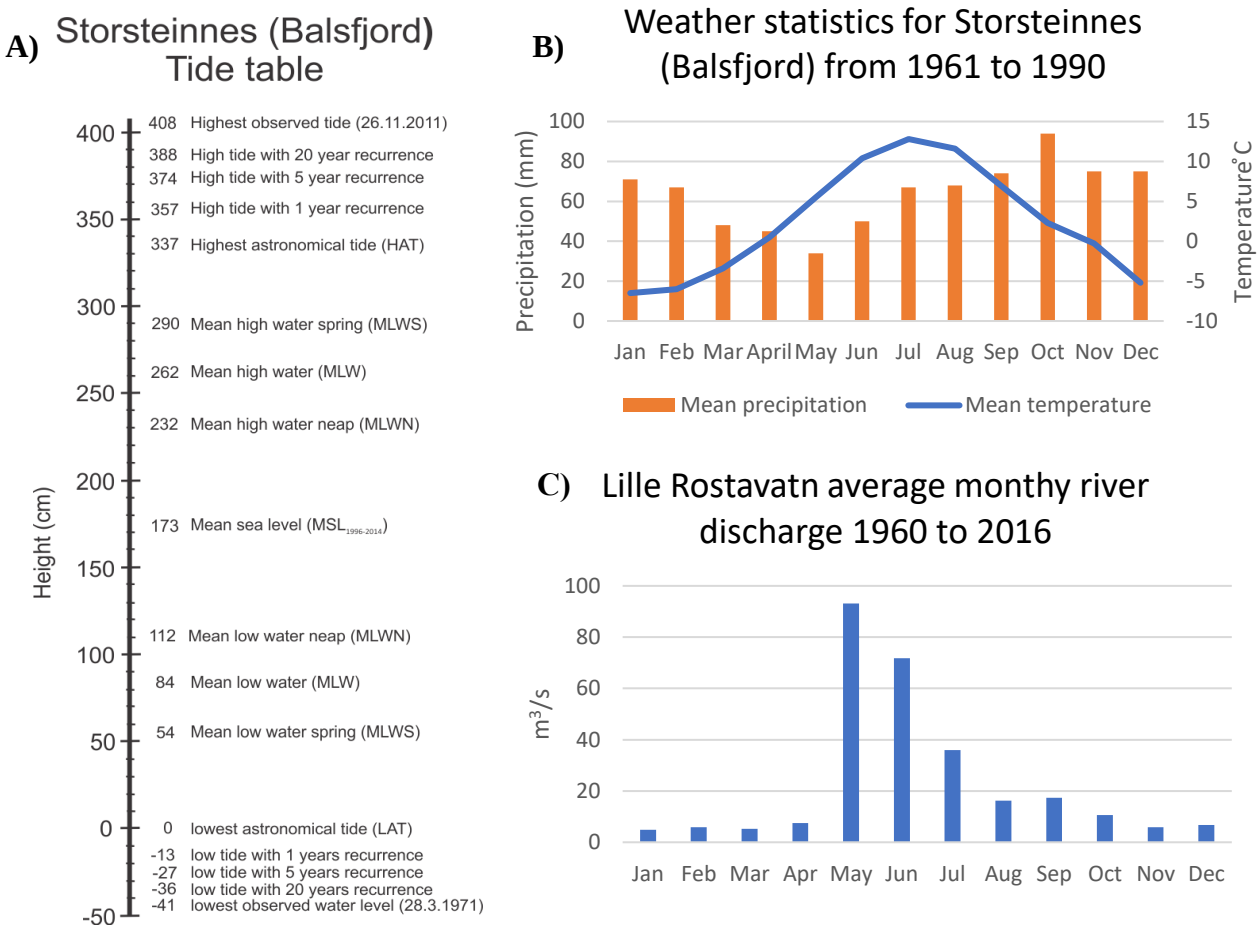

Figure 3: A) Tide table for Storsteinnes, Balsfjord, which is located 10 km northwest of Russenes (Figure 1A). The tide table shows the mean tidal levels and extreme values. The tide table has been modified from (Kartverket, 2016) B) Graph showing the monthly mean precipitation and temperature measured at the Storsteinnes weather station from 1961 to 1990. The data was downloaded from the Norwegian Meteorogisk Institutt and is available at met.no. C) Graph showing the average monthly river discharge of the Lille Rostavatn river from 1960 to 2016. The Lille Rostavatn is located 25 km SSE of Russenes and the lake is surrounded by tall mountains that host small cirque glaciers. Data provided by the Norwegian Water Resources and Energy Directorate (NVE).

1.2.2 Bedrock Geology

Most of the bedrock in Troms county is composed of Caladonian nappes, which are part of the Caledonian Orogenic Belt that was formed during a Himalaya-type collision between the Baltic and Laurentian Shields in the Early to Mid Paleozoic (Andersen, 1988, Corner, 2005b, Fossen et al., 2008). The Caladonian nappes can be divided into four main complexes, called the Lower, Middle, Upper and Uppermost Allochthon, based on how far the rock units have been transported and their degree of metamorphism (Fossen et al., 2008). The rocks within Troms county primarily belong to the Upper Allochthon, which consists of metasedimentary rocks of Ordovician and Lower Silurian age and oceanic crust (ophiolites) bounded by major thrusts and extensional or strike-slip faults (Fossen et al., 2008, Corfu et al., 2014). Rock types include gabbros, greenstones, granitoids, polymict conglomerates, marbles, mylonites, mica schists, gneisses and ultra-mafic rocks.

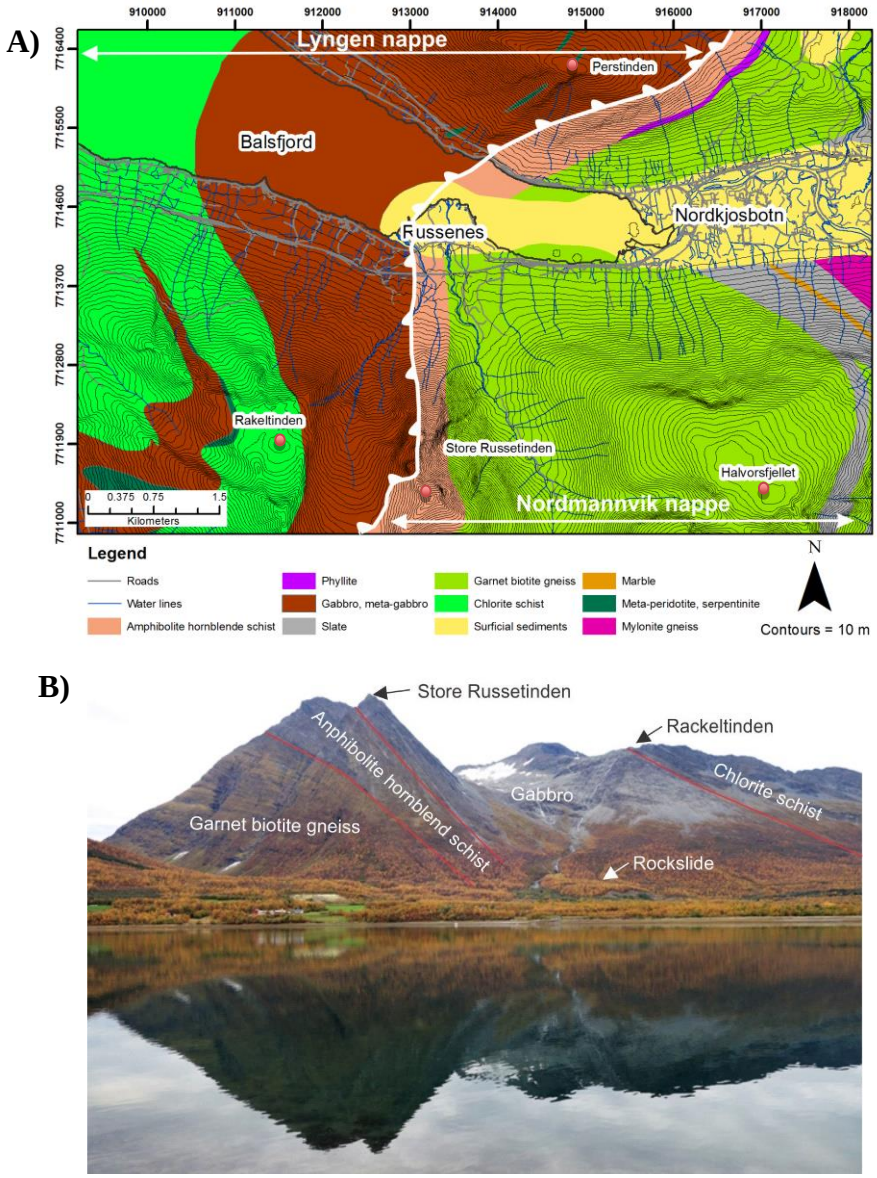

Figure 4: A) Bedrock geological map (1:50 000 scale) of the study area created from the Berggrunn N50 digital dataset available from Norges Geologiske Undersøkelse (NGU, 2015a). This dataset is a national-scale bedrock geology map of Norway. B) Photograph of the Store Russetinden and Rakeltinden mountains taken from across the fjord with the bedrock geology annotated. The vegetation on the Store Russetinden mountain highlights the change in bedrock geology.

The basement rocks in the study area belong to two different nappes; the Nordmannvik nappe and the Lyngen nappe (Figure 5 and Figure 4). The Nordmannvik nappe occurs on the eastern side of the study area and it is a high grade tectonic unit that consist of high-temperature granulites as well as Early Silurian gabbroic intrusions and some lower-grade metasedimentary and metavolcanics rocks (Andersen, 1988, Corfu et al., 2014). Figure 4 shows that the east side of the Store Russetinden mountain and the Russedalselva valley are part of the Nordmannvikk nappe. They are composed of garnet biotite gneiss and amphibolite hornblende schist and the boundary between these rock units can be identified by changes in vegetation on the mountain (Figure 4B).

The Lyngen nappe has been thrust on top of the Nordmannvik nappe (Figure 4) and contains an ophiolite fragment known as the Lyngen Gabbro. This gabbro forms most of the Lyngen Alps and it is the largest layered mafic complex within the Scandinavian Caledonides (Bergh and Andresen, 1985, Andersen, 1988). The Lyngen ophiolite has been assigned a relative age of 469 to 481 Ma based on tonalities that intrude related units (Corfu et al., 2014). Figure 4 shows that a large area above the Russenes fjord-side fan delta is composed of gabbro, from the west side of the Store Russetinden mountain to the east side of the Rackeltinden mountain and a cirque glacier is located within this area. Therefore, a lot of the rocks deposited within the Russenes fjord-side fan delta are sourced from this gabbro bedrock.

The large-scale structure of the Caladonian nappes is controlled by the overall northwest to southeast emplacement of the major thrust units (Figure 5) (Corfu et al., 2014). In Troms county, post-Caladonian brittle, rift-related faults occur form NNE-SSW and ENE-WSW trending normal faults that are steeply to moderately dipping (Indrevær et al., 2013). Many of the valleys and fjords in the Lyngen region are structurally controlled, including the Lyngen peninsula (Figure 6A) (Osmundsen et al., 2010). A continental-scale tectonic lineament map has been produced using Landsat™ 7 data for Norway (Gabrielsen et al., 2002) and Figure 6B shows the lineaments mapped within Troms county are dominated by NE-SW lineament sets.

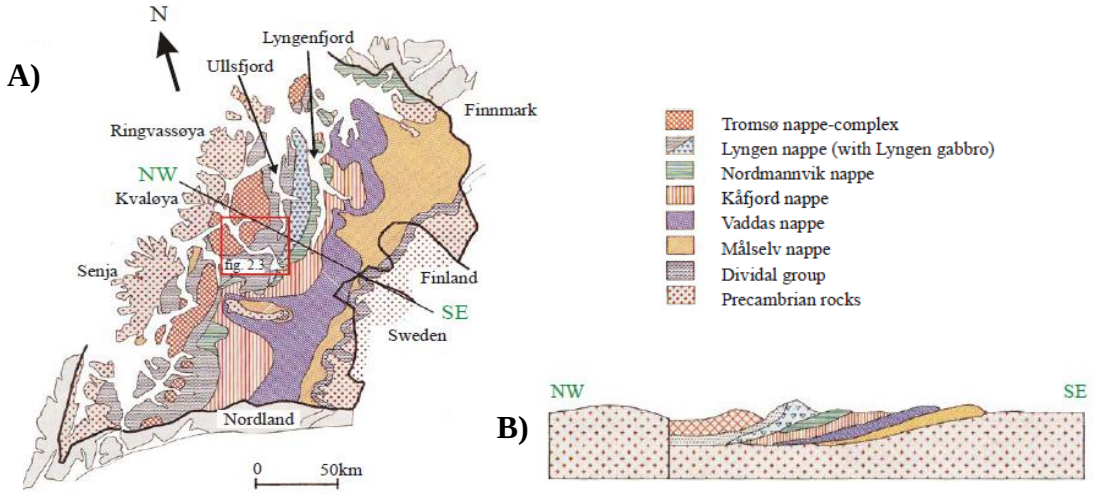

Figure 5: A) A geological map showing the distribution of Precambrian and Caledonian rocks in Troms County B) Schematic west-east profile showing the geology between Kvaløya and Sweden/Finland. Reproduced from Forwick (2001).

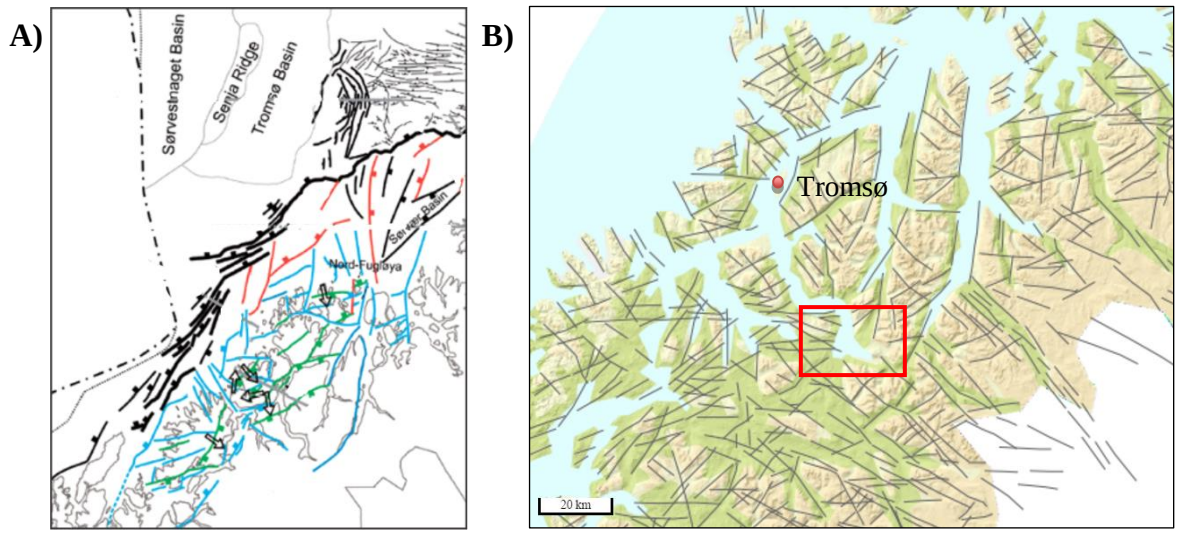

Figure 6: A) Regional tectonic map of the SW Barents Sea margin based on interpreted lineaments from onshore fieldwork (green lines), digital elevation model (blue lines), magnetic anomaly data (red lines) and seismic interpretation (black lines). Modified from Indrevær et al. (2013) B) Map of Troms county showing the lineaments identified using Landsat data (Gabrielsen et al., 2002). The head of Balsfjord is located within the red box.

Additionally, there is a lot of evidence of postglacial deformation in northern Norway (Olesen et al., 2013). For example, there is a 2 km long, NE-SW striking postglacial normal fault, called the Nordmannvikdalen fault, located near Kåfjord (Figure 1A) and a high concentration of rock-avalanche deposits occur within the vicinity of this fault (Olesen et al., 2013). Neotectonics within Troms county has been dominated by gravitational faulting resulting in slope failure and large-scale rock-avalanches. The distribution and timing of the rock-avalanches suggests there was major seismic activity immediately after deglaciation whereby several magnitude 7 or 8 earthquakes triggered rock-slope failures (Olesen et al., 2013).

1.2.3 Quaternary Geology

1.2.3.1 Glaciation and Deglaciation History

The Quaternary was a period of major environmental change. It is characterised by large and frequent temperature fluctuations creating a series of glacial periods separated by interglacials (Vorren and Mangerud, 2008, Olesen et al., 2013). These fluctuations resulted from a number of different factors including changes in the position of the continents, uplift of mountains, changes in the Earth's orbit (Milankovitch cycles), and changes in atmospheric chemistry (Bradley, 2015). Quaternary ice sheets have had a large effect on the Norwegian landscape creating deep fjords, U-shaped valleys and cirques (Corner, 2005a). Figure 7 shows the maximum extent of the ice sheets over northern Europe during the Quaternary. The Last Glacial Maximum (LGM) occurred in the Late Weichselian between 20 and 15 ka BP, and during the glacial maximum the Fennoscandian Ice Sheet advanced across the continental shelf to reach the shelf break along the entire length of Norway from the Norwegian Channel to Svalbard (Vorren and Mangerud, 2008, Olsen et al., 2013, Rydningen et al., 2013).

Figure 7: The extent of ice sheets in northern Europe during the Quaternary. Red line = LGM. White line = Saalian and Elsterian glaciations. Yellow stippled line = Quaternary maximum glacial extent. Reproduced from Olsen et al. (2013).

Deglaciation of the Fennoscandian Ice sheet occurred between 15.5 and 10 Ka BP due to increasing solar insolation. Deglaciation was rapid and the western margin of the Fennoscandian Ice Sheet was characterised by fjord-filling outlet glaciers that drained large parts of the ice sheet (Marthinussen, 1960, Marthinussen, 1962, Andersen, 1968, Sollid et al., 1973, Corner, 1978, Vorren and Elvsborg, 1979, Andersen, 1980, Corner, 1980, Kverndal and Sollid, 1993, Vorren and Plassen, 2002, Hald et al., 2003, Eilertsen et al., 2005, Mangerud et al., 2013, Stokes et al., 2014) and the Balsfjord glacier in northern Norway was one of these outlet glaciers (Fimreite et al., 2001, Forwick and Vorren, 2002).

Glacier readvancement occurred during a climatic cooling a period known as the Younger Dryas and Younger Dryas marginal moraines occur almost continuously along the coast of Norway (Vorren and Elvsborg, 1979, Andersen, 1980, Andersen et al., 1995). In Troms county, these marginal moraine deposits are called the Tromsø-Lyngen moraines (Figure 8). Retreat from the Tromsø-Lyngen moraines occurred rapidly around 12.1 ± 0.2 cal. Ka BP (10.4 Ka BP) (Forwick and Vorren, 2002, Stokes et al., 2014) and the chronology of the ice recession has been determined by radiocarbon dating of moraines and correlation to raised shorelines (Marthinussen, 1960, Marthinussen, 1962, Corner, 1980, Andersen et al., 1995, Forwick and Vorren, 2002, Stokes et al., 2014).

End moraines of Preboreal age occur inside the Tromsø-Lyngen moraines and they were deposited during a halt or readvancement of the retreating glaciers (Andersen, 1968, Andersen, 1980, Corner, 1980). These Preboreal climatic cooling events are called Stordal events (Andersen, 1968) and within the Lyngen-Storfjord area three Stordal events have been recorded: the Ørnes event 11.4 ± 0.2 cal. Ka BP (9.8-9.9 ± 150 Ka BP), the Skibotn event 10.8 ± 0.2 cal. Ka BP (9.5-9.6 ± 150 Ka BP), and a younger event 10.4 ± 0.2 cal. Ka BP (9.4 ± 250 Ka BP) (Corner, 1980, Stokes et al., 2014). Forwick and Vorren (2002) document the retreat of the glacier in Balsfjord and show that the Skjevelnes moraine was deposited during a the first Stordal event 11.4 ± 0.2 cal. Ka BP (10.3 – 9.9 Ka BP) (Andersen, 1968, Corner, 1980, Forwick and Vorren, 2002) and two minor end moraines, Tennes and Ryvoll, were deposited during further retreat of the Balsfjord glacier (Figure 8). Balsfjord was deglaciated by 10,942 ± 77 cal. BP (9.6 Ka BP) before the second Stordal event (Forwick and Vorren, 2002, Fenton et al., 2011).

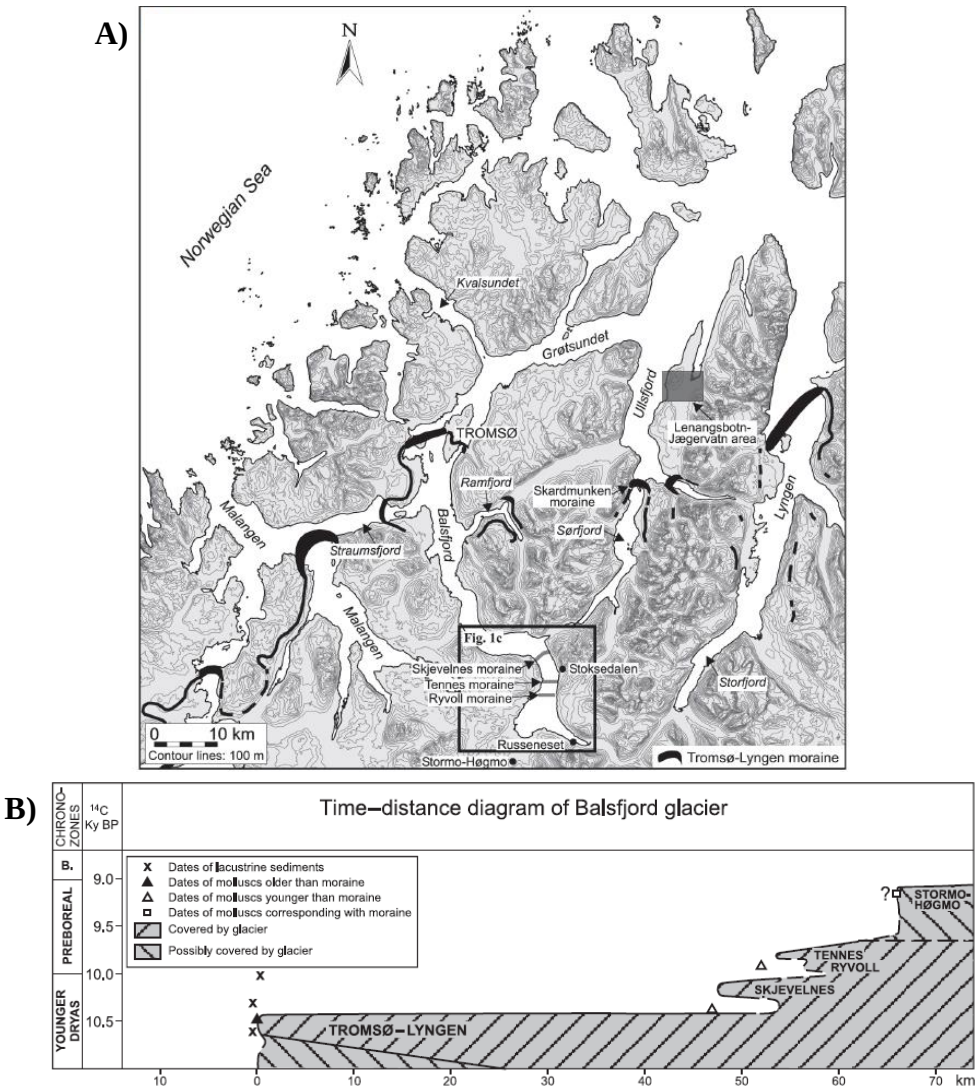

Figure 8: A) Map of the Troms county showing the location of the Tromsø-Lyngen moraines. The Preboreal moraines that were deposited within Balsfjord are shown within the black box. B) Time-distance deglaciation diagram of the Balsfjord glacier. Reproduced from Forwick and Vorren (2002).

1.2.3.2 Sea Level Change

The Fennoscandian Ice Sheet exerted a large load on the crust during glaciation, which created an isostatic crustal depression beneath the ice (Eronen, 2005, Vorren et al., 2008). Therefore, glacio-isostatic uplift has occurred across Fennoscandia during the deglacial and postglacial periods order to restore isostatic equilibrium (Vorren et al., 2008, Lowe and Walker, 2015). The rate of uplift is directly related to the thickness of ice, which creates uneven rates of uplift across Norway with the lowest rates occurring along the coast and the highest rates occurring inland where the ice was the thickest (Figure 9A).

In Norway, glacio-isostatic uplift has exceeded eustatic sea-level rise during the majority of the deglacial and postglacial period causing a relative sea-level fall (Corner, 2006). This has resulted in a sea level regression whereby old shorelines have been raised and coastal landforms such as deltas, spits, and ridges, are now located above sea level (Vorren et al., 2008, Lowe and Walker, 2015). Therefore, the position of past shorelines can be identified across Norway based on the identification

of both erosional and depositional geomorphological features, however, measurement of these features can be difficult and requires experience (Sollid et al., 1973, Corner, 1980).

The marine limit is a term given to the highest lying shore features (Vorren et al., 2008). The marine limit formed diachronously along the fjord as the glacier retreated and inner areas were progressively inundated by the sea and therefore, the marine limit becomes progressively younger inland (Figure 9B) (Marthinussen, 1960, Marthinussen, 1962, Corner and Haugane, 1993, Corner, 2006, Vorren et al., 2008). Due to differences in the rate of glacio-isostatic uplift, the height of marine limit varies from approximately 100 m.a.s.l. in the inner fjord areas to approximately 20 m.a.s.l. in the outer fjords areas in Troms county (Corner, 1980, Corner, 2006). Additionally, higher rates of uplift towards the former ice-sheet centre cause older (and higher) shorelines to have a greater tilt than younger shorelines (Sollid et al., 1973, Corner, 2006).

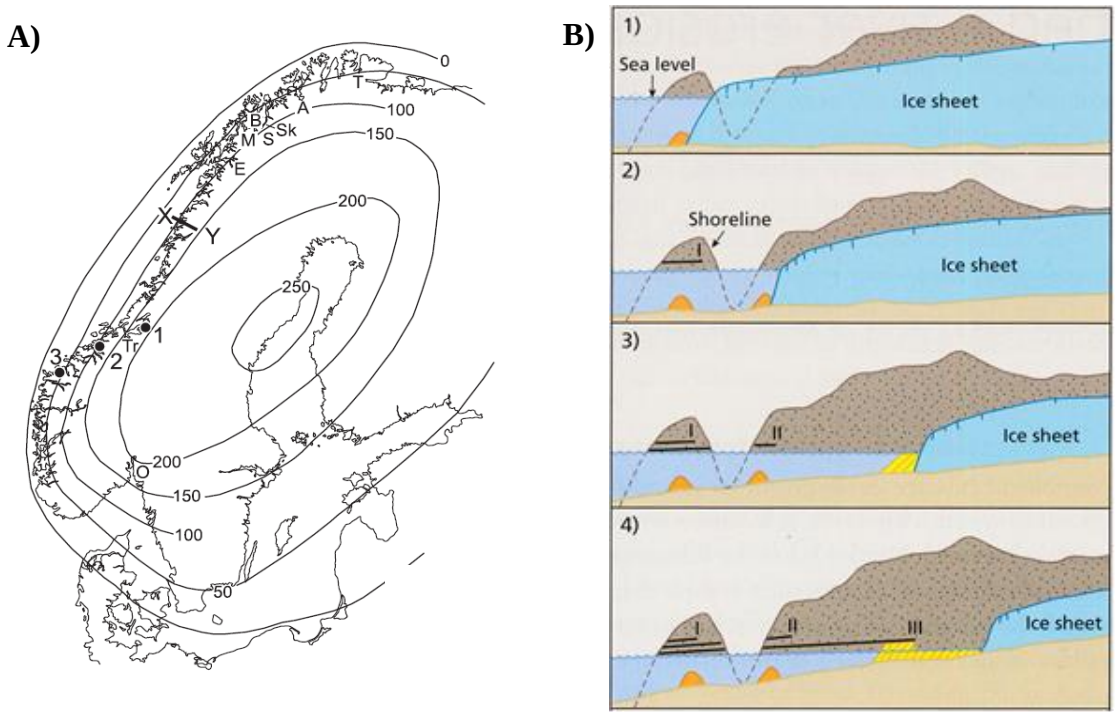

Figure 9: A) Isobases (in metres) showing the elevation of the postglacial marine limit across Scandinavia. Reproduced from Corner (2006). B) Schematic showing how the marine limit is formed diachronously as the glacier retreats. Reproduced from Vorren et al. (2008)

In the outer fjord regions of Troms county there are two particularly distinctive and laterally extensive raised shorelines, which were created during periods of sea level still stand or relative sea level rise: (1) the late glacial main shoreline (denoted S_0); and (2) postglacial Tapes shoreline (Andersen, 1968, Vorren et al., 2008). The main shoreline formed during the Younger Dryas (12.1 ± 0.2 cal. Ka BP; 11-12 ka BP) (Corner, 1980, Stokes et al., 2014) and corresponds to the Tromsø-Lyngen moraine. Therefore, it does not occur in the inner fjord areas that were still glaciated at the time of shoreline formation. The Tapes shoreline formed during an interval known as the Tapes transgression, which occurred in the mid-Holocene, c. 8 000 cal. yr BP, when the sea level rose faster than the rate of uplift in the outer fjord areas (Corner and Haugane, 1993, Bakke et al., 2005, Eronen, 2005, Corner, 2006, Vorren et al., 2008).

The deglacial and postglacial relative sea-level history of northern Norway is known from shoreline displacement curves (Marthinussen, 1962, Donner et al., 1977, Corner, 1980, Hald and Vorren, 1983, Møller, 1989, Corner and Haugane, 1993, Corner et al., 2001, Bakke et al., 2005) and shoreline

diagrams (Marthinussen, 1960, Marthinussen, 1962, Andersen, 1968, Sollid et al., 1973, Corner and Haugane, 1993). Isobases for the extended S_0 shoreline (main shoreline) over Balsfjord are shown in Figure 10A. In Troms county, four Holocene shoreline displacement curves have been constructed (Corner, 1980, Hald and Vorren, 1983, Corner and Haugane, 1993, Bakke et al., 2005) and most of the reconstructions are based on the early works of Marthinussen (1960, 1962).

A shoreline emergence curve for inner Balsfjord, Troms county, has been constructed for this study based on the elevation of the marine limit and Tapes shorelines at Russenes and the rates and trends in sea level fall obtained from the previously published shoreline emergence curves (Figure 10B). This curve shows two different rates of sea level change during the Holocene; (1) sea level fall was relatively rapid during the deglacial period (before 10,000 cal. yr BP); and (2) sea level fall was much slower during the postglacial period (after 7,000 cal. yr BP) (Corner and Haugane, 1993). Today the rate of uplift along the coast of Troms county is 1 – 1.5 mm/yr (Olesen et al., 2000).

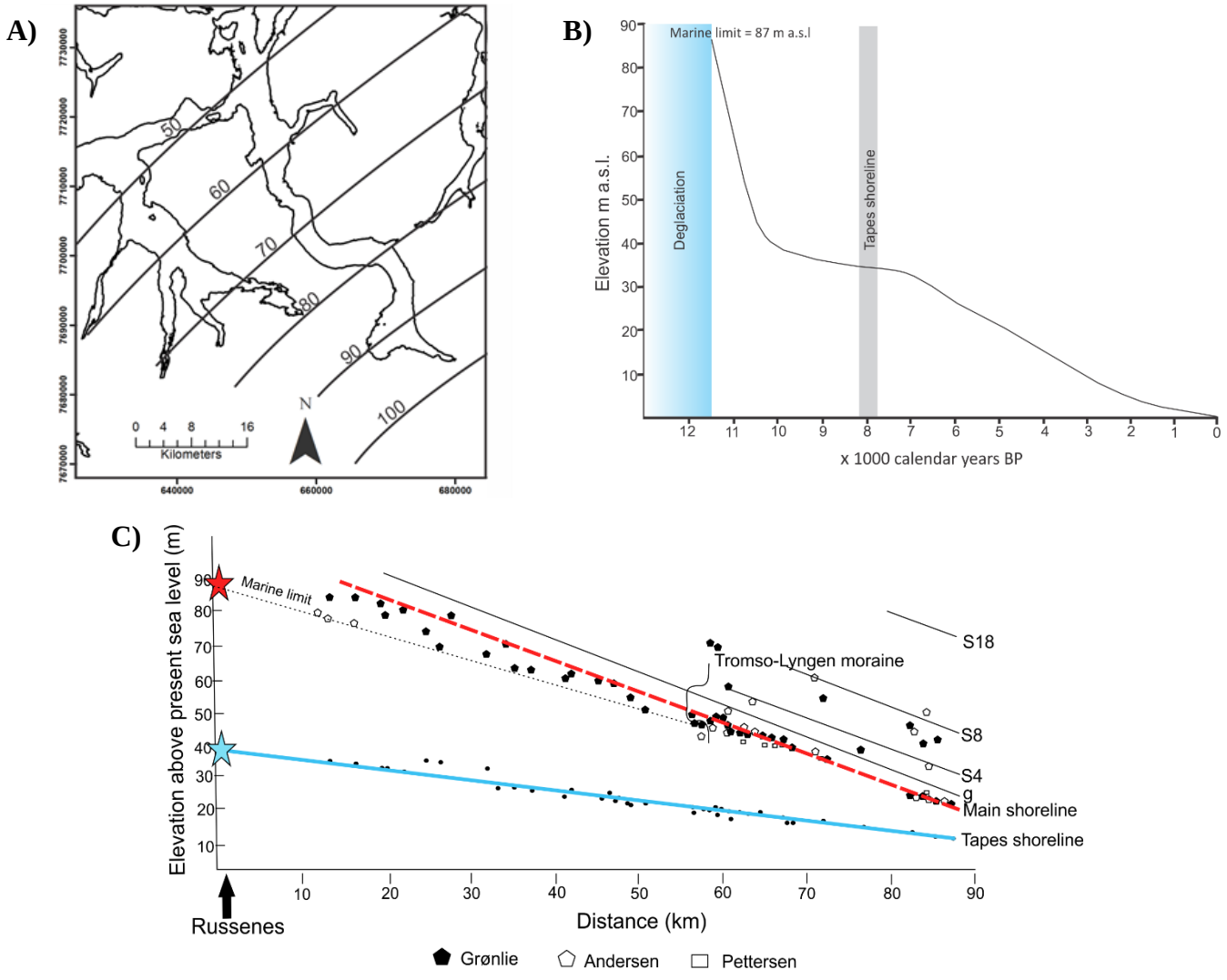

Figure 10: A) Isobases over Balsfjord for the extended S_0 (main shoreline) constructed using isobases from Corner (1980) as well as Marthinussen (1960), Andersen (1968) and Møller (1989). B) Shoreline emergence curve for inner Balsfjord, Troms county. This curve has been produced based on the elevation of marine limit and Tapes shorelines at Russenes and the trends in the rate of sea level fall documented by other shoreline emergence curves from Norway (Corner, 1980, Corner and Haugane, 1993, Bakke et al., 2005, Romundset et al., 2010). C) Equidistant shore-line diagram for the Balsfjord area modified from Andersen (1968). The points represent field observations of raised shorelines collected across the Balsfjord (Pettersen, 1880, Pettersen, 1884, Helland, 1899, Grønlie, 1914, Grønlie, 1940, Grønlie, 1951, Andersen, 1968). The data points outside the Tromsø-Lyngen moraine represent the highest observed raised shorelines in Balsfjord. The stars show the approximate location of the marine limit (red) and Tapes (blue) shorelines at Russenes.

Andersen (1968) constructed an equidistant shoreline diagram for the Balsfjord area (Figure 10C) based on the identification of raised shorelines by a number of different researchers (Pettersen, 1880, Pettersen, 1884, Helland, 1899, Grønlie, 1914, Grønlie, 1940, Grønlie, 1951, Andersen, 1968). Figure 10C shows that measurements of the Tapes shoreline in Baslfjord plot close together, which confirms the shoreline is very distinctive. The elevation of the Tapes shoreline has been extrapolated to show that the approximate elevation at Russenes is 40 m a.s.l. In contrast, it is often difficult to identify the exact height of the marine limit. Figure 10C shows a wide spread of data corresponding to the highest observed raised shorelines in Balsfjord and many of the measurements for the marine limit are too high (e.g. almost as high as the So shoreline). Therefore, the approximate position of the marine limit at Russenes has been extrapolated based on the lowest recorded shorelines on the diagram of Andersen (1968) to give an elevation of 87 m a.s.l.

1.2.3.3 Postglacial Sedimentation

Glaciers are powerful agents of erosion and therefore, the present-day sedimentary deposits within Balsfjord were deposited during the deglacial and postglacial periods following the LGM. Figure 11 presents a Quaternary geological map of the study area created from digital data available from Norges Geologiske Undersøkelse. This map shows that landslide and till deposits are the dominant sediment type deposited on the steep slopes surrounding the fjord and fluvial and marine deposits are the dominate sediment type deposited below the marine limit. Sedimentary depositional processes within fjords are discussed in detail in Chapter 0.

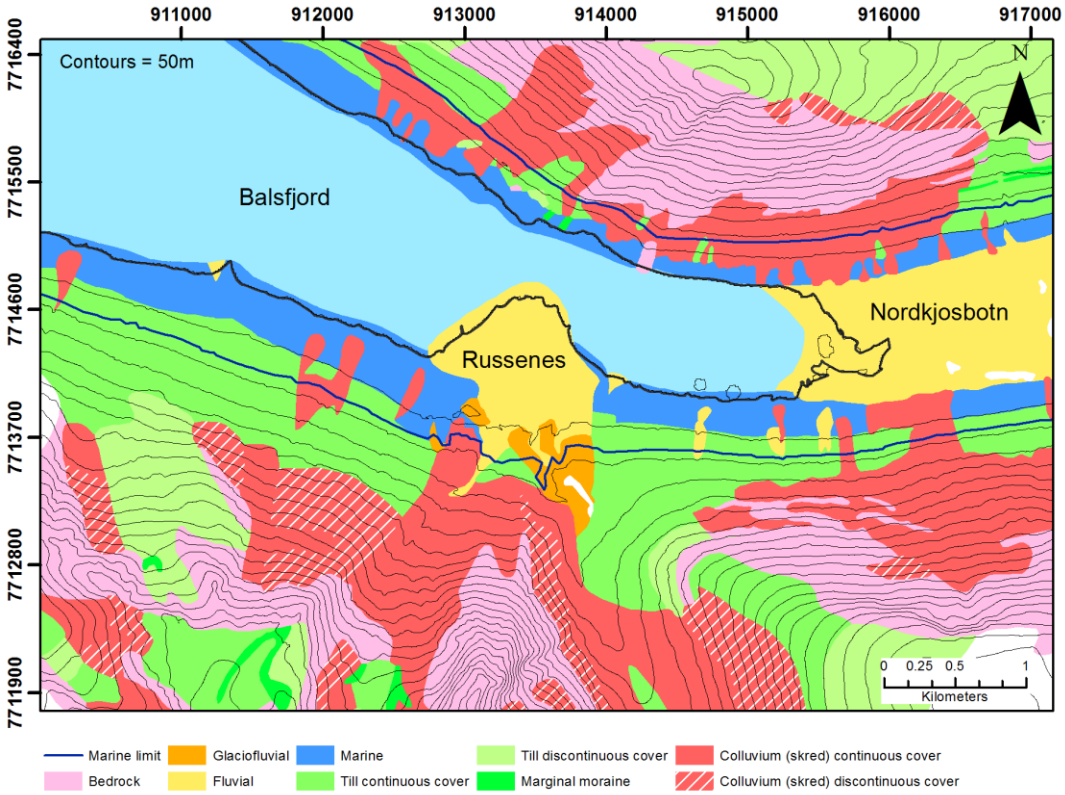

Figure 11: Quaternary geology map of the study area created from the Løsmasser N50/N250 digital dataset available from Norges Geologiske Undersøkelse (NGU, 2015b). This dataset provides national-scale information about the surficial sediments in Norway at various scales. The sediment boundaries shown in this figure have primarily been produced from Sletten et al. (2006) at the 1:15 000 scale. The sediment type displayed in the legend has been translated from Norwegian.

1.2.3.4 Holocene Climate Reconstructions

Global Holocene climatic fluctuations have been determined using a wide range of different proxies, such as ice cores, pollen, foraminifera, and speleothems. In northern Scandinavia, there are a few continuous temperature reconstructions for the Holocene based on proxies, such as pine-tree limit fluctuations, pollen, chironomids and speleothems (Figure 12) (Alm, 1993, Vorren and Alm, 1999, Seppä and Birks, 2001, Korhola et al., 2002, Seppä et al., 2002a, Seppä and Birks, 2002, Seppä et al., 2002b, Bakke et al., 2005, Lilleøren et al., 2012).

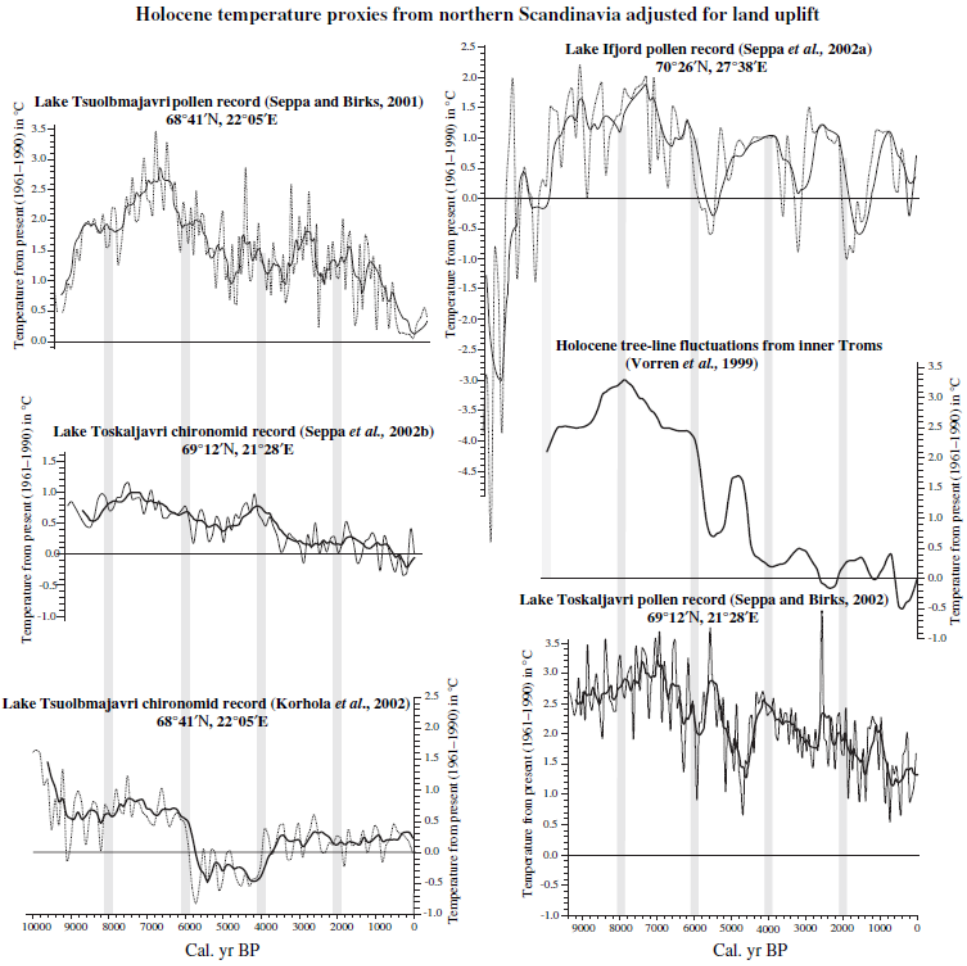

Figure 12: Continuous temperature reconstructions of the Holocene across northern Scandinavia, which have been adjusted for uplift. The source of the data is given in the graph titles. Reproduced from Bakke et al. (2005).

Nonetheless, the major climatic trends of the Holocene have been reconstructed for northern Norway and consist of: (1) a humid oceanic climate during the early Holocene (Bjune et al., 2004); (2) a warm period, known as the Holocene Thermal Optimum (HTO), in the mid-Holocene (8,500 and 4,500 cal. yr BP); and (3) a period of gradual cooling, known as the Neoglacial cooling period, which commenced approximately 4,000 cal. yr BP (Bakke et al., 2005). However, the coldest part of the Neoglacial period did not occur until the Little Ice Age (LIA) between $_{AD}$ 1600 to 1900.

Many high altitude polythermal (subpolar) glaciers occur within a zone of discontinuous permafrost across Norway (Bakke et al., 2005) and fluctuations in glacier size and equilibrium-line altitude (ELA) are another sensitive proxy for variations in climate. Consequently, glacier fluctuations during the Holocene have been determined at a number of locations across Norway in order to reconstruct the

paleoclimate (Dahl and Nesje, 1992, Dahl and Nesje, 1996, Bakke et al., 2005, Bakke et al., 2010). In addition, the study of glacier fluctuations in Norway during the Holocene can provide information about the dynamics of the cirque glaciers within the study area.

Figure 13 shows a reconstruction of fluctuations in the ELA for a glacier located in the northern Lyngen Alps (Bakke et al., 2005). This area was deglaciated well before inner Balsfjord and the reconstruction shows that cirque glaciers fluctuated during the early Holocene (11,500 – 8,800 cal. yr BP) whereby three glacial advances have been recorded (Bakke et al., 2005). The climatic warming period that occurred during the mid-Holocene (HTO) caused most cirque glaciers in northern Norway to disappear including the glaciers in Lyngen. Glacier growth recommenced in the Late Holocene (3,800 cal. yr BP), but, in most locations the evidence of major glacier advancement events has been destroyed by the most recent glacier advance of the Little Ice Age glacier, which reached its maximum extent at *c.* $_{AD}$ 1910 (Ballantyne, 1990, Bakke et al., 2005).

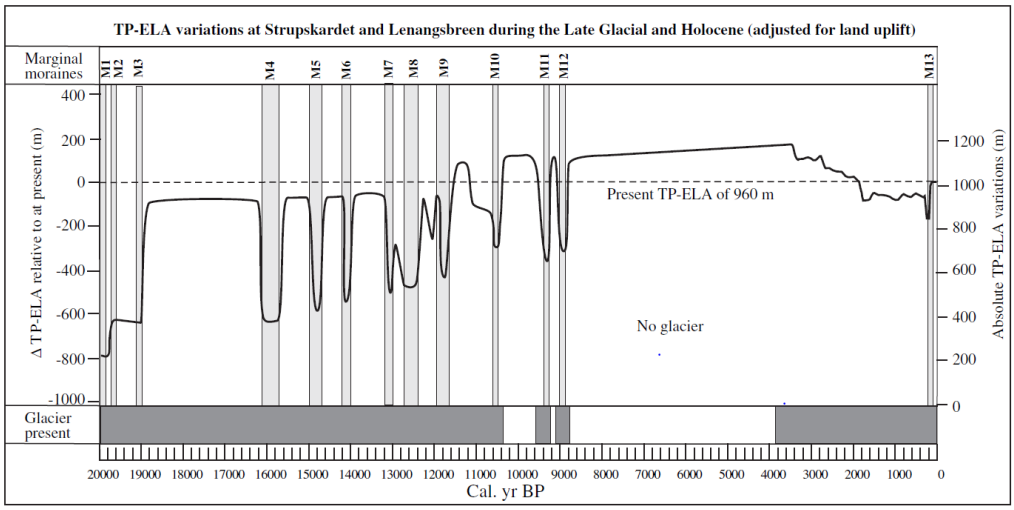

Figure 13: Mean Temperature-Precipitation-Wind Equilibrium Line Altitude of Lenangsbreene in Strupskardet, Lyngen, from 20,000 cal. yr BP to the present. Reproduced from Bakke et al. (2005).

1.3 Previous Work

The deglaciation history of Troms county has been studied over several decades by many different researchers (Marthinussen, 1962, Andersen, 1968, Vorren and Elvsborg, 1979, Andersen, 1980, Corner, 1980, Stokes et al., 2014) and the deglaciation history of Balsfjord has been documented by Forwick and Vorren (2002). The study area is included in a number of Quaternary geological maps produced by Norges Geologiske Undersøkelse (NGU) including maps by Sveian et al. (2005) and Sletten et al. (2006). These maps are now available digitally as a combined Løsmasser N50/N250 dataset, which represents the surficial material at various scales and Figure 11 shows a map of surficial sediment within the study area produced using this dataset.

The tall mountains surrounding Balsfjord make it susceptible to mass movement processes (Forwick and Vorren, 2002) and many of the landslide deposits within the Russenes fan delta have been previously mapped (Sletten et al., 2006). For example, the front of the rock avalanche deposit has been studied in detail (Blikra et al., 2006, Sletten et al., 2006, Fenton et al., 2011). Recently, the Norwegian Geotechnical Institute (NGI) and the Norwegian Water Resources and Energy Directorate (NVE) have assessed the risk of "skred" mass movement processes and created hazard risk maps for various locations (Sandersen, 2011, Eidsvåg and Øystein, 2016). Skred is a Norwegian term that represents many different mass movement processes in English including flooding, debris flows and snow avalanches. Figure 14 shows the results of the "skred" hazard mapping within the study area. The results suggest that the highest probability of mass movement processes occurs along the Buktelva river.

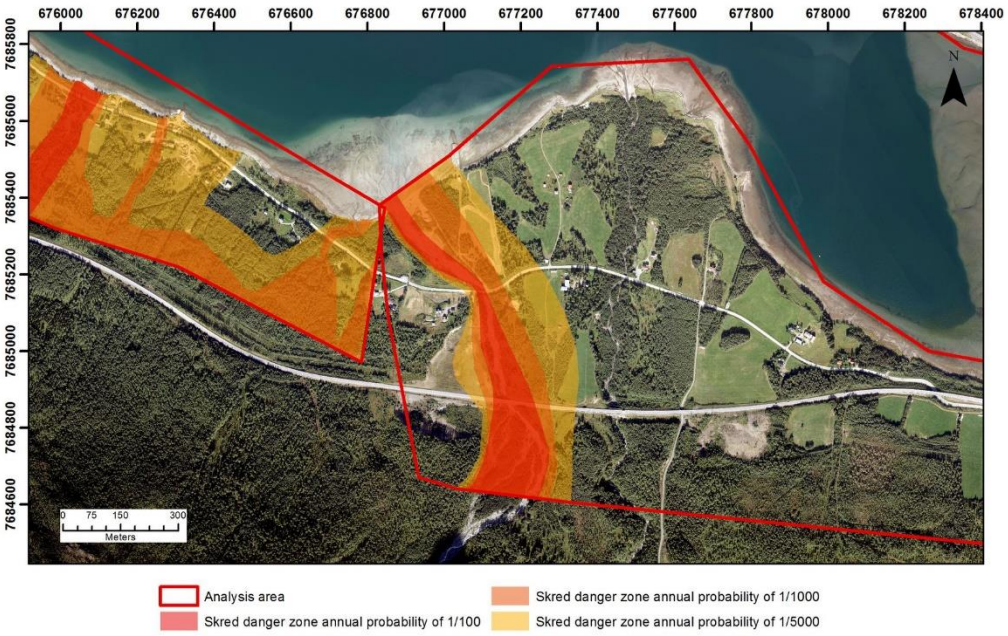

Figure 14: Map of the skred danger zones for Russenes that have been identified by NVE and NGI. Skred is a Norwegian term that is difficult to translate into English. The term corresponds to many different mass movement processes in English, including flood, debris flow, landslide and snow avalanche processes. These danger zones are defined by Eidsvåg and Øystein (2016) and Sandersen (2011) and the polygons can be downloaded from www.nve.no/flaum-og-skred/.

2 Fjord Geomorphology and Sedimentary Processes

A fjord is a deep high latitude estuary that has been (or is presently being) excavated or altered by land-based ice (Syvitski et al., 1987, Syvitski and Shaw, 1995). Fjords are formed by extensive glacial erosion and occur along fault or lithology controlled zones or incisions created by fluvial activity. Therefore, the location of fjords is controlled by the presence of current or former ice sheets. Fjords are a geomorphological landform, which consists of a long steep sided coastal trough that has been inundated by the sea (Figure 15) (Syvitski et al., 1987, Howe et al., 2016). Fjords are U-shaped in cross-section and often have a sill at their entrance, which restricts the movement of deep water (Skei, 1983, Syvitski and Shaw, 1995, Vorren et al., 2008). Fjords occur at the transition of the terrestrial and marine environments and their sediments often preserve a high resolution continuous record of climate and environmental change (Syvitski and Shaw, 1995, Corner, 2005a, Howe et al., 2016).

Figure 15: Photograph of Ersfjord in northern Norway, which has a characteristic fjord geomorphology with a long, narrow and deep coastal inlet and mountainous steep-sides. Photo by Rowan Romeyn.

2.1 Fjord Sedimentation

Fjords are semi-enclosed marine basins that have a large accommodation space (Skei, 1983, Howe et al., 2016). Fjords are efficient sediment traps (Syvitski and Shaw, 1995). Large volumes of sediment are deposited within fjords during interglacial periods and subsequently removed by erosion during glacial periods (Corner, 2006, Howe et al., 2016). Most of the sediment accumulated within fjords relates to the deglacial and postglacial sedimentary processes after the last major ice advance (Syvitski and Shaw, 1995). Fjords usually have a high sedimentation rate and the sediment is primarily transported to the fjords through fluvial, glaciofluvial and mass movement processes. This sediment commonly completely fills the inner part of the fjord creating a fjord valley (Corner, 2006, Eilertsen et al., 2006).

Fjord sediments are derived from many different sources (Hambrey, 1994). Corner (2006) divides fjord sedimentation into two stages: (1) a deglacial stage whereby glacier meltwater deposits a large amount of sediment in front of a retreating glacier; and (2) a postglacial stage whereby most of the sediment that is deposited into the fjord is derived from fluvial discharge. Sediment deposited within

fjords during the deglacial stage results from a complex interplay of different processes, such as glacier meltwater discharge, suspension settling, iceberg rafting and mass movement process. These processes can form a range of different depositional features, including ice-front accumulations and glaciomarine and glaciofluvial deposits (Hambrey, 1994, Corner, 2006, Howe et al., 2016). These processes and products are outlined in Figure 16A.

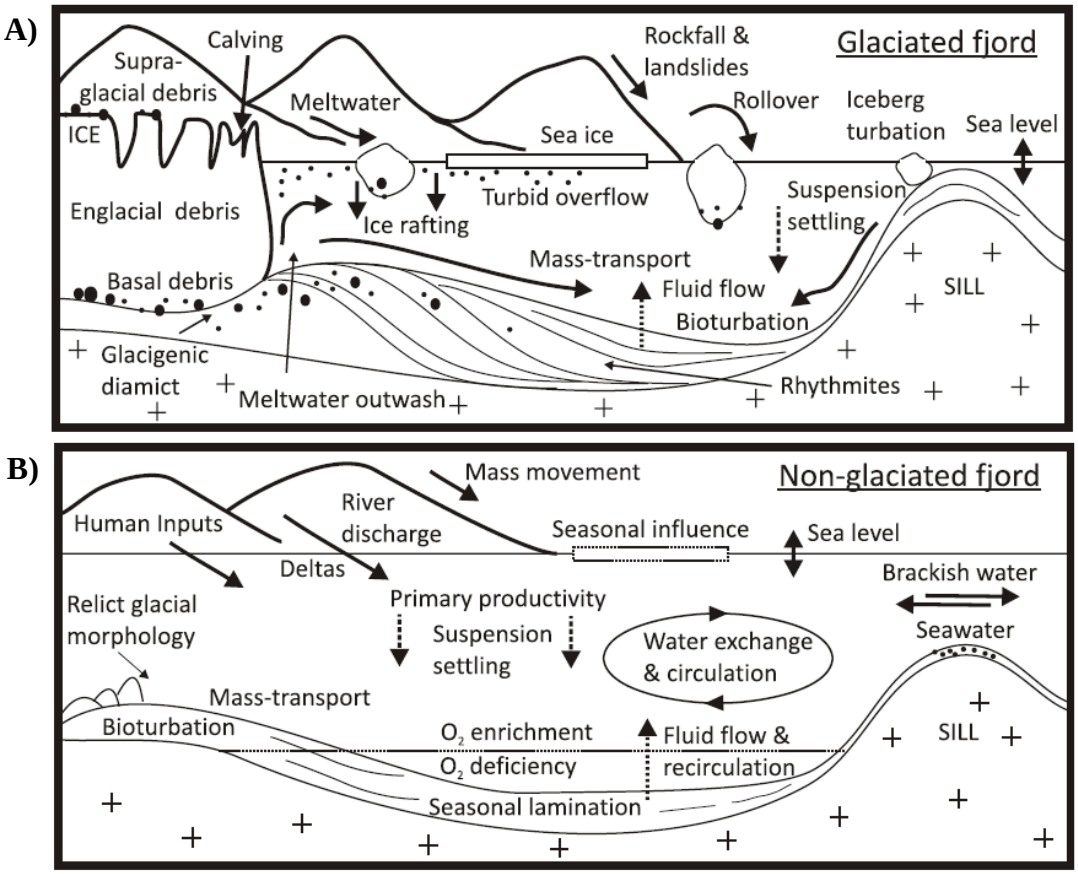

Figure 16: Principle processes and deposits within fjords A) during the deglaciation stage and B) during the postglacial stage. Reproduced from Howe et al. (2016).

During the postglacial stage the majority of sediment is supplied to the fjord by rivers and the rate of sediment accumulation is often directly connected to river dynamics (Syvitski and Shaw, 1995). Glacio-isostatic uplift can cause rapid fluvial erosion (Figure 10B) (Vorren et al., 2008). The sediment is usually locally derived, immature, and coarse-grained. The coarsest sediment (e.g. gravel and sand) is usually deposited at the head of the fjord forming deltas and outwash fans (Howe et al., 2016), whilst the fine-grained component (e.g. silt and clay) is carried by hyperpycnal plumes and turbidity currents to the base of the fjord. Subaqueous slope instabilities are common due to the deposition of a high sediment load on steep slopes (Howe et al., 2016). The deposition of fluvial sediment varies seasonally and can occur in a rapid or pulsed manor (Skei, 1983). Other sources of fjord sediment include rockfall, aeolian sediment and mass movement deposits, however, the total sediment input from these sources is low (Hambrey, 1994).

2.1.1 Glaciofluvial Deposits

Glaciofluvial deposits are formed by the deposition of sediment from glacial meltwater. Glaciofluvial sediment is usually composed of sand, gravel and cobbles that have been transported by the glacier and the sediment is sorted and stratified by fluvial processes. Glaciofluvial sediment is deposited in a wide variety of different settings, for example, as esker ridges, kames or ice front accumulations deposited directly in contact with the ice (Leeder, 1999). If glaciers terminate on land, glaciofluvial sediment is deposited as outwash plains or sandurs, which are dominated by braided streams fed by glacier meltwater. Glaciofluvial deltas occur where glacial meltwater enters a standing body of water and these deltas can be classified as Gilbert-type deltas with steeply dipping foreset beds composed of gravel and sand (Gilbert, 1885, Corner, 2006).

2.1.2 Ice Front Accumulations

Ice front accumulations are sedimentary deposits that are formed in contact with a glacier (Powell, 1990, Lønne, 1995, Lowe and Walker, 2015). During continuous retreat of a glacier ice-proximal sediments are deposited as a thin layer on the floor of the fjord, whilst thick ice front accumulations are created during halting or readvance of the glacier (Corner, 2006). Ice front accumulations can have a range of sizes and shapes and they often have a complex structure, including fans, ridges and ice-contact deltas (Powell, 1990, Lønne, 1995, Corner, 2006).

Ice front accumulations are a type of glaciofluvial deposit because they are predominately formed through the discharge of subglacial and englacial streams, which can carry large amounts of fluvial bedload and suspended load sediment directly into the marine environment (Benn and Evans, 1998). Submarine discharge occurs as a turbulent jet, which creates a plume that rises upwards because the sediment-laden water is less dense than the surrounding seawater (Hambrey, 1994, Syvitski and Shaw, 1995, Benn and Evans, 1998). The coarsest sediment is deposited quickly close to the discharge point, whilst the finer material is transported further by the jet. Therefore, ice front accumulations consist of relatively coarse sand and gravel, which fines rapidly down the fjord (Syvitski and Shaw, 1995, Benn and Evans, 1998, Corner, 2006).

2.1.3 Glaciomarine Deposits

Glaciomarine sediments are usually composed of sand, silt and clay that is deposited in the fjord by suspension settling of fine material from meltwater plumes, or through turbidity currents created by slope failure (Corner, 2006). Glaciomarine sediments usually have parallel laminated bedding, however, some sedimentary structures, such as cross-bedding, can occur in proximal high energy settings (Corner, 2006, Howe et al., 2016). Glaciomarine rhythmites can also occur due to variations in discharge or tidal energy and iceberg-rafted debris may be present in glaciomarine sediment (Corner, 2006, Howe et al., 2016).

2.2 Deltas

Deltas are coastal landforms that occur where rivers discharge sediment into a standing body of water (e.g. a lake or the sea). Deltas have both subaerial and subaqueous components and are regressive landforms (Giosan and Goodbred Jr, 2007, Bhattacharya, 2010). Deltas are complex sedimentary systems and the morphology of a delta results from the interplay between sediment supply (fluvial sediment discharge), accommodation space and the redistribution of sediment by coastal processes (e.g. tides and waves) (Giosan and Goodbred Jr, 2007). Deltas are often classified based on the tripartite classification system of Galloway (1975) where it was recognised that different ratios of fluvial, wave and tidal processes in delta systems produces different and recognizable plan-view morphologies (Figure 17A) (Bhattacharya, 2010).

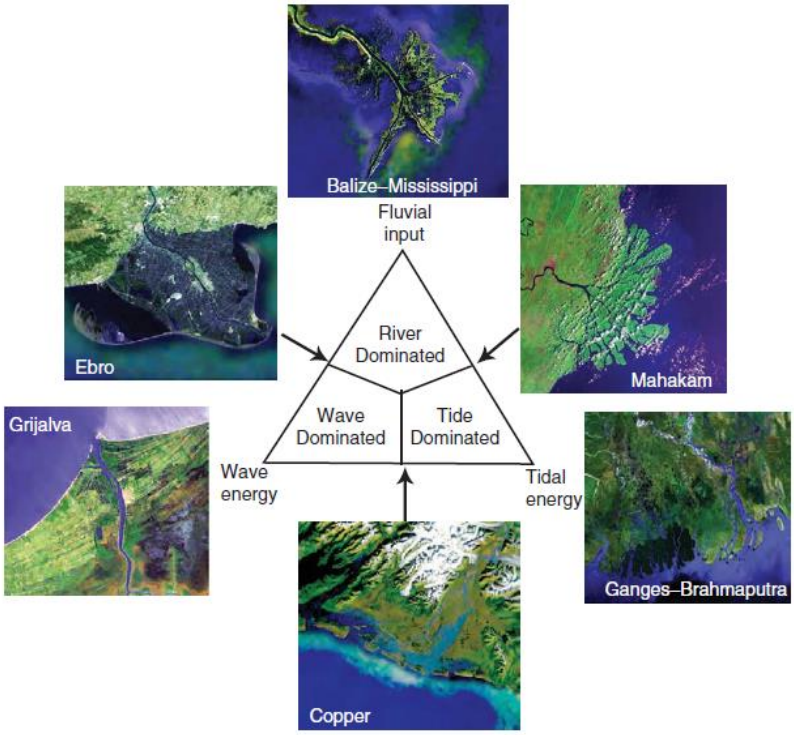

Figure 17: Process-based tripartite classification of delta morphology based on the relative influence of fluvial discharge and wave and tidal energy. Reproduced from Giosan and Goodbred Jr (2007) after Galloway (1975).

A delta is formed when sediment-rich river water enters a standing body of water and loses its ability to carry the sediment resulting in a deposit at the month of the river (Bhattacharya, 2010). The flow of a river entering a standing body of water is described as a free turbulent jet and the competence and capacity of the flow decline with distance from the river mouth (Anderson and Anderson, 2010). As the river water is discharged into the standing body of water the sediment load carried by the river separates into two components: the coarse-grained bedload and the fine-grained suspended sediment. The bedload material is rapidly deposited onto the delta slope as the competence of the flow decreases, whilst the suspended sediment is carried seaward by a sediment plume and undergoes suspension settling (Syvitski and Shaw, 1995). The subaqueous delta slope is highly unstable and the rapid deposition of the bedload can result in over steepening of the delta slope (Leeder, 1999, Anderson and Anderson, 2010). This causes the redistribution of sediment by slumping or gravity flows to maintain slope stability. The unstable sediment often completely liquefies and develops into turbidity currents (Syvitski and Shaw, 1995).

2.2.1 Fjord-Head Deltas

Fjord-head deltas are very common across Norway and other high latitude countries such as Canada and Greenland (Corner et al., 1990, Corner et al., 1996, Corner, 1998, Gutsell et al., 2004, Eilertsen et al., 2006, Eilertsen et al., 2011). These deltas occur at the interface between fjords and fjord valleys and they usually undergo rapid progradation due to a high sediment supply and a restricted accommodation space created by the steep-sided fjord setting (Gutsell et al., 2004). Figure 18 shows the dominant sedimentary processes that occur within fjords that are not currently influenced by glaciers and the processes forming a fjord-head delta are shown.

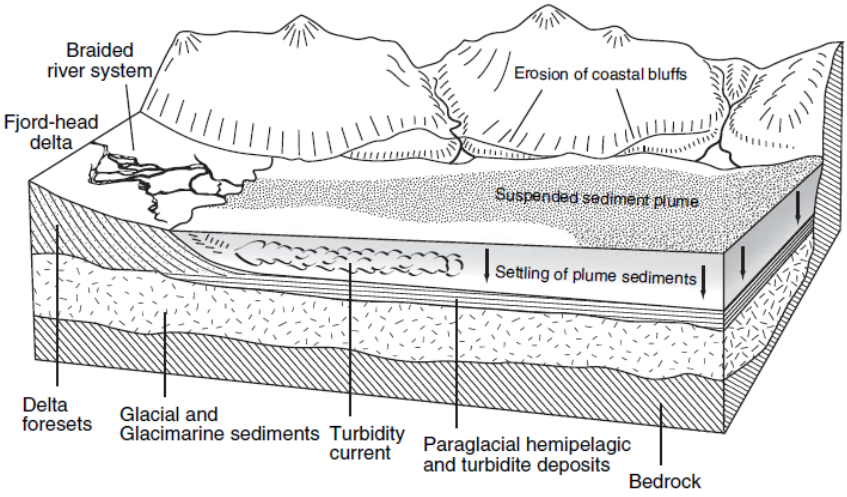

Figure 18: Sketch showing the dominant sedimentary processes that occur within a fjord environment. Most of the sedimentation occurs at the head of the fjord and results in the progradation of a fjord-head delta. Reproduced from Ballantyne (2007).

There is currently no universal nomenclature system for classifying the different geomorphological environments within deltas. In northern Norway, a classification system is being developed for fjord-head deltas. The flatly lying intertidal to subtidal region is called the delta plain and the delta plain terminates at a sharp boundary called the delta rim. The delta slope occurs after the delta rim and it has a concave profile with an initial steep gradient of 35° that decreases to approximately 5° at the base. The delta slope transitions into a deep, flatly lying prodelta area (3 to 4°) followed by an open fjord environment (Figure 18) (Corner et al., 1990, Eilertsen et al., 2006).

Fjord-head deltas can be classified as Gilbert-type deltas (Gilbert, 1885) because they are coarse-grained deltas with a steep foreset slope and tripartite structure (Corner et al., 1990, Gutsell et al., 2004). The tripartite structure forms a distinctive prograding clinoform morphology with a flat top (topset), steeply dipping front (foreset) and relatively flat lying bottom sediment (bottomset) (Figure 19) (Anderson and Anderson, 2010). The prodelta bottomset forms in the distal part of the delta and is composed of fine grain sediment deposited from suspension settling and turbidity flows. The prodelta forest beds are steeply inclined and deposited on pre-existing bottomset beds. These foreset beds are formed by the deposition of river bedload material and the redistribution of sediment by gravitational mass movement processes. The topset beds are predominately deposited by fluvial processes on the subaerial delta plain and can erode pre-existing foreset beds (Bhattacharya, 2010). This prograding clinoform architecture produces an upward coarsening facies succession (Giosan and Goodbred Jr, 2007).

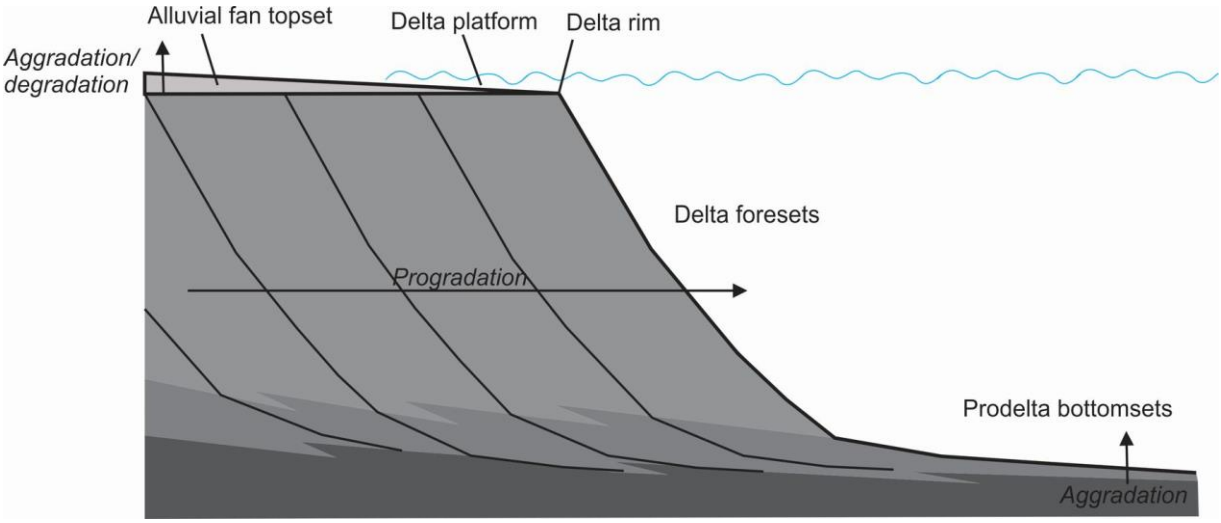

Figure 19: Idealized cross-section showing the different depositional environments and internal geometry of a prograding Gilbert-type delta. Modified from Eilertsen et al. (2011) and Corner et al. (1990).

2.2.2 Fan Deltas

A fan delta is defined as an alluvial fan that is prograding directly into a standing body of water from an adjacent highland (Holmes, 1965, McPherson et al., 1987). Therefore, fan deltas only occur in specific physiographical settings such as in front of mountains, volcanic highlands and escarpments produced by active faulting (McPherson et al., 1987). Fan deltas can develop along the edge of fjords that are surrounded by high mountains, however, they are not commonly observed in northern Norway.

Fan-deltas are coarse-grained (gravel-rich) Gilbert-type deltas that have a very steep gradient (McPherson et al., 1987). Therefore, fan deltas usually have the foreset, topset and bottomset bedding structure of Gilbert-type deltas (Gilbert, 1885) and their sediment is immature due to their close proximity to the source area (Wescott and Ethridge, 1990). Fan deltas have an overall wedge or prism shaped geometry that thins away from the mountain front (Wescott and Ethridge, 1990). The thickness and extent of a fan delta depends on the complex interplay of the following processes: uplift or sea level fluctuations, sediment supply and basin subsidence (Wescott and Ethridge, 1990, Corner, 2006).

Fan deltas have distinctive subaerial and subaqueous depositional environments (Figure 20). The subaerial component is aggradational and consists of an alluvial fan, which is a fan-shaped (radial) accumulation of sand and gravel deposited by water (channelized and unchannelized flow) and sediment gravity processes (cohesive and non-cohesive) (McPherson et al., 1987, Galloway and Hobday, 1996). The depositional processes may include debris flows, debris avalanches, hypoconcentrated stream flows and mud flows and these processes are often highly irregular, flashy and sometimes catastrophic in nature (McPherson et al., 1987). Fan deltas have a transitional zone between the subaerial and subaqueous depositional environments where fluvial processes are modified by marine processes, such as waves, tides and currents (McPherson et al., 1987, Wescott and Ethridge, 1990). The subaqueous depositional environment of a fan delta is very similar to that of a fjord-head delta with sediment gravity processes, such as debris flows, slumping and turbidity currents, redistributing sediment on the delta slope.

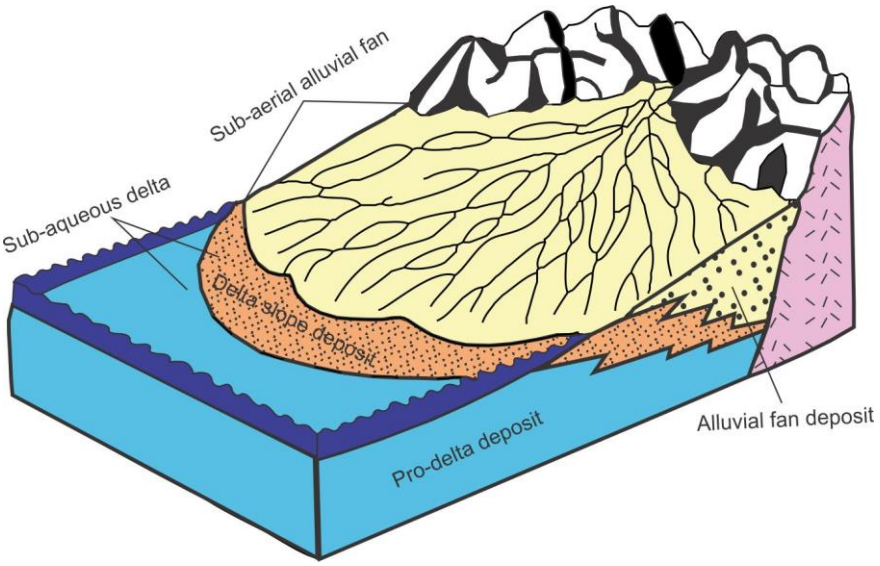

Figure 20: Schematic of an ideal unconfined fan delta showing the different subaerial and subaqueous depositional environments. Modified from Nemec and Steel (1988).

2.3 Mass Movement Processes

Retreat of glaciers during deglaciation often leaves mountain slopes over-steepened, unsupported and unstable and a large amount of unconsolidated paraglacial sediment can be exposed on the steep-sided fjords (Benn and Evans, 1998, Ballantyne, 2007, Vorren et al., 2008). Therefore, these slopes often undergo a phase of high landslide activity in order to restore slope stability and the gravitational mass movement of sediment is an important process for sediment transport (Benn and Evans, 1998). Mass movement processes are significant for transporting and redistributing sediment within two different environments on fan deltas: (1) the subaerial alluvial fan; and (2) the subaqueous delta.

2.3.1 Mass Movement Processes within Alluvial Fans

Mass movement processes, such as rockfalls, rockslides, rock-avalanches and debris flows, can transport sediment from the catchment area of alluvial fans onto the fan surface (Blair and McPherson, 2009). These mass movement processes are primarily triggered by intense rainfall or earthquakes, and therefore, they are usually infrequent, short-lived events that result in the aggradation of sediment within the alluvial fan (Blair and McPherson, 2009).

2.3.1.1 Rock Slope Failures

Rock slope failures have had fatal consequences in Norway in recent times. For example, tsunamis were created from rockfall in western Norway (Tafjord in 1934 and Loen in 1905 and 1936), which resulted in a combined loss of 174 lives (Braathen et al., 2004, Vorren et al., 2008, Romstad et al., 2009). In Troms county there is one historical record of a rock-avalanche, which created a tsunami in Lyngen fjord in 1810 that killed 14 people (Vorren et al., 2008). Consequently, it is important to be able to predict rockfalls in the future. 150 gravitational slope failures have been mapped in the Balsfjord-Lyngen-Kåfjord region and these are shown in Figure 21 (Olesen et al., 2000, Vorren et al., 2008).

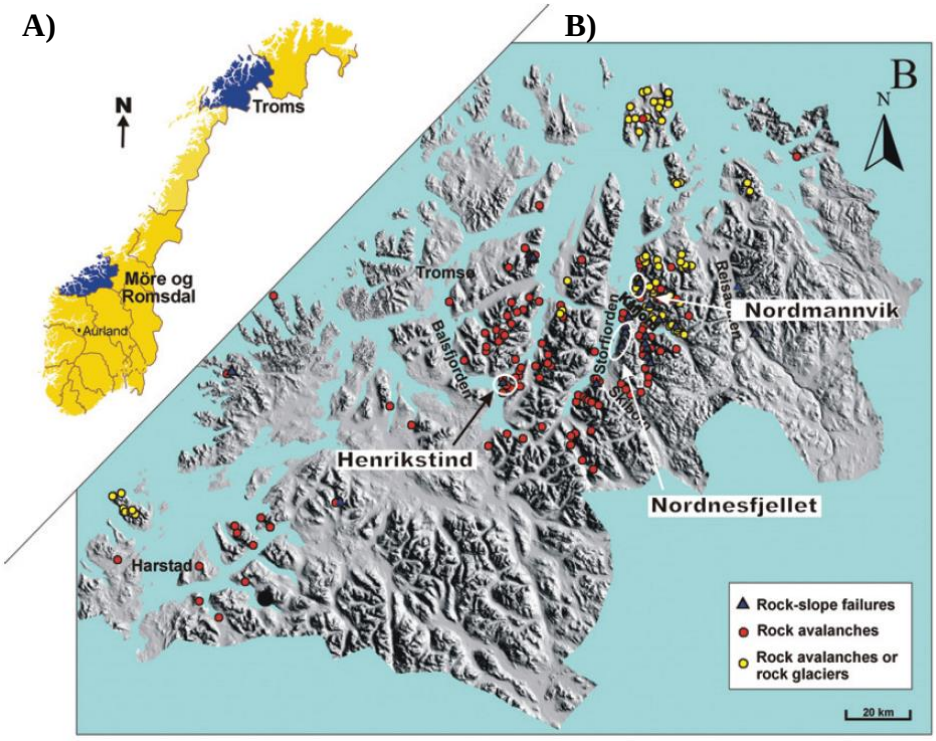

Figure 21: A) Outline map of Norway showing regions where a high number of rock slope failures have been recorded. B) Location of rock avalanches and rock slope failures in Troms county, Northern Norway. Reproduced from Braathen et al. (2004).

Rock slope failure involves the detachment of rock from a very steep slope and subsequent disintegration of the rock as it bounces, falls and slides down the mountain slope (Benn and Evans, 1998, Olesen et al., 2000, Braathen et al., 2004, Evans et al., 2006). Massive rock slope failures often transform into debris flows or rock-avalanches (Blikra et al., 2006, Evans et al., 2006). Rockslides, rockfalls and rock-avalanches are a frequent type of mass movement deposit observed in recently glaciated areas and rock-avalanches are the dominating type of event in Norway (Blikra et al., 2006, Hermanns and Longva, 2012). Rock slope failures are trigged on bedrock slopes that are greater than 40 to 45° and they often occur as catastrophic slope failures that result in the rapid redistribution of debris downslope (Benn and Evans, 1998, Vorren et al., 2008). Rock-avalanches are defined as very coarse deposits from a single high-magnitude event and they can have large run-out distances (Benn and Evans, 1998).

Rock-avalanches are created by instabilities in mountain slopes caused by local forces such as earthquakes, glacial debuttressing (a reduction of slope support due to the removal of glaciers) and frost shattering (the expansion of freezing water causing fractures to open or grow) (Benn and Evans, 1998, Vorren et al., 2008, Blikra and Christiansen, 2014). In northern Norway, it is suggested that rapid glacio-isostatic uplift immediately following deglaciation caused major earthquakes that triggered multiple mass movement events, such as rock-avalanches and debris flows (Blikra et al., 2006, Vorren et al., 2008, Hermanns and Longva, 2012, Olesen et al., 2013).

2.3.1.2 Subaerial Debris Flows

Debris flows are a very important mass movement processes within alluvial fans. Subaerial debris flows occur when sediment on steep slopes (27-56°), such as colluvium or till, is mixed with water and air and moves downhill under the force of gravity in a viscous state (Blair and McPherson, 2009).

Debris flows are usually initiated by the addition of a large amount of water to the sediment. This water can be produced by rapid precipitation (e.g. thunderstorm) or rapid snow and ice melt. Consequently, debris flows are common in recently glaciated terrain where unconsolidated sediment is abundant and there is a large water supply from ice and snow melt (Benn and Evans, 1998). The presence of clay and water within debris flows is important for lowering the yield strength of the flow allowing it to transport larger particles (Galloway and Hobday, 1996). Debris flow deposits consist of unsorted, muddy to gravelly sediment that usually has a lobe-shaped morphology (Jones and Lee, 1994, Blair and McPherson, 2009).

2.3.2 Mass Movement Processes within Deltas

The steep subaqueous delta slope is highly unstable and the sediment on the slope can be redistributed by mass movement processes to restore slope stability, such as slumping, sliding, or debris flows. The sediment transport mechanism can evolve over time and sometimes the sediment completely liquefies forming turbidity currents (Leeder, 1999, Anderson and Anderson, 2010).

2.3.2.1 Slides and Slumps

Slumping and sliding involves the movement of a coherent body of rock or unconsolidated sediment downslope. Movement usually originates from a point and occurs along a basal rupture surface known as a slip surface or shear plane (Jones and Lee, 1994). Slides occur along a planar glide plane and show no internal deformation, whilst slumps occur along a concave-up glide plane and often contain extensive evidence of internal deformation, such as folds, faults and clast imbrication (Benn and Evans, 1998, Shanmugam, 2016). Slumps often evolve into debris flows (Figure 22).

2.3.2.2 Subaqueous Debris Flows

Debris flows have a plastic rheology and laminar state and they are dominated by inter-granular movements (Shanmugam, 2016). Debris flows have the same flow behaviour in both subaqueous and subaerial environments, however, the mechanism of formation is different within each environment. Subaqueous debris flows occur due to the build-up of sediment on a slope, which results in the redistribution of sediment downslope or they can be triggered by earthquakes. Subaqueous debris flows can transform into turbidity flows.

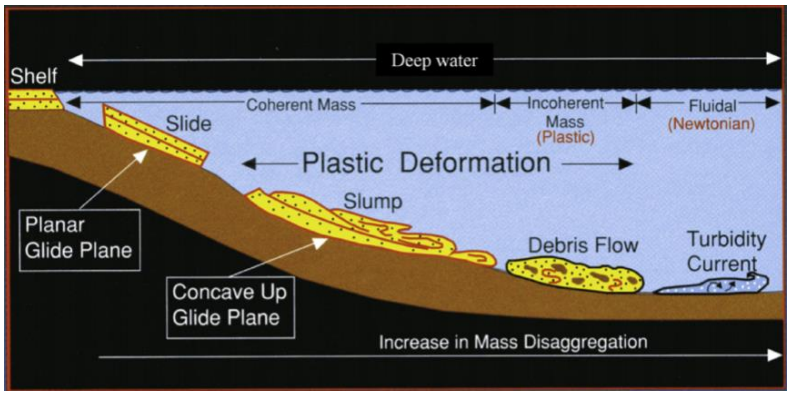

Figure 22: A schematic diagram showing four common types of subaqeuous mass movement processes. The mass movement process can evolve during sediment transport depending on the properties of the flow. Adapted from Shanmugam (2016).

2.3.2.3 Turbidity Flows

A turbidity current is a type of density flow where the sediment is maintained in turbulent suspension within the flow. Turbidity currents can originate from the acceleration of sediment slumps on the slope or they can form when a large amount of river sediment is deposited onto the slope during flood conditions. Turbidite deposits are often found in the prodelta region of deltas and they are composed of a characteristic graded vertical sequence called the Bouma Sequence. The full Bouma sequence from top to bottom is:

- Massive clay or silt (E);
- Interlaminated silt and/or clay (D);
- Ripple cross-laminated sand and silt (C);
- Planar laminated sand (B); and
- Massive or normally graded sand or gravel (A).

2.3.3 Mass Movement Deposits at Russenes

There is a lot of evidence of mass movement processes within Balsfjord. Mass movement deposits have been observed along the fjord margins (Blikra and Longva, 1999, Olesen et al., 2000, Blikra et al., 2006) and within the fjord sediments (Forwick and Vorren, 2002). At Russenes there is a 1 km long rock-avalanche deposit located above the fan delta. Field evidence indicates that the front of the rock-avalanche was deposited into the sea (Blikra et al., 2006, Fenton et al., 2011). *Balanus* shells have been found on boulders at the front of the rock-avalanche and radiocarbon dated giving a reliable minimum age of 10 942 ± 77 cal. BP (1σ) (Blikra, 1998, Blikra and Longva, 1999, Forwick and Vorren, 2002, Fenton et al., 2011). This date supports the hypothesis that many of the rock-avalanches located in the Troms county occurred shortly after deglaciation. Blikra (1998), Blikra and Longva (1999) and Olesen et al. (2000) suggest that the period between 10.0 and 9.5 Ka BP is characterised by increased activity of rock-avalanches due to seismic triggering created by significant uplift after deglaciation (Vorren et al., 2008).

2.4 Anthropogenic Activity

In recent times the study area has been influenced by human activity primarily created due to agriculture and transportation. Most of the anthropogenic changes to the fan delta can be identified on aerial photography and occur below 70 m a.s.l. A large proportion of the lower fan delta has been cleared for farming and 10 farming properties are located across the study area. Additionally, a shooting range facility is located in the south-east of the study area at 100 m a.s.l. Two bitumen roads have been built through the study area in an east-west direction; a small country road named Fv295 and the European route E6 highway. The Fv295 road services the properties located within the study area and there are a few dirt roads and tracks that branch out from the Fv295. The E6 is a large two lane highway, which forms part of the main north-south road through Norway. It was constructed in the 1960s and its construction altered the morphology of the surrounding landscape. 6 gravel pits of varying size have been identified within the study area. None of the gravel pits are currently operational. Finally, some man-made spit structures protrude into the fjord in the intertidal area of the fan delta.

3 Methods and Materials

This study involves a detailed investigation of different components of the postglacial Russenes fjord-side fan delta, including the modern subaerial and subaqueous environments, the subsurface structure and the associated deglacial landforms. The range of different datasets and methods have been applied in this investigation and they are described in detail below.

3.1 Quaternary Geological Map

A Quaternary map can contain a variety of information about the surface including information about the morphology, grain size, origin and age of the landforms (Knight et al., 2011) and a Quaternary Geological Map of the surficial sediments within the postglacial Russenes fjord-side fan delta and associated deglacial landforms has been produced during this study. Many different methods have been used to produce this Quaternary Geological Map, including direct methods, such as field mapping, and remote sensing methods, such as interpretation of aerial photography, satellite imagery and digital terrain models. The Quaternary Geological Map was produced in ArcMap 10.4.1 and all datasets used to create the geological map were georeferenced using the ETRS 1989 datum and UTM zone 33N projection. The techniques that were used to produce the Quaternary Geological Map of the study area are explained below.

3.1.1 Visual Interpretation of Aerial Photography

Geomorphological mapping is the identification of landforms according to their morphology and formational processes (Hubbard and Glasser, 2005, Knight et al., 2011). Aerial photographs can be used to identify many types of geomorphological features such as landslides, beach ridges and terraces. These features are identified using the following characteristics: shape, size, colour, tone, mottling, texture, pattern of objects, topography and setting (Guzzetti et al., 2012).

The aerial photographs that were used in this study are listed in Table 1. The aerial photograph that was most commonly used is titled Midt-Troms 2013 and this dataset has the best resolution (0.1 m). The aerial photographs were primarily viewed and interpreted in ArcMap 10.4.1, however, some of the aerial photographs were also viewed in 3 dimensions using a virtual 3D globe, which is available at www.norgei3d.no. A preliminary geomorphological map was produced from aerial photograph interpretation before field investigations commenced and the aerial photographs were used to refine the Quaternary map throughout the study.

Stereoscopy is a technique that allows photographs to be viewed in three-dimensions because stereoscopic vision creates an illusion of depth. Viewing photographs stereoscopically increases the morphological appearance of the terrain and assists with the recognition of geomorphological features (Guzzetti et al., 2012). If two aerial photographs that are taken from different positions overlap they can be viewed stereoscopically and are called stereoscopic pairs. One stereoscopic pair that was taken in 1960 is available for the study area: WF_1133_F7 and WF_1133_F8. This pair allowed the western side of the fan delta to be viewed stereoscopically and this was extremely useful because the geomorphological landforms that were destroyed by the construction of the E6 highway could be viewed with their original morphology (Figure 23).

Table 1: The aerial photographs used in this study. Many of these photographs are available as orthophotographs from www.norgeibilder.no.

Name	Date	Resolution	Type	Source
Midt-Troms 2013	11 August 2013	0.1 m	Colour	Norge i bilder
Troms 2011	17 August 2011	0.4 m	Colour	Norge i bilder
Troms 2006	29 July 2006	0.5 m	Colour	Norge i bilder
Balsfjord 2003-2004	5 August 2004	0.2 m	Colour	Norge i bilder
WF_3380_016	2 August 1969	1:15 000	Black and white	Widerø's flyveselskap A/S
WF_1133_F7	22/24 July 1960	1:10 000	Black and white	Widerø's flyveselskap A/S
WF_1133_F8	22/24 July 1960	1:10 000	Black and white	Widerø's flyveselskap A/S

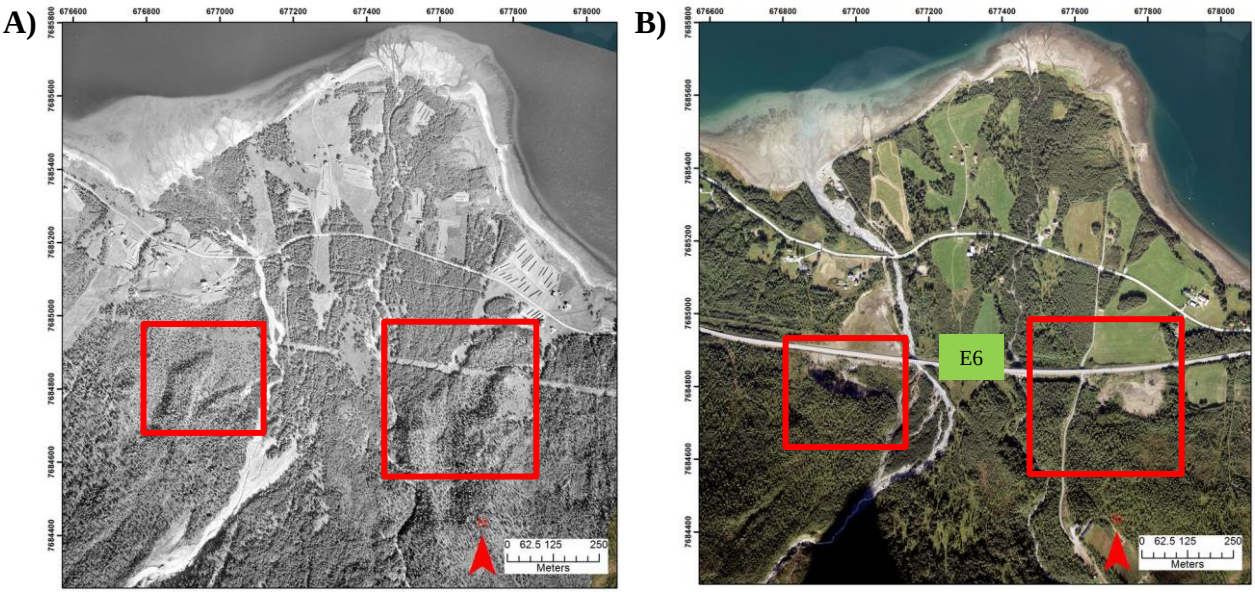

Figure 23: A) Aerial photograph WF_1133_F8 taken between 22 and 24 July 1960. This photograph was taken before the E6 highway was built. B) Aerial photograph Midt-troms 2013 taken on 11 August 2013. The red boxes highlight some of the areas that have changed between 1960 and 2013 due to construction of the main road.

3.1.2 Field Mapping

Collecting observations and data in the field is a direct method for obtaining information about the geomorphology and Quaternary geology of an area (e.g. measurements, descriptions, photographs and samples) (Knight et al., 2011). Field mapping allows the researcher to become familiar with the landscape, however, information collected is subjective and dependant on the skills and experience of the researcher (Hubbard and Glasser, 2005). Field mapping can be used to validate remotely sensed observations.

Field mapping was undertaken at Russenes in May, July, September and October 2016 to obtain direct observations and measurements on the geomorphology and sediment distribution in the study area. Mapping of the breaks in slope and the surface and subsurface material was performed by visual inspection and interpretation. Observations were recorded in a field notebook. Aerial photographs and topographic maps were used for navigation in the field. A hand-held GPS (Garmin eTrex 30) was used to mark tracks and way points, and this allowed the observations recorded in the field to be spatially located in ArcMap 10.4.1 upon return from the field (Figure 24). Furthermore, the photographs that were taken during fieldwork could be georeferenced using the hand-held GPS track upon return from the field (Appendix 1).

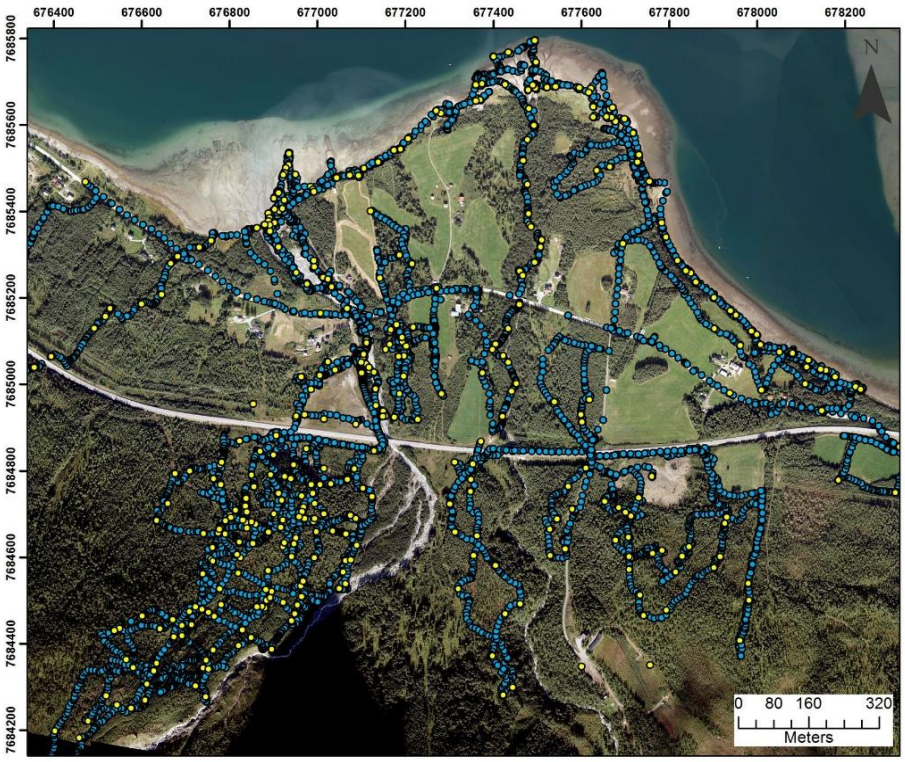

Figure 24: Map of the study area showing the GPS tracks (blue) and waypoints (yellow) that were recorded during fieldwork. Background map = Midt_troms 2013.

3.1.3 Surface Sediment Analysis

During fieldwork the clast size, shape and roundness of the surficial sediments was recorded at many locations. Grain size was divided into size fractions based on the Udden-Wentworth-Krumbein scale (Udden, 1914, Wentworth, 1922, Krumbein, 1934) (Table 2). Sediment grain size was recorded at many locations across the study area (Figure 25 and Appendix 3). At each location the percentage of each size fraction in the sample was estimated visually and the facies codes shown in Table 3 were used to represent all main fractions comprising >5% according to the method used by Corner (1977) and Lyså and Corner (1994). The name of the dominant size fraction is used substantially and the names of the other size fractions are used adjectivally in order of increasing importance. For example, a sample containing 60% sand, 30% gravel and 10% cobbles would be called a gravelly cobbly sand. When the sediment grain size was greater than 0.5 mm a mode and maximum grain size was also recorded. In addition to grainsize analysis, clast roundness was recorded using the six-category chart of Powers (1953) (very angular to well-rounded).

Table 2: The Udden-Wentworth-Krumbein grainsize scale (Udden, 1914, Wentworth, 1922, Krumbein, 1934)

Ø Scale	Size range (metric)	Name
<-8	>256 mm	Boulder
-6 to -8	64 – 256 mm	Cobble
-5 to -6	32 – 64 mm	Very coarse gravel
-4 to -5	16 – 32 mm	Coarse gravel
-3 to -4	8 – 16 mm	Medium gravel
-2 to -3	4 – 8 mm	Fine gravel
-1 to -2	2 – 4 mm	Very fine gravel
0 to -1	1 – 2 mm	Very coarse sand
1 to 0	0.5 – 1 mm	Coarse sand
2 to 1	0.25 – 0.5 mm	Medium sand
3 to 2	125 – 250 µm	Fine sand
4 to 3	62.5 – 125 µm	Very fine sand
9 to 4	2.0 – 62.6 µm	Silt
10 to 9	0.98 – 2 µm	Clay

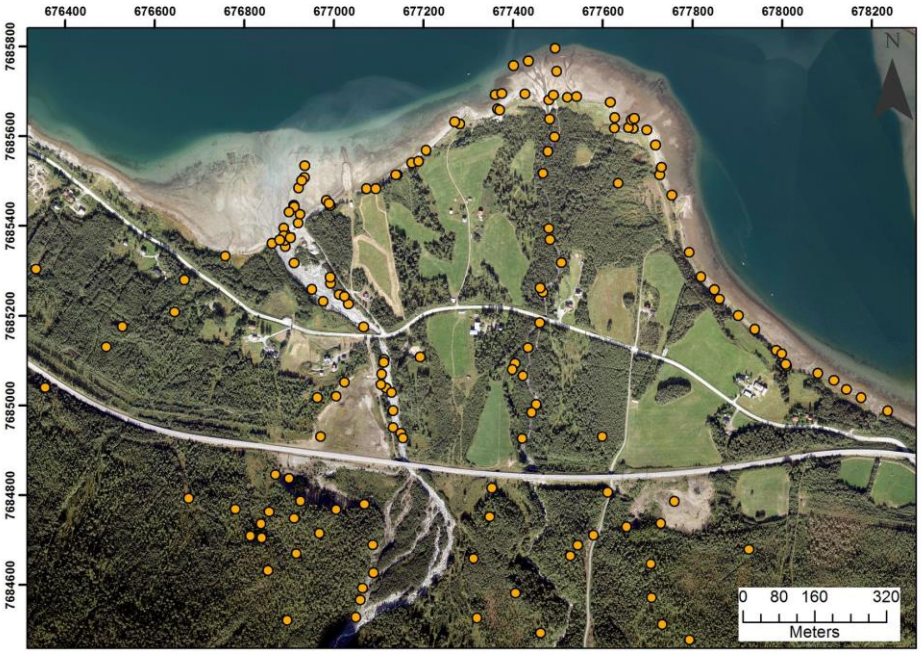

Figure 25: Map showing the location of sediment grainsize data recorded during fieldwork (orange points). Background map = Midt_troms 2013.

Table 3: Lithofacies codes for the sorted sediments at Russenes based on the distribution of major grain-size fractions comprising > 10 %. Adapted from Corner (1977) and Lysså and Corner (1994).

Facies code	*Description*	*Facies code*	*Description*
L	Clay	Z	Silt
zL	Silty clay	lZ	Clayey silt
szL	Sandy silty clay	sZ	Sandy silt
		sgZ	Sandy gravelly silt
		gsZ	Gravelly sandy silt
		scZ	Sandy cobbly silt
S	Sand	G	Gravel
zS	Silty sand	sG	Sandy gravel
zgS	Silty gravelly sand	scG	Sandy cobbly gravel
zcS	Silty cobbly sand	csG	Cobbly sandy gravel
gS	Gravelly sand	cG	Cobbly gravel
gzS	Gravelly silty sand	szG	Sandy silty gravel
C	Cobbles	B	Boulders

3.1.4 Digital Terrain Models

A digital terrain model (DTM) is a topographic model of the bare earth whereby spatial elevation data is presented in a rectangular grid. A DTM that was regularly used in this study is a national scale DTM gridded to 10x10 m that is available from the Norwegian Mapping Authority (www.data.kartverket.no). This DTM was used in various ways throughout the study. For example, elevation profiles of the fan delta were created using the DTM to investigate the surficial morphology and a few raster surfaces were created using the DTM, such as hillshade and slope surfaces (Appendix 1). Hillshade surfaces use shading to give an impression of depth information from a three-dimensional surface on a two-dimensional image (Figure 26) and these surfaces were particularly useful in this study.

Another important DTM used in this study was created by Statens Kartverk using airborne Lidar data (Light Detection and Ranging), which is an active remote sensing technique that uses infrared light from a pulsed laser to measure ranges to the terrain and objects. This is currently the most accurate method of creating a digital elevation model. Airborne Lidar data used in this study was acquired by Terratec on behalf of the Norwegian Mapping Authority (Statens Kartverk) in 2013. A Leica ALS70-II laser scanner was used to collect the data with a minimum point density of 3 points/m^2.

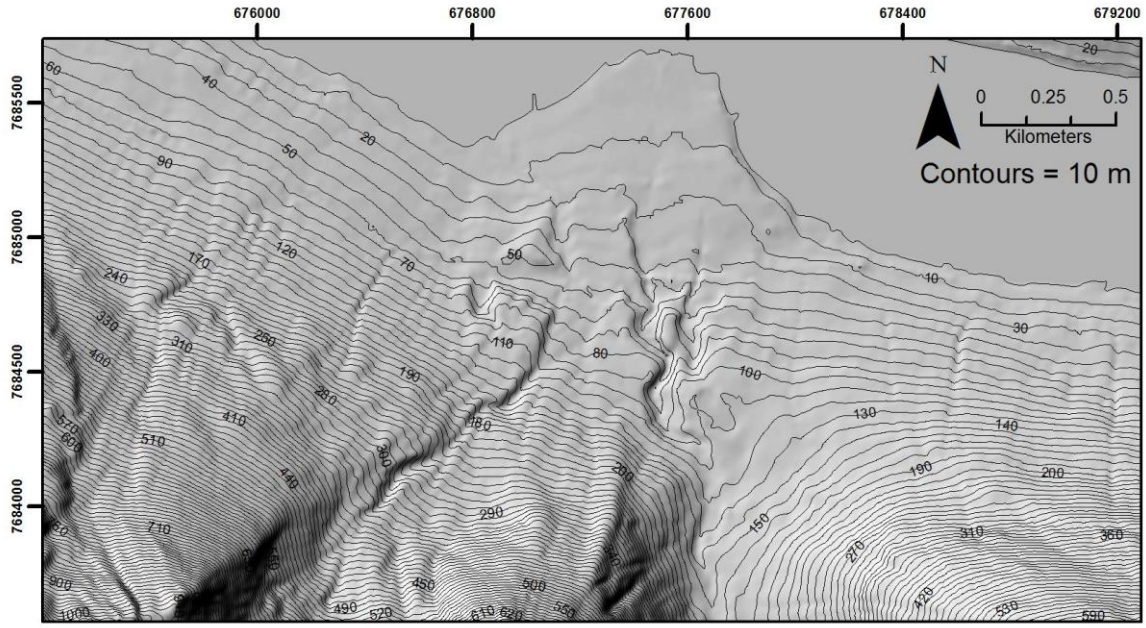

Figure 26: A hillshade image of the study area (azimuth = 315° and sun elevation = 45°). This hillshade image was created using a national scale digital terrain model with a 10 m resolution that is available at www.data.kartverket.no.

The Lidar data that is available over the study area occurs as a narrow band (300 m wide) over the E6 highway. A digital terrain model (DTM) created from the Lidar data can be download at https://hoydedata.no/LaserInnsyn/. This DTM provides high resolution elevation data (0.5 m resolution) and hillshade images were created using this data and used to identify morphological features (Figure 27).

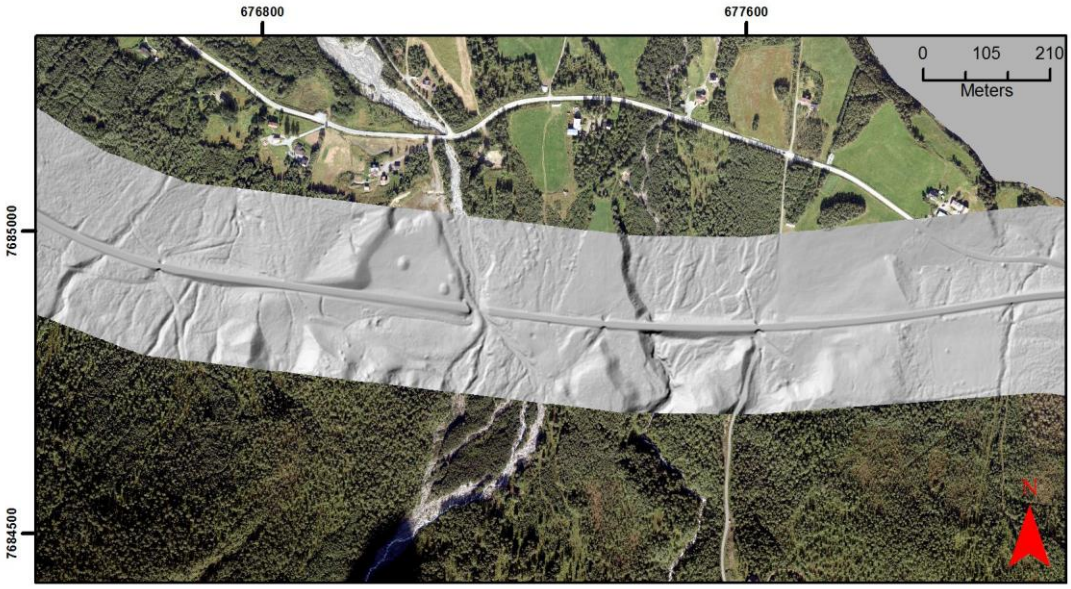

Figure 27: Hillshade image of the DTM created from the Lidar data that is available over the study area. The DTM can be downloaded from Statens Kartverk (https://hoydedata.no/LaserInnsyn/). The hillshade image uses a light source with an azimuth of 315 degrees and a sun elevation of 45 degrees to create a 3D shadow effect. This dataset provides detailed morphological information, which can be extrapolated to other areas of the fan delta.

3.1.5 Global Positioning Systems (GPS)

Global Positioning System (GPS) is a global satellite navigation system that allows GPS receivers to record information about position, velocity and time (Hubbard and Glasser, 2005). A minimum of four GPS satellites are required to record location information. Two different GPS receivers were used during this study: (1) a hand-held GPS receiver; and (2) a differential GPS receiver. The single hand-held GPS receiver (Garmin eTrex 30) was used to mark tracks and way points with a 3 m accuracy. Occasionally, the differential GPS receiver was used to obtain more precise elevation data and this information was collected using a Trimble R4 GPS with a Juno T41 X Handheld tablet. For example, the Trimble R4 GPS was used to obtain precise elevation data along the ground penetrating radar (GPR) profiles so that they could be corrected for changes in elevation. The Trimble R4 GPS has a horizontal accuracy of ± 8 mm and a vertical accuracy of ± 15 mm. The GPS measurements were taken by attaching the Trimble R4 GPS to a 1.36 m long pole. Measurements were either taken as point measurements or collected continuously along a profile. Point measurements are more accurate because the pole is kept level (vertical) and stationary whilst the measurement is taken.

3.2 Subaqueous Morphology

The subaqueous morphology of the present-day fan delta has been investigated using a detailed multibeam bathymetry dataset that was collected over the subaqueous component of the Nordkjosbotn and Russenes deltas (Corner and Eilertsen, 2013). This dataset was displayed in a few different ways during this study, including as bathymetric maps, slope maps and cross-profiles on order to determine the subaqueous geomorphology of the present-day fan delta.

3.2.1 Multibeam Bathymetry

Sidescan sonar systems send out acoustic pulses into the sea and measure the time taken for the pulses to reflect from the sea floor and return to the receiver. The elapsed time is a measure of the water depth and it can be used to determine the bathymetry of the sea floor (Hubbard and Glasser, 2005). Multibeam bathymetry data was collected over the subaqueous component of the Nordkjosbotn and Russenes deltas on a marine geological cruise with the RV *Hyas* in September 2013 (Corner and Eilertsen, 2013). The multibeam equipment consisted of a GeoAcoustics 125 kHz GeoSwath interferometric sidescan sonar that was provided by NGU (Corner and Eilertsen, 2013). The sidescan sonar transponder was mounted onto the bow of the boat and a GPS antenna (Trimble R4 GNSS GPS/GLONASS Rover receiver) was mounted onto a vertical steel pole and place directly above the transponder to record location information. The accuracy of data acquisition is in the cm to dm scale. Sound velocity profiles (SVP) of the water column were made at selected locations in the survey area using a Valeport 650 SVP. Processing of the data was performed in GeoSwath software. Further information about the data acquisition on the cruise can be found in the post survey report by Corner and Eilertsen (2013).

3.3 Subsurface Composition and Structure

The structure and composition of the deglacial and postglacial sediment located below the surface of the Russenes fjord-side fan delta was investigated through the interpretation of vertical sedimentary successions and the collection and interpretation of ground penetrating radar (GPR) profiles. Additionally, some marine shells that were identified within the deltaic subsurface sediments have been radiocarbon dated.

3.3.1 Sedimentary Logs

Sedimentary successions were exposed at a few locations within the study area, including river banks, road cuttings and gravel pits. Graphical logs were drawn in the field to represent and record information about the vertical sedimentary successions. A sedimentary graphical log records the bed thickness on the vertical axis and grainsize variations on the horizontal axis (Hubbard and Glasser, 2005). A lot of additional information can be included in the graphical log including lithology, bed boundaries (sharp, erosive, transitional etc.) sedimentary structures, colour and fossils. This information is displayed using symbols, patterns, colours and text. Consequently, there are many different styles of graphical logs depending on the purpose of the log and the type of information being displayed. One of the graphical logs produced in this study is shown in Figure 28. Facies codes, which represent the interpreted depositional process, have been included in the lithological log and the sediment grainsize distribution is also represented. Table 4 shows the facies codes used in this study.

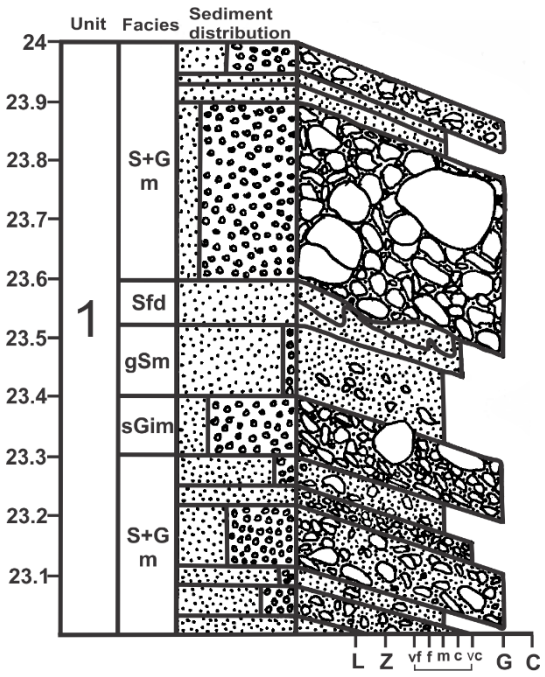

Figure 28: Example of a lithological log created during this study. The vertical axis records the bedding thickness and the horizontal axis records the dominant grainsize. The bedding orientation and sedimentary structures are also shown and the facies and units have been defined (left-hand columns).

Table 4: Lithofacies codes for the different types of bedding at Russenes and their interpretation. Modified from from Lysså and Corner (1994).

Facies code	***Description***	***Interpretation***
m	Massive to crudely bedded	Suspension settling, cohesionless debris flows
l	Horizontal/sub horizontal (parallel bedding)	Longitudinal bars, lag deposits, planar bed flow
d	Deformed bedding	Slump, liquefied flow
g	Normal graded bedding. Fining upwards	Turbidity current, debris flow waning current
l	Inverse graded bedding. Coarsening upwards	Cohesionless grain flows
im	Preferential alignment of clasts	Gravity flows

3.3.2 Ground Penetrating Radar

3.3.2.1 Theory

Ground penetrating radar (GPR) is a non-destructive geophysical subsurface imaging technique. It uses high-frequency electromagnetic waves (in the microwave band) to image the subsurface. The principles of GPR are comparable with reflection seismology, except electromagnetic energy is used instead of acoustic energy. Most GPR instruments contain a transmitter and a receiver in a fixed geometry, which are moved across the ground to detect reflections from the subsurface (Annan, 2009). A transmitter emits the electromagnetic radiation into the ground, and this energy is reflected, refracted and scattered by boundaries in the subsurface with different electrical properties (Figure 29). The changes in dielectrical properties within the subsurface may be caused by changes in sediment grain-size, mineralogy, density, water content and consolidation (Mauring et al., 1994, Eilertsen et al., 2011). Although a lot of the energy is dissipated, a component of the energy is reflected back to the surface and recorded by the receiver. The arrival time of the reflected energy is related to the depth and location of different boundaries.

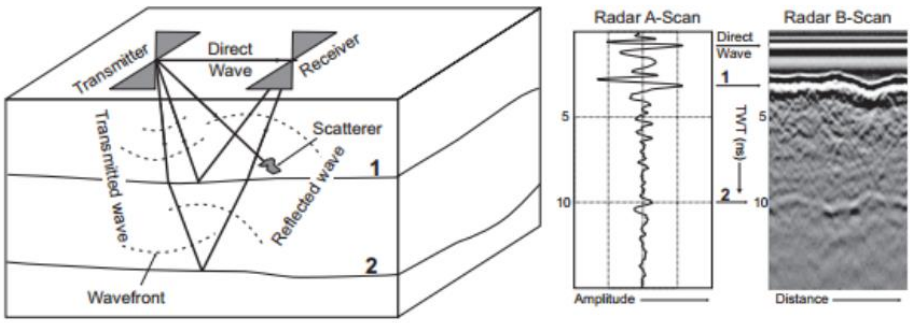

Figure 29: Schematic showing the principles of ground penetrating radar (GPR). The transmitted wave travels through the subsurface and is reflected from boundaries with different electrical properties. The time taken for the wave to return to the receiver is recorded. Radar A-Scan and Radar B-Scan show how the return signal can be displayed for interpretation. Reproduced from Milsom and Asger (2011)

The penetration depth of GPR systems is determined by the electrical conductivity of the subsurface (soil type), the source frequency and the size of the target. Radio waves are attenuated or absorbed differently by different soil conditions. The electromagnetic waves become attenuated with increasing electrical conductivity, which decreases the penetration depth. Therefore, the penetration of GPR is very limited in highly conductive materials, such as soils contaminated with salt. Lower frequency electromagnetic waves penetrate further than higher frequency waves, however, the resolution increases with higher frequencies. Therefore, when deciding what frequency to use there is a trade-off between resolution and penetration. Radar frequencies between 50 and 200 MHz give the best resolution and penetration for clastic coarse-grained sediments (Hubbard and Glasser, 2005).

3.3.2.2 GPR Data Acquisition

The GPR system used in this study was a PulseEKKO^{TM} IV (Sensors & Software Inc., Mississauga, ON, Canada) and the instrument is shown in Figure 30. 100 MHz antennae were used for the transmitter and receiver and the distance between the antennae was 1.0 m. The data was collected in step mode and measurements were taken every 0.25 m (step size) across the entire profile. The step size was measured using markers on the antennae. Other system specifications used during data acquisition include a time window of 500 ns, a pulser voltage of 400 V and 4-fold stacking. The instrument supports higher degrees of stacking, which could be applied in the future to improved data quality in the deeper section. 11 GPR profiles were collected in the study area (Table 5 and Appendix 3) and the location of these GPR profiles is shown in Figure 31.

Figure 30: Photograph of the PulseEKKO^{TM} IV GPR instrument used in this study. The antennae have a fixed position 1.0 m apart. Two people are required to operate the system: one person to move the GPR antennae; and one person to operate the computer.

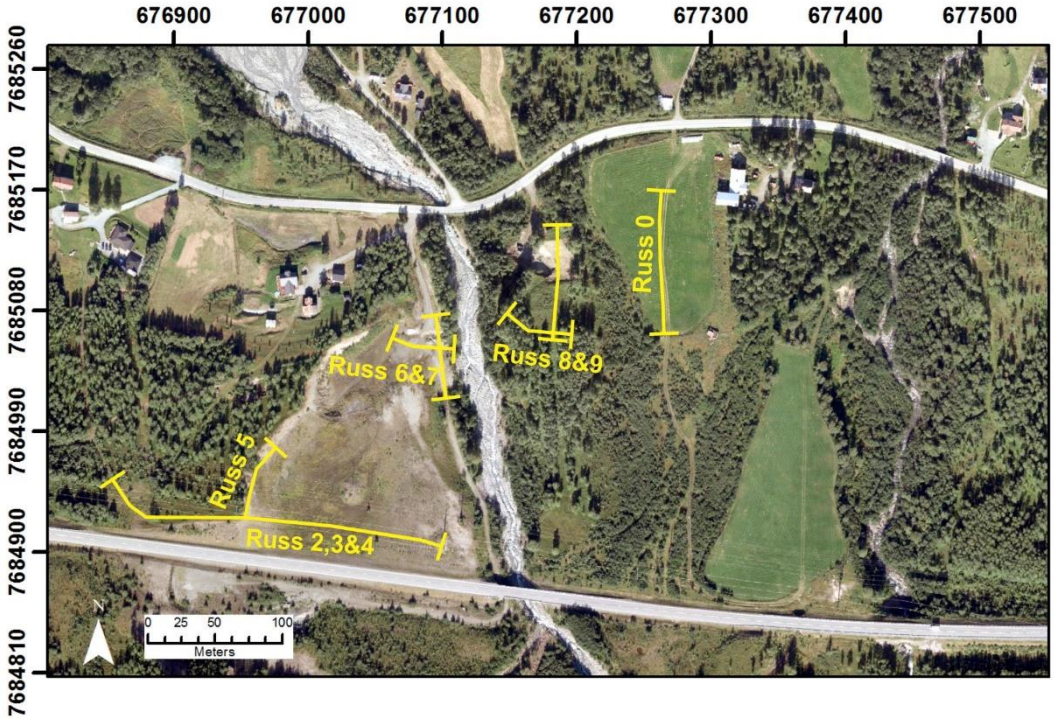

Figure 31: Orthophotograph Midt_Troms_2013 showing the location of the GPR lines collected during this study.

Table 5: List of the GPR lines collected in this study.

Line Name	Length (m)	Trace number	Location description	Comments
Russ0	92	370	South-north line across fluvial material	The top section of the profile is distorted.
Russ 1	55.75	224	North-south line above gravel pit	No data beyond 37 m due to battery failure.
Russ 2, 3 and 4 (merged)	258.5	915	West-east line across ice front deposit	Lines were acquired consequently and merged during processing.
Russ 5	86.75	348	South-north line across ice front deposit	
Russ 6	48	193	North-south line above deltaic material	
Russ 7	35.75	144	East-west line above deltaic material	
Russ 8	62	249	North-south line above gravel pit	
Russ 9	38.75	156	East-west line above fluvial sediment	
Russ 10	26.75	108	Line following terrace above gravel pit.	Direction of acquisition changes towards the end of the line

3.3.2.3 GPR Data Editing and Processing

The GPR data was edited and processed using Ekko View Deluxe software and the lines were viewed using Ekko View software (Sensors & Software Inc., Mississauga, ON, Canada). Two-way-travel time was converted to depth using a velocity value of 0.1 m/ns, which is a typical velocity value for coarse-grained sediment (Sensors & Software Inc., Mississauga, ON, Canada). The data processing sequence is outlined in the following section. For further information refer to the Ekko View Enhanced and Deluxe instruction manual (Software and Sensors, 2003).

Elevation data

The PulseEKKO^{TM} IV GPR instrument does not have an inbuilt GPS system and therefore, elevation data for the GPR lines was obtained from other sources. For example, lidar data with a 0.5 m resolution exists over GPR profile Russ1,3&4 (merged) and Russ 5 (Section 3.1.4). The resolution of this data was sufficient to determine the elevation changes along these lines and this information was added to the GPR profiles using EKKO view deluxe. There was no Lidar coverage for the other GPR lines and therefore, the changes in elevation along these lines were determined using the Trimble R4 GPS (Section 3.1.5). Figure 32 gives an example of a GPR line before and after topographic correction was applied.

Topographic information was added to the GPR profiles in Ekko View Deluxe using the following procedure:

- Create a text file with a .TOP extension listing the changes in distance along the line next to the associated elevation changes.
- Add the .TOP file. Data editing > file > Add topography using topo file…
- Shift the topography. Data editing > file > Shift topography

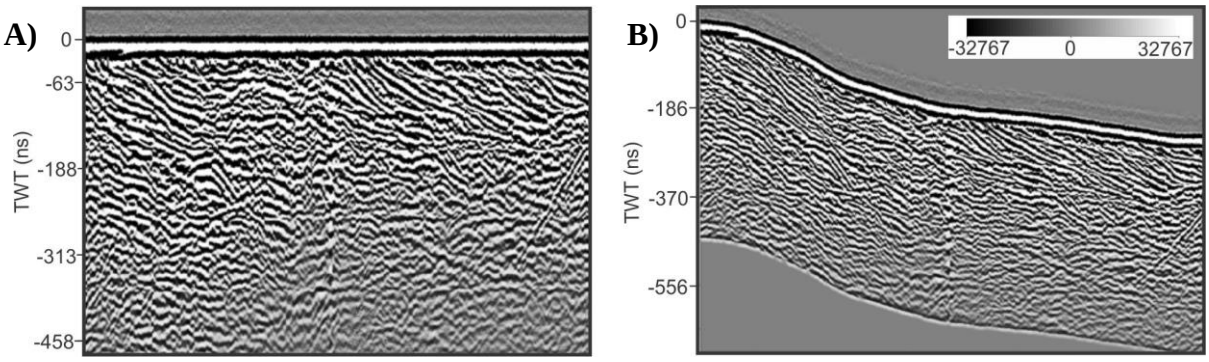

Figure 32: GPR line Russ5 (A) before topography information was added, and (B) after topography information was added to the line.

Re-picking timezero

Timezero is the first large deflection (either a positive peak or negative trough) in the trace that shows the arrival of the direct air wave to the receiver (Software and sensors, 2013). If GPR data collection is commenced before the instrument has warmed-up, then the initial timezero may not be in the right position. This causes the topmost reflectors in the GPR profile to start below timezero and gradually increase towards timezero as the instrument warms up (Figure 33). This occurred for GPR profiles Russ1, Russ6 and Russ8. Ekko view deluxe allows the user to redefine timezero using an

input threshold and this function was applied for GPR profiles Russ1, Russ6 and Russ8 with a threshold value between 5 and 10% (Software and Sensors, 2003).

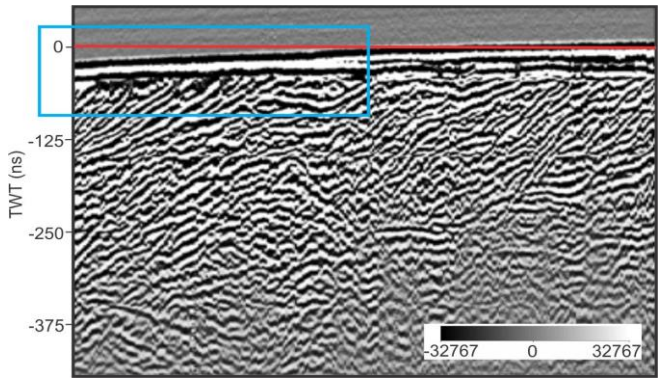

Figure 33: GPR profile Russ8 showing the profile is initially not located at timezero.

GPS coordinates

GPS coordinates were added to each GPR line using a text file with a .GTP extension. The text file must have the X, Y and Z (optional) coordinates for at least two trace numbers within the line. The text file was added to the line using the following method: data editing > file > Add GPS data. The GPS coordinates were added so that the lines could be viewed in 3D, however, unfortunately the coordinate information could not be exported with the lines from Ekko View Deluxe.

Migration

Automatic gain control (AGC) was applied during data collection and this process destroyed most of the frequency dynamic range in the data causing most reflections to have the maximum available positive or negative values. This meant that there was limited potential to improve the data. Migration is the only processes that was observed to enhance the GPR profiles (Figure 34).

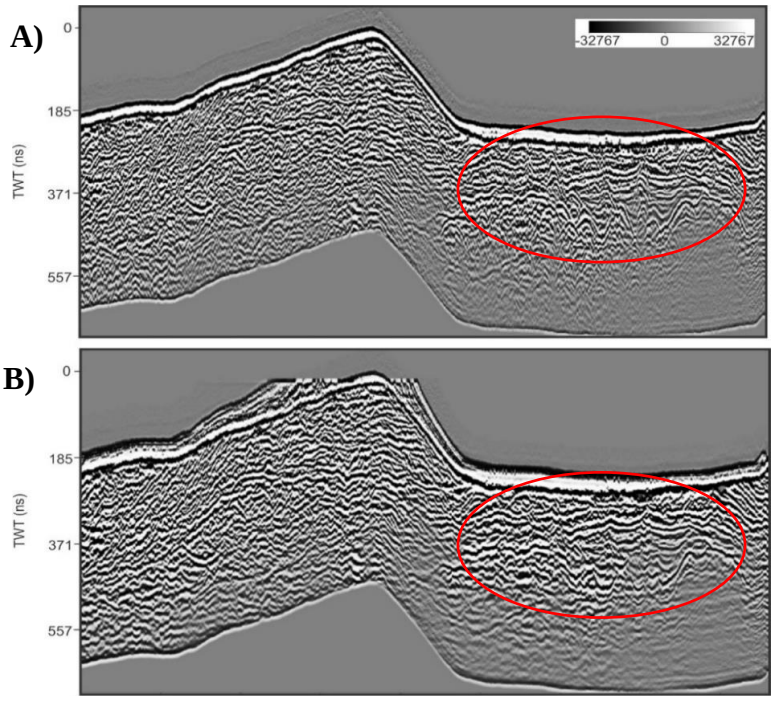

Figure 34: GPR profiles Russ2, 3 and 4 (merged) (A) before migration and (B) after migration (velocity value used = 0.03 m/ns). The red circle highlight the diffractions that were improved by the migration processing.

Migration is a processing technique that moves dipping reflectors to their true subsurface positions and collapses diffractions. This processing technique was applied to all the GPR profiles in EKKO View Deluxe through the following method: Instant process > 2D filters > migration. A velocity of 0.03 or 0.02 m/ns was used for all GPR profiles because it was found to produce the best results. Some migration artefacts remain because only a single migration velocity could be used.

After editing and processing of the GPR profiles the data was exported to a SEG-Y and imported into Petrel software for interpretation.

3.3.3 Radiocarbon Dating

3.3.3.1 Theory

Radiocarbon dating is a commonly used method for determining the age of organic material that is less than 50 000 years old (Libby, 1955, Bradley, 2015, Lowe and Walker, 2015). Carbon has three naturally occurring isotopes whereby two of the isotopes are stable, carbon-12 (^{12}C) and carbon-13 (^{13}C) and one is unstable (radioactive), carbon-14 (^{14}C). Carbon-14 is continually produced in the upper atmosphere by neutron bombardment of atmospheric nitrogen atoms according to the following equation: $n + {}^{14}_{7}N \rightarrow {}^{14}_{c}C + p$

^{14}C is rapidly oxidised to $^{14}CO_2$ and this compound diffuses through the atmosphere. Carbon-14 has a half-life of 5,730 years and an equilibrium exists between the rate of new Carbon-14 creation in the upper atmosphere and the rate of decay of Carbon-14 in the atmosphere and biosphere. Therefore, it is assumed the concentration of Carbon-14 is constant over time (Bradley, 2015, Lowe and Walker, 2015). Carbon-14 is dissolved in the ocean and assimilated into plants and animals through photosynthesis. As living plants and animals are continually exchanging carbon, the carbon-14 content of living organisms is assumed to be equilibrium with the atmosphere. However, when an organism dies the system becomes closed. Therefore, the organism stops obtaining Carbon-14, but, the existing Carbon-14 within the organism will continue to decay to nitrogen (Bradley, 2015, Lowe and Walker, 2015). Since the decay rate of ^{14}C is known, the time an organism died can be determined by measuring the amount of ^{14}C atoms within an organic sample of the organism. Radiocarbon dating is based the following key assumptions: (1) the production of ^{14}C is constant over time; (2) The $^{14}C/^{12}C$ ratio in organisms is in equilibrium with the atmosphere; (3) the decay rate of ^{14}C known and precise; and (4) the system is closed after the death of an organism (Bradley, 2015).

However, there are some problems with some of the assumptions. For example, CO_2 is transferred from the atmosphere to the ocean by dissolution of CO_2 at the surface. The mixing time of the ocean is much longer than that of the atmosphere and therefore, it takes a long time for the ^{14}C atoms to be distributed throughout the ocean. Therefore, the $^{14}C/^{12}C$ ratio in marine organisms is not in equilibrium with the atmosphere and this causes radiocarbon dated marine fossils to appear too old. This is known as the marine reservoir effect and consequently, a correction is applied to marine samples to account for the reservoir effect (Bradley, 2015, Lowe and Walker, 2015).

3.3.3.2 Accelerator Mass Spectroscopy (AMS)

Conventional radiocarbon dating measures the amount of ^{14}C atoms in a sample indirectly by counting β-particle emission. In the 1970s and early 1980s, radiocarbon dating was revolutionised by the development of the Accelerator Mass Spectroscopy (AMS) technique, which uses an accelerator coupled to a mass spectrometer to directly count the number of ^{14}C atoms relative to ^{12}C and ^{13}C to give a direct ratio of $^{14}C/^{12}C$ (Bradley, 2015). Ions that are accelerated to very high velocities are passed through a magnetic field that separates the ions allowing them to be counted. AMS radiocarbon dating can be performed on much smaller samples than conventional ^{14}C dating (approximately 1 mg of carbon).

3.3.3.3 Laboratory Analysis

AMS radiocarbon dating was performed on three of the samples that were collected from the field by the Beta Analytic Inc. laboratory located in Miami, Florida, United States of America (Table 6). A conventional radiocarbon age (corrected for isotopic fractionation) has been determined by the laboratory. The resulting ^{14}C dates were calibrated to calibrated radiocarbon years (cal. yr BP) by the laboratory using the MARINE13 database and the 2013 INTCAL program (Ramsey, 2009, Reimer et al., 2013). A global marine reservoir correction of -200 to 500 years and a local reservoir correction of 71±21 (DeltaR) was applied during calibration (Mangerud et al., 2006). The calibrated ages are given within the ±2σ interval.

A few previously published radiocarbon ages were also used in this study. These ages were primarily obtained from the Radiocarbon Laboratory in Trondheim, Norway and all ages have been corrected for a reservoir effect of 440 years (Corner, 1980, Forwick and Vorren, 2002). Therefore, to compare these conventional ages with the radiocarbon ages obtained during this study 440 years must be added to the previously published ages. Additionally, the previously published radiocarbon ages have been recalibrated during this study using the MARINE13 database, the 2013 INTCAL program and a DeltaR value of 71±21 (Mangerud et al., 2006, Ramsey, 2009, Reimer et al., 2013).

Table 6: Information about the samples prepared for AMS ^{14}C radiocarbon dating.

Lab reference	Location number	Sample depth (m)	Species	Weight (g)	Easting	Northing
Beta - 463114	HD2016-Russ01	25	*Macoma Calcarea* (Gmelin, 1791)	0.67	677101	7685062
Beta - 463115	HD2016-Russ04	25	*Mya Truncata* (Linné, 1758)	1.69	677104	7685050
Beta - 463116	HD2016-Russ05	51	Balanus sp.	6.9	676974	7684851

4 Results

A comprehensive study of the Russenes postglacial fjord-side fan delta and landslide complex has been undertaken. This study examines the surficial morphology and subsurface structure of the postglacial fjord-side fan delta and associated deglacial landforms. A Quaternary Geological Map of the postglacial fjord-side fan delta has been produced during this study. The results have been divided into two sections: (1) a description of the deglacial sediment that has been mapped within the study area; and (2) an investigation of the present-day morphology and subsurface structure of the postglacial fjord-side fan delta. The progradation history of the fan delta and associated deglacial deposits provides an important record of the deglacial and postglacial history of Balsfjord.

4.1 Quaternary Geological Map

A 2 km^2 Quaternary Geological Map of the Russenes postglacial fjord-side fan delta and landslide complex has been produced during this study (Figure 35). This map is at the 1:10 000 scale and it shows the surficial sediments and geomorphological features identified within the upper 0.5 m of the Russenes fjord-side fan delta. The map has been constructed in ArcMap 10.1.4 using a wide range of data (Section 3.1) and it is displayed in the ETRS 1989 datum and UTM zone 33N projection. Polygons, lines and point symbols are all used to represent the surficial sediment and geomorphological landforms on the map.

Sediment within the mapped area has been deposited from approximately 11,500 cal. yr BP to present and some areas of the fan delta are still actively developing through sediment depositional and erosional processes. Older postglacial fan delta sediment and associated deglacial landforms have been raised above present-day sea level due to glacio-isostatic uplift. Mapping of this raised surficial sediment and present-day surficial landforms allows the postglacial depositional history of the fjord-side fan delta to be determined. As the land has been uplifted since the deglaciation, the morphology of some of these depositional elements has been altered by post depositional fluvial, wave and tidal processes. In many cases these processes have created distinct geomorphological features, such as shore notches, beach ridges and erosional gullies and these features have been included on the Quaternary Geological Map.

The identification of raised shorelines is particularly useful for determining the rate of relative sea level change within the study area and a several raised shorelines have been identified. These shorelines have been recognised by the presence of shore notches, which are erosional features that has been cut into the deglacial and postglacial sediment by wave and tidal processes when the sediment was located at sea level. Shore notches usually correspond to periods of sea level stand still and therefore, the most prominent shore notches within the study area correspond to the marine limit and the Tapes transgression, which occur at 83 m a.s.l and 35 m a.s.l respectively (Section 1.2.3.2).

Active surficial features are also shown on the Quaternary Geological Map, such as river channels, streams, gullies and areas of active fluvial incision. For example, the intertidal region of the fan delta, called the delta platform, is a very active component of the present-day fan delta because the geomorphology and sedimentology of the intertidal region is influenced by fluvial, wave and tidal processes. The delta platform is exposed at low tide and therefore, the present-day morphology of the intertidal delta platform has been mapped and included in the Quaternary Geological Map.

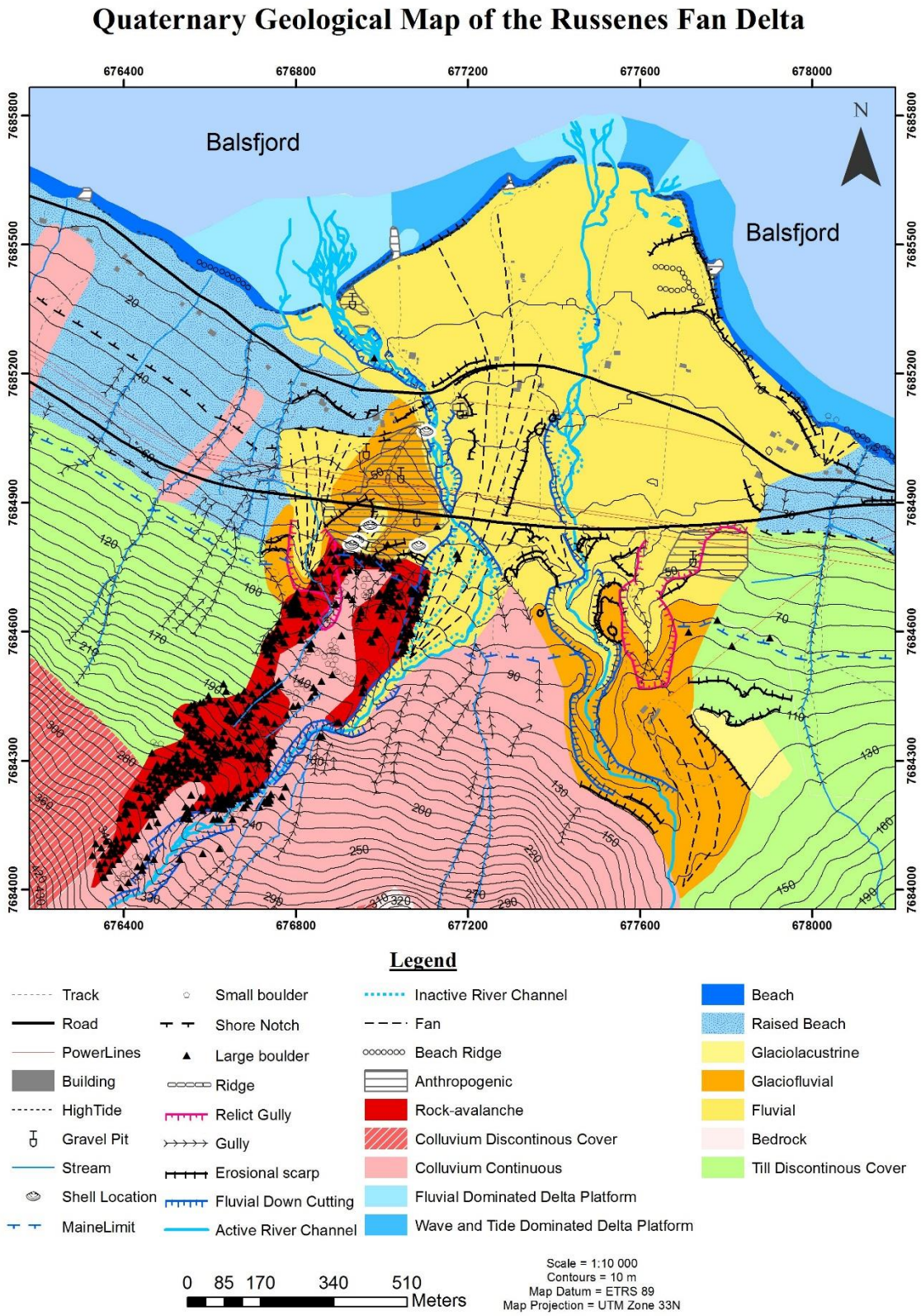

Figure 35: Quaternary Geological Map produced during this study. The map shows the surficial sediment and geomorphological features of the postglacial Russenes fjord-side fan delta and associated deglacial sediment. The map has been produced using a wide variety of data sources including aerial photographs, previous geological maps, digital terrain models, and fieldwork data. The legend has been adapted from a legend supplied by NGU.

4.2 Deglacial Sediment

A large volume of sediment was deposited in Troms county during the deglaciation of the Fennoscandian Ice Sheet. The Quaternary Geological Map produced during this study contains several deglacial deposits that are associated with the postglacial fjord-side fan delta, including deposits of till, glaciolacustrine, glaciofluvial, rock-avalanche and colluvial sediment (Figure 35). Most of these deglacial deposits are located immediately above the postglacial fjord-side fan delta and they provide a source of sediment for the fan delta. These deglacial deposits are described in detail below.

4.2.1 Till

Till is a generic term for a poorly sorted diamicton that has been deposited directly from a glacier (Hambrey, 1994, Benn and Evans, 1998). Till usually contains a wide variety of clast sizes and it is often dominated by coarse, poorly sorted, matrix-rich sediment (Leeder, 1999). Till can also form a wide variety of morphologies, including ridges, mounds and sheets. Till has been mapped on the edges of the Quaternary Geological Map as a patchy, thin layer of till that has been deposited directly over the bedrock. The till is composed of clay, silt and very fine sand with interspersed cobbles and boulders of various lithologies. The fine-grained component of the till often has a silver colour.

4.2.1.1 Interpretation

Till can be deposited within many different glacial environments. For example, it can be deposited from the melt out of stationary ice or by direct emplacement from subglacial flow (lodgement till) (Hambrey, 1994, Benn and Evans, 1998, Leeder, 1999). Till is commonly deposited as a thin layer of sediment during glacial retreat. Therefore, surficial till was probably deposited over the entire study area during glacier retreat and most of the younger sediment within the study area has probably been deposited onto a thin layer of till.

4.2.2 Glaciolacustrine Deposit

A deposit of well sorted silt sediment has been mapped on the upper eastern side of the fan delta (Figure 36 and Figure 37A). This deposit is located next to a shooting range. According to a local resident, the landscape surrounding the shooting range has not been disturbed by anthropogenic activity. The upper surface of the deposit forms a gently dipping terrace and a 1 m high scarp occurs in the south-western side of the deposit, which exposes a section of sorted silt sediment (Figure 37A). The northern edge of the deposit is also defined by an erosional scarp (Figure 36) and another erosional scarp occurs 5 m below the sorted silt deposit (Figure 37B).

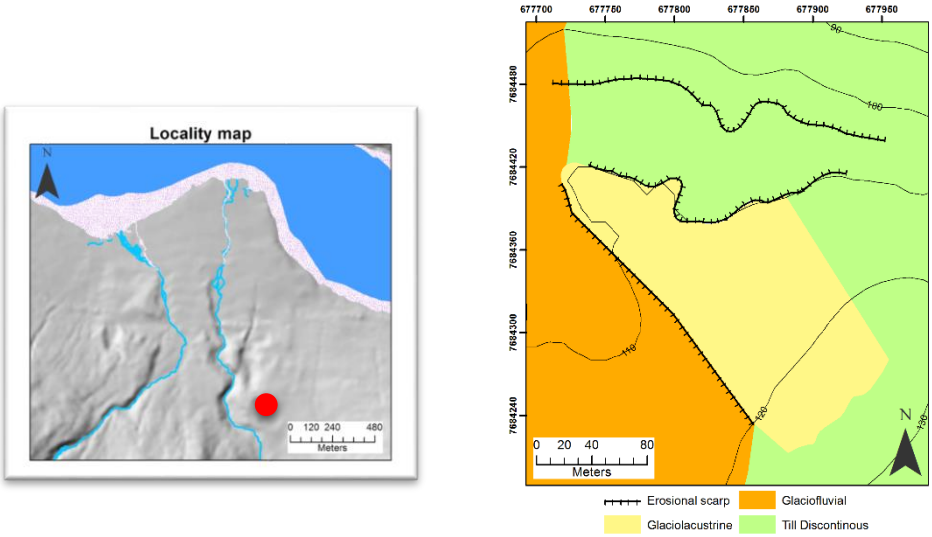

Figure 36: Detailed map of the sorted silt sediment (glaciolacustrine deposit) located on the upper eastern side of the fan delta.

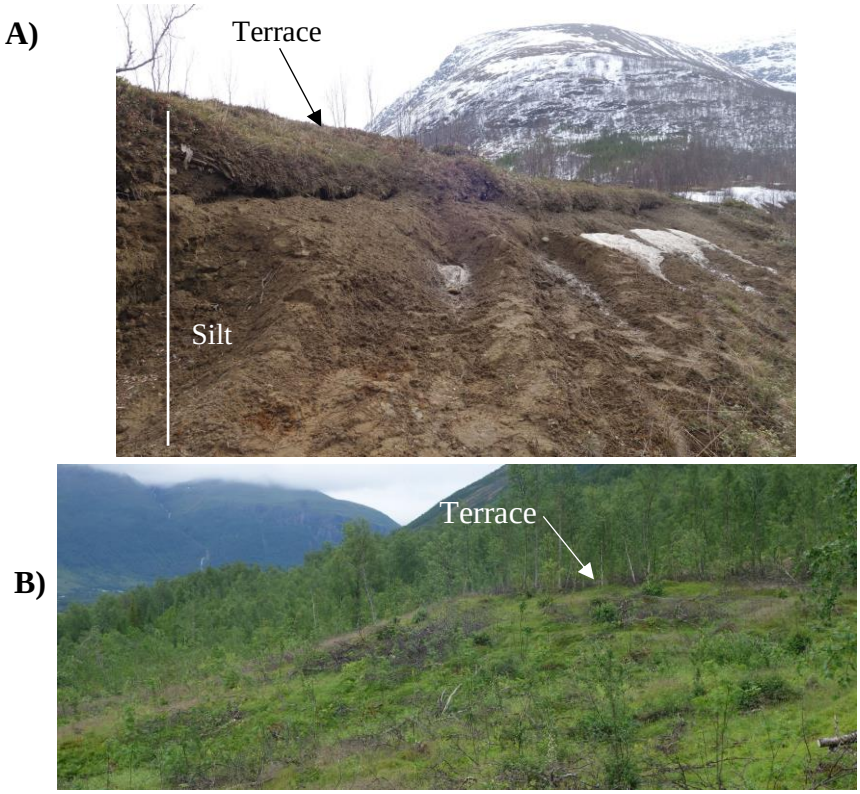

Figure 37: A) Photograph of the well sorted silt sediment located within an erosional scarp on the south-western side of the deposit. B) Photograph of the terrace-like surface located below the deposit of sorted silt. This surface occurs above the marine limit.

4.2.2.1 Interpretation

The sorted nature of the sediment indicates it must have been deposited into standing water. However, the sediment is located above the marine limit. Therefore, it is likely that the silt was deposited within a lacustrine environment. Ice-dammed lakes can be formed when a glacier forms a barrier to the natural drainage and they are common in all present-day glaciated regions of the world (Benn and Evans, 1998). Therefore, we suggest that an ice-dammed lake formed at the side of the Balsfjord glacier during deglaciation and the silt sediment was deposited into this ice-dammed lake. Figure 38 shows one possible glacier configuration that could have resulted in the formation of an ice-dammed lake. Ice-dammed lakes often drain catastrophically, producing outburst floods (jökulhlaups) that are orders of magnitude larger than the normal river discharge (Benn and Evans, 1998). However, no evidence of outburst floods has been found in the study area.

The erosional scarp on the south-western side of the deposit is interpreted to be produced by post depositional erosion of the glaciolacustrine sediment by glaciofluvial processes. The east-west orientated terrace-like features that occur below the glaciolacustine deposit and parallel to the fjord are interpreted to represent erosional surfaces created by the Balsfjord glacier. The sedimentology and lithofacies of the sorted silt sediment was not investigated in detail during fieldwork due to the proximal location of the shooting range to the deposit. Therefore, a more detailed investigation of the deposit could be undertaken to determine the specific glaciolacustrine lithofacies, which could include rhythmites, varves and deltas.

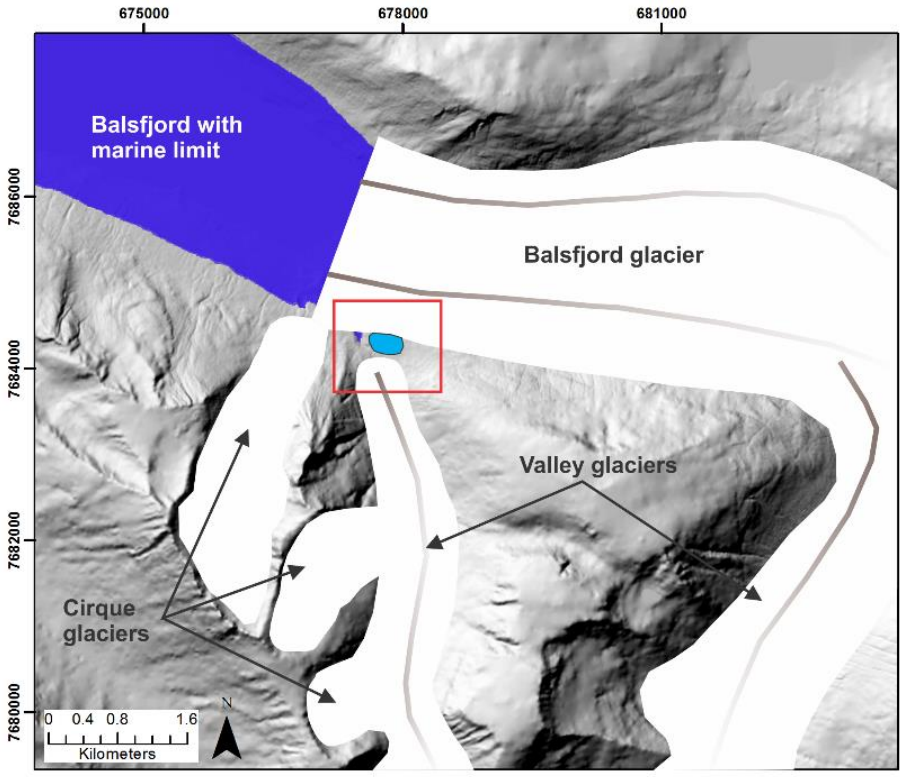

Figure 38: Schematic diagram of the interpreted depositional environment of the glaciolacustrine deposit. It is hypothesised that the sorted silt sediment was deposited into an ice-dammed lake at the end of the Russedalselva valley. The background image is a DTM-derived shaded-relief map of the study area (azimuth = 315° and sun elevation = 45°) and the position of the glaciers has been drawn using elevation information from this DTM.

4.2.3 Ice Front Accumulation

A large gravel pit is located on the western side of the Buktelva river directly below the E6 highway (Figure 39). This gravel pit occurs within an accumulation of coarse-grained sediment and the original surface morphology of this accumulation has been destroyed by gravel pit operations. At the edges of the gravel pit the sediment consists of sorted cobbly, sandy gravel with a maximum clast size of 7 cm (Figure 39C). It is likely that this course sediment is representative of the sediment that has been removed. Additionally, poorly-drained fine-grained sediment is located at the base of the gravel pit. This sediment is composed of well sorted fine sand and silt with occasional gravel. Two aerial photographs taken in 1960 were used stereoscopically to investigate the original morphology of the area (WF_1133_F7 and WF_1133_F8) and a large ridge was observed in the location of the current gravel pit (Figure 40). This ridge is approximately 350 m long, 260 m wide and has a sinuous crest.

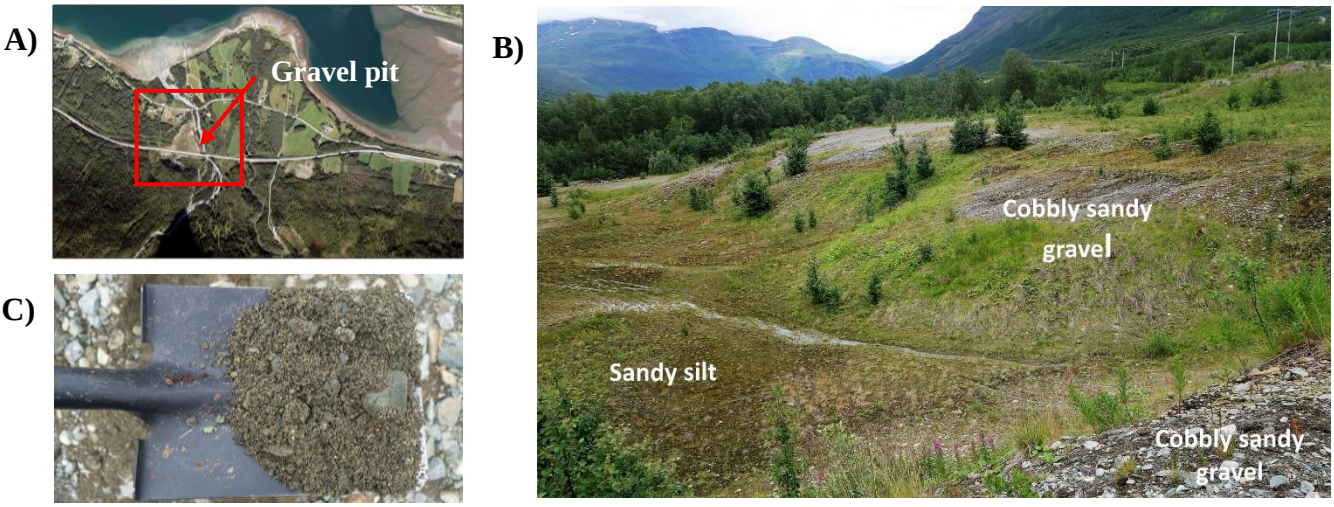

Figure 39: A) Aerial photograph of the fan delta showing the location of the gravel pit on the western side of the Buktelva river. B) Photograph of part of the gravel pit showing the present-day grainsize distribution C) Photograph of the cobbly sandy gravel located at the edge of the gravel pit.

The present-day morphology of the gravel pit is shown in Figure 41. Some of the glaciofluvial sediment was not disturbed during the extraction. For example, there is a prominent 125 m long ridge on the western side of the gravel pit that still has its original morphology and is covered by vegetation. Therefore, the western side of the glaciofluvial ridge is interpreted to be undisturbed. Additionally, three small circular mounds are located beneath electricity poles within the gravel pit. The electricity poles existed before earth moving operations commenced and therefore, it is believed that these sediment mounds were not disturbed and they show the height of the original glaciofluvial deposit at these three specific locations.

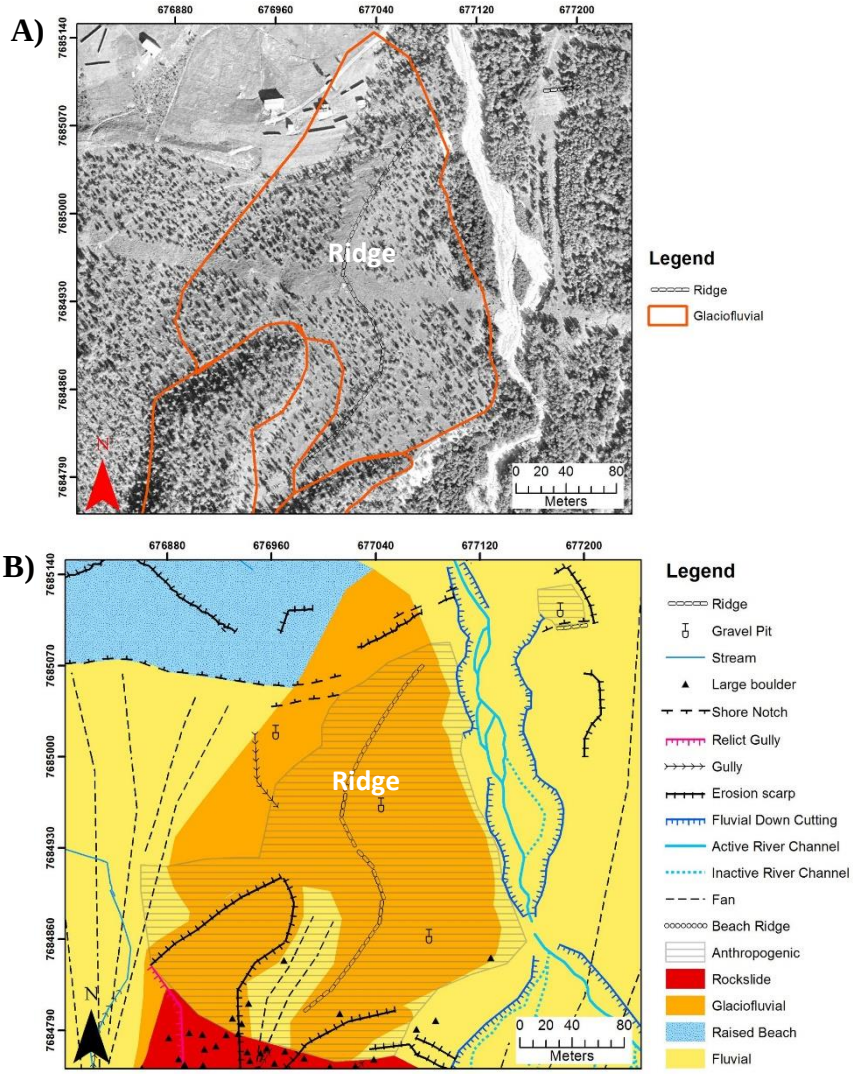

Figure 40: A) Aerial photograph WF_1133_F8 showing the landscape in 1960 before gravel pit operations commenced. The glaciofluvial sediment is outline in orange. B) Detailed map of the ridge. The original morphogenic features have been mapped using stereophotogrammetry.

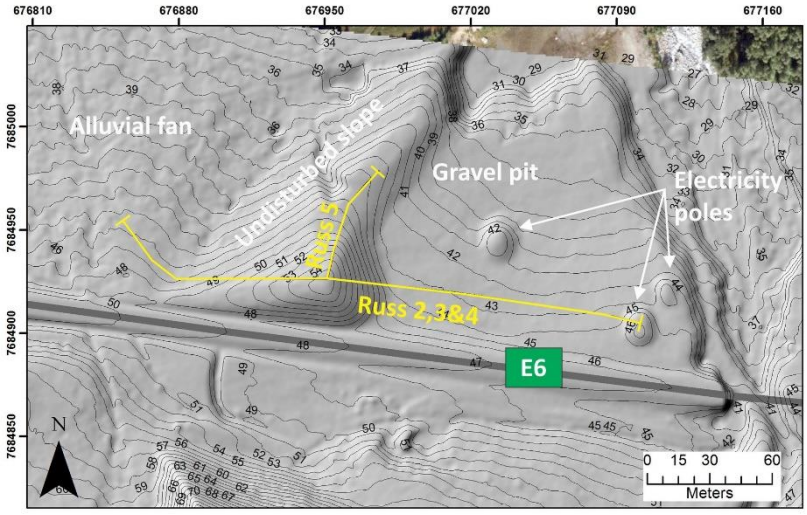

Figure 41: Lidar-derived shaded-relief map of the present-day gravel pit created from a DTM available from Statens Kartverk (https://hoydedata.no/LaserInnsyn/). The location of GPR profiles Russ2, 3 & 4 (merged) and Russ5 are shown. Contours = 1 m.

Two ground penetrating radar (GPR) profiles were taken perpendicular to each other across the ridge composed of coarse cobbly sandy gravel: Russ5 and Russ2,3&4 (merged). The location of these GPR profiles is shown in Figure 41. These profiles provide information about the sub-surface structure of the sediment accumulation and they are presented and interpreted below.

GPR profile Russ2,3&4 (merged)

GPR profile Russ2,3&4 (merged) is a 258.5 m long west-east profile taken across cobbly sandy gravel ridge (Figure 42). A large section of the profile was taken within the present-day gravel pit (Figure 41 and Figure 42). Several deep high amplitude reflections (below -400 ns) are observed on the eastern side of the profile. These reflections have a large relief and are interpreted to be produced by the presence of bedrock. Above the bedrock reflections two different sediment packages have been identified based on reflection geometry and continuity.

Unit A has been divided into two units. Unit A1 occurs below the gravel pit and consists of continuous wavy sub-horizontal reflections, which are interpreted to be produced by marine or till sediment. Unit A2 represents the possible continuation of Unit A beneath Unit B. Unit B predominantly occurs beneath the present-day ridge and consists of semi-continuous gently dipping reflections, which are truncated on the eastern side due to the removal of sediment by gravel pit operations. Some of these reflections appear chaotic. Unit B corresponds to the cobbly sandy gravel sediment exposed at the edges of the gravel pit. Finally, there are two high amplitude continuous reflections below Unit B, which could represent till material deposited before the deposition of the coarse-grained ridge.

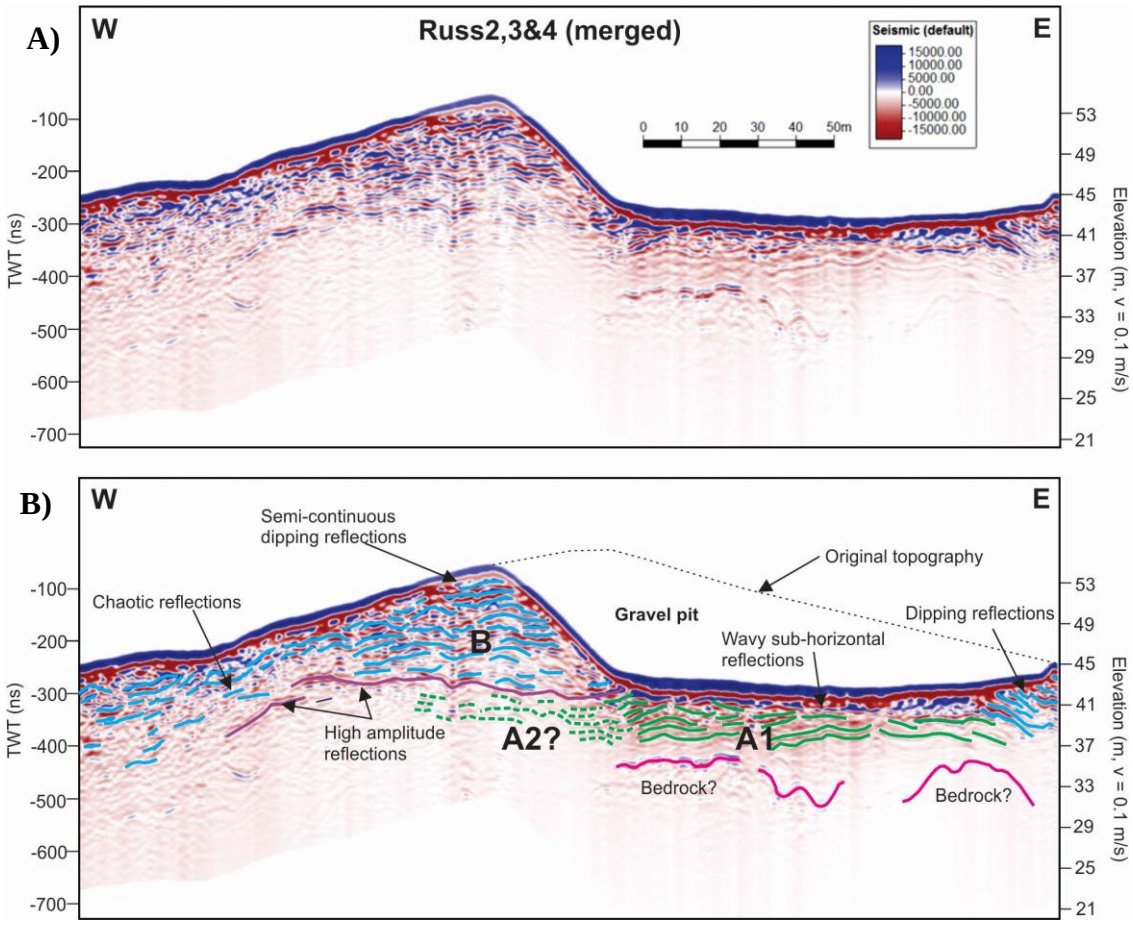

Figure 42: A) Uninterpreted GPR profile Russ2,3&4 (merged). B) Interpreted GPR profile Russ2,3&4 (merged). Two sediment packages have been identified: Unit A (green) and Unit B (blue).

GPR profile Russ5

GPR profile Russ5 is located perpendicular to Russ2,3&4 (merged) (Figure 41 and Figure 43). Most the reflections in the top -300 ns of this profile have a high amplitude and are steeply dipping. Some of the reflections have a sigmoidal shape. These dipping reflections are interpreted as foreset beds, which form part of Unit B identified in GPR profile Russ2,3&4(merged) (Figure 42B) and therefore, they are composed of the cobbly, sandy gravel sediment identified at the surface.

The geometry of the reflections indicates there are two different sediment packages, labelled B1 and B2. Unit B1 occurs on the southern side of the profile and consist of continuous, high-amplitude reflections that have a sigmoidal shape. Unit B2 downlaps onto Unit B1 and contains shorter sigmodal semi-continuous dipping reflections. The dipping reflections in units B1 and B2 are interpreted as foreset beds, however, the different units represent different periods of deposition whereby Unit B1 was deposited before Unit B2. Additionally, the downlapping nature of reflectors in Unit B2 indicates an unconformity exists between the two sediment packages. Both GPR profiles Russ2,3,4 (merged) and Russ5 show obliquely dipping foreset beds, which indicate that the true dip is towards the centre of the fjord in a north-west direction.

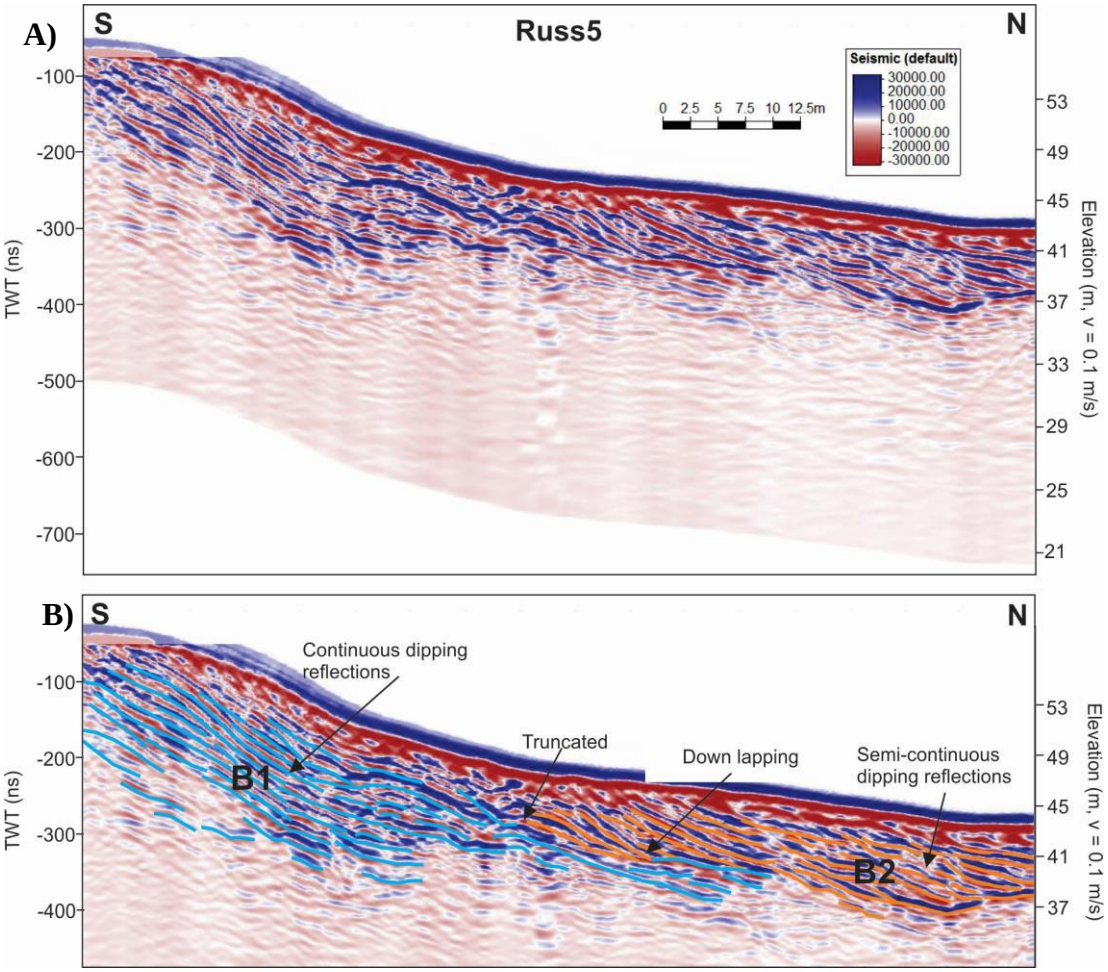

Figure 43: A) Uninterpreted GPR profile Russ5. B) Interpretation of GPR profile Russ5. One unit has been identified within the GPR profile (B), which contains two different sediment packages (B1 and B2).

4.2.3.1 Interpretation

This large ridge-shaped accumulation of cobbly sandy gravel is interpreted as an accumulation of glaciofluvial sediment that was deposited during deglaciation. The sea level was very close to the marine limit (83 m a.s.l) at this time and the fine-grained sand and silt sediment located beneath the ridge is interpreted to have a marine origin. The maximum height of the present-day glaciofluvial sediment at the edge of the gravel pit is 54 m a.s.l (Figure 41). This is not the true maximum height of the deposit because the crest of the ridge has been removed (Figure 40). However, it indicates this ridge of glaciofluvial sediment was deposited well below the marine limit. It follows that this sediment must have been deposited directly from subglacial and englacial streams during a halt in the retreat of the Balsfjord glacier because this is the only depositional process that allows an accumulation of coarse-grained glaciofluvial sediment to form within an open marine environment (Powell, 1990, Hambrey, 1994, Lønne, 1995, Benn and Evans, 1998).

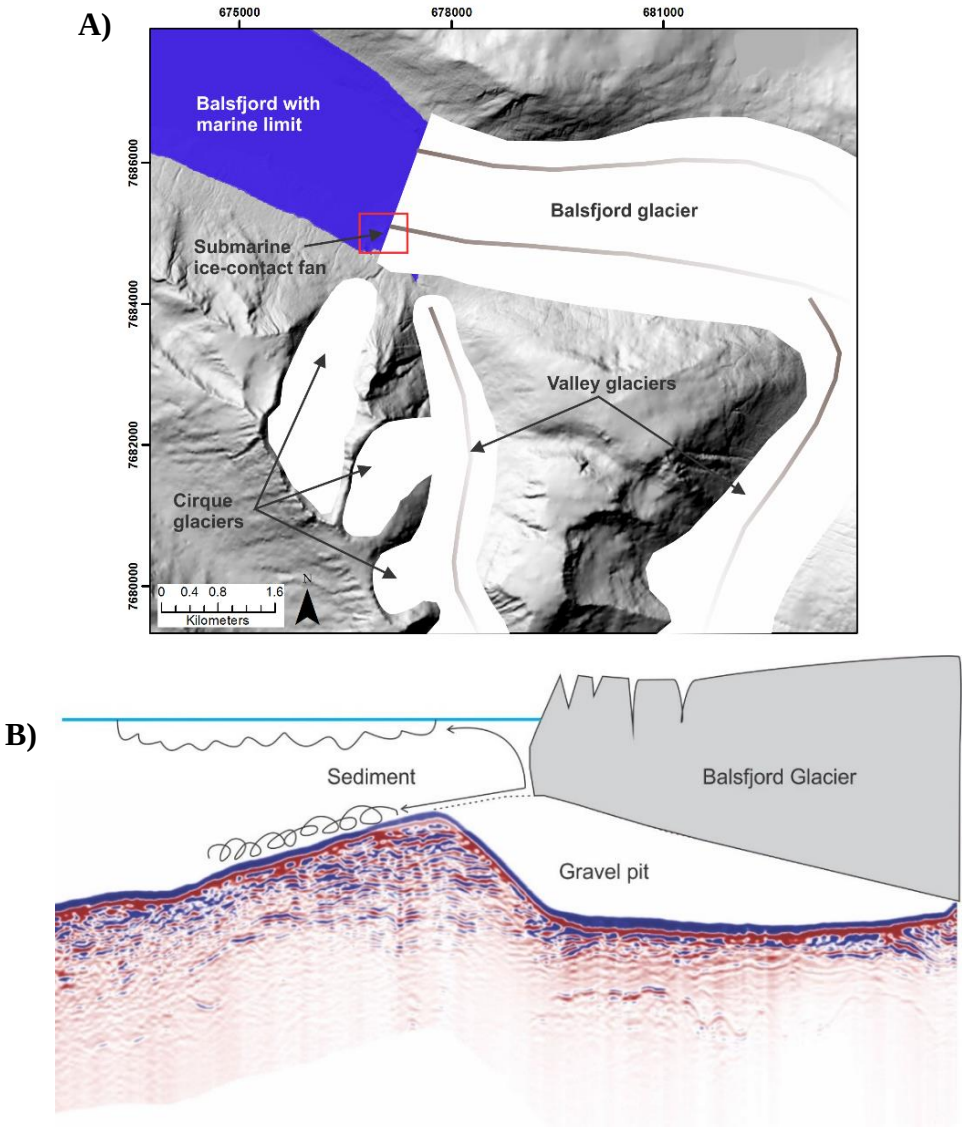

Figure 44: Sketches of the interpreted depositional environment. The glaciofluvial sediment was deposited as a submarine ice-front fan directly in front of the Balsfjord glacier during a halt in the retreat of the glacier. A) Plan-view interpretation. The background image is a DTM-derived shaded-relief map of the study area (azimuth = 315° and sun elevation = 45°) and the position of the glaciers has been drawn using elevation information from this DTM. B) Cross-section interpretation.

The glaciofluvial sediment did not build up to the contemporaneous sea level, and therefore, the glaciofluvial ridge is interpreted as a submarine ice-contact fan (Powell, 1990, Lønne, 1995). The morphology of the glaciofluvial ridge supports this interpretation. A submarine ice-contact fan is defined as a wedge of coarse-grained sediment deposited subaqeuously at the grounding line of a glacier (Lønne, 1995) and the internal structure of a submarine ice-contact fans consists of bottomset beds overlaid by steeply dipping foreset beds created by sediment gravity flows (Figure 44A). The steeply dipping foreset beds of the submarine ice-contact fan have been identified on the GPR profiles taken across the deposit. Figure 44 shows the interpreted depositional environment whereby the eastern side of the deposit represents the ice-contact slope. Ice-contact submarine fans are usually deposited due to a halt in the retreat of the glacier (Benn and Evans, 1998, Corner, 2006) and therefore, the identification of this landform indicates that the retreating Balsfjord glacier halted in the location of the present-day fjord-side fan delta.

4.2.4 Glaciofluvial and Rock-Avalanche Complex

A distinctive deposit of glaciofluvial and rock-avalanche sediment is located on the upper western side of the study area, immediately above the postglacial fan delta (Figure 45). Within the complex, the cobbly sandy gravel sediment and rock-avalanche boulders interfinger and therefore, this sediment will be described together. The description focuses on three different areas within the complex (A, B and C) and the location of the descriptions is shown in Figure 45A.

The rock-avalanche deposit is one of the most distinctive morphogenetic elements within the study area. A lot of the rock-avalanche and glaciofluvial sediment is covered by a thick sub-boreal birch forest. Therefore, it is difficult to determine the true thickness of the deposit and mapping is primarily based on the surface expression. The boundaries of the rock-avalanche deposit were mapped during fieldwork using a hand-held GPS. Where vegetation cover is thin, rock-avalanche boulders were identified, and mapped using aerial photographs. Additionally, the frequency and size of rock-avalanche boulders was also recorded in the field. Detailed mapping of the morphology of the rock-avalanche deposit found that it is complex and has been altered by post depositional processes.

In plan-view the rock-avalanche deposit is elongate (Figure 45). It is 1 km long and its width varies between 100 and 300 m. In cross section, the morphology of the rock-avalanche deposit consists of long elongate north-south orientated lobes and ridges (200 to 400 m long and up to 10 m high). The Buktelva river flows along the eastern edge of the rock-avalanche and glaciofluvial complex and a distinctive bend in the river that is shown in Figure 45 indicates that it could have been diverted by deposition of the rock-avalanche boulders. Colluvial sediment has been deposited from this bend in the river over the lower section of the rock-avalanche deposit (Figure 45). The front of the rock-avalanche complex interfingers with coarse cobbly, sandy gravel sediment.

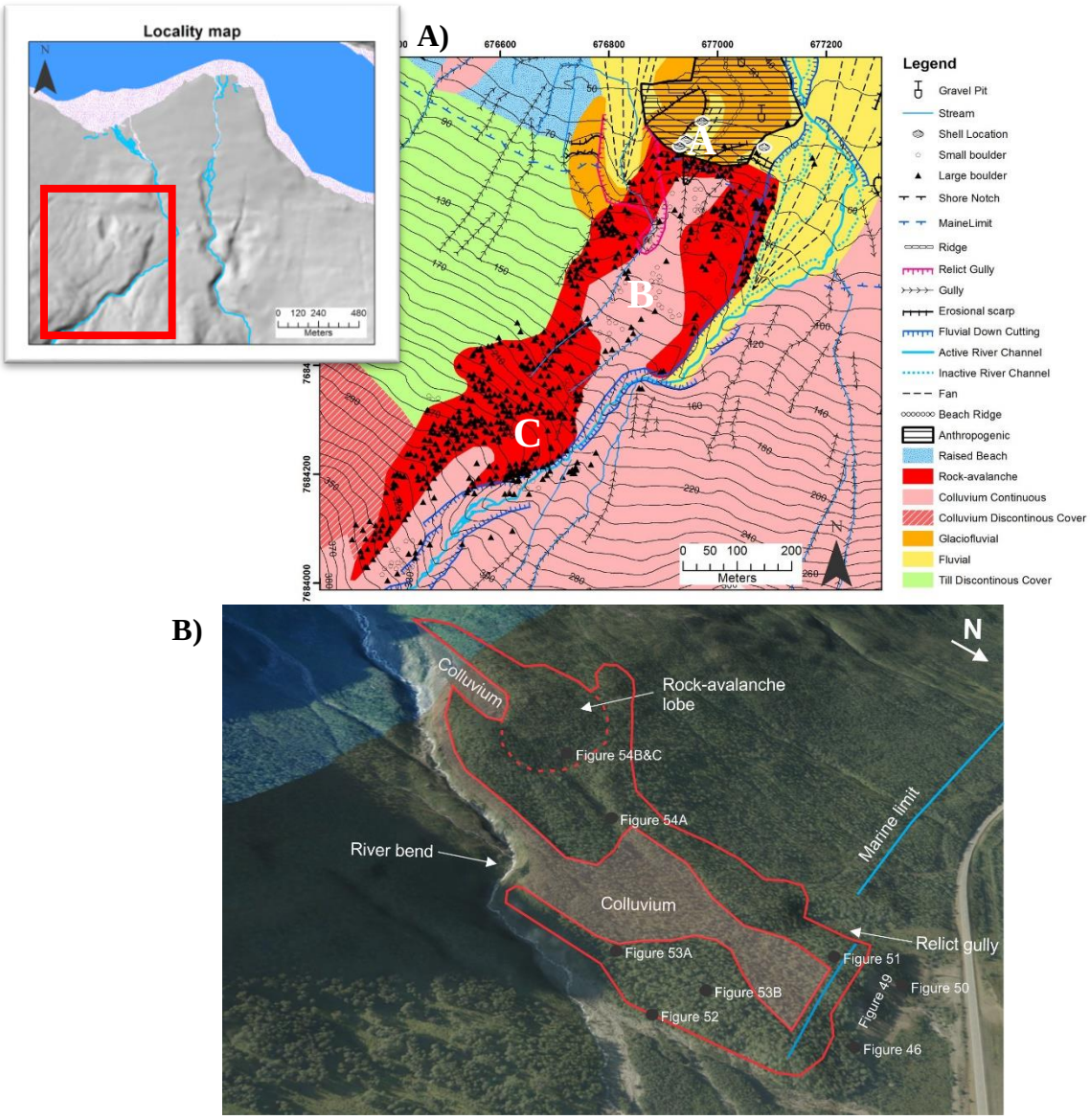

Figure 45: A) Detailed map of the rock-avalanche deposit (red) and glaciofluvial sediment (orange) created through field mapping and aerial photograph interpretation. B) Oblique aerial view photograph of the rock-avalanche deposit taken from norgei3D (looking south west) (www.norgei3d.no). The boundaries of the rock-avalanche and important geomorphological features have been annotated on this photograph.

4.2.4.1 Area A: Front of rock-avalanche and glaciofluvial complex

Unfortunately, the original morphology of the front section of this deposit has been destroyed by the construction of the E6 highway and gravel pit operations. Figure 46 shows an abandoned gravel pit, which has exposed a very thick accumulation of glaciofluvial sediment and rock-avalanche boulders. This slope represents the present-day northern-most extent of the deposit. This glaciofluvial sediment is composed of sub-rounded to sub-angular cobbly sandy gravel. The gravel size fraction has a mode of 2 cm and a maximum clast size of 15 cm (Figure 46B).

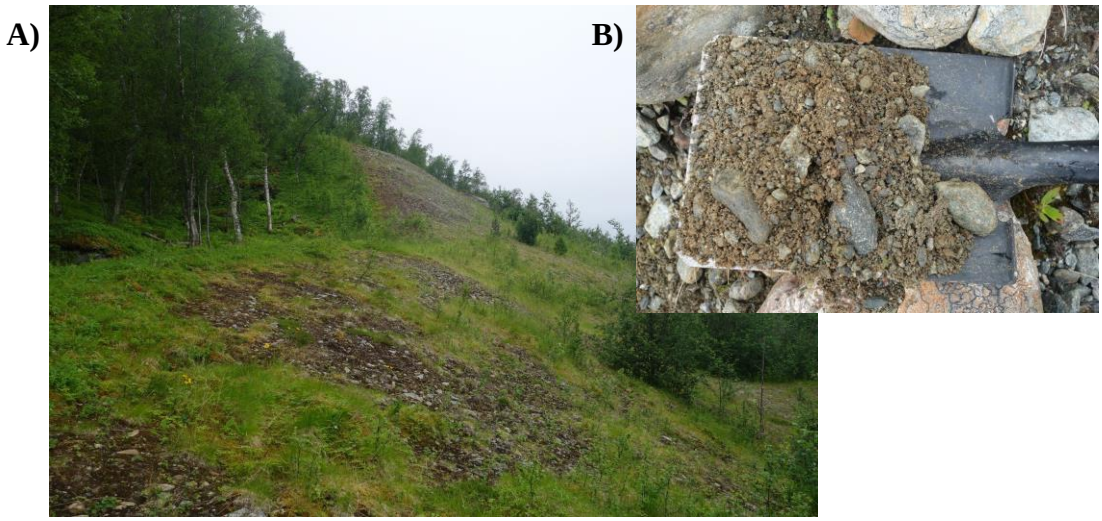

Figure 46: A) Photograph of the front of the present-day glaciofluvial deposit. A lot of sediment has been removed during gravel pit operations and the front of the deposit now consists of a smooth, sparsely vegetated gravel slope. B) Photograph of the glaciofluvial sediment, which consists of sub-rounded to sub-angular cobbly sandy gravel. The location of the photographs is shown in Figure 46.

The original morphology of this glaciofluvial sediment has also been investigated and mapped stereoscopically. Figure 47 shows the original morphology consists of three distinctive elongate accumulations of sediment with an approximate north-south orientation that are separated by wide erosional gullies. It is hypothesized the glaciofluvial sediment originally had a larger extent. However, following deposition, the glaciofluvial sediment has been subjected to headward erosional processes, which has eroded and redistributed the sediment forming the large gullies. This headward erosion will be discussed in more detail in section 4.2.7. The glaciofluvial sediment is graded to the marine limit (83 m a.s.l).

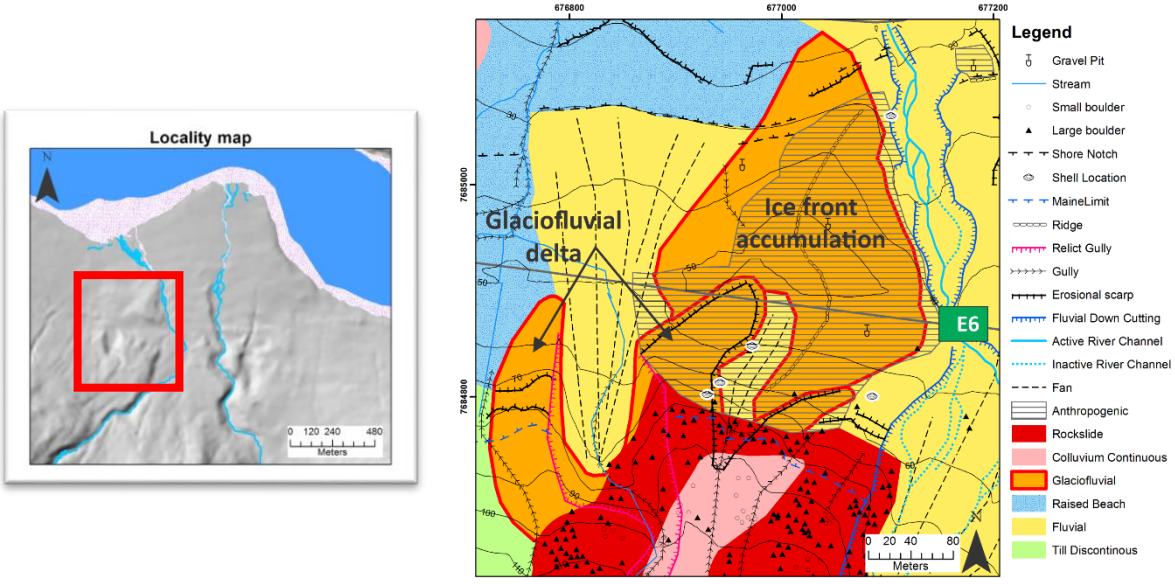

Figure 47: Detailed map of the front of the glaciofluvial and rock-avalanche complex, which is located immediately behind the submarine ice-contact fan. The original morphology has been mapped based on stereoscopic interpretation of aerial photographs.

The front-most boulders of the rock-avalanche was deposited deposit onto this glaciofluvial sediment (Figure 45) and these boulders were subsequently buried by glaciofluvial and fluvial sedimentation. Excavation of a gravel pit within this sediment has exposed a vertical sedimentary section (Figure 46) and six large boulders at the front of the rock-avalanche deposit occur within this section. The elevation of these boulders ranges from 80 to 50 m above the present-day mean sea level (Figure 48 and Figure 49).

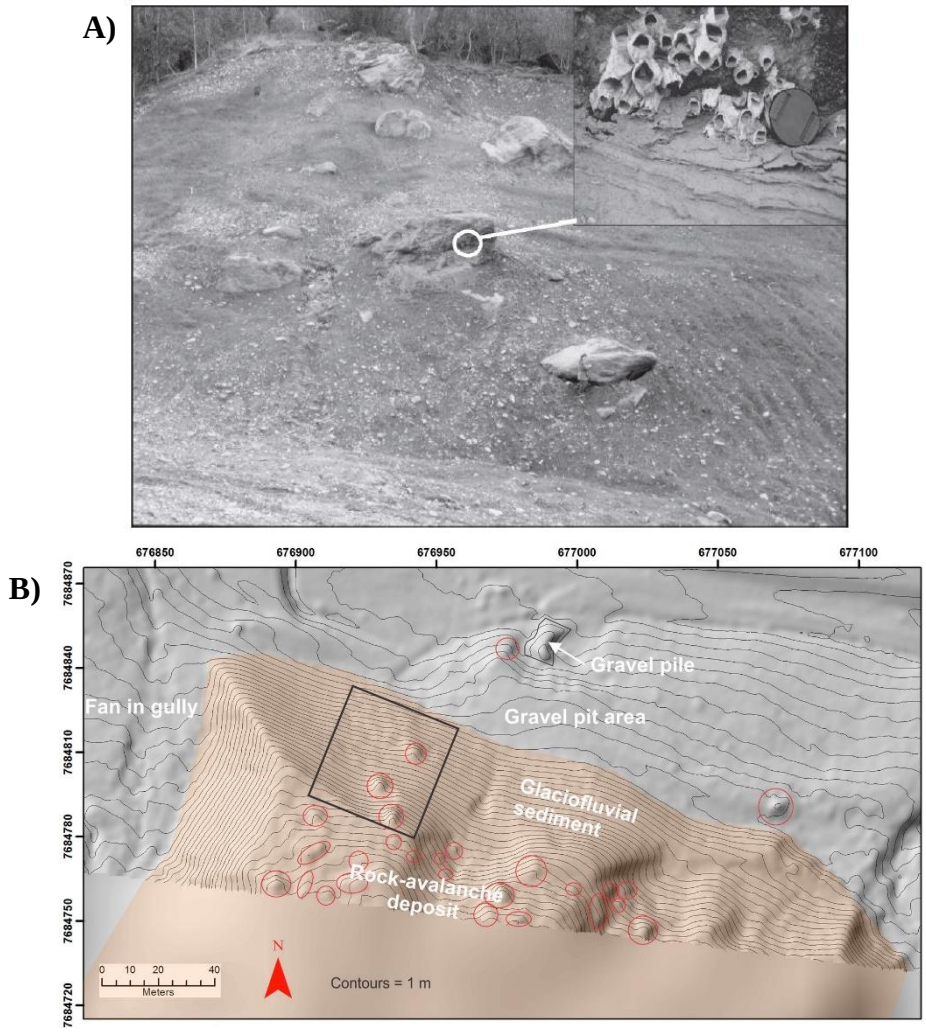

Figure 48: A) Photograph of a vertical sedimentary section of glaciofluvial sediment and rock-avalanche boulders taken shortly after the section was exposed by gravel pit operations. Reproduced from Blikra et al. (2006). B) Lidar-derived shaded-relief map of the front of the rock-avalanche deposit showing the present-day morphology, which has been altered by anthropogenic gravel pit operations (Sun azimuth = 315° and Sun elevation = 45°) (https://hoydedata.no/LaserInnsyn/). The black box shows the approximate position of the photograph shown in (A). Orange colour = glaciofluvial material and red circles = rock-avalanche boulders.

Unfortunately, the vertical sedimentary section has degraded over time and it is now difficult to observe the original sedimentary structures (Figure 49). For example, more rock-avalanche boulders could be observed within the sedimentary section when it was first exposed (Figure 48A) compared with the present-day section (Figure 48B). However, Blikra et al. (2014) documented the section shortly after it was exposed. They describe the sediment as large boulders with the interstitial spaces filled with undeformed, stratified and laminated sediments consisting of silt, sand and gravel. The boulders are between 4 and 7 m in length and are sub-rounded to sub-angular. Some of the front-most rock-avalanche boulders are covered in *Balanus* shells, which are filled with silty sand (Figure 50). This indicates that the shells were buried and they have been recently exposed by the

excavation activity (Figure 48 and Figure 49). The growth of *Balanus* shells indicates the front-most rock-avalanche boulders were deposited into the sea. One *Balanus* sample that was attached to a rock-avalanche boulder located at 51 m a.s.l was radiocarbon dated during this study (Table 7). This age has been added to the three previously published ages to give a reliable weighted mean age of 10 884 ± 96 cal. yr BP (1σ) (Blikra, 1998, Blikra and Longva, 1999, Fenton et al., 2011).

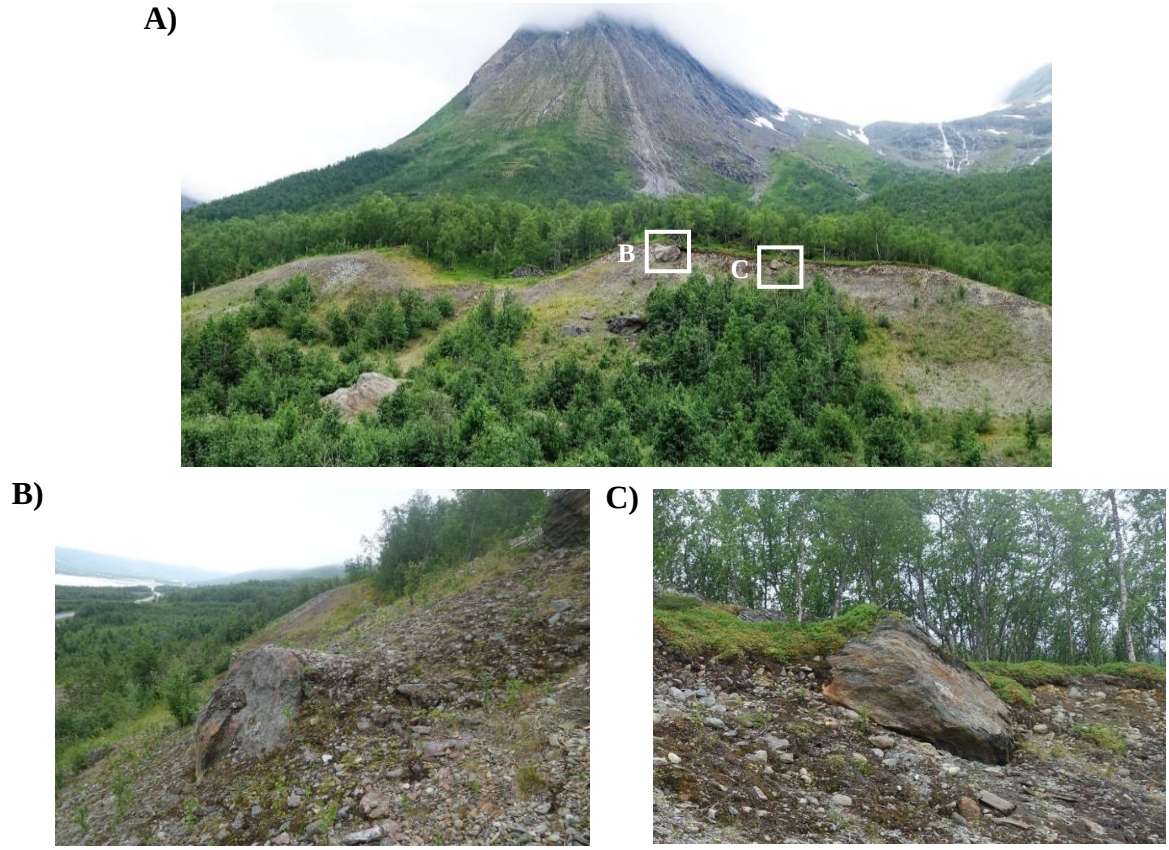

Figure 49: A) Photograph showing the vertical sedimentary section at the back of the gravel pit. It is composed of glaciofluvial sediment and rock-avalanche boulders. B and C) Photographs of large rock-avalanche boulders located on the slope of the gravel pit. These boulders are partially buried by glaciofluvial sediment. The location of the boulders is shown by the white boxes in A. The location of the photographs is shown in Figure 46.

Figure 50: Balanus shells observed on one of the large rock-avalanche boulders at the front of the deposit (65 m a.s.l). Sand was observed within some of the *Balanus* shells indicating that they have been buried by sediment. *Pencil = 14.5 cm. The location of the photograph is shown in Figure 46.*

Table 7: Ages of material attached to the rock-avalanche boulders. All radiocarbon dates from Forwick and Vorren (2002) were corrected for a reservoir effect of 440 years and calibrated using the INTCAL98 database. All ages have been recalibrated using the MARINE13 database.

Lab number	Dated material	Published Age (^{14}C BP) corrected for reservoir effect	Conventional Age (^{14}C BP)	Published calibrated age (cal. yr BP; 1σ)	Recalibrated age (cal. yr BP; 2σ)	Weighted mean calendar age (± 1σ) (cal. yr BP)*	Reference
T-13805	*Mya truncata*	9555 ± 75	9995 ± 75	10 369 - 11 122	10 674 – 11 108	10 884 ± 96	(Forwick and Vorren, 2002)
T-13806	*Balanus sp.*	9610 ± 80	10 050 ± 80	10 609 - 11 136	10 719 – 11 155		(Forwick and Vorren, 2002)
T-13807	*Balanus sp.*	9615 ± 70	10 055 ± 70	10 609 - 11 136	10 738 – 11 148		(Forwick and Vorren, 2002)
Beta - 463116	*Balanus sp.*	-	9930 ± 30	-	10 664 - 10 974		Obtained during this study

**Weighted mean calculated using inverse variance weighting*

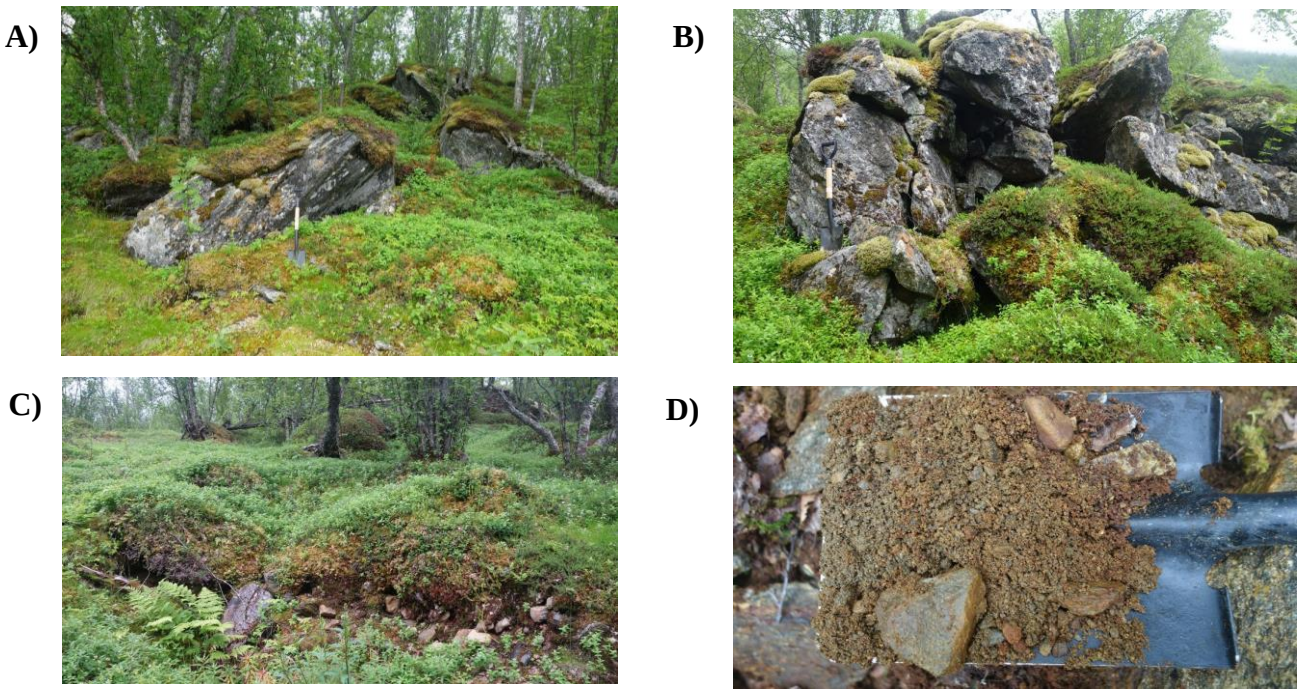

Figure 51: A and B) Photographs of the rock-avalanche boulders located above the gravel pit. The boulders are angular and chaotically distributed. C) Photograph of the terrace surface surrounding the rock-avalanche boulders. D) Photograph of the glaciofluvial sandy gravel. The location of the photographs is shown in Figure 46.

There are a many rock-avalanche boulders located immediately above the gravel pit (Figure 51). These boulders are angular and vary in size from 50 cm to 6 m. The boulders have no preferred orientation and frequently occur in piles. Additionally, the surface has a ridge and furrow morphology whereby ridges occur in a north-south orientation and are 100 to 150 m long and approximately 20 m wide.

A few different rock-types have been identified at the front of the rock-avalanche deposit. Blikra et al. (2006) and Fenton et al. (2011) have identified boulders of quartz mica schist. Samples collected during this study have been identified as biotite gneiss and garnet biotite gneiss. Occasionally, some of the boulders have a jigsaw fit texture that indicates they were broken *in situ*. An irregular terrace surface with a gentle upward slope has been identified close to the marine limit on the rock-avalanche deposit. The sediment within the terrace surface is composed of cobbly sandy gravel (Figure 51 C and D).

River downcutting by the Buktelva river on the eastern boundary of the rock-avalanche deposit has exposed rock-avalanche boulders (Figure 52). These boulders are angular to sub-angular and randomly distributed. Occasionally an unusual sub-rounded boulder was observed (e.g. Figure 52A), which indicates the boulder has been subjected to abrasion. Exposures in the river bank show that the boulders have been deposited onto sorted sandy gravel. The gravel clasts are sub-angular and have a maximum clast size of 10 cm. Some boulders were also observed on the eastern side of the Buktelva river.

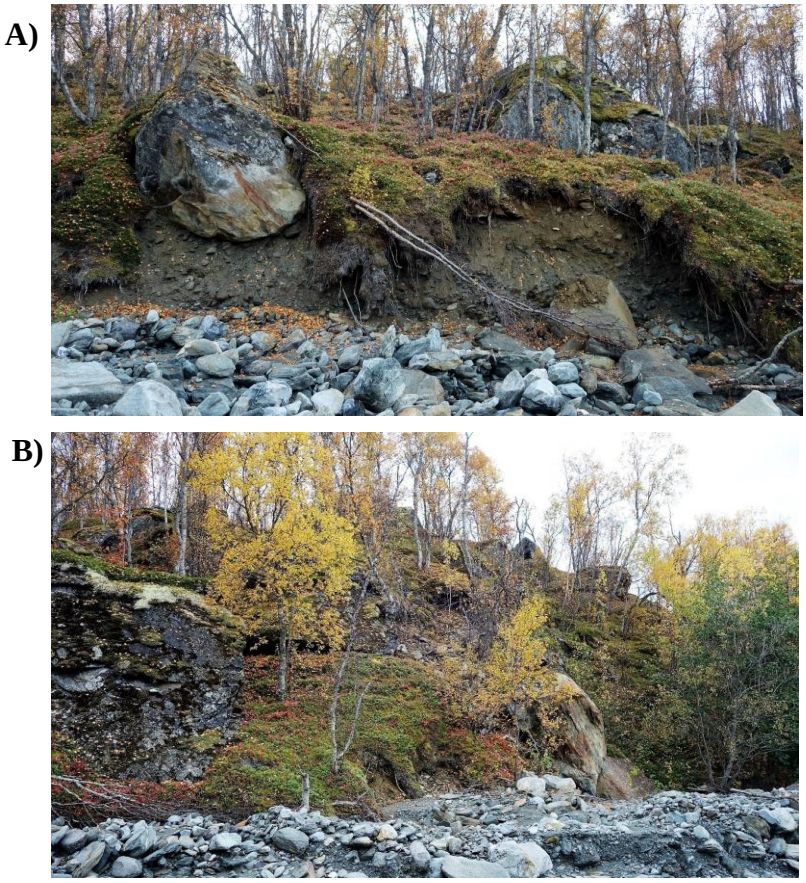

Figure 52: A and B) Photographs of the rock-avalanche boulders located next to the Buktelva river. The location of the photographs is shown in Figure 46.

4.2.4.2 Area B: Colluvium

Colluvium has been mapped through the centre of the rock-avalanche deposit (Figure 45). The colluvium commences at the bend in the Buktelva river shown in Figure 45 and occurs as an elongate band (approximately 400 m long and 150 m wide). The colluvium is characterised by an undulating surface morphology with common ridges and gullies (Figure 53). Some boulders are observed within the colluvial sediment but most of these boulders are less than 1 m long and are interpreted to be deposited as part of the colluvium. Occasionally large rock-avalanche boulders were observed (>1 m). Two small streams flow through this area and the presence of colluvium is often accompanied with a change in vegetation, whereby the sub-boreal birch forest becomes much thicker.

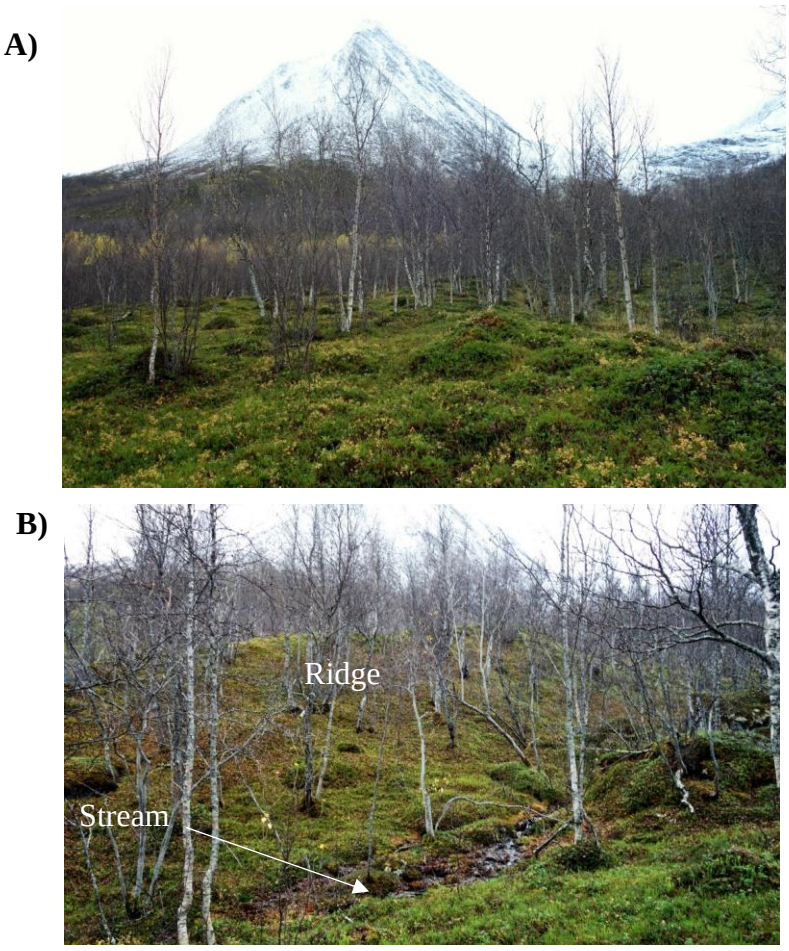

Figure 53: A and B) Photographs showing the colluvial sediment that is located in the middle of the rock-avalanche complex. The photographs show the surface is undulating and can contain ridges and streams. Small boulders are common and large isolated rock-avalanche boulders occur sporadically. The location of the photographs is shown in Figure 46.

4.2.4.3 Area C: Top of rock-avalanche deposit

The upper part of the rock-avalanche deposit has a steep gradient (25°) and there is a very high concentration of rock-avalanche boulders (Figure 54). These boulders are angular, vary in size from 50 cm to 10 m and are distributed chaotically. The rock-avalanche boulders frequently form distinctive ridges. The rock-avalanche boulders within this area are composed on gabbro and metagabbro. Figure 55 shows a distinctive rock-avalanche lobe that is located at the top of the rock-avalanche deposit. This lobe is 500 m long and has a characteristic head and tail region. The front half

of the lobe forms the head (150 m wide), whilst the back of the lobe thins to an apex point forming the tail. Figure 55B shows a cross section of the rock-avalanche lobe, which is approximately 10 m high. Colluvium has been deposited around this rock-avalanche lobe.

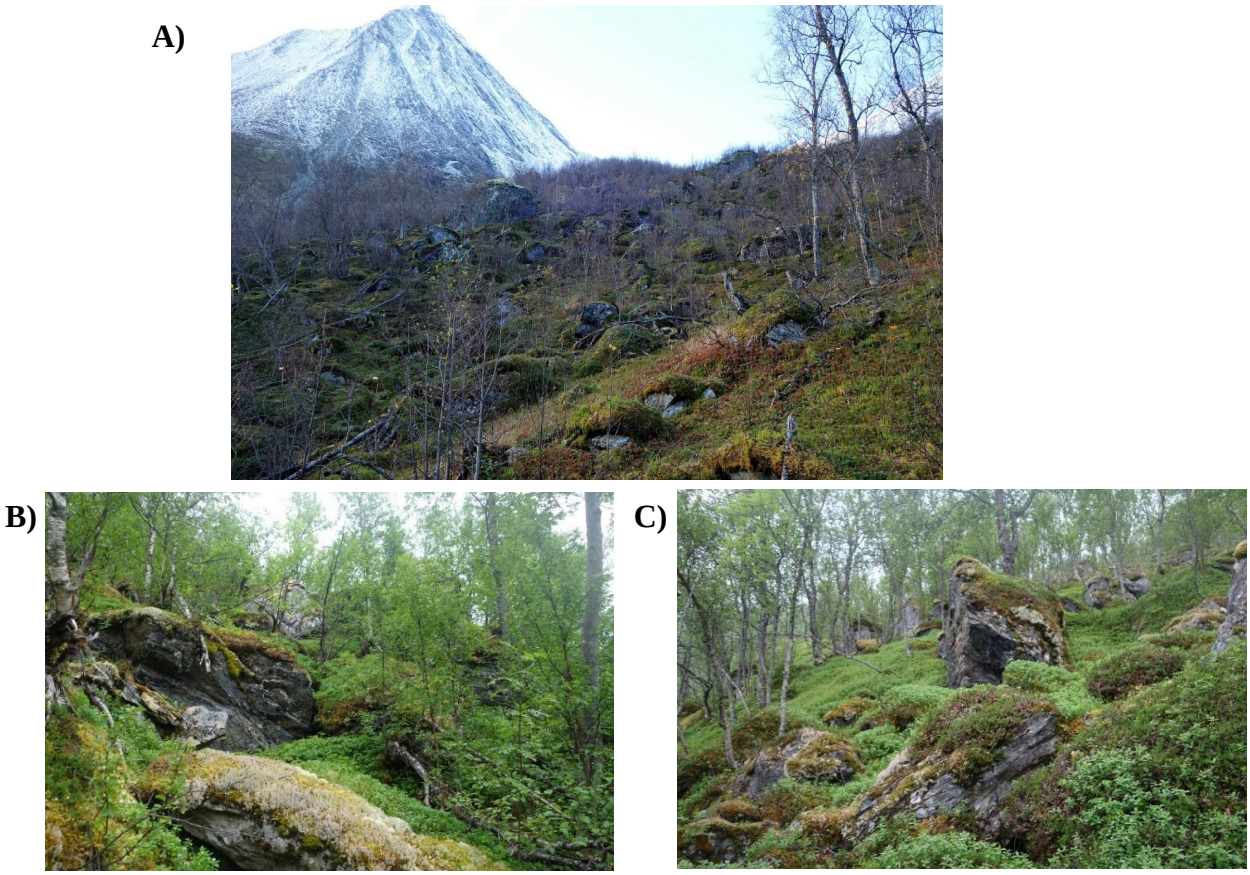

Figure 54: A to C) Photographs of rock-avalanche boulders in the upper section of the deposit. There is a high concentration of boulders in this area. The boulders are randomly distributed and are often piled on top of each other. The location of the photographs is shown in Figure 46.

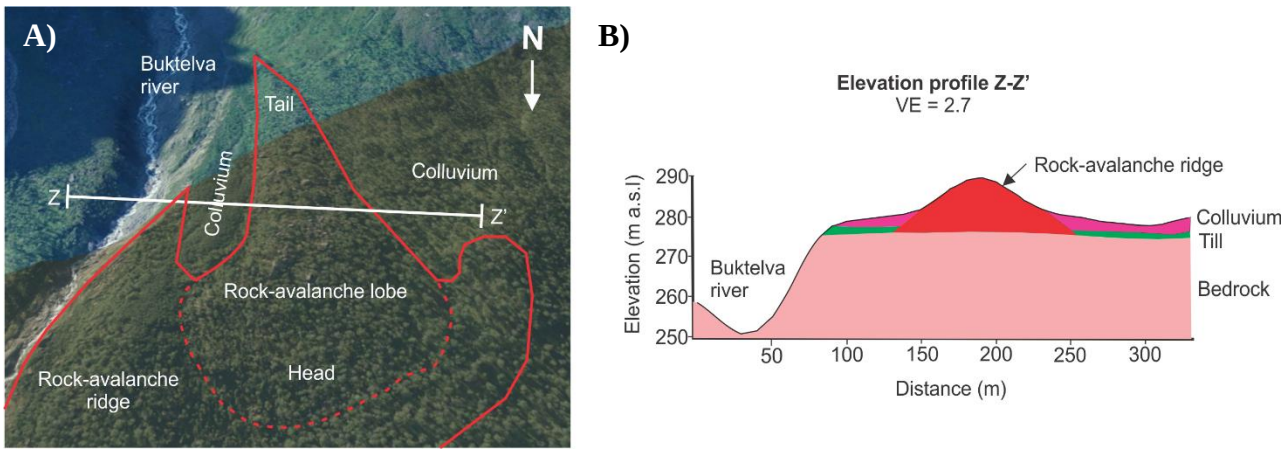

Figure 55: A) Oblique aerial view looking south of the upper section of the rock-avalanche deposit from norgei3D (www.norgei3D.no). The morphology of the rock-avalanche deposit is annotated and a 500 m long rock-avalanche lobe with a distinctive head and tail is shown. B) Elevation profile Z-Z' across the rock-avalanche lobe showing the rock-avalanche lobe is 10 m high (location shown in A).

4.2.4.4 Source of rock-avalanche

Several different rock types have been identified within the rock-avalanche complex, which indicates that the boulders have been deposited by multiple rock-avalanche events. The slopes directly above the rock-avalanche complex are greater than 45° and belong to the Store Russetinden and Rakeltinden mountains. The composition of the bedrock directly above the rock-avalanche deposit is dominated gabbro and metagabbro (Figure 56). Therefore, the grabbro and metagabbro rock-avalanche boulders identified in the upper section of the rock-avalanche complex probably originated from this gabbro bedrock and the possible rock-avalanche paths are shown in Figure 56. The head and tail morphology of the rock-avalanche lobe shown in Figure 55 supports this conclusion because it shows the flow direction of the rock-avalanche boulders and indicates that they originated from the tall mountains located directly above the deposit. The present-day cirque glaciers located above the rock-avalanche deposit could have had a larger extent during the deposition of the rock-avalanche and therefore, the rock-avalanche could have partially travelled along the glaciers.

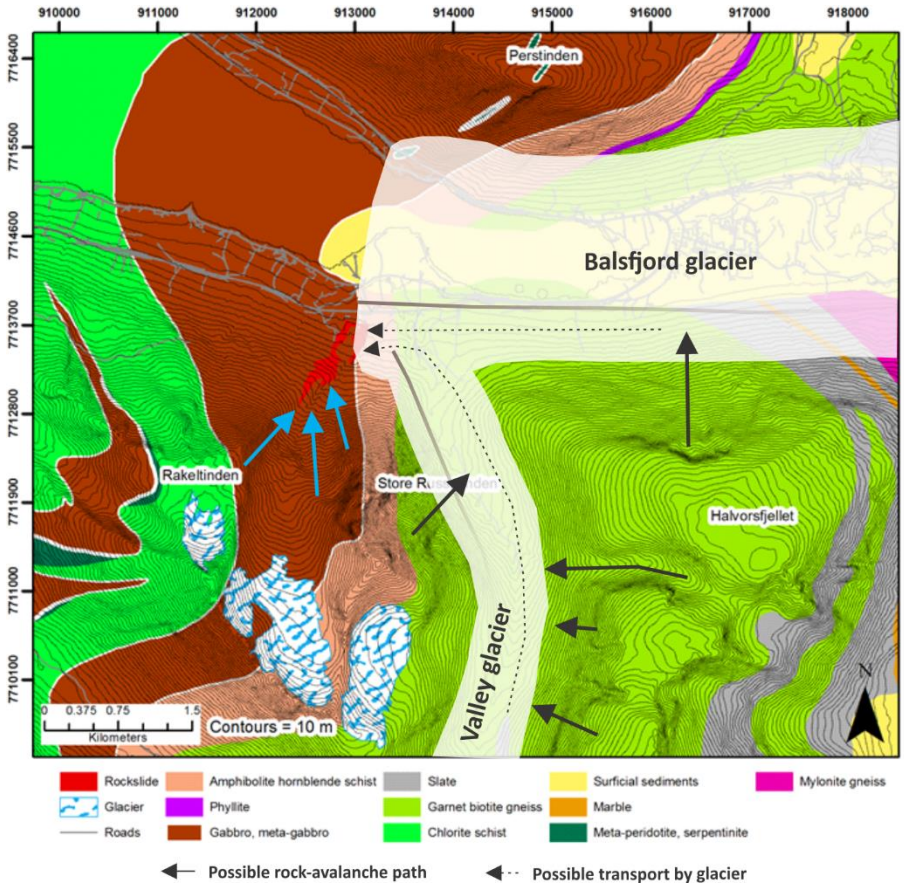

Figure 56: Map showing the bedrock geology above the Russenes rock-avalanche. The blue arrows show the possible rock-avalanche paths for the gabbro and metagabbro boulders located in the upper section of the rock-avalanche complex. The garnet biotite gneiss boulders in the bottom section of the rock-avalanche complex must have been partially transported by a glacier and the black arrows show the possible transport paths. This map has been created from the Berggrunn N50 digital dataset available from Norges Geologiske Undersøkelse (NGU, 2015a).

The rock-avalanche boulders located at the bottom of the rock-avalanche complex have been identified as garnet biotite gneiss, biotite gneiss and quartz mica schist. Therefore, these boulders have been sourced from the garnet biotite gneiss located in the study area (Figure 56). However, the bedrock geology map indicates that this rock types does not occur on the slopes immediately above

the rock-avalanche deposit (Figure 56). Therefore, these rock-avalanche boulders must have been partially transported by a glacier or glacier ice must have occupied the run-out zone of the rock-avalanche. Figure 56 shows some hypothesised rock-avalanche trajectories and subsequent glacier transport paths (black arrows). Further fieldwork is required to determine the source areas, boundaries and relationship between the two rock-avalanche deposits.

4.2.4.1 Interpretation

The cobbly sandy gravel-dominated glaciofluvial sediment is interpreted as a glaciofluvial delta deposit that is graded to the marine limit. This glaciofluvial delta could have been deposited within two different depositional environments: (1) as an ice-contact delta that was deposited directly from the Balsfjord glacier; or (2) as a valley-side glaciofluvial delta. However, the interfingered nature of the glaciofluvial and rock-avalanche sediment can be used to differentiate these two glaciofluvial deltaic environments.

The front of the rock-avalanche was deposited onto this glaciofluvial delta and subsequently partially buried by glaciofluvial and fluvial sediment. It has been determined that the biotite garnet gneiss rock-avalanche boulders have been sourced from outside the catchment area and therefore, they must have been transported on the Balsfjord glacier. Consequently, these rock-avalanche boulders would have been deposited from the melt-out of glacier ice and the geomorphology of the rock-avalanche complex supports this interpretation. The melting of ice from the rock-avalanche debris following deposition can produce the following morphologies: chaotic topography, openwork texture, dominantly angular class with occasional glacially rounded boulders, piles of boulders and a lack of fine material (Hewitt, 2009) and most of these characteristics have been observed at the front of the rock-avalanche complex. For example, most of the rock-avalanche boulders are angular but occasionally rounded, abraded boulders occur, which suggests that have been deposited from a glacier.

Therefore, it is likely that both the glaciofluvial sediment and rock-avalanche boulders have been deposited by the Balsfjord glacier as an ice-contact glaciofluvial delta (Figure 57A). This hypothesis is supported by the identification of the submarine ice-contact fan that is aligned with the ice-contact glaciofluvial delta and rock-avalanche complex (Section 4.2.3) because all this sediment could have been deposited simultaneously during a halt in the retreat of the Balsfjord glacier. Therefore, the radiocarbon dates obtained from the *Balanus* shells located on the front-most rock-avalanche boulders give a minimum age of 10 884 ± 96 cal. yr BP (1σ).

Some of the rock-slide boulders that were deposited below the marine limit show signs of abrasion suggesting that they were eroded by waves and currents when they were exposed on the sea floor. Following the retreat of the Balsfjord glacier, the front-most rock-avalanche boulders were later infilled and covered by silt, sand and gravel from the progradation of a valley-side glaciofluvial and subsequent fluvial delta and the *Balanus* shells were buried (Figure 58) (Blikra et al., 2006). The glaciofluvial terrace that has been identified surrounding the rock-avalanche boulders immediately above the marine limit indicates that some sediment was transported and deposited in this area by fluvial processes following the deposition of the rock-avalanche.

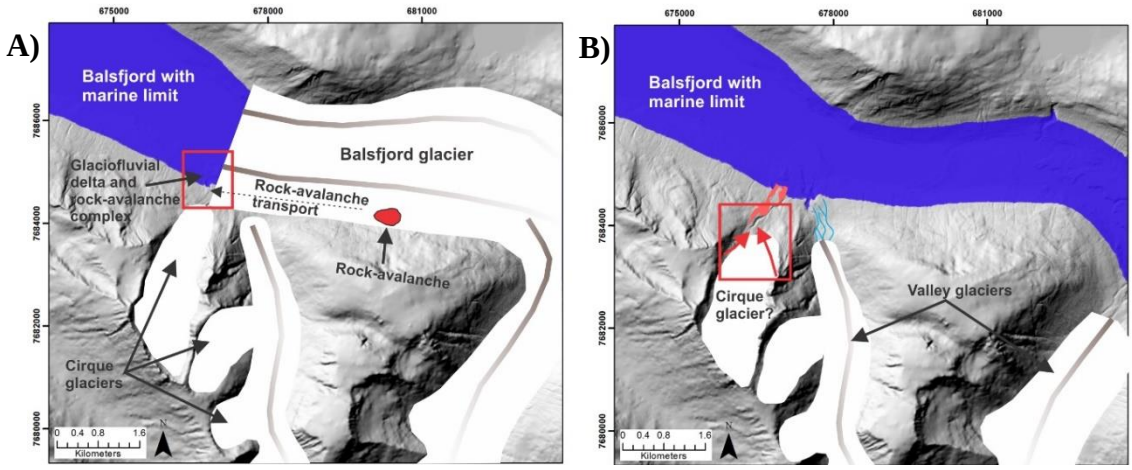

Figure 57: Schematic model showing the depositional environment of the multiphase rock-avalanche and glaciofluvial complex. A) Interpreted depositional environment of the ice-contact glaciofluvial delta and rock-avalanche deposit during a halt in the retreat of the Balsfjord glacier. B) Interpreted depositional model of the upper section of the rock-avalanche deposit that originated from the Store Russetinden or Rakeltinden mountains. The glacier configuration and timing of this deposit is unknown. The background image of both models is a DTM-derived shaded-relief map of the study area (azimuth = 315° and sun elevation = 45°) and the position of the glaciers has been drawn using elevation information from this DTM.

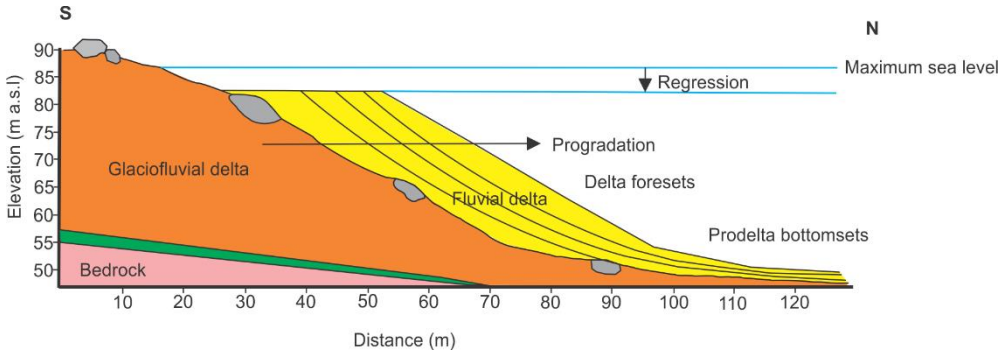

Figure 58: Reconstruction of how the front-most rock-avalanche-boulders were buried by sediment from a side entry fluvial delta.

The schematic diagram presented in Figure 57 shows the multi-phase nature of the rock-avalanche deposit. The timing of the deposition of the upper section of the rock-avalanche complex has not been constrained and it is unknow whether the rock-avalanche boulders partially travelled on the cirque glaciers. The colluvium sediment mapped through the centre of the rock-avalanche deposit is interpreted to be deposited after both rock-avalanche events. Colluvium is deposited by mass movement processes, such as debris flows and catastrophic debris flows can be triggered by rock-avalanches. However, they are usually triggered within the unconsolidated, water-saturated sediment at the front of the rock-avalanche (Evans et al., 2006). Therefore, it follows that the colluvium sediment located in the centre of the rock-avalanche deposit, was deposited after the rock-avalanche. The location of the colluvium indicates it could be been deposited due to flooding of the Buktelva river or from debris flows that originated on the Store Russetinden mountain. However, it is hypothesised that this section of the rock-avalanche deposit only contained sparse rock-avalanche boulders because it is unlikely that the colluvium sediment could have buried the large rock-avalanche boulder ridges observed elsewhere within the deposit.

4.2.5 Eastern Glaciofluvial Delta Complex

Another deposit of sandy gravel is located on the upper eastern side of the fan delta adjacent to the glaciolacustrine deposit (Figure 59). The morphology of this deposit is complex and results from the interplay between depositional processes, marine and fluvial erosional processes and anthropogenic activity. In plan-view, this deposit has a fan-shaped morphology with the sediment originating from an apex point (Figure 59). Most of the deposit is located above the marine limit and the upper section is characterised by a very shallow gradient (0.8°) compared with the surrounding steep slopes (10°) (Figure 59). Bedrock is located close to the surface in this area and the shallow gradient is attributed to a natural break in the bedrock slope (Figure 60). This indicates that there is only a thin cover of sandy gravel sediment in the upper part of this deposit.

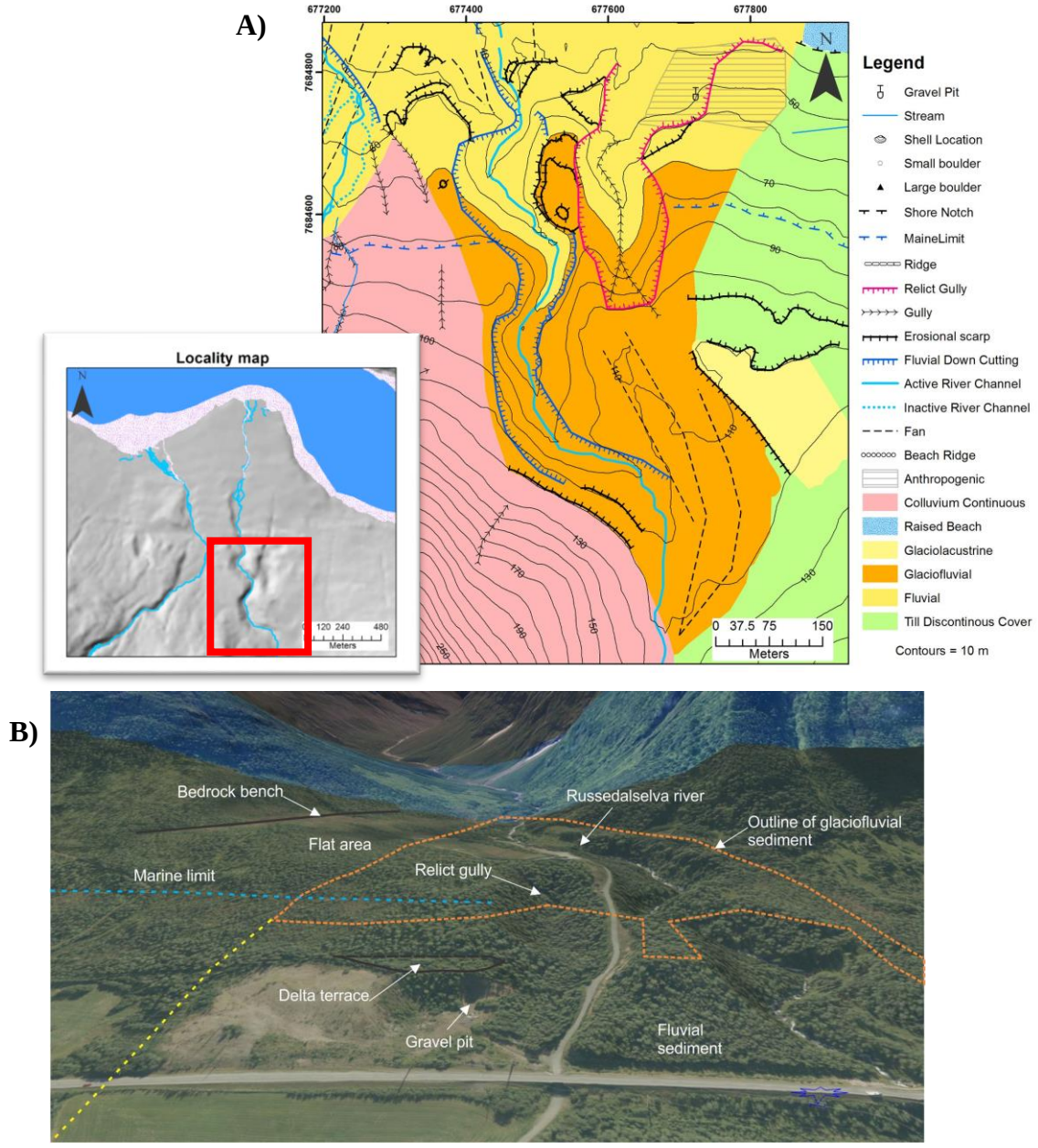

Figure 59: A) Detailed map of the glaciofluvial sediment on the eastern side of the fan delta. B) Oblique aerial view image (looking south) of the upper eastern side of the fan delta produced using norgei3D. The approximate position of the glaciofluvial sediment is shown by the orange, dashed outline. The glaciofluvial sediment has a complex morphology and some of the morphological features are highlighted in this image.

The bottom section of the glaciofluvial deposit is located below the marine limit (Figure 59) and therefore, this sediment was deposited below sea level. The Russedalselva river cuts steeply into the glaciofluvial and fluvial sediment on the western side of the deposit, which indicates that the river has been in this location for a long time (Figure 59 and Figure 60). There is also a steep relict gully in the centre of the glaciofluvial sediment (Figure 59) that will be discussed further in Section 4.2.7. The large extent of fluvial downcutting by both the Russedalselva river and relict gully indicates that there is a thick accumulation of glaciofluvial and fluvial sediment at the bottom of the deposit.

4.2.5.1 Interpretation

This deposit is interpreted as a glaciofluvial delta that was graded to the marine limit. The fan shaped morphology indicates that the sediment was deposited from a retreating valley glacier rather than from the main Balsfjord glacier (Corner, 2006, Eilertsen et al., 2006). Therefore, it is interpreted as a valley-side glaciofluvial delta fed by remnant valley glaciers following the deglaciation of Balsfjord. Although the morphology of the deposit is fan-shaped, it is interpreted as a common glaciofluvial delta rather than a fan delta because the subaerial component does not have an alluvial fan.

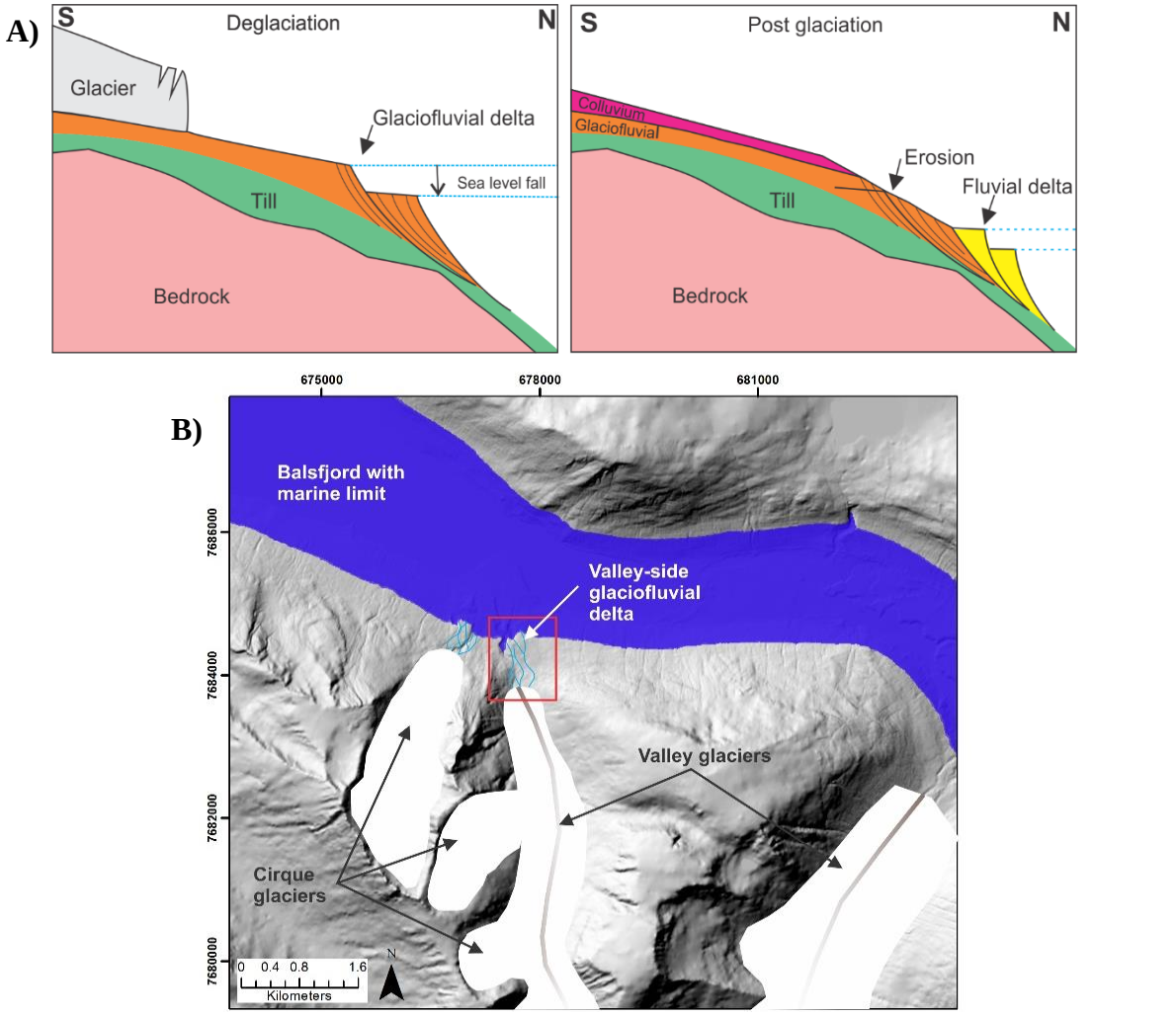

Figure 60: Schematic diagrams showing the interpreted depositional environment of the valley-side glaciofluvial delta A) Cross-sections showing the depositional environment of the glaciofluvial and subsequently fluvial deltas. During the postglacial period the sediment has been altered by erosion and the deposition of colluvium and fluvial sediment. B) Interpretation of the depositional environment of the valley-side glaciofluvial delta deposit. The background image is a DTM-derived shaded-relief map of the study area (azimuth = 315° and sun elevation = 45°) and the position of the glaciers has been drawn using elevation information from this DTM.

Figure 60A presents a schematic model of the depositional environment of the valley-side glaciofluvial delta. The model shows that delta terraces should have formed due to sea level fall, and recorded the progradation history of the delta. However, these terraces have not been identified within the deposit and it is hypothesised that they have been destroyed by fluvial depositional and erosional processes. Figure 60B shows that following deglaciation, progradation of the delta continued as fluvial sediment was delivered to the sea by the Russedalselva river. A single postglacial delta terrace has been preserved at 60 m a.s.l (Figure 59).

4.2.6 Colluvium

The proximity of the Russenes fjord-side fan delta to high mountains directly influences the type and nature of the sediment supplied to the alluvial fan component of the fan delta. The gradient of many of the slopes within the catchment area of fan delta ranges from 30° to 80° and over time colluvium has been deposited onto these slopes by mass wasting processes. Whilst colluvium has not been mapped on the postglacial alluvial fan, it has accumulated on the steep slopes directly above the fan and next to the rock-avalanche deposit during both the deglacial and postglacial periods (Figure 35) and Figure 61 shows that many of the slopes located above the fjord-side fan delta are covered with colluvium sediment. The colluvium is composed of loose, angular, unsorted, surficial sediment with a wide range of grainsizes and vegetation is usually spars surrounding the colluvium. Some debris flow deposits were also identified in the catchment area above the fan delta and consist of unconsolidated poorly sorted sediment (Figure 62A), which form ridges or mounds covered by thick vegetation (Figure 62B).

Figure 61: A) Photograph of part of the catchment area of the Russenes fjord-side fan delta taken from across the fjord by Rowan Romeyn. B) Panarama photograph of the Russetinden mountain taken from the middle of the rock-avalanche deposit. Both photographs show many of the steep slopes above the Russenes alluvial fan are covered with colluvium.

A)

B)

Figure 62: A) Photograph of the colluvium sediment located adjacent to the rockslide deposit. The sediment consists of thin deposit of loose sub-angular to sub-rounded cobbles and boulders. B) Photograph showing the surface morphology of colluvium sediment located immediately above the postglacial alluvial fan. The surface is undulating and elongate ridges or mounds often occur.

4.2.6.1 Interpretation

The loose, unconsolidated colluvium and till sediment located on the steep slopes within the catchment area of the Russenes fjord-side fan delta can be transported by mass movement processes, such as snow avalanches and debris flows (Blair and McPherson, 2009). Debris flows are particularly good at delivering large volumes of sediment to alluvial fans and they can be initiated infrequently on the slopes above the alluvial fan during periods of intense rainfall or due to rapid snow or ice melt (Section 2.3.1.2: Debris flows) (Galloway and Hobday, 1996, Blair and McPherson, 2009). Numerous gullies occur along the colluvium-covered slopes above the fan delta, which form pathways for debris flows. Deposition of debris flows has occurred periodically above the fan delta, during short-lived high-energy events throughout the deglacial and postglacial periods. However, debris flows are not a dominate mode of sediment transport on the Russenes fjord-side fan delta.

4.2.7 Headward Erosion

The glaciofluvial delta deposits contain large relict gullies (Figure 63). The eastern relict gully is 236 m long, 125 m wide, 15 to 20 m deep and this gully is currently dry (Figure 60). The western relict gully is 280 m long, 110 m wide at the widest point, approximately 15 m deep and this gully currently contains a small perennial stream (Figure 64). The top of western relict gully contains boulders from the rock-avalanche deposit (Figure 63). Apart from the small present-day stream within the western gully, there is no evidence of fluvial depositional or erosional processes above the relict gullies. For example, there is no geomorphological or sedimentological evidence to indicate the Russedalselva river once flowed through the eastern relict gully.

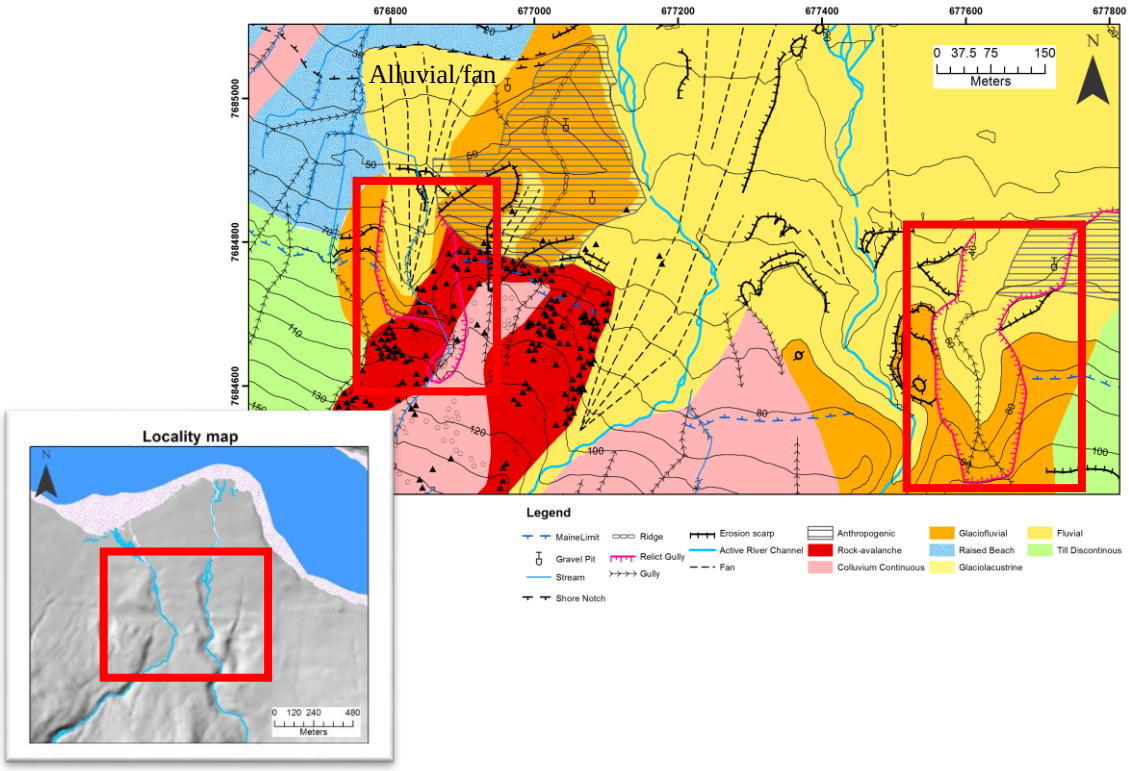

Figure 63: A section of the Quaternary Geological map of the study area. The relict gullies (pink dashed lines) are shown within the red boxes.

Erosion has removed a lot of sediment from the gullies and this sediment has been transported and redistributed within the postglacial fjord-side fan delta. On the western side of the fan delta the eroded sediment has been redeposited below the relict gully as an alluvial fan (Figure 63 and Figure 64). The apex of this fan occurs within the relict gully and the fan widens towards the sea with a maximum width of 217 m at its base. Figure 64C shows the alluvial fan has an overall concave cross-profile that contains small depressions, which are interpreted as channels created by fluvial processes. The sediment within the alluvial fan is composed of medium to coarse gravelly sand with occasional sub-rounded cobbles.

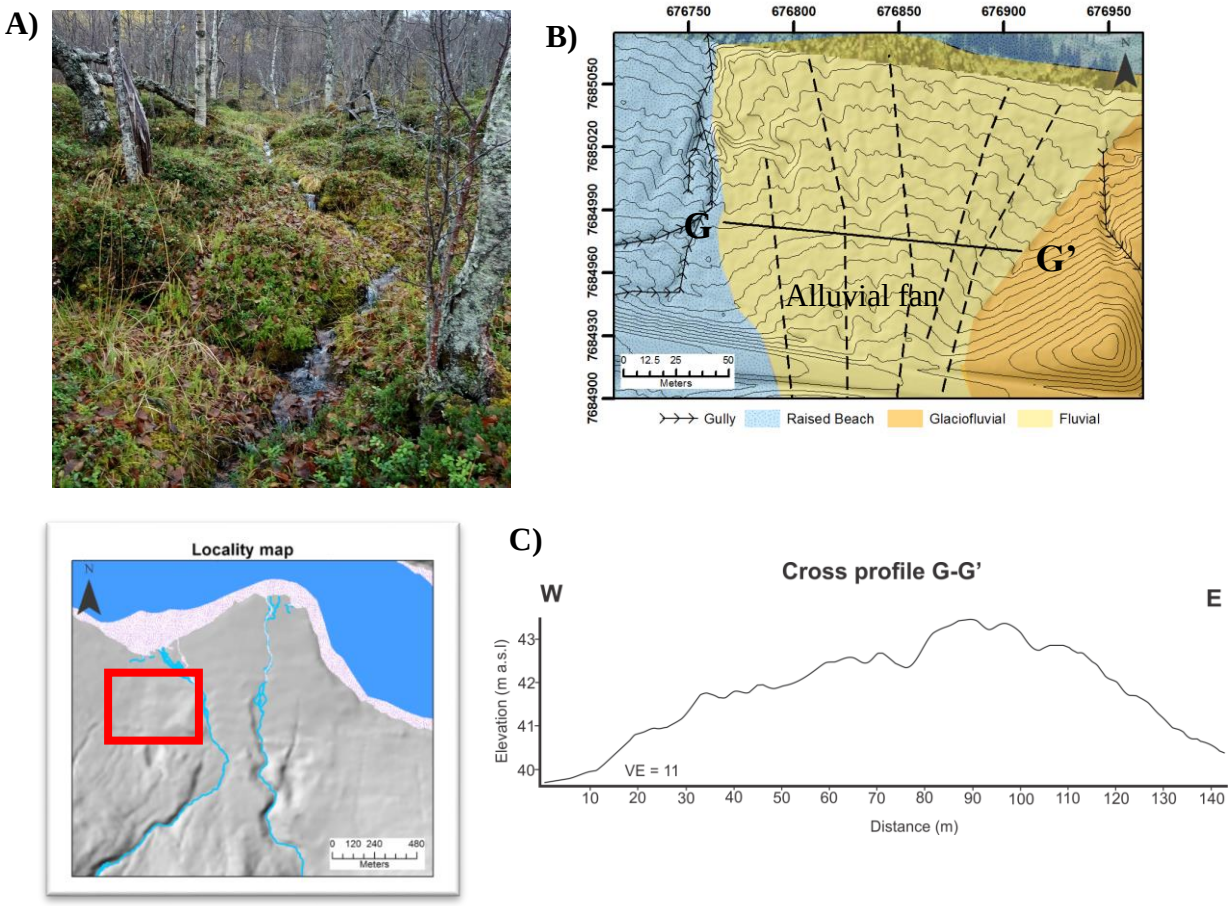

Figure 64: A) Photograph of the small stream that is currently flowing through the western gully. B) Detailed map of the alluvial fan created using a lidar-derived shaded relief map overlayed with the Quaternary Geological Map produced during this study. The Lidar-derived DTM available from Statens Kartverk (https://hoydedata.no/LaserInnsyn/) Contours = 1 m. C) Cross-profile G-G' showing the elevation changes across the fan. The location of the profile is shown in B

4.2.7.1 Interpretation

Both relict gullies are interpreted to be produced by headward erosion, which is the process of fluvial erosion at the top of the gully that causes the head of the gully to erode and move backward. Gullies formed by headward erosion are common features of alluvial fans and they often form in the inactive areas of the fan (Blair and McPherson, 2009). The headward erosion could either be created by streams or groundwater located close to the surface. It is hypothesised that headward erosion is not possible within course-grained sediments (e.g. gravel). Therefore, the sediment that has been removed from the gullies must be easily transportable and predominately composed of fine-grained sediment, such as sand. The rock-avalanche boulders located at the top of the western relict gully are too large to be transported by headward erosional processes and the presence of these boulders could prohibit further headward erosion of the gully.

4.2.8 Raised Beach

A relatively thin cover of well-sorted gravel and sand occurs along the edges of the fjord (Figure 35). This sediment can also contain geomorphological features, such as beach ridges and it is interpreted as raised beach sediment. Surficial raised beach sediment has been primarily mapped outside the extent of the fan delta. However, some raised beach features are preserved in the inactive parts of the alluvial fan. Additionally, there is a small vertical section of raised beach sediment exposed above the present-day beach at the top of the fan delta (Figure 65). This sediment consists of a clast-supported conglomerate with a mode of 3 cm and the maximum clast size is 40 cm. The clasts are sub-rounded to rounded and have no preferred orientation. This raised beach sediment is capped by a thin fluvial unit.

Figure 65: Photograph of a 40 cm tall vertical sedimentary section containing raised beach sediment located just above the present day beach.

4.2.8.1 Interpretation

Sediment within the intertidal zone of the fjord can be reworked by wave and tidal processes to produce well sorted beach sediment with sub-rounded to rounded clasts and the present-day beach sediment within the fan delta is described in Section 4.3.2.1.1. Norway has been uplifted due glacio-isostatic uplift for most of the deglacial and postglacial periods (Section 1.2.3.2: Sea level change). Therefore, beach sediment has been simultaneously uplifted to form raised beach deposits and a relatively thin cover of beach sediment occurs along the edges of the fjord (Figure 35). Raised beach sediment has been primarily mapped outside the extent of the fan delta because most of the beach sediment deposited within the fan delta has been reworked or eroded by fluvial sediment from the aggrading alluvial fan.

4.3 Postglacial Fjord-Side Fan Delta

The Russenes fjord-side fan delta has been prograding into Balsfjord throughout the postglacial period. The present-day morphology of the fan delta has been investigated in this study and the subaerial component has been included within the Quaternary Geological Map of the study area (Figure 35). A description of the surficial morphology of the postglacial fjord-side fan delta and the subsurface structure of the deltaic sediment is presented and discussed below.

4.3.1 Subaerial Morphology

The Russenes fan delta is a radial, fan-shaped accumulation of sand- and gravel-dominated sediment that protrudes 500 m into the fjord and has a maximum width of 1.5 km. The extent of the postglacial fjord-side fan delta is shown in Figure 66. This map shows that there are two different apex points because the fan delta is fed by two separate perennial river systems (Figure 66). The extent of the fjord-side fan delta is restricted on the western side due to the rock-avalanche and ice-front accumulation complex.

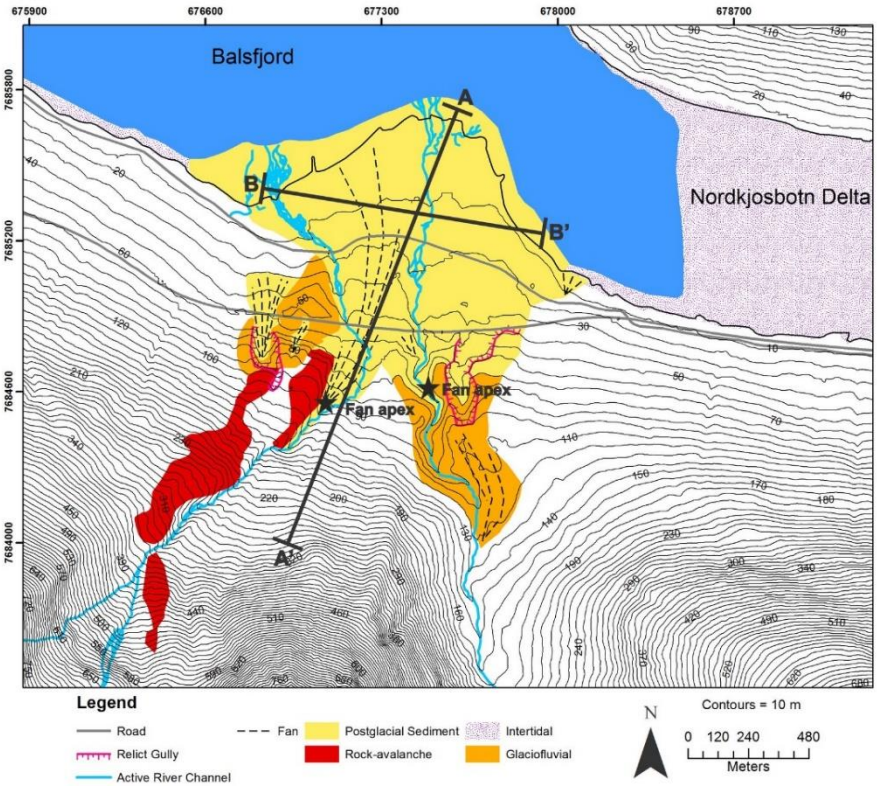

Figure 66: Map of the extent of the postglacial fjord-side fan delta (yellow). The stars show the location of the fan apexes. The rock-avalanche complex and glaciofluvial sediment located above the fan delta are also shown in the map. The lines A-A' and B-B' show the location of the profiles in Figure 67. The background information on map has been produced from digital data available at www.kartverket.no.

The subaerial component of the postglacial fjord-side fan delta has a very steep gradient (3° to 10°) and consists of an alluvial fan that is prograding directly into the sea. Figure 67A shows a longitudinal profile of the postglacial fan delta from the western fan apex (100 m a.s.l) to the sea. This concave profile shows the maximum gradient of the subaerial alluvial fan is 10° and the fan gradient decreases to 3° towards the sea. The fan delta has an asymmetric cross profile (Figure 67B) because

there is a 10 m high scarp on the eastern side of the fan delta and the western side slopes gently into the sea. This indicates that the eastern side of the delta has been eroded by waves and tides, whilst the western and northern sides experience net sediment deposition.

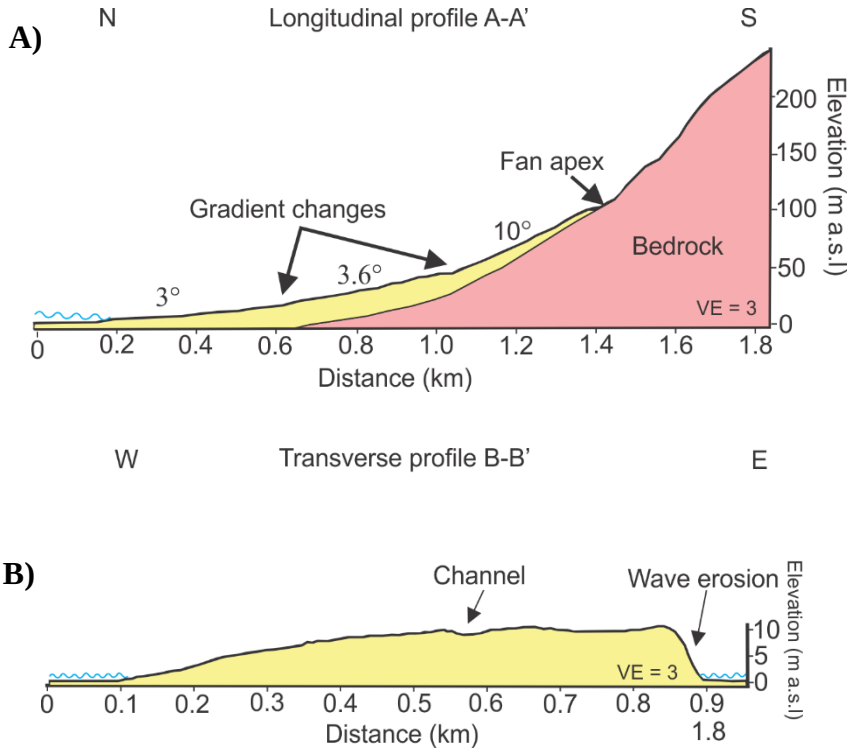

Figure 67: Elevation profiles of the fan delta created using the 10 m DTM available for the study area (www.data.kartverket.no). A) Longitudinal profile of the fan delta showing the alluvial fan steepens towards the fan apex. B) A transverse profile across the fan delta showing the delta has an asymmetric cross-profile with a wave cut escarpment on the eastern side. The location of both profiles is shown in Figure 66. VE = vertical exaggeration.

The postglacial fjord-side fan delta is dominated by fluvial sediment deposited by the two perennial river systems. There is an overall decrease in grainsize from the fan apex towards the sea created by a decreasing slope gradient, which reduces the competency of the rivers (Figure 68 and Figure 74). The morphology and sedimentology of the present-day rivers and fluvial sediment is described below.

4.3.1.1 Rivers

A slope map of the catchment area is presented in Figure 68 and all the sediment deposited within the fan delta is locally derived from this catchment area. This map shows steep gradients (>40°) occur immediately above the fan delta, which causes the delta to be affected by mass movement processes. However, two perennial river systems within the catchment area, called the Buktelva and Russedalselva rivers, are the main conduits for sediment transport within the fan delta.

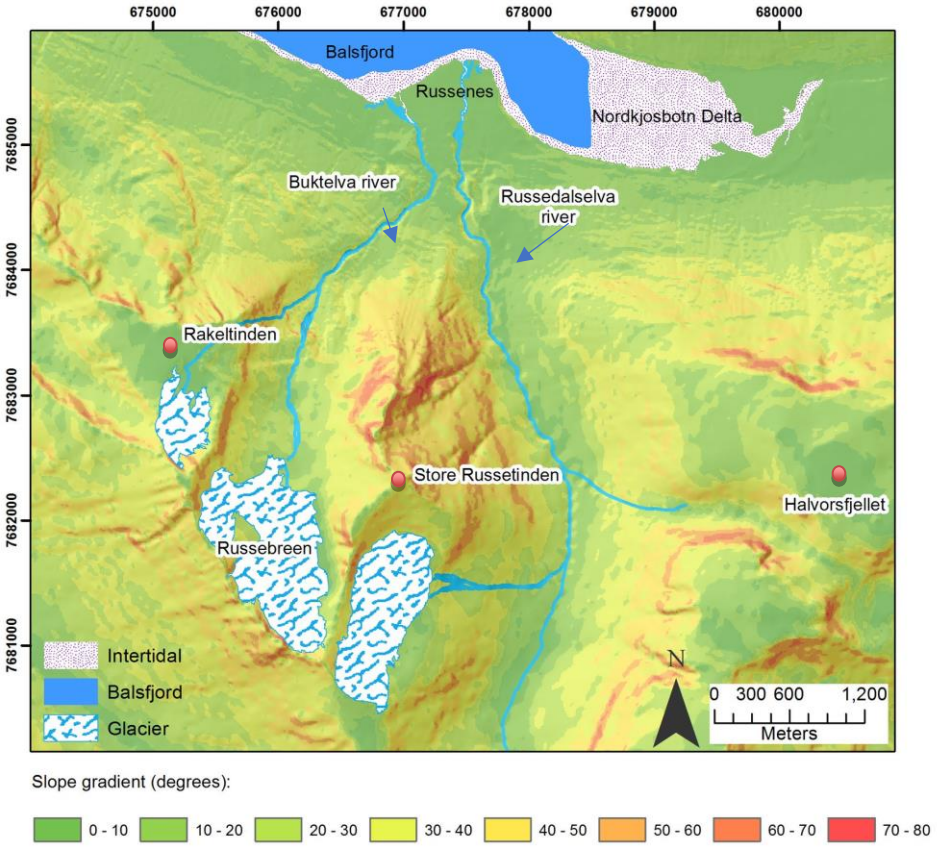

Figure 68: Slope map created from the 10 m DTM available for the study area overlayed on a shaded-relief map created from the same DTM (azimuth = 315° and elevation = 45°). This map shows that some of the slopes directly above fan delta have a gradient that is greater than 40°. The DTM is available at [www.data.kartverket.no.](http://www.data.kartverket.no)

4.3.1.1.1 Buktelva river

The Buktelva river is currently the largest river supplying the fan delta and it is most active conduit for sediment transport. The Buktelva river is steep (Figure 69) and the catchment area is small (5.3 km^2). Two small cirque glaciers are located at the top of the catchment, between 1000 and 1200 m a.s.l, (Figure 68) and these glaciers are the main river source. The river has its highest discharge during the spring and summer melt seasons (Figure 3C).

The upper part of the Buktelva river is downcutting through till and colluvium as the river equilibrates with falling sea level. Below the apex of the alluvial fan the river profile is smooth and has a convex shape (Figure 69). Most of the lower section of the Buktelva river is downcutting through existing fluvial deltaic sediment (Figure 70A) and downcutting terminates just 80 m from the river mouth. This creates steep scarps (0.5 to 4 m) along the edges of the present-day river, which exposes vertical sections of sediment. The lower section of the Buktelva river has a medium sinuosity (1.25) with an irregular width variation. Most of the sediment transport occurs by bedload processes when the river floods. Flooding occurs due to snow melt in spring and summer and during infrequent large storms in (Figure 71). Figure 72 shows a section of the Buktelva river in flood in August 2004. This flooding was a localised event that occurred due to unusual torrential rain created by a thunderstorm (Geoffery Corner, pers. comm.). When the river velocity decreases at the end of a flood, sediment within the river is deposited and a lot of fluvial sediment accumulates as midchannel bars and side bars along the river (Figure 70).

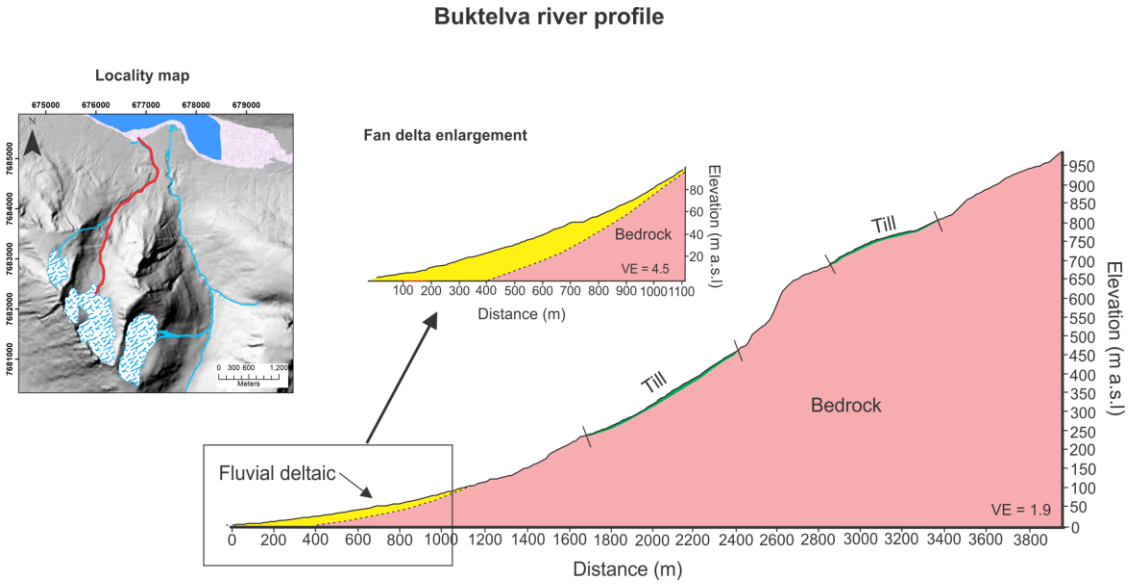

Figure 69: Elevation profile of the Buktelva river. The location of the profile is shown by the red line on the locality map. The profile starts at the sea and terminates at the Russebreen cirque glacier. An enlargement of the river profile through the fan delta is also shown. VE = vertical exaggeration. Profile has been created from the national scale DTM that is available at [www.data.kartverket.no.](http://www.data.kartverket.no)

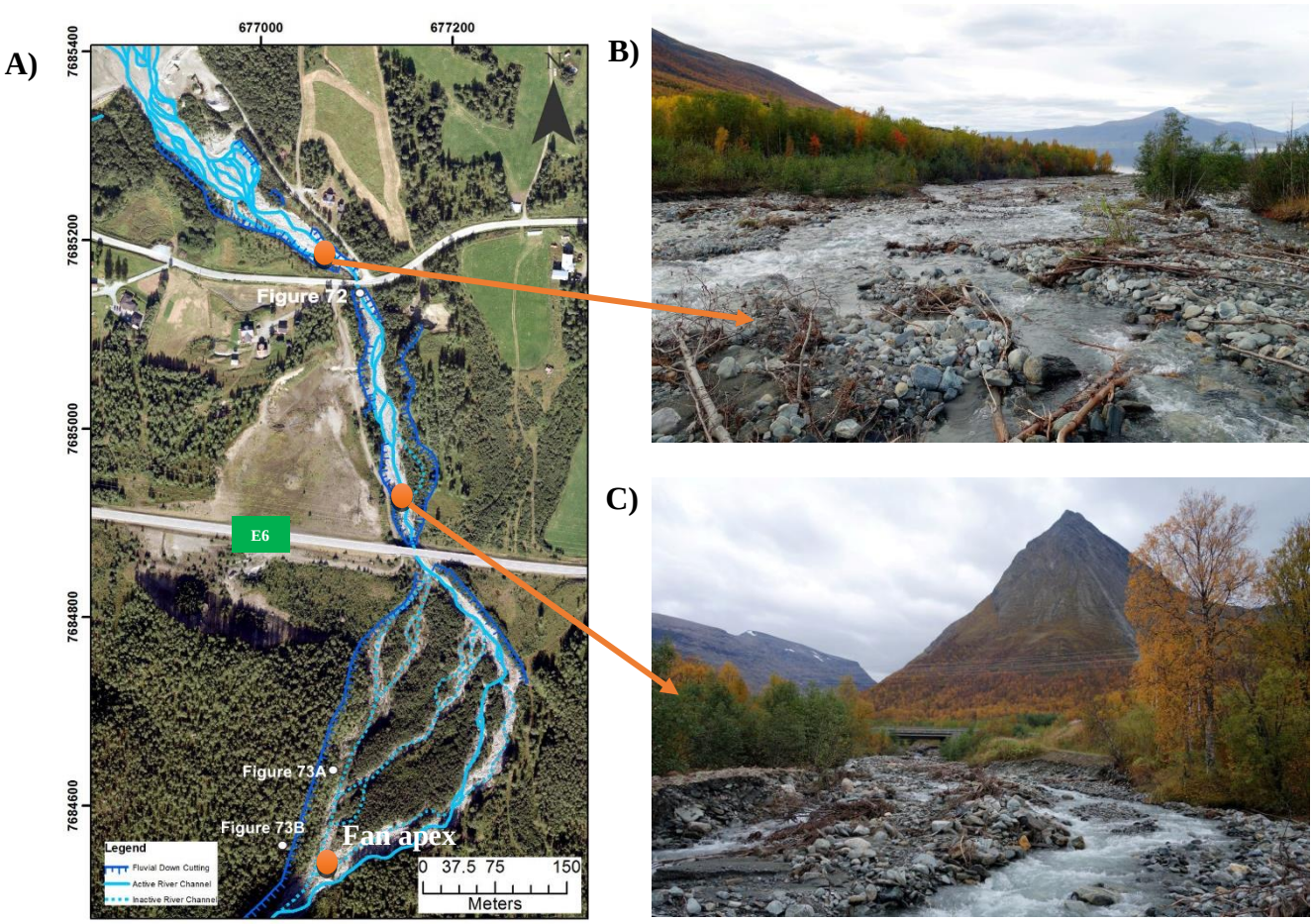

Figure 70: A) Orthophotograph (Midt_troms_2013) of the lower section of the Buktelva river located within the fan delta. The active and inactive river channels and areas of fluvial downcutting are shown. B) Photograph looking north of the lowest section of the Buktelva river before it enters the sea. C) Photograph looking south of the Buktelva river below the E6 highway. Both photographs were taken on 18 September 2016.

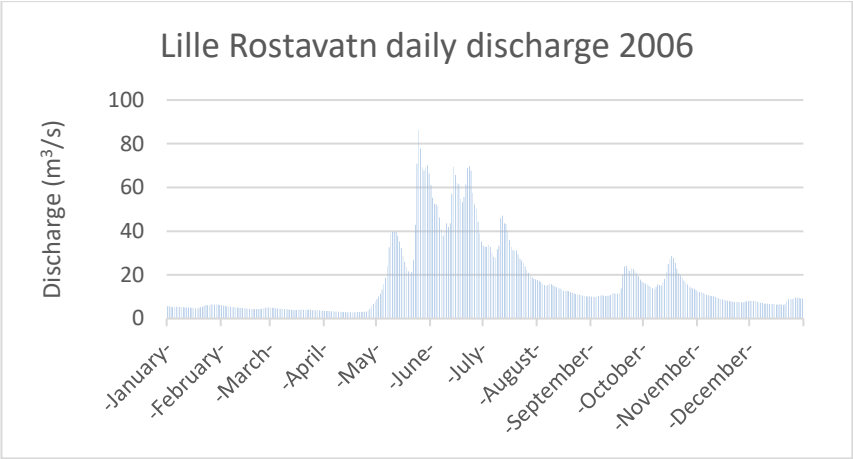

Figure 71: Graph showing the daily river discharge of the Lille Rostavatn river in 2006. The Lille Rostavatn river is located 25 km SSE of Russenes and small cirque glaciers occur within the catchment area. Therefore, the yearly variations in discharge shown in this graph should be similar to the rivers within the Russenes fan delta. However, the daily discharge values are probably much larger than that of Russenes because the catchment area of Lille Rostavatn (638 380 km^2) is much larger than that of Russenes (20.5 km^2). Data provided by the Norwegian Water Resources and Energy Directorate (NVE).

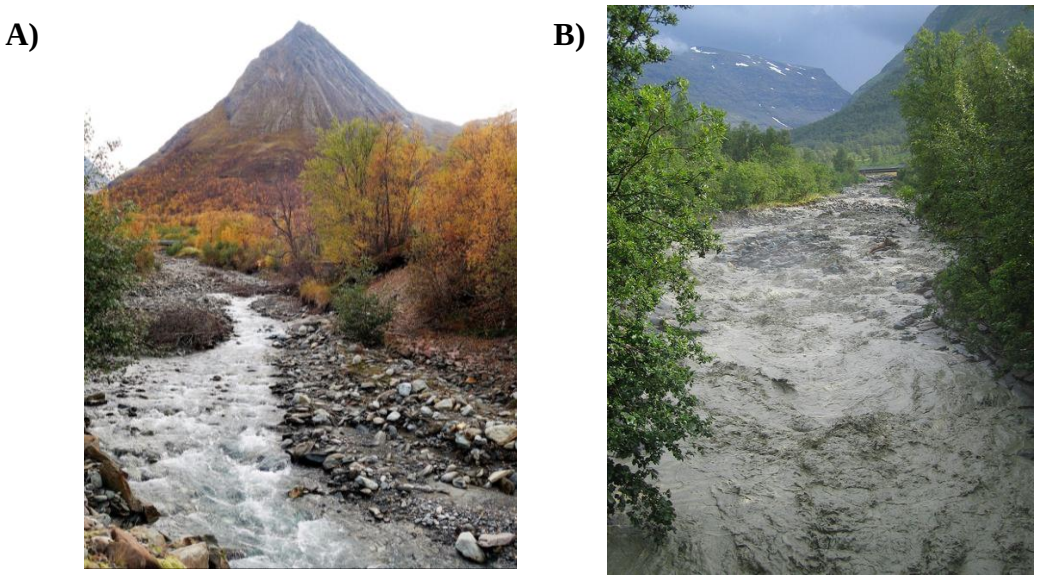

Figure 72: A) Photograph of the Buktelva river with low water flow on 18 September 2016. B) Photograph of the same section of the Buktelva river in flood on 6 August 2004. Photograph by Geoffery Corner. The location of the photographs is shown in Figure 70.

Sediment is temporarily stored within bars during periods of low water level, which gives the Buktelva river a braided character. The degree of braiding is approximately 50%, however, the amount of braiding increases to 65% for the final 300 m of the river and likewise, the width of this final section of the river also increases from 20 m to 165 m. Two different facies occur within the Buktelva river: (1) gravelly sand; and (2) sub-rounded cobbles and boulders. The cobbles and boulders are primarily equant and imbrication was sometimes observed. The overall sediment gainsize increases towards the fan apex and Figure 73 shows the cobbles and boulders are common immediately below the fan apex because the competency of the river flow is reduced by a decrease in slope gradient at this location (Figure 69).

A)

B)

Figure 73: A and B) Photographs of the Buktelva river fan just below the fan apex. These photographs were taken on 13 July 2016 and show the Buktelva river at 80 m a.s.l. The location of the photographs is shown in Figure 70.

4.3.1.1.2 Russedalselva river

The catchment area of the Russedalselva river is much larger than that of the Buktelva river (15.2 km^2; Figure 68). A 4 km long valley, called the Russedalselva valley, feeds the river. However, most the river water does not originate at the head of the valley and instead, it is sourced from the valley sides. For example, melt from a small cirque glacier located behind Store Russetinden is currently the main source of the Russedalselva river (Figure 68). Figure 74 shows the convex river profile of the Russedalselva river from the sea to the cirque glacier located behind Store Russetinden. Interestingly, an 800 m long section of the river located above the apex of the fan delta is aggrading, and therefore, the sediment being deposited within the present-day fan delta is primarily sourced from below this aggrading section. Above the fan apex the river is steeply downcutting through existing sediment and bedrock (Figure 75A) and the sediment eroded by this section of the river will be deposited within the fan delta system.

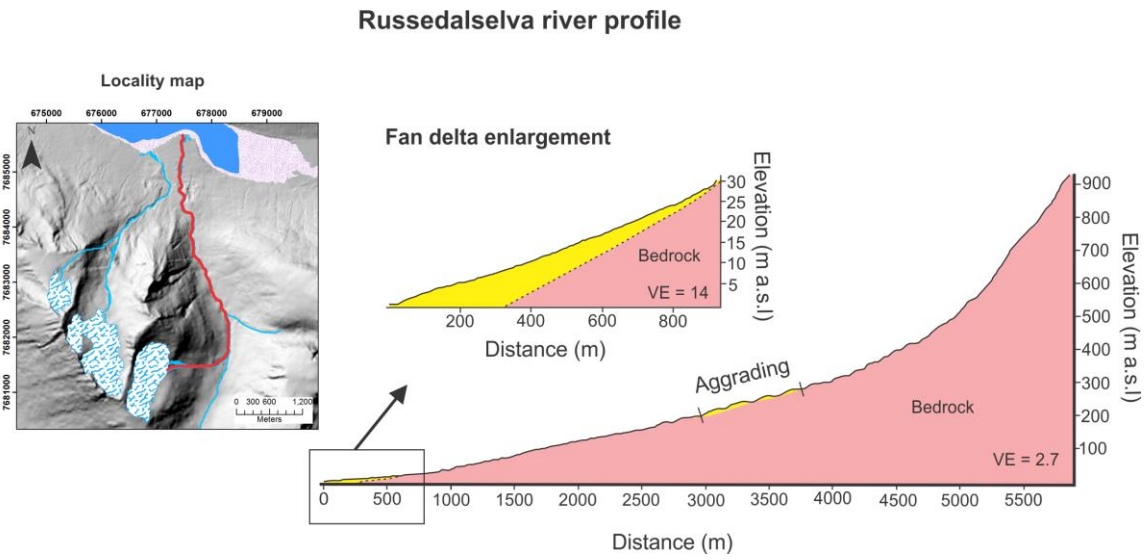

Figure 74: Elevation profile of the Russedalselva river. The location of the profile is shown by the red line in the locality map. The profile starts at the sea and terminates at the small cirque glacier located behind Store Russetinden. This glacier is the main source of the present-day river. An enlargement of the river profile through the fan delta is also shown. VE = vertical exaggeration. Profile has been created from the national scale DTM that is available at www.data.kartverket.no

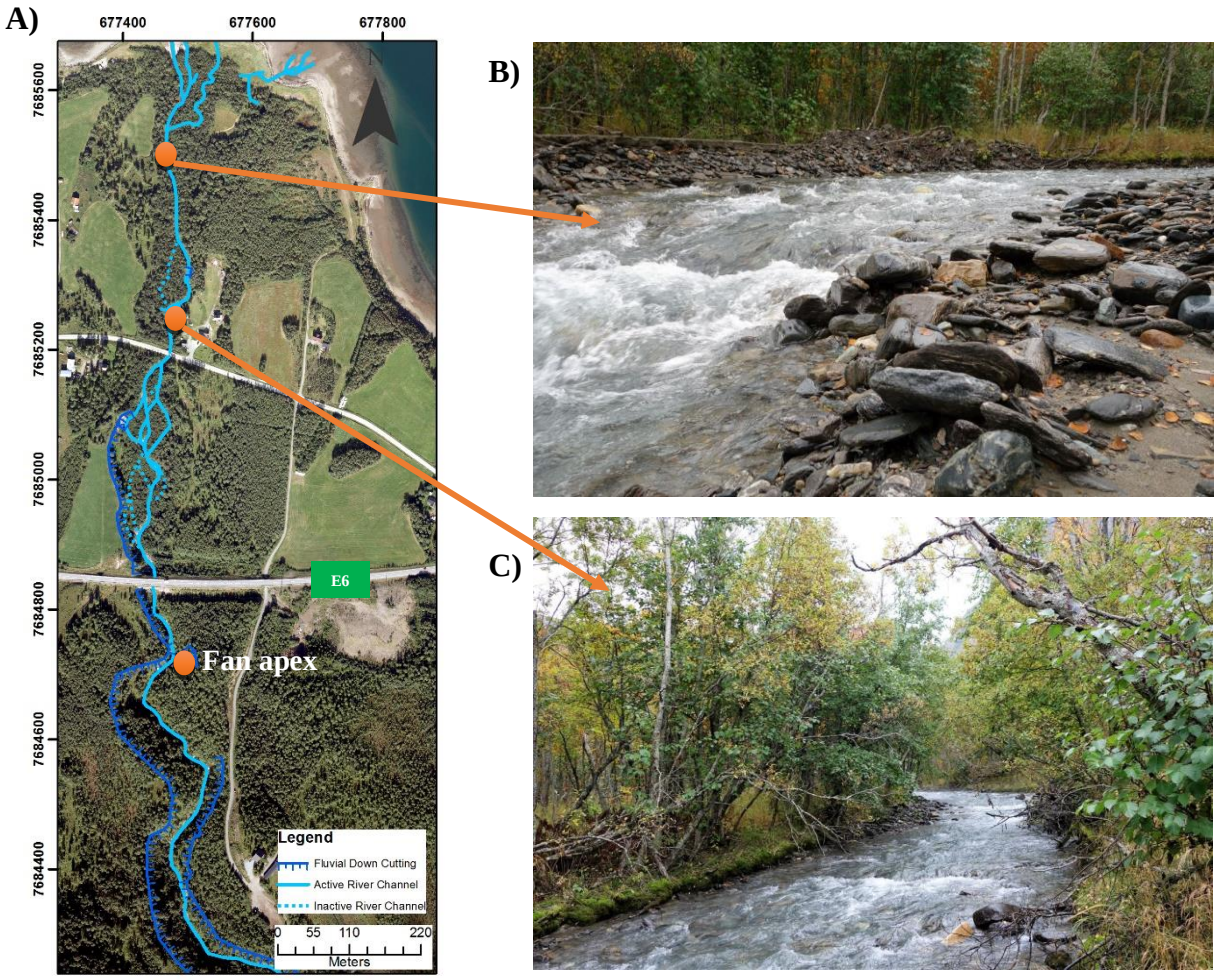

Figure 75: A) Orthophotograph (Midt_troms_2013) of the lower section of the Russedalselva river. The active and inactive river channels and areas of fluvial downcutting are shown. B and C) photographs taken at different locations along the Russedalselva river. The photographs were taken on 19 September 2016.

The character of the lower section of the Russedalselva river has similarities and differences with that of the Buktelva river. Figure 75 shows immediately after the fan apex the river is downcutting, which creates a very high erosional scarp. Below the fan apex the river channel has a medium sinuosity (1.07) and one main active channel. Sediment transport processes are similar to that of the Buktelva river with transport occurring through bedload processes during flooding. Thick vegetation occurs along the banks of the river, which indicates that the Russedalselva is more stable than the Buktelva river. Sidebars commonly occur whilst midchannel bars are rare (Figure 75) and the degree of braiding is 30%. The width of the river varies from 10 m to 40 m. The bars contain two different facies composed of: (1) well sorted medium sand; and (2) sub-rounded cobbles. The cobbles are often oblate and preferably orientated and dip in the upstream direction (Figure 75B). The grainsize mode increases towards the fan apex. Bifurcation of the Russedalselva river occurs in the final 300 m whereby the river splits into numerous channels.

4.3.1.2 Raised fluvial sediment

The surficial fluvial sediment located above the present-day rivers gently dips towards the south and has a mound and furrow morphology (Figure 76). The mounds are primarily orientated in a north-south direction and approximately 6 m long and 1.5 m wide. A detailed Lidar-derived DTM is available over the E6 Highway and this data provides detailed information about the morphology of the fluvial sediment (Figure 77).

A)

B)

Figure 76: A and B) Photographs showing the surface morphology of some of the fluvial sediment within the study area. The surface of the fluvial sediment often contains elongate ridges or a mound and furrow morphology. Photo A was taken on 16 September 2016 and photo B was taken on 14 July 2016 (location shown in Figure 77).

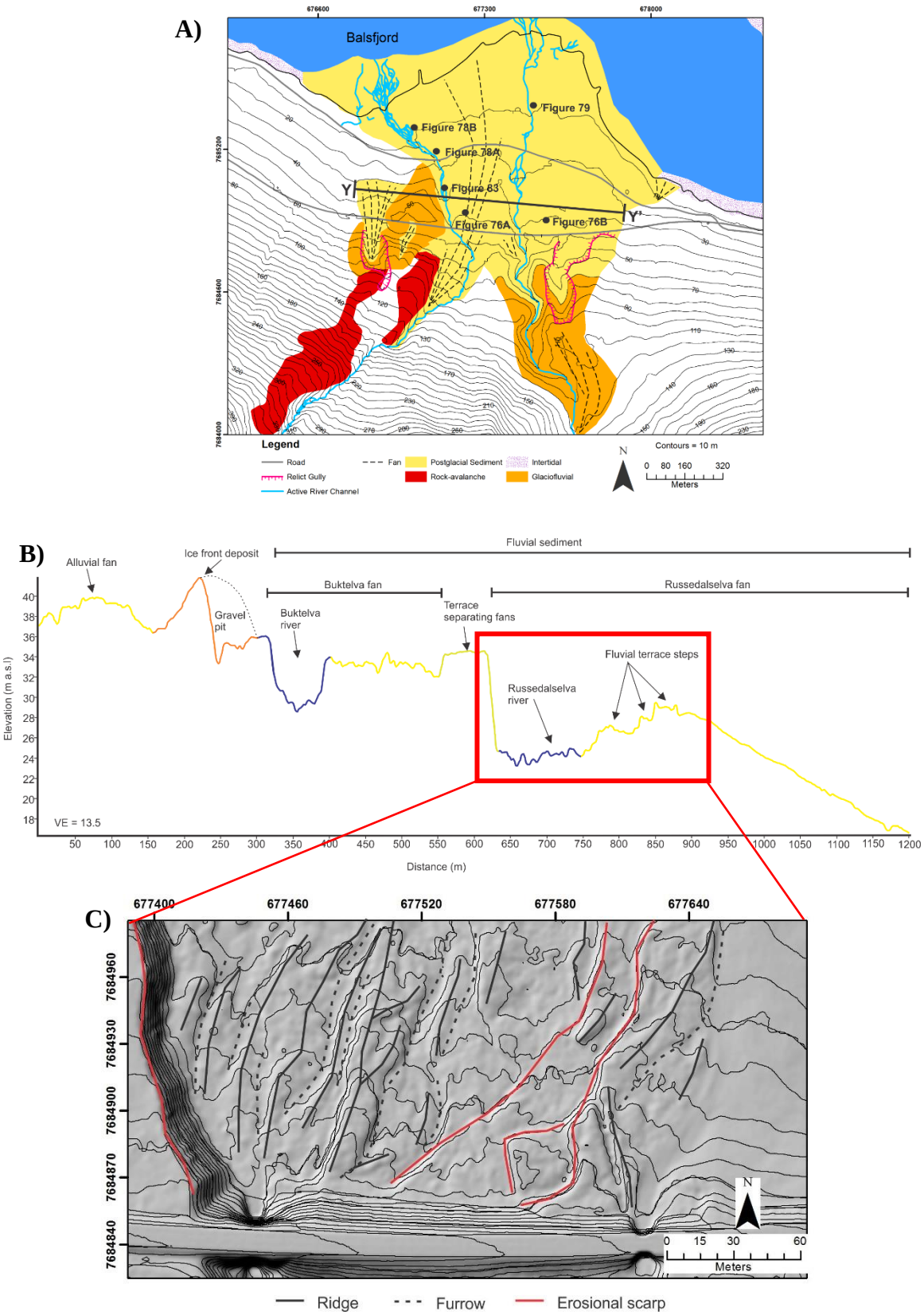

Figure 77: A) Locality map. B) Vertical cross-section of the fan delta (Y-Y') produced from the lidar-derived DTM data with a 0.5 m resolution. This cross-section shows the changes in elevation across the alluvial fan, which correspond to distinct morphological features. C) Lidar-derived shaded-relief map (0.5 m resolution) showing that fluvial sediment next to the Russedalselva river is characterised by elongate ridges and furrows. Erosional scarps also occur where the river has cut down through the fluvial sediment. The lidar data is available from Statens Kartverk (https://hoydedata.no/LaserInnsyn/).

Downcutting along the Buktelva river has exposed thick (1 – 2.5 m high) sections of fluvial sediment along the edges of the river (Figure 78). Figure 78C shows a graphical log of one of the vertical sediment exposures. Two different units have been identified within the log. Unit 1 is 40 cm thick and it is dominated by sand. This unit has discontinuous horizontal laminations and lenses of coarse sand and silt. Imbricated gravel clasts occur at the base of the unit.The boundary between Unit 1 and 2 is erosional. Unit 2 mainly consists of cobbly sandy gravel. The clasts are sub-rounded to rounded and some of the clasts have an oblate shape. Many of the cobble sized clasts are imbricated and dip in the upstream direction. The grainsize mode is 1 cm and maximum clasts size is 6 cm. Both of the units logged are interpreted as fluvial sediment. Unit 1 is interpreted to be deposited as part of the finer grained component of the fluvial system, whist Unit 2 represents the dominate sediment-type deposited by the Buktelva river.

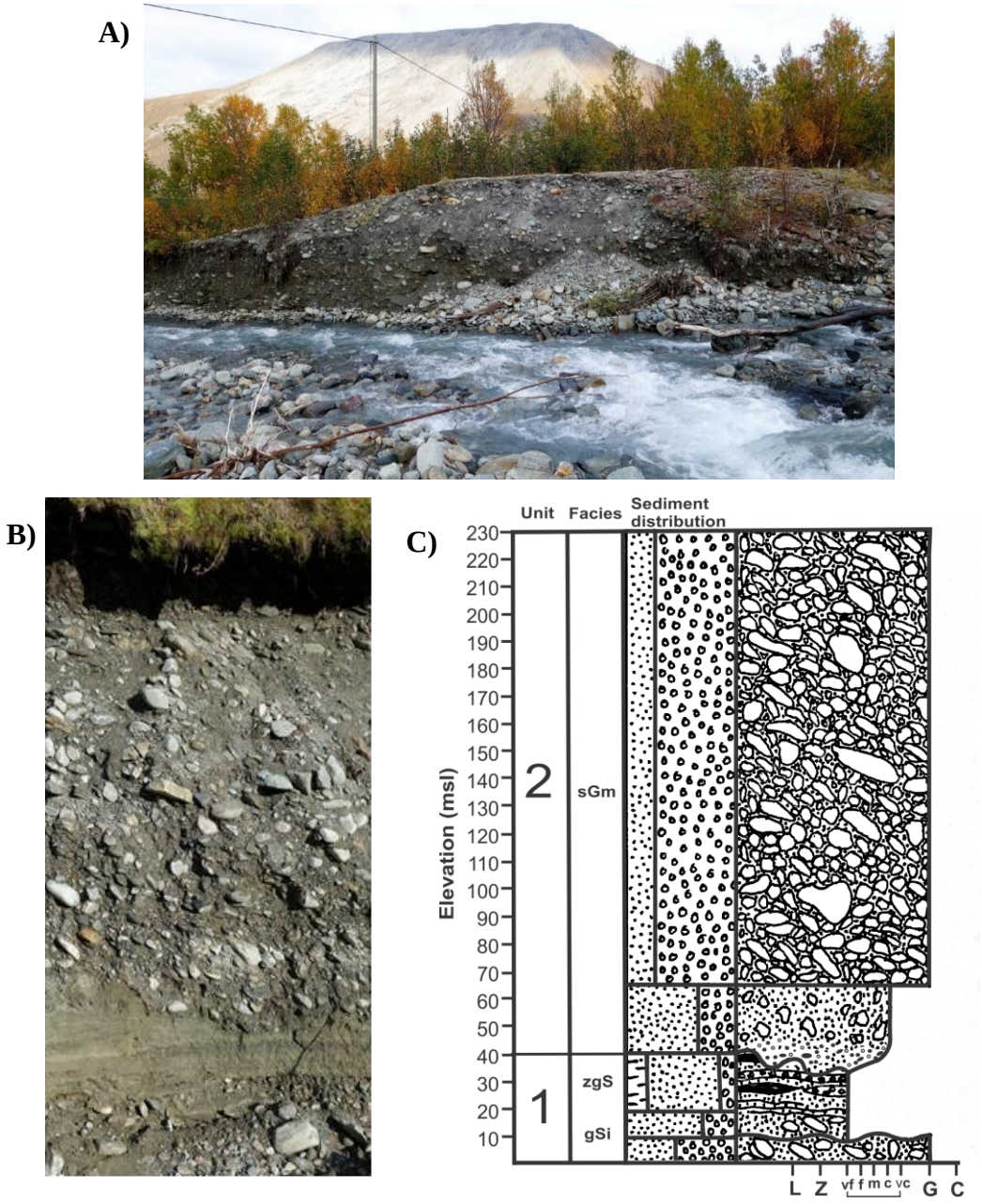

Figure 78: A) Photograph of a thick accumulation of fluvial sediment that has been exposed along the Buktelva river. B and C) Photograph and graphical log of fluvial sediment exposed by the downcutting Buketlva river. Two different depositional units have been logged. Location shown in Figure 77A. Photographs taken on 18 September 2016.

Fluvial sediment is also exposed in the banks of the Russedalselva river, however, the banks are a lot lower than the banks of the Buktelva river. Figure 79 shows a small vertical sedimentary section located on one of the river banks. This section contains 55 cm of gravelly cobbles that are rounded and have an oblate shape. This cobble unit is capped by 15 cm of well sorted medium sand, which was massive to finely laminated.

Figure 79: Photograph of a 70 cm high river bank located on the Russedalselva river. The bottom section of the river bank is dominated by cobbles and the top 15 cm consits of well sorted medium sand. Photograph taken on 19 September 2016 (location shown in Figure 77).

4.3.1.2.1 Fluvial terraces

Rivers within northern Norway adjust to the gradually falling base sea level by downcutting through existing sediments (Corner, 2006, Eilertsen et al., 2006). River downcutting often creates fluvial terraces as steps down to the present-day river level. Therefore, the highest terrace is usually the oldest. Fluvial terraces are not commonly observed within the Russenes fan delta, however, they have been recorded in a few locations. For example, a series of fluvial terraces occur on the eastern side of the Russedalselva river, immediately below the eastern fan apex (Figure 80) and these terraces record the downcutting history in the upper section of the fan delta. The fluvial terraces identified within the study area often have an uneven surface created by the presence of ridges or mounds.

One prominent, isolated, fluvial terrace occurs below the E6 highway. This terrace is located at 36 m a.s.l in the centre of the alluvial fan and the terrace surface is 205 m long and 125 m wide at its widest point. The terrace narrows and gently dips towards the south. This terrace surface represents the oldest fluvial sediment deposited below the E6 highway and the sediment could have been deposited by either river or a combination of both rivers. The terrace is bound by a 3 m erosional scarp on the western side and a 10 m erosional scarp on the eastern side. This terrace separates the present-day surficial alluvial fans from the Buktelva and Russedalselva rivers.

4.3.1.2.2 Interpretation

The subaerial component of the Russenes fan delta consists of a streamflow-dominated alluvial fan. The alluvial fan has been formed by the aggradation of fluvial sediment as two perennial river channels undergo periods of channel infilling and avulsion. Therefore, both present-day rivers can be used as a modern analogue for the deposition of fluvial sediment located elsewhere in the alluvial fan. The mound and furrow morphology commonly observed on the surface of the alluvial fan is interpreted to be abandoned fluvial midchannel and side bars, which are very common within the present-day rivers (Figure 81). These mounds are composed of cobbly sandy gravel and have been abandoned on the surface of the alluvial fan during the channel infilling and avulsion process. The

well-sorted medium sand observed within the vertical sedimentary sections is interpreted to have been deposited during sheetflooding of the river following intense rainfall events. Fluvial and deltaic terraces are uncommon on the surface of the alluvial fan because they are destroyed by fluvial aggradational and erosional processes.

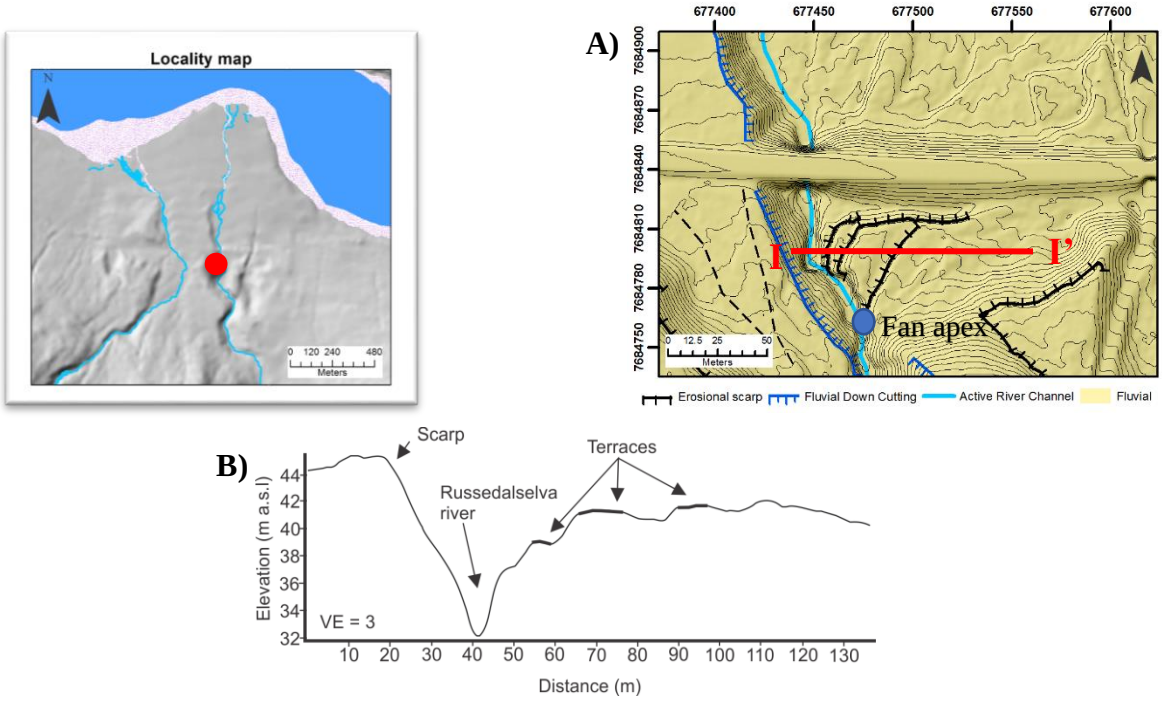

Figure 80: A) Lidar-derived shaded relief map of the fluvial sediment below the eastern fan apex overlaied by the Quaternary Geological map. The lidar data is avalaible from Statens Kartverk (https://hoydedata.no/LaserInnsyn/). B) Elevation profile I-I' showing the fluvial terraces located beneath the eastern fan apex.

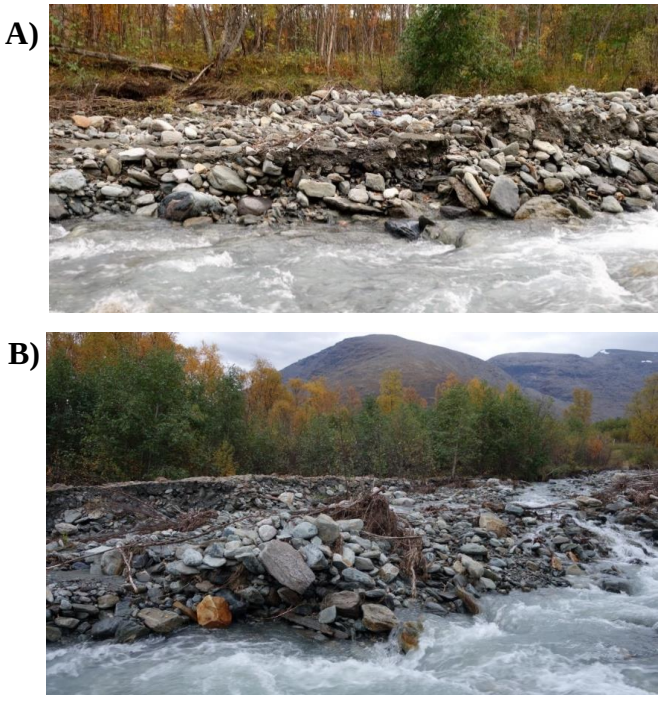

Figure 81: A) and B) Photographs of fluvial bars located in the present-day Buktelva river. These bars primarily consist of sub-rounded cobbles and boulders. The photographs were taken on 18 September 2016 (location shown in Figure 77).

4.3.2 Subaqueous Morphology

The modern delta has three major environments: (1) the intertidal to subtidal delta platform; (2) the subaqueous steeply dipping delta slope; and (3) subaqueous gently dipping prodelta area (Figure 82). The delta rim is a sharp boundary between the delta platform and the delta slope that is located 2 m below mean sea level. The delta platform was studied in the field at low tide, whilst the delta slope and prodelta have been investigated using a multibeam bathymetry dataset (Corner and Eilertsen, 2013). The modern delta is an analogue for the older deltaic sediment within the study area and the morphology can be related to the tripartite structure of Gilbert-type deltas whereby the bottomset sediment is deposited in the prodelta, foreset beds are deposited on the delta slope and topset beds are deposited on the delta platform.

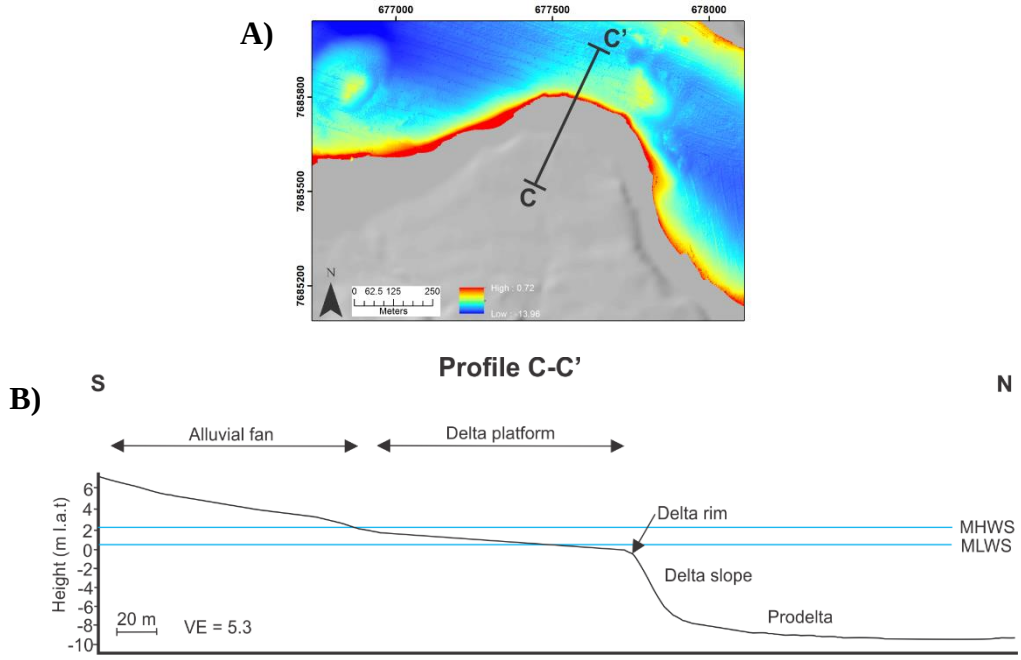

Figure 82: A) Locality map. B) Morphogenic profile of the modern Russenes fjord-side fan delta. The elevation data has been obtained from two sources: the subaerial data is from the national-scale 10 m DTM (www.data.kartverket.no) and the subaqueous data is from the multibeam bathymetry dataset (Corner and Eilertsen, 2013). The data has been corrected to the lowest astronomical tide map datum. The different delta morphogenic features are annotated and the mean high and low water spring tidal levels are shown (MHWS and MLWS).

4.3.2.1 Delta platform

The delta platform is the gently sloping intertidal region of the fan delta located between the mean high water spring (MHWS) tidal level and the delta rim, which occurs just below the mean low water spring (MLWS) tidal level. Therefore, most of the delta platform is exposed at low tide. The delta platform is located where the rivers discharge into the sea and therefore, it occurs at the interface between the terrestrial and marine environments and the morphology of the delta platform records subtle changes in environmental conditions. The delta platform unconformably overlies delta slope sediment.

The Russenes fan delta has an extensive flat lying delta platform that protrudes into the fjord. The delta platform has been included on the Quaternary Geology Map of the study area because the morphology and sedimentology of the delta platform could be studied at low tide (Figure 83). The

plan-view width of the delta platform varies from 90 m on the east side of the delta to 260 m where the Buktelva river discharges into the fjord. The geomorphology of the delta platform is variable and results from the complex interplay between fluvial, wave and tidal processes. Consequently, the delta platform can be divided into two major zones based on morphogenetic criteria: the fluvial-dominated zone and the wave- and tide-dominated zone.

4.3.2.1.1 Wave- and tide-dominated zone

The wave- and tide-dominated zone of the delta platform has a very distinctive beach morphogenic element, which occurs almost continuously along the top of the delta platform (Figure 83). The upper limit of the beach is defined by the highest lying high-tide mark (formed during spring tide) and the lower limit is defined by a decrease in gradient that is usually accompanied by a decrease in sediment grainsize (Figure 84). In some places, the lower boundary can be hard to determine because there is a gradational change at the bottom of the beach. The position of the beach facies can be identified using the aerial photographs and it has been mapped along the top of the entire delta platform except for directly in front of river discharge channels. The beach morphogenic element has distinctive geomorphological features, such as beach ridges and high tide seaweed marks. The morphology of this element provides information about the depositional and erosional regime along the delta platform and variations in the beach morphogenic element are described in detail below.

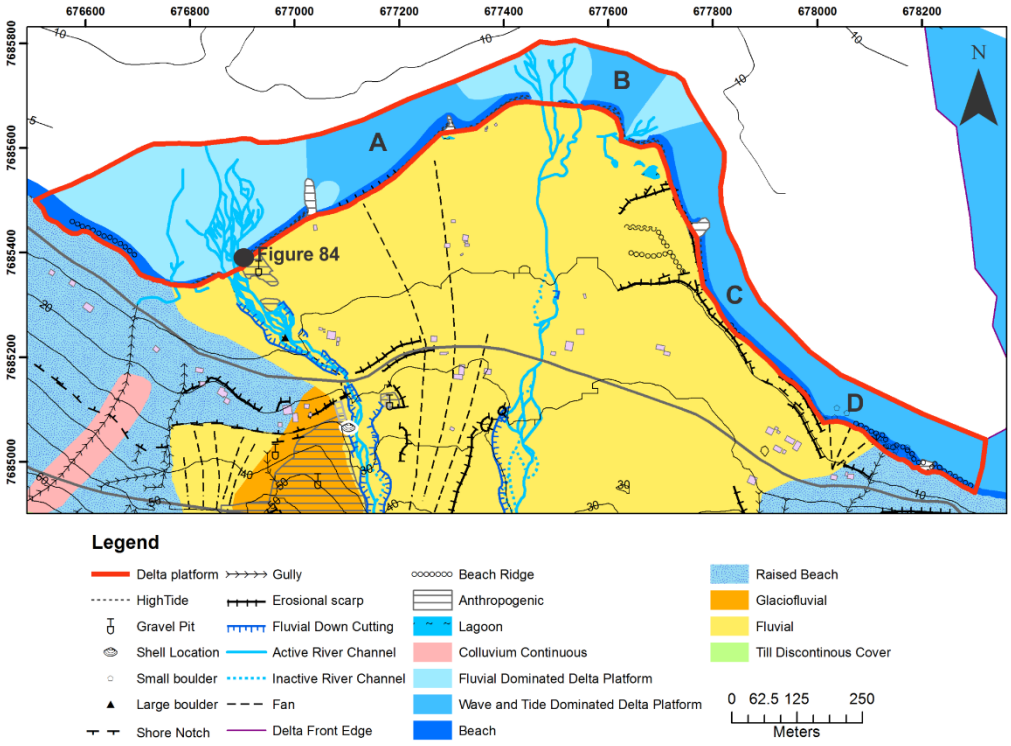

Figure 83: Detailed map of the front-most section of the fan delta. The extent of the delta platform is shown by the red outline. The beach and fluvial dominated delta platform units are distinctive geomorphological elements that occur within the delta platform. Letters A to D correspond the location of the descriptions given below.

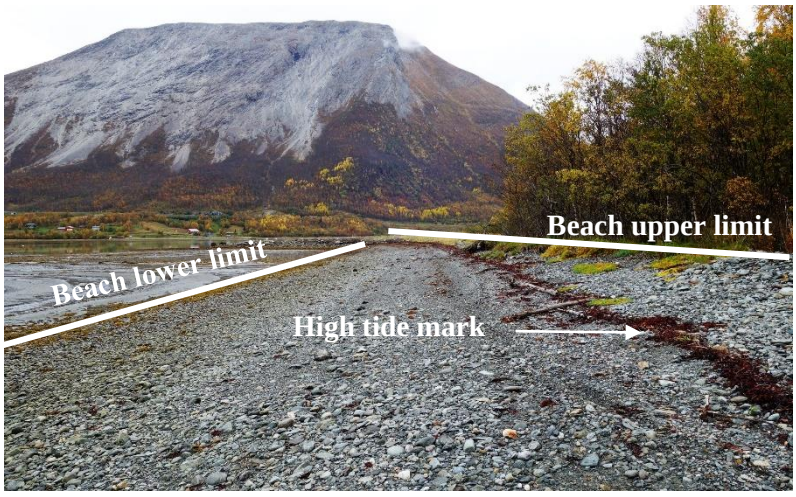

Figure 84: Photograph of a beach exposed at low tide on the western side of the Russenes delta platform. The upper and lower morphogenic boundaries and geomorphic features, such as high tide marks, have been annotated on the photograph.

Beach Area A

Area A has a wide delta platform, which can be attributed to the deposition of sediment from fluvial discharge of the nearby Buktelva river (Figure 85). The beach sediment in Area A is mainly composed of well-sorted sandy gravel with a grainsize mode of 2 cm. There is a distinct change in the gradient between the beach sediment and the flat lying delta platform below (Figure 86), which is also accompanied by a change in grainsize whereby sandy gravel dominates the beach element and the delta platform is predominately composed of well-sorted sand.

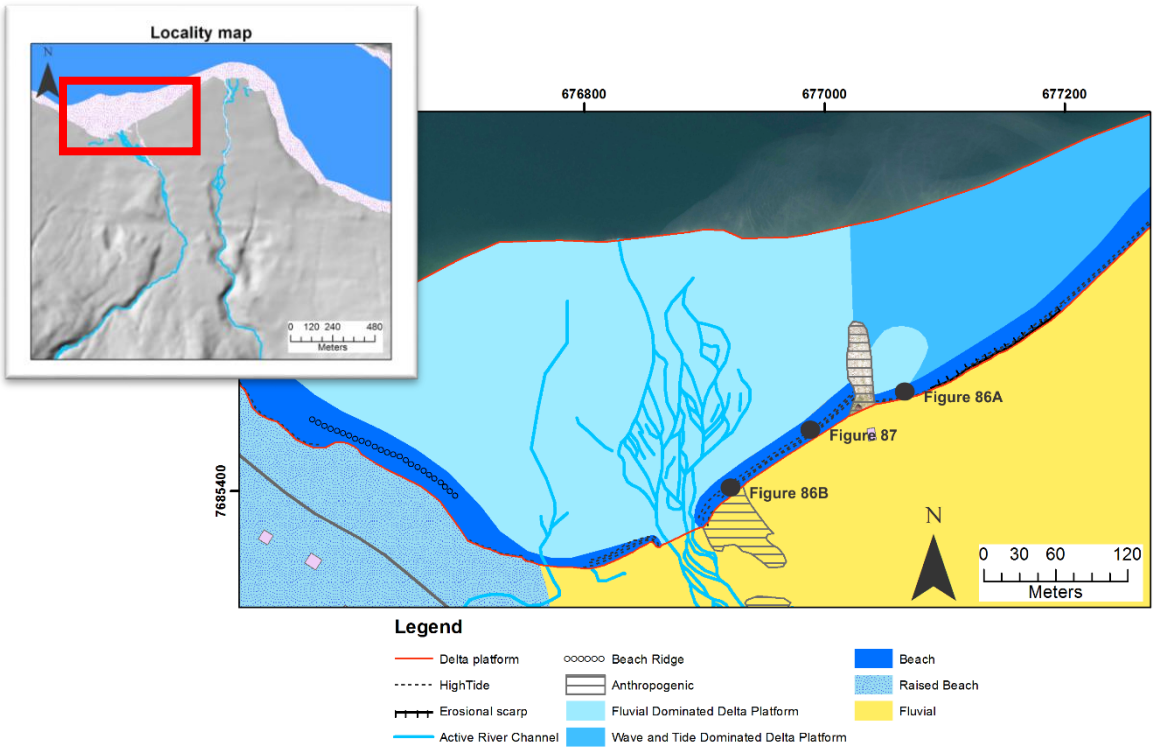

Figure 85: Detailed map of the delta platform surrounding Area A showing that the platform is dominated by fluvial discharge from the Buktelva river, however, a large continuous present-day beach element occurs at the top of the delta platform.

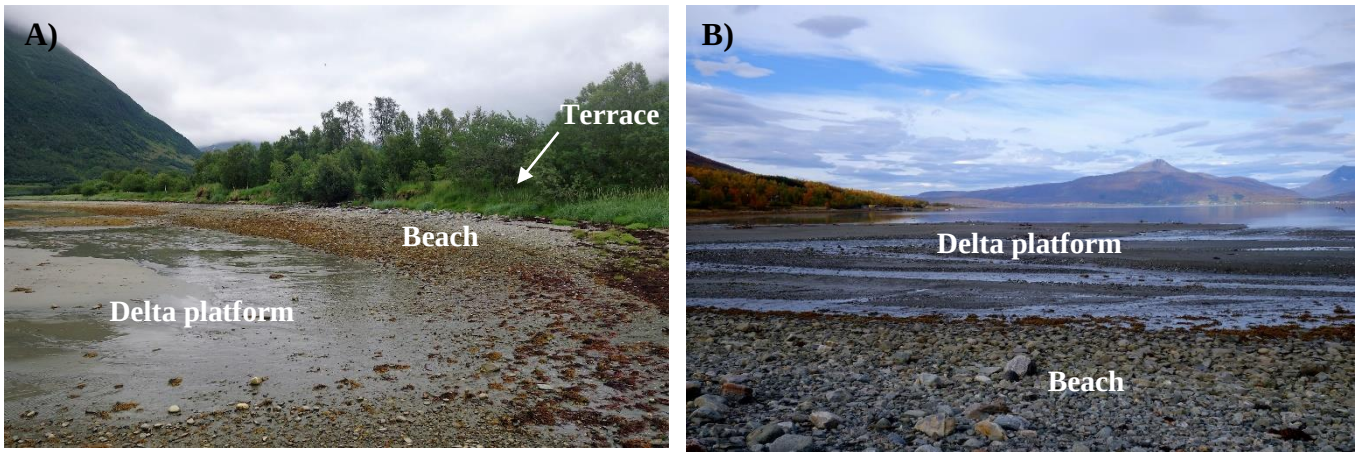

Figure 86: A and B) Photographs of some of the beaches in Area A. Distinct changes in the gradient and sediment grainsize distinguishes the beach sediment from the rest of the delta platform. Photographs taken in July and September 2016.

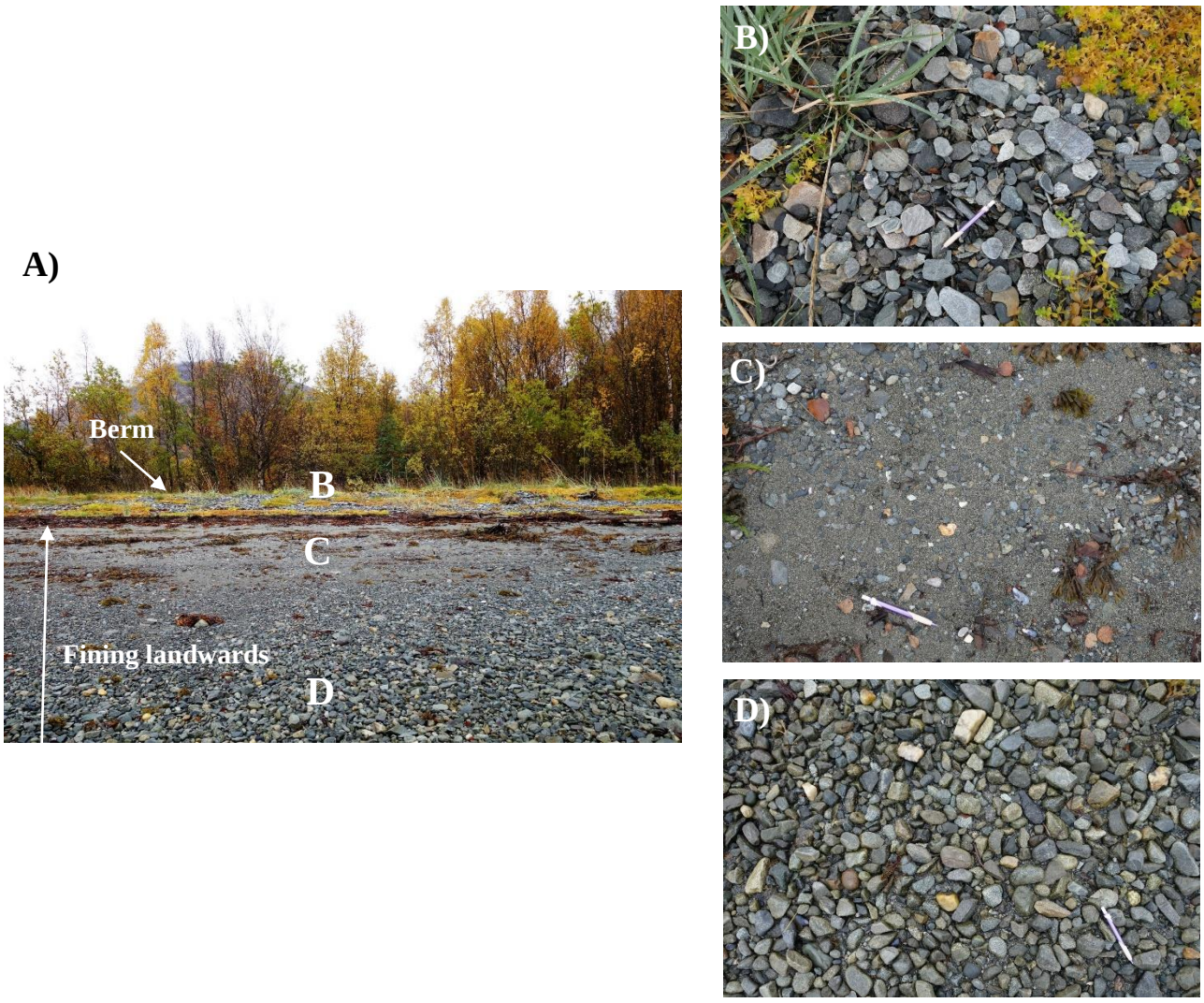

Figure 87: A) Photograph of one of the beaches in Area A. A gravel berm occurs at the top of the beach and below the berm there is a coarsening downwards grainsize trend. B, C and D) Photographs of the sediment located at different places on the beach (position shown in A). Photographs taken on 20 September 2016.

Figure 87 shows the variations in grainsize at one of the beaches in Area A. This beach is unusual because the sediment fines landwards whilst most beaches in the fan delta fine seawards. The sediment at the base of the beach is composed of gravel with a grainsize mode of 3 cm and a maximum grainsize of 6 cm. The clasts are sub-rounded to rounded and well sorted (Figure 87D). The sediment near the top of the beach is a gravelly sand (Figure 87C). The gravel fraction has a grainsize mode of 1 cm and a maximum clast size of 4 cm. The gravel clasts are sub-rounded and often have an oblate shape. A gravel berm occurs at the top of the beach (Figure 87B). The berm consists of an elongate mound composed of well sorted, sub-rounded, oblate clasts with a grainsize mode of 2 cm and maximum grainsize of 7 cm.

Area A has both constructive and destructive beaches. A 1 m high terrace occurs behind the beach on the eastern side of Area A, which indicates that the area has been subjected to erosion (Figure 86A). Large sub-rounded cobbles occur on the beach below the terrace. These cobbles have a mode of 7 cm and a maximum grainsize of 30 cm and are interpreted to be sourced from erosion of the terrace. However, the beach element widens towards the west indicating that the western part of the beach is constructive and it is possible that longshore drift processes occur, transporting sediment in a westerly direction.

Beach Area B

This part of the delta platform is located at the front of the fan (Figure 88). The delta platform becomes wider in this area and the beach element is further characterised by a thicker and wider accumulation of sediment. There are no erosional terraces along Beach Area B and the backshore consists of a large flat lying grassy plain (Figure 89).

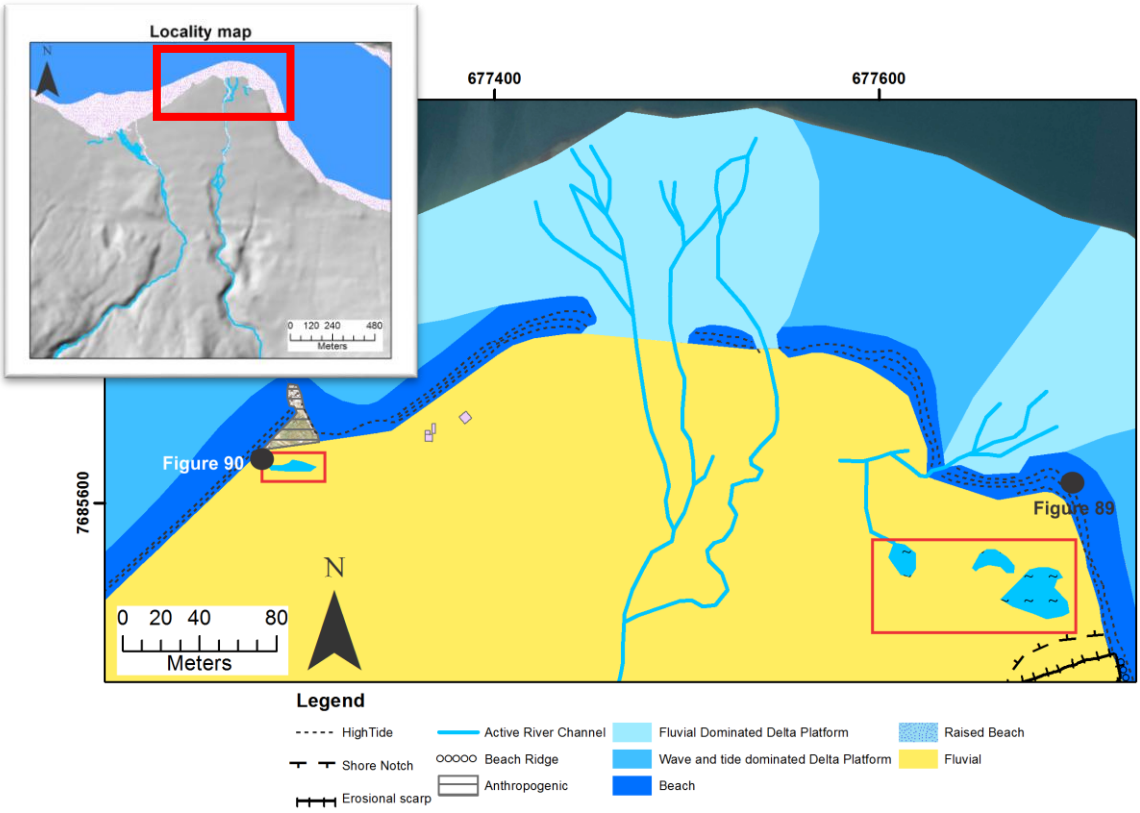

Figure 88: Detailed map of the beach morphogenic element located at the front of the fan delta (Beach Area B). This area has thick accumulations of beach sediment and the beach element is interrupted by fluvial discharge channels. Lagoonal features occur within the red boxes.

A prominent beach face has been built up by the deposition of a large amount of sediment. The beach face is steeper than elsewhere in the delta platform, which indicates that this area currently receives a net accumulation of sediment. The sediment consists of well-sorted sandy gravel with a grainsize mode of 1 cm and a maximum grainsize of 3 cm. No boulders are observed in this area and the sediment becomes finer towards the bottom of the beach. Figure 89 shows seaweed commonly marks different high tide levels. The beach element in Area B is interrupted by channels that occur where fluvial material from the Russedalselva river discharges into the fjord.

Figure 89: A and B) Photographs of beaches located in Area B. Both beaches have a flatly lying grassy backshore, steep beach face and multiple seaweed high tide marks. Location of the photographs is shown in Figure 88.

A few standing bodies of water have been identified in the backshore area behind the present-day beach sediment in Area B (Figure 88). These standing bodies of water are interpreted to be small, enclosed lagoons whereby the water is separated from the sea by the build-up of beach sediment forming a beach ridge. Beach ridges are common in coastal environments and consist of elongate ridges of unconsolidated sand and gravel that are formed by wave and tidal processes (Van Heteren, 2014). Figure 90 shows one of these lagoonal features and a beach ridge is clearly visible at the front of the lagoon, which prevents the regular transfer of water from the lagoon to the sea. This beach ridge is composed of well-sorted, sub-rounded, sandy gravel with a grainsize mode of 2 cm and maximum grainsize of 4 cm. All the clasts have an oblate shape and the sediment forms an elongate ridge.

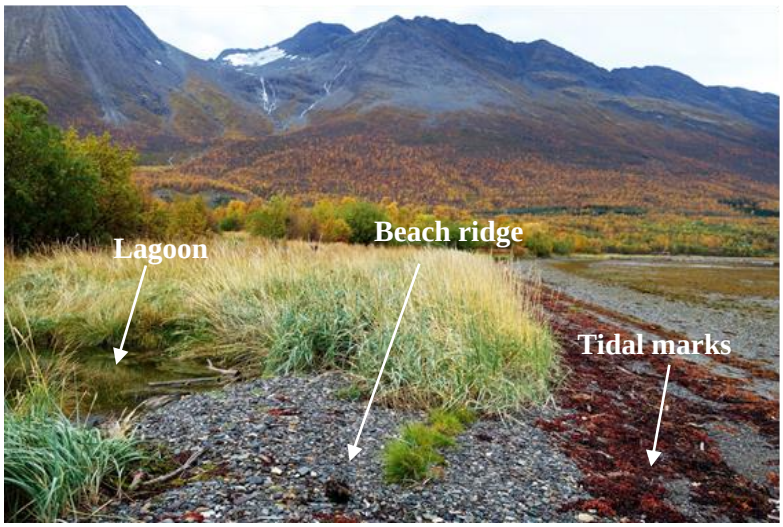

Figure 90: Photograph of one of the lagoons located within the study area (location shown in Figure 88). The water within the lagoon has been blocked by the beach ridge shown in the photograph.

Beach Area C

Beach Area C contains two prominent 6 to 10 m high erosional scarps with very steep gradients (approximately 40°). These scarps are located along the back of the beach (Figure 92). A shore notch has been mapped within one of the erosional scarps. The steep slopes are covered with vegetation, however, some sub-rounded cobbles between 10 to 20 cm long were observed on the slope, which indicates the sediment within the erosional scarp is very coarse. These high terraces gives the fan delta an asymmetric profile (Figure 67) and they are the result of net sediment erosion by wave and tidal processes.

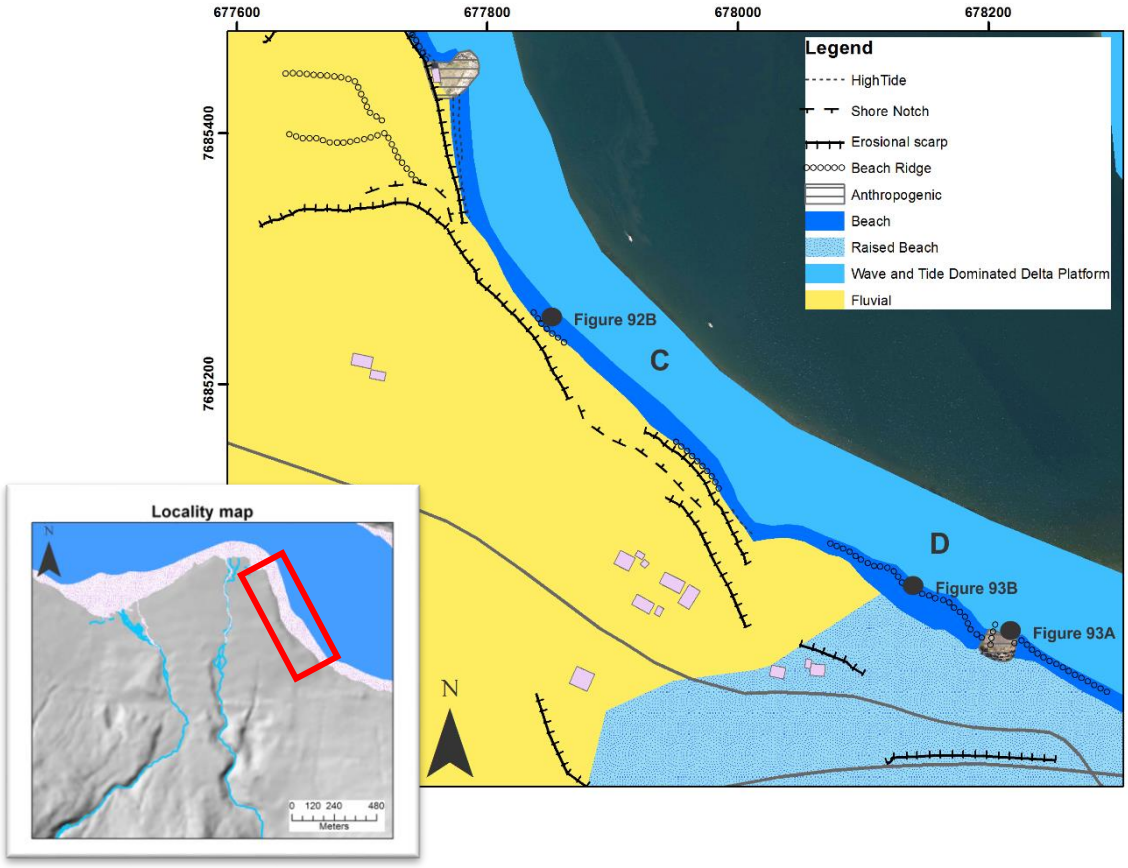

Figure 91: Detailed map of the beach morphogenic element located on the eastern side of the fan delta.

Large boulders and cobbles are often observed at the base of the erosional scarp and this sediment appears to have been eroded and deposited directly from the scarp. This provides further evidence that the sediment within the erosional scarp is very coarse. Occasionally, the boulders and cobbles occur as a 4 to 5 m long beach ridge at the top of the beach, directly beneath the erosional scarp (Figure 92). These boulders are sub-rounded, show a preferential orientation and have a mode of 25 cm and a maximum clast size of 35 cm. A well-sorted gravel with a mode of 1 cm occurs beneath the beach ridges.

It is difficult to determine the lower beach boundary in this area because there is a gradational decrease in grainsize between the bottom of the beach sediment and the start of the delta platform. The steep erosional scarps terminate at the end of Area C and large boulders are not observed to the north of the erosional scarps. Additionally, a few groundwater seeps or springs were observed along the beach in both Area C and D. These seeps occur as small areas of flowing water on the beach that

do not have an obvious source or identifiable channels. The beach gravel and cobbles located in the path of the groundwater springs are sometimes stained red.

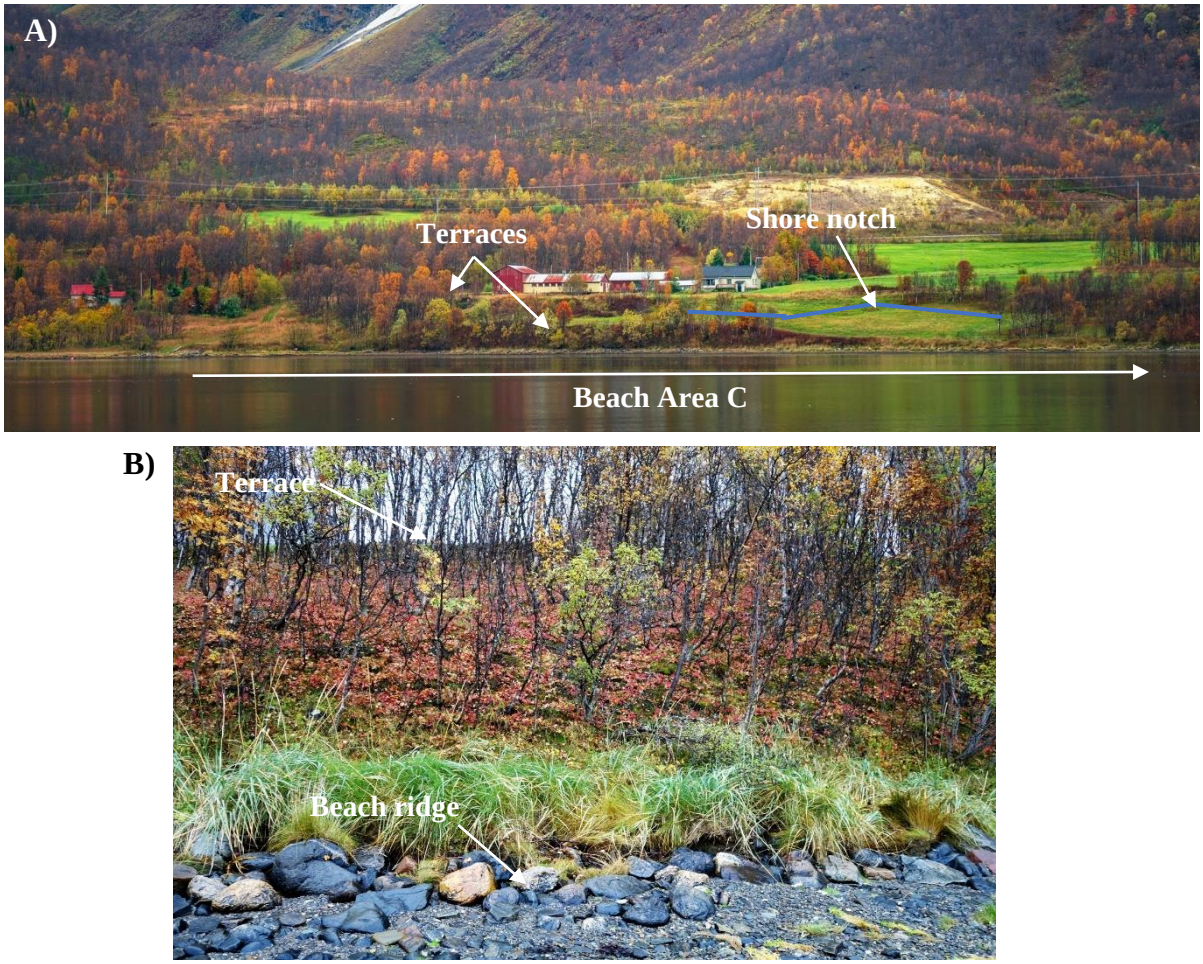

Figure 92: A) Photograph the eastern side of the Russenes fan delta taken from across the fjord by Rowan Romeyn. The steep scarp and terraces located directly behind Beach Area C are clearly visible. B) Photograph of high erosional scarp located immediately behind the beach in Area C (location given in Figure 91). A line of cobbles and boulders is observed at the base of the erosional slope forming a 4 m long beach ridge.

Beach Area D

The beach element in Area D has a very distinctive profile with a flat grassy backshore region and a prominent boulder beach ridge located in the middle of the beach. This ridge is elongate, semi-continuous and approximately 3.5 m wide (Figure 93). The beach ridge is composed of cobbles and boulders with a grainsize mode of 50 cm and a maximum grainsize of 135 cm. The boulders are sub-rounded to sub-angular and show imbrication. The beach ridge does not have a matrix. The thickness and height of the beach ridge varies and the maximum height is 80 cm. The gradient of the beach is steepest at the beach ridge. The mean high tide level is located at the top of the beach ridge.

The backshore consists of a flat grassy area located directly behind the beach ridge. This grassy area is sometimes boggy and contains occasional boulders and seaweed marking the storm high tide level. Some of the boulders show evidence of frost shattering. The sediment in front of the beach ridge is well sorted and has a bimodal grainsize distribution. It is composed of: (1) coarse to very coarse sand; and (2) gravel and cobbles with a grainsize mode between 1.5 and 3 cm and a maximum clast size of 12 cm. There is a decrease in grainsize from the top of the beach towards the sea as well as some variations in the gravel and cobble size fraction along the beach.

Area D is undergoing net sediment erosion and therefore, the cobbles and boulders located on the beach could be representative of the sediment that have been eroded from the fan delta. For example, the large boulders that occur along this section of the beach could indicate that very course sediment was deposited in this part of the fan before net erosion commenced. However, the distribution and morphology of the boulder beach ridge suggests that the boulders have been deposited by sea ice, which forms in the fjord during winter. Similar boulder beach ridges deposited by sea-ice-pushed boulders have been recorded in on the Kola Peninsula in northwest Russia (Møller et al., 2002).

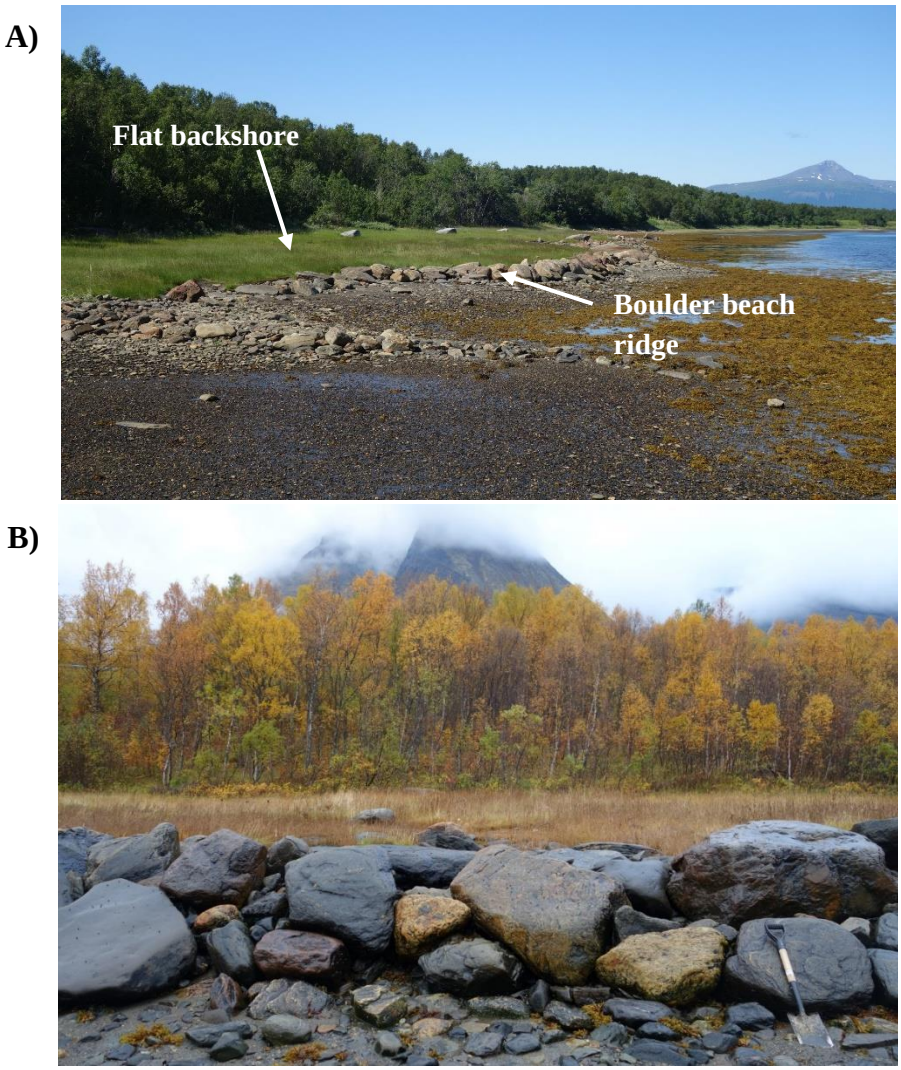

Figure 93: A) Photograph of the beach on the south-eastern part of the delta platform (Area D). This beach has a very distinctive morphology with a large semi-continuous bouldery beach ridge and a flat grassy backshore area. B) Photograph of a bouldery beach ridge that is 100 cm high. Spade = 75 cm. The location of the photos is shown in Figure 91.

4.3.2.1.2 Fluvially-dominated zone

There are a few areas on the delta platform where fluvial processes dominate over wave and tidal processes. These areas can be recognised on aerial photographs by the presence of channels traversing across the delta platform and are defined as the fluvial dominated zone on the Quaternary Geology Map (Figure 83). This morphological element predominately occurs where the Buktelva and Russedalselva rivers discharge into the fjord.

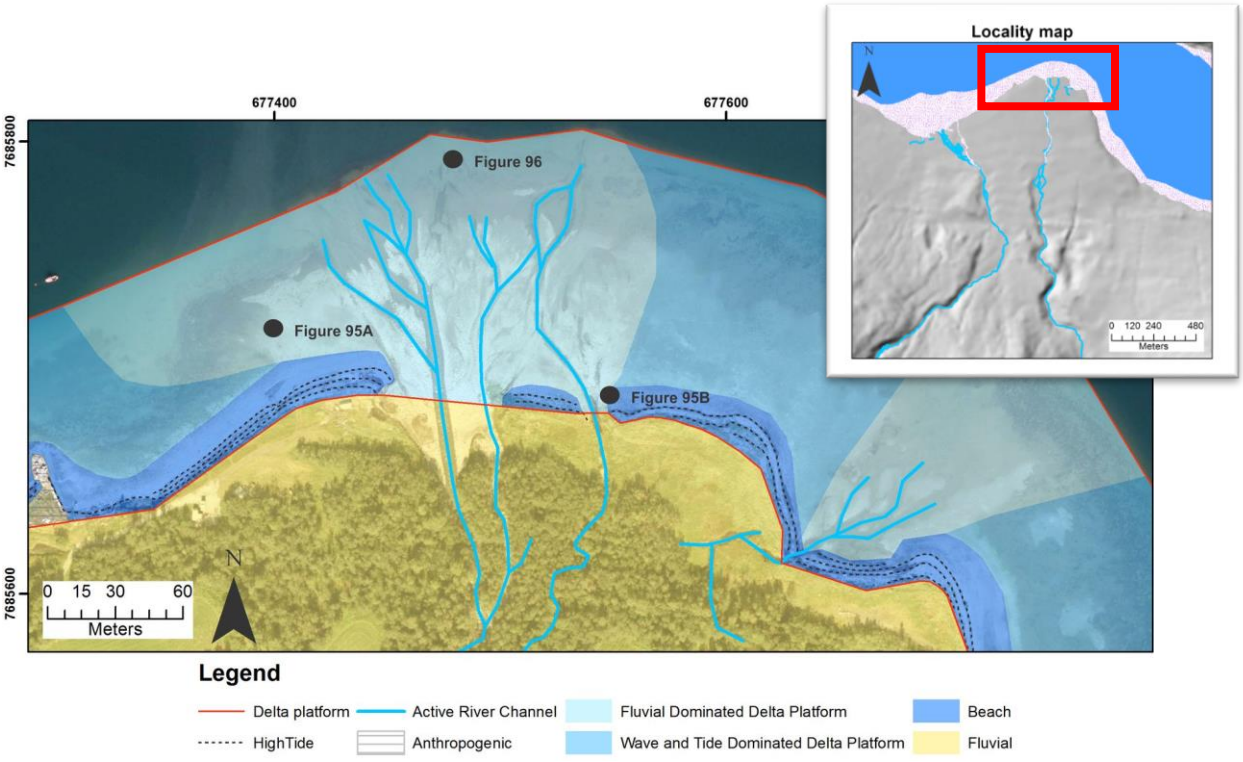

Figure 94: Detailed map of the fluvial dominated zone of the delta platform located at the top of the fan delta where the Russedalselva river discharges into the sea.

A 100 m wide delta platform is exposed at low tide where the Russedalselva river discharges into the fjord and this part of the delta platform is traversed by fluvial channels (

Figure 94 and Figure 95). Sediment within the channels is composed of well-sorted, sub-rounded gravel with a grainsize mode of 3 cm (Figure 96). The bars commonly have an elongate rhombohedral shape and a bimodal grainsize distribution of well-sorted medium sand and coarse gravel. The gravel is usually preferentially located at the top or along the edges of the bars and there is often a decrease in grainsize down the bar. There is also a general decrease in grainsize from the top of the fluvially dominated delta platform where the grainsize mode is 7 cm to the edge of the delta platform where sand becomes more abundant and ripple marks were observed on some bars. Gravel is observed within the channels at the edge of the delta platform (Figure 96).

A)

B)

Figure 95: A and B) Photographs of the fluvial dominated delta platform located in front of the Russedalselva river. The photographs were taken at low tide on 20 September 2016 and show a distinctive channel and bar morphology. The closest bars are outlined in white and the location of the photographs is given in Figure 94.

A)

B)

Figure 96: A and B) Photographs of a channel located near the delta lip that were taken on 20 September 2016. The sediment within the channel consists of well-sorted gravel whilst the bar next to the channel is dominated by gravelly sand. The location of the photographs is given in Figure 94.

Four orthophotographs of the study area are available from www.norgeibilder.no and these photographs have been taken over a 10 year period from 2003 to 2013 (Section 3.1.1). Figure 97A to D shows how the channel and bar morphology of the fluvial dominated delta platform has changed

over time. It should be noted that the resolution of the photographs is not constant and therefore, in some cases it can be difficult to distinguish all of the channels and bars. Nonetheless, the channels that could be distinguished have been digitised on each orthophotograph and these digitized channels are displayed together in Figure 97E. This shows the position of the channels has been very dynamic over the last 10 years.

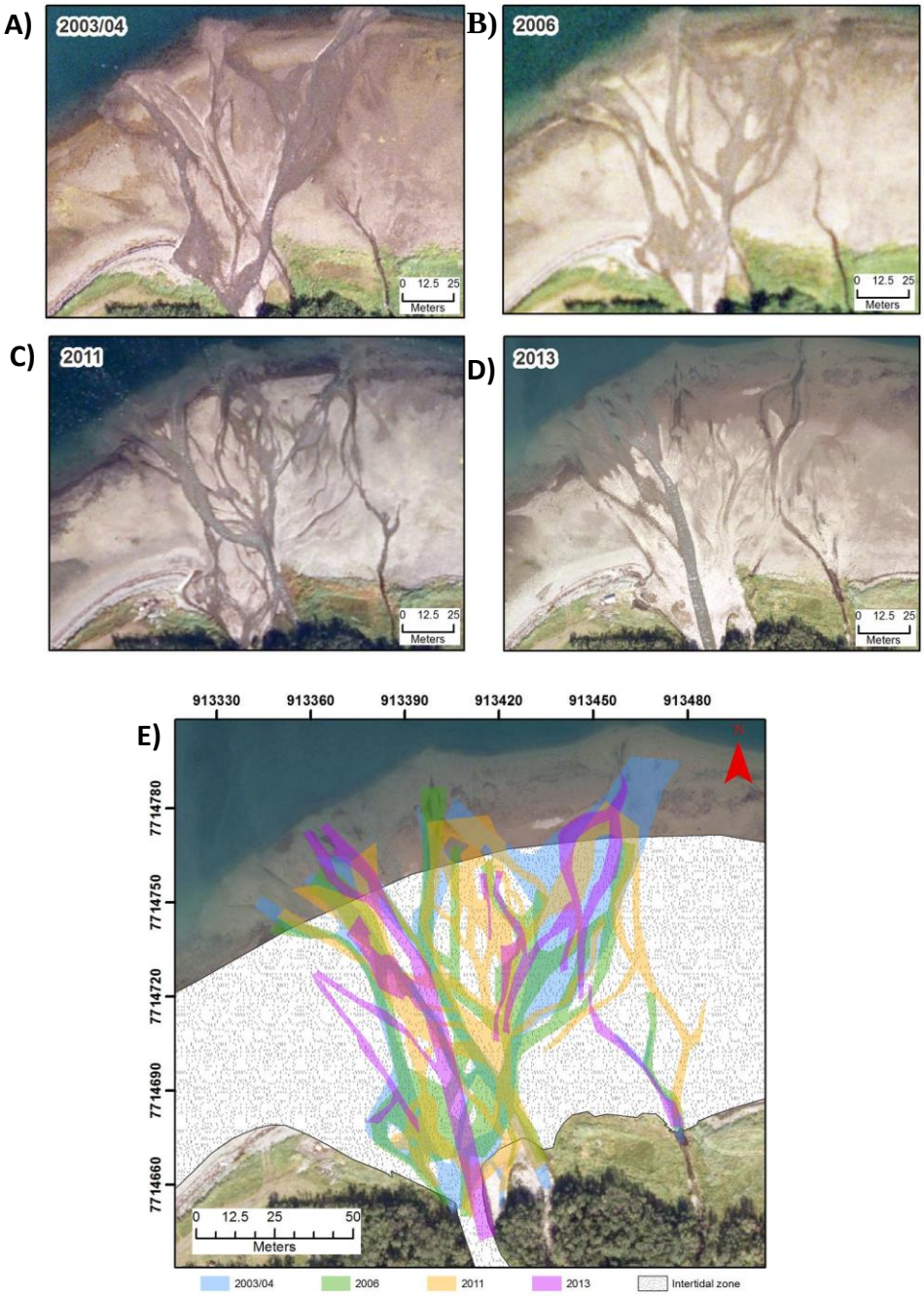

Figure 97: A to D) A series of orthophotographs over the fluvial dominated delta platform in front of the Russedalselva river mouth. The orthophotographs have been acquired over a 10 year period and show changes in the distribution of channels and bars on the delta platform over time. Details about the orthophotographs, including resolution, can be found in Section 3.1.1. E) The channels observed in the orthophotographs shown in A to D have been digitised and are displayed together to show the changes in the position of channels over time.

Where the Buktelva river discharges into the fjord the fluvial dominated delta platform has its widest extent with a width of approximately 230 m (Figure 98). This extensive delta platform occurs due to the large accumulation of sediment at the mouth of the Buktelva river, which indicates that this river is currently very active in transporting sediment. This part the delta platform is also traversed by channels and bars that are exposed at low tide (Figure 99).

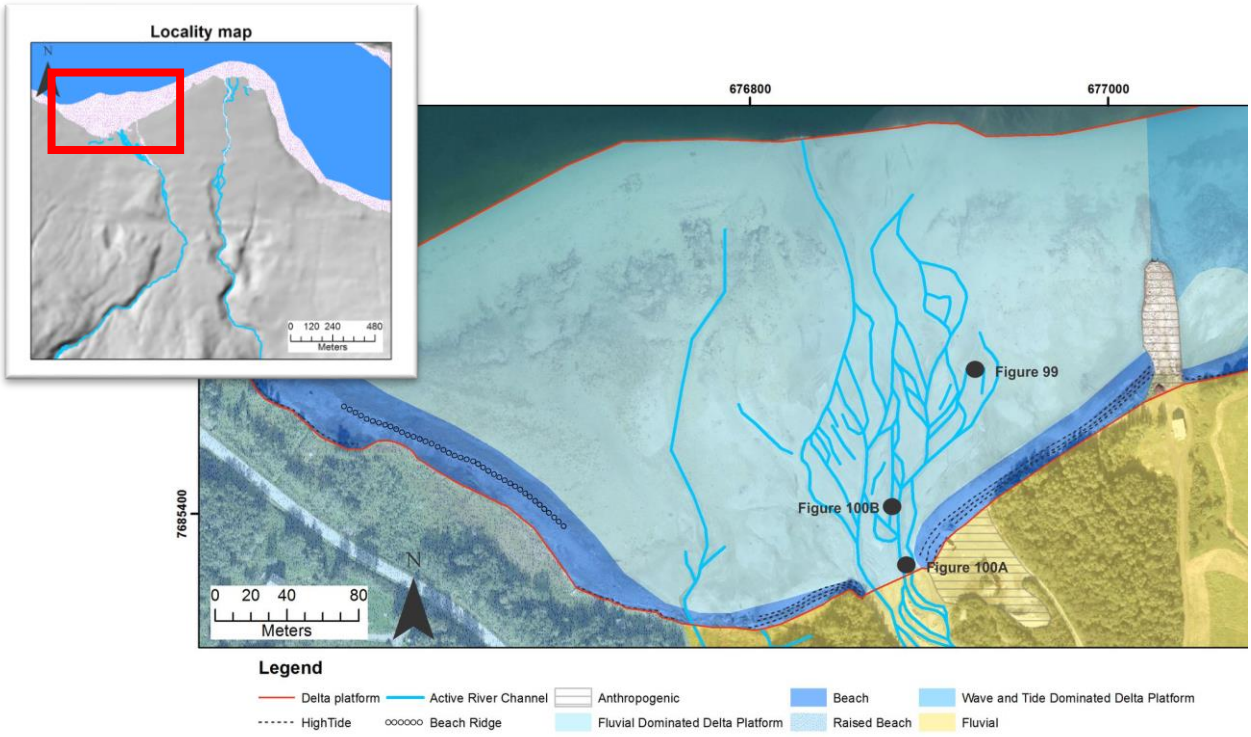

Figure 98: Detailed map of the fluvial dominated zone of the delta platform located where the Buktelva river enters the fjord.

Figure 99: A) Panorama photograph of the fluvial-dominated delta platform where the Buktelva river discharges into the sea, showing the distinctive channel and bar morphology. The closest bars are outlines in white. The photograph was taken during a rising tide on 18 September 2016 and therefore, the full extent of the delta platform is not shown.

The sediment grainsize decreases away from the river mouth. The bars located on the upper delta platform are high (approximately 30 cm) and elongate in the direction of channel flow (Figure 99). The bars are composed of bimodal sediment that consists of wel- sorted coarse gravel with a grainsize mode of 5 cm (70%) and medium to coarse sand (30%) (Figure 100).

A)

B)

Figure 100: A and B) Photographs of bars located in the upper section of the fluvial-dominated delta platform. Both bars are elongate in the direction of flow. The bar shown in (A) is most proximal to the river mouth and has a larger grainsize than that of the bar shown in (B). The location of the photographs is given in Figure 98 and they were taken on 18 September 2016.

There is a significant decrease in grainsize away from the river mouth. On the lower part of the fluvial-dominated area of the delta platform, the channels are dominated by gravel and the bars are predominately composed of medium to fine sand with occasional gravel (Figure 101). The finer grainsizes of silt and clay are also observed. The sandy bars of the lower delta platform are much larger and shallower than the gravelly bars of the upper platform and contain abundant ripple marks and bioturbation (Figure 101). The ripple marks have a wavelength of 4 cm, are slightly asymmetric with occasional branching.

A)

B)

Figure 101: A) and B) Photographs of ripple marks on the sand-dominated bars of the lower fluvial-dominated delta platform beneath the Buktelva river mouth.

The intertidal delta platform component of the Russenes fjord-side fan delta has a complex morphology. The wave- and tide-dominated zone has a distinctive beach morphogenic element, whilst the fluvial-dominated zone is traversed by a dendritic network of channels. The morphological and sedimentological analysis of the delta platform presented above indicates that some sections of the present-day delta platform are constructive due to the net deposition of sediment, whilst other sections are destructive due to net erosion, which results in the formation of erosional scarps at the back of the beach. Figure 102 shows the areas of the present-day delta platform that are constructive and destructive. The constructive areas occur under two conditions: (1) where sediment derived from the river mouths is being deposited by fluvial processes; and (2) through redistribution of sediment along the delta platform by wave and tidal processes.

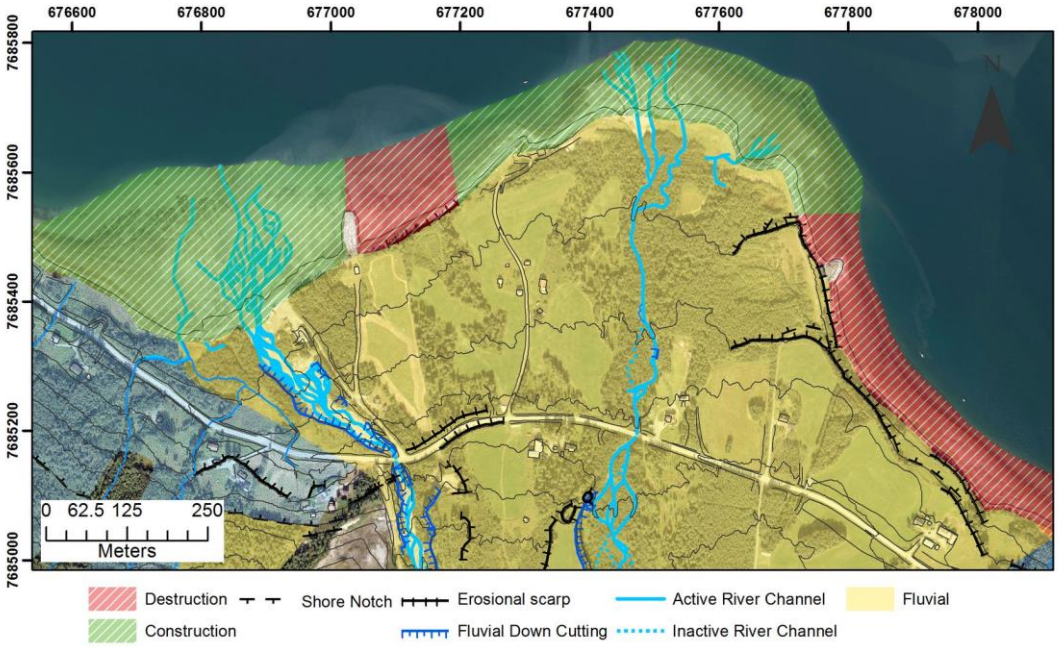

Figure 102: Map of the top of the Russenes fjord-side fan delta showing the present-day constructive and descructive areas of the delta platform. Some associated morphogenic elements are shown. Base map = Orthophotograph Midt_Troms_2013.

4.3.2.2 Delta slope

The morphology of the present-day subaqueous component of the Russenes fjord-side fan delta has been investigated using a multibeam bathymetry dataset collected beneath the Russenes and Nordkjosbotn deltas (Section 3.2) (Corner and Eilertsen, 2013). A shaded-relief map of this dataset is presented in Figure 103 and this map shows the fjord is very shallow beneath both deltas with a maximum water depth of 14 m. The delta rim is located at the intersection of the delta platform and the delta slope and it is located 2 m below the mean sea level. The radius of the delta rim was observed directly at low tide to be 1 to 2 metres wide (Corner and Eilertsen, 2013).

The multibeam bathymetry map shows the Nordkjosbotn delta has a steep and featureless delta slope, whilst the morphology of the Russenes fan delta slope is more variable (Figure 103). Figure 104 shows that the gradient of the slope surrounding the fan delta is highly variable. The steepest slopes are located directly in front of the present-day fluvial discharge channels, with maximum slope gradients between 30 and 40 degrees. In contrast, the delta slope is shallow (less than 20 degrees) on the eastern-most and western-most sides of the fan delta (Figure 104). The gradient of

the delta slope is the steepest directly in front of the present-day river mouths because these are the areas that are actively prograding. Additionally, Figure 105 shows small bulges in the slope at the sites of fluvial discharge indicating there is a lot of sediment on the slope at these locations. In contrast, the gradient of the delta slope is shallower away from the sites of active delta progradation because wave and tidal processes have eroded and redistributed the sediment on the delta slope.

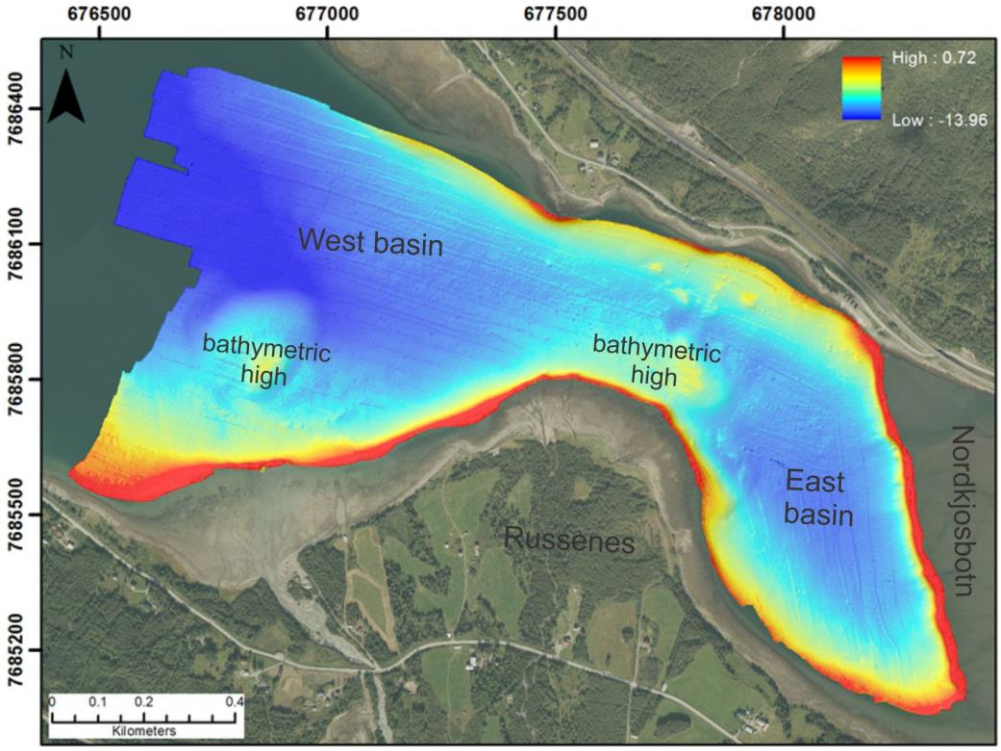

Figure 103: A) Orthophotograph Midt_troms_2013 overlaid by a shaded-relief multibeam bathymetry map of the subaqueous component of the fan delta (azimuth = 315° and elevation = 45°). Data collected by Corner and Eilertsen (2013). Bathymetry map datum = lowest astronomical tide.

4.3.2.3 Prodelta

The prodelta is defined by a shallow gradient (3-4°) and it is usually composed of mud. It is difficult to differentiate the end of the delta slope and subsequent commencement of the prodelta from bathymetric data alone. The prodelta and fjord beyond is generally between 10 and 14 m deep. The distal prodelta and fjord-bottom sediments interfinger. The shallow water depths provide a limited accommodation space for the accumulation of sediments, which will result in the rapid forward progradation of both deltas.

The multibeam bathymetry shows some interesting features within the prodelta and fjord area beyond the delta. Two elevated mounds have been identified on the sea floor (bathymetric highs) (Figure 103). One is located directly in front of the Russenes fan delta and the other is located on the western side of the fan delta. Both mounds have minimum depth of -8 m l.a.t. The protrusion of the Russenes fan delta 500 m into the fjord and accompanying bathymetric high beneath the delta creates two separate basins around the fan delta (Figure 103) and the circulation of deep water between these basins may be restricted by the bathymetric high. These elevated mounds on the fjord floor could be caused by the presence of bedrock directly beneath the fjord sediments or they

could be further deglacial ice-contact landforms deposited during the halt in the Balsfjord glacier (Section 4.2.3 and 4.2.4).

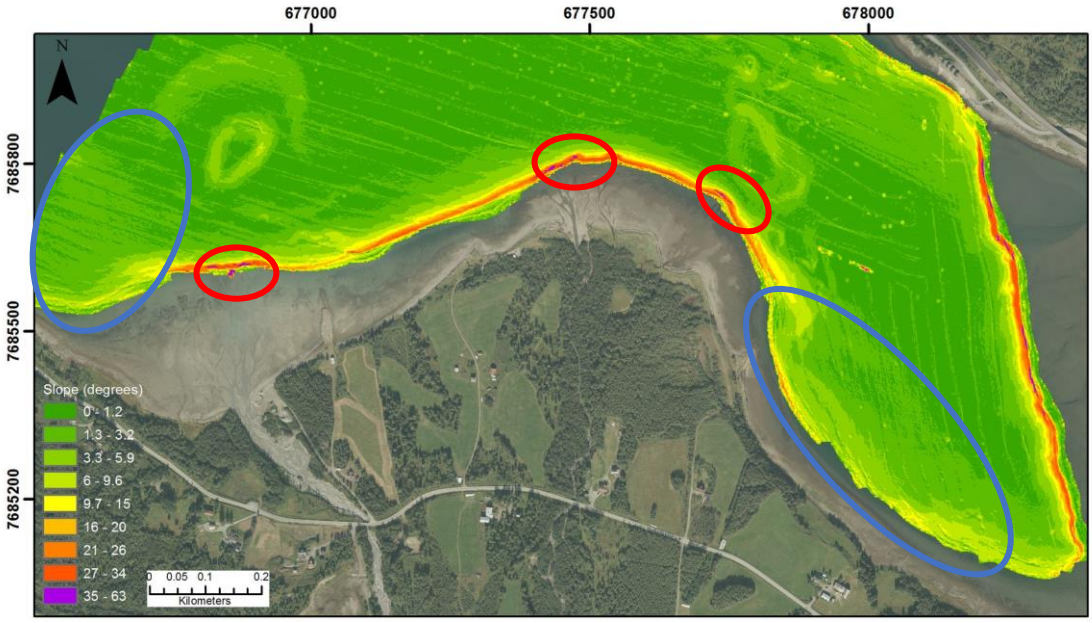

Figure 104: Slope map of the sea floor created from the multibeam bathymetry data (Corner and Eilertsen, 2013). The steepest slopes along the front of the Russenes fan delta are highlighted by the red circles and are located at the site of present-day fluvial discharge, whilst the areas with the shallowest delta slope are shown by the blue circles.

Figure 105 shows a number of small mounds (20 m wide) that occur on the northern side of the fjord, which are interpreted as rockslide debris because the mountain located immediately above the debris contains a lot of evidence of mass movement processes (Sletten et al., 2006). There are also a number of small circular depressions observed within the sediment in the deeper parts of the fjord, below a depth of 10 m l.a.t. Figure 105 shows a section across one of these depressions, which is very shallow (approximately 2 cm deep and 6 m wide) and they are interpreted as pockmarks that were formed during dewatering of the sediment.

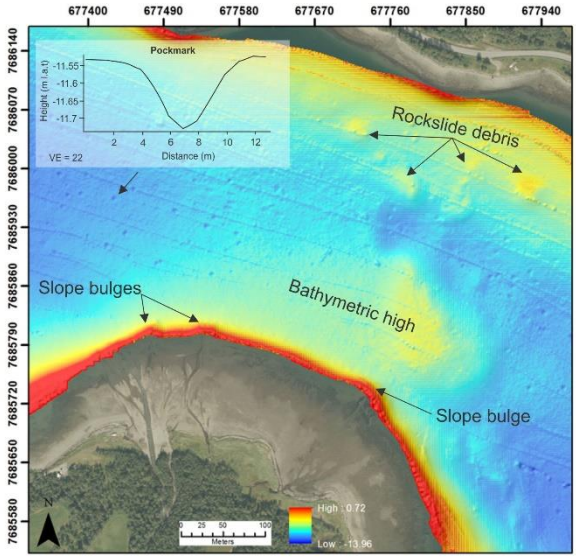

Figure 105: Enlargement of the multibeam bathymetric map at the front of the Russenes fjord-side fan delta. Some of the morphogenic features are highlighted. Data collected by Corner and Eilertsen (2013)

4.3.2.4 Summary

The postglacial Russenes fjord-side fan delta has two distinctive subaerial and subaqueous environments: (1) a subaerial alluvial fan; and (2) a subaqueous delta. The alluvial fan consists of a steep fan shape accumulation of alluvial sediment (3° to 10°) that has two apex points. The western fan apex is located at 100 m a.s.l and it is fed by the Buktelva river and the eastern fan apex is located at 65 m a.s.l and it is fed by the Russedalselva river. Both rivers have a braided character and sediment transport occurs by bedload processes during flooding. Sediment can be transported from the fan apex to the subaqueous component of the fan delta or it can be stored within the alluvial fan.

Below the subaerial alluvial fan, the modern delta has three major environments: (1) the intertidal delta platform, (2) the subaqueous delta slope; and (3) prodelta. The delta platform is the gently sloping intertidal region of the fan delta, which occurs at the interface between the terrestrial and marine environments and it is formed where the rivers discharge their sediment load into the sea. The delta platform is divided into two major zones due to the variations in the amount of fluvial, wave and tidal processes: (1) the wave- and tide-dominated zone; and (2) the fluvial dominated zone. The delta platform is generally constructive within the fluvial dominated zone and destructive within the wave- and tide-dominated zone. The delta rim is located 2 m below mean sea level and it has a radius of 1 to 2 m. The delta slope is steepest directly in front of the river mouths where it has a maximum gradient of 40 degrees. The delta slope has a concave-upward parabolic, longitudinal profile that decreases towards the prodelta region. The prodelta has a shallow gradient (3° to 2°) and occurs between a depth of 10 and 14 m. Consequently, the fan delta has a very shallow marine accommodation space.

4.3.3 Deltaic Subsurface Sediments

The subsurface of the Russenes fjord-side fan delta is composed of deltaic sediment that has been deposited into Balsfjord under a forced regressive depositional regime created by a falling sea level. Investigation of the delta subsurface indicates that the fan delta has a Gilbert-type tripartite structure consisting of bottomsets, foreset and topsets beds (Figure 19). This structure produces a coarsening-upward sedimentary succession and the present-day delta morphology can be used as an analogue for the depositional environment of the older deltaic subsurface sediment.

4.3.3.1 Facies Architecture

Three deltaic depositional units (bottomsets, foresets and topsets) have been identified beneath the subsurface of the Russenes fjord-side fan delta through the interpretation of exposed vertical sedimentary sections and the collection and interpretation of a few ground penetrating radar (GPR) profiles. The key characteristics that were used to identify and define the different deltaic units are presented below.

4.3.3.1.1 GPR profiles

The bottomset, foreset and topset facies architecture of the Gilbert-type delta is recognised by specific reflection characteristics and configurations within the GPR profiles. The GPR reflection character of each unit is shown in Figure 106.

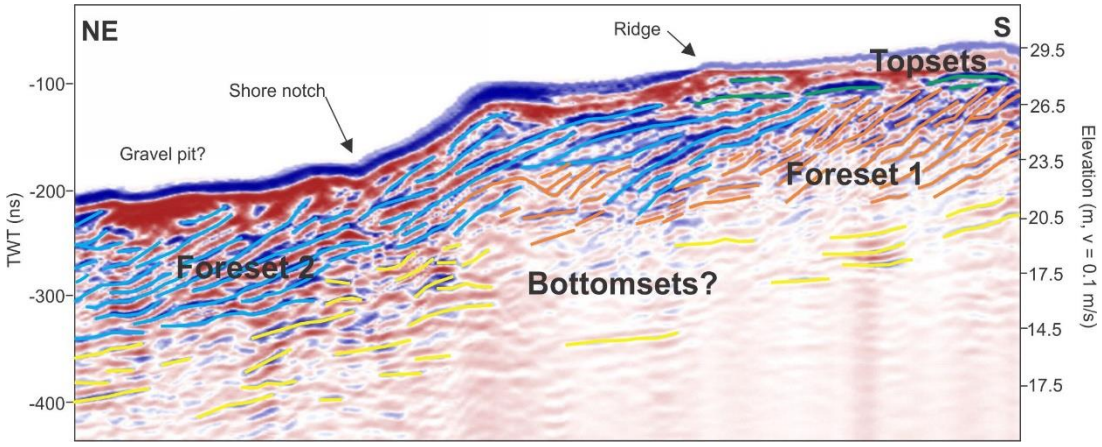

Figure 106: A ground penentrating radar profile collected in the study area showing the GPR facies architecture of topset (green), foreset (blue and orange) and possible bottomset (yellow) reflections.

Bottomset reflections

Bottomset reflections consist of gently dipping parallel continuous to discontinuous reflections located below foreset reflections. It can be difficult to recognised bottomset reflections because they are often located 5 to 10 m below the surface and the GPR signal is attenuated with depth. Therefore, the bottomset reflections usually have a low amplitude and low frequency, which often makes the identification uncertain.

Foreset reflections

Foreset reflections are easily identifiable within GPR profiles that are collected parallel to the dip direction of the foresets beds because in this direction they occur as oblique, parallel, continuous reflections with a steep gradient (20 to 30°) (Figure 106). These foreset reflections usually have a high amplitude that decreases with depth and the angle of the foreset reflections may also decrease with depth. The continuity of the foreset reflections can vary laterally and they commonly dip towards the fjord. Where GPR profiles are collected perpendicular the dip direction of the foresets, the reflections are characterised as high amplitude, semi-continuous, sub-horizontal reflections.

Topset reflections

Delta topset reflections consist of a thin unit (2 to 3 m) of sub-horizontal reflections that unconformably overly the delta foreset reflections. The character of the reflections can have considerable lateral variation, whereby reflections can be laterally continuous or chaotic and hummocky. Topset reflections always occur at the top of the GPR profiles. The lower boundary is often erosive and truncates the foreset reflections. Additionally, the first reflection can be difficult to interpret because it often has a high amplitude and low frequency caused by differences in the electric properties of the subsurface and the atmosphere.

4.3.3.1.2 Sedimentary sections

Within the exposed vertical sedimentary sections the tripartite structure of the deltaic sediment was identified based on several characteristics including: the orientation of the beds; the character of the contact between different units (e.g. conformable, erosional etc.); sedimentary structures; and grainsize (e.g. silt, sand and gravel). A summary of the key characteristics of the deltaic bottomset, foreset and topset sediment is presented below.

Bottomset sediment

The bottomset sediment consists of horizontal to sub-horizontal, laterally continuous beds of clay silt, silty clay, sandy silt and silty sand. The dominant lithofacies is massive beds. However, laminated and deformed beds were also observed. Marine macrofossils are common (Section 4.3.3.3.1).

Foreset sediment

The foreset sediment consists of inclined (20 to 30°) beds of alternating sand and gravel. The beds are dominantly massive. However, other lithofacies occur including normal grading, inverse grading and deformed beds. The dip of the foreset beds often decreases with depth and some of the foreset beds pinch out. There is considerable lateral variation in grainsize and the long-axis of many of the gravel clasts is aligned with the dip of the foreset bed.

Topset sediment

The topset sediment is dominated by massive sandy gravel beds that erosively overlie the foreset sediment. Occasional laminated sand and silt sediment occurs. As the topset sediment occurs at the surface of the alluvial fan, the topset sediment has also been described in Section 4.3.1.2.

Deltaic sediment is exposed at two locations in the study area. At each location the exposed sedimentary sections have been examined and logged. Additionally, GPR profiles have been collected above the sedimentary sections. Therefore, the results have been combined and are presented below.

4.3.3.2 Locality 1: Gravel pit

The subsurface structure of deltaic topset, foreset and bottomset sediment has been investigated within the gravel pit shown in Figure 107 where both topset and foreset sediment is exposed in vertical sedimentary sections. In addition, three GPR profiles of the subsurface have been collected near the gravel pit to assist with interpretation.

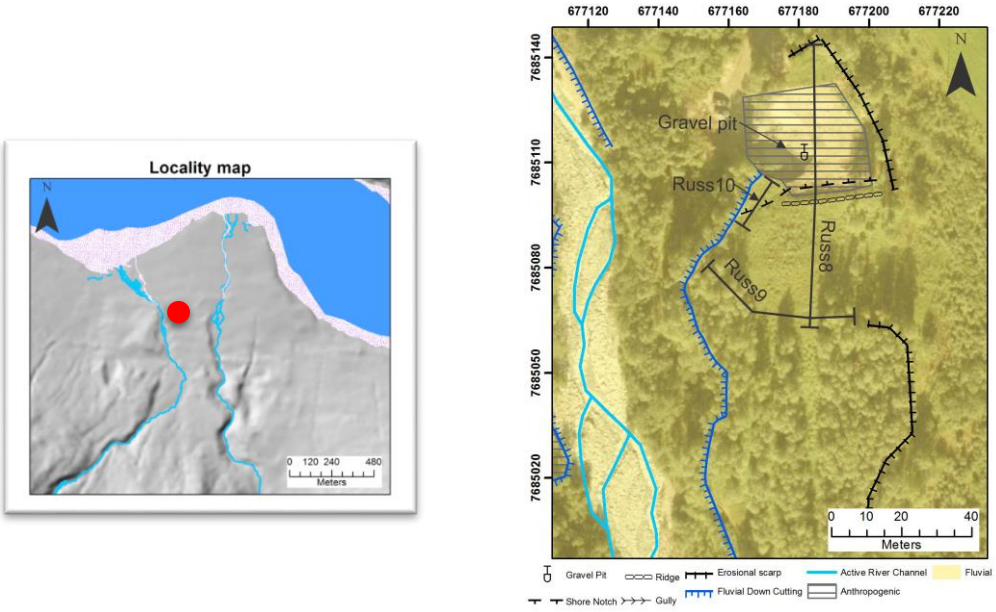

Figure 107: Aerial photograph of the gravel pit (Midt_troms_2013). The location of the GPR profiles obtained near the gravel pit are shown. Additionally, the morphological and geological features surrounding the gravel pit are also indicated.

4.3.3.2.1 Topsets

A small fluvial terrace is located at the southwestern edge of the gravel pit and sediment within the terrace is shown in Figure 108A. This sediment is composed of massive, sub-rounded cobbly sandy gravel and it is interpreted as a topset unit that is erosively overlying foreset beds. The subsurface structure of this topset sediment was further investigated by the collection of a GPR profile across the fluvial terrace (GPR Profile Russ10) (Figure 108). Two different units have been identified within the profile: (1) a foreset unit; and (2) a topset unit. The foreset unit consists of dipping high amplitude continuous reflections. The topset unit unconformably overlies the foreset unit. The topset unit has a variable character. On the southwestern side of the profile the reflections are chaotic and on the northwestern side continuous high amplitude reflections occur. This indicates that there is considerable lateral variation in the character of the unit. The topset reflections are sub-horizontal and truncate the underlying dipping foreset reflections. The topset unit correlates to the fluvial sediment observed within the gravel pit (Figure 108A).

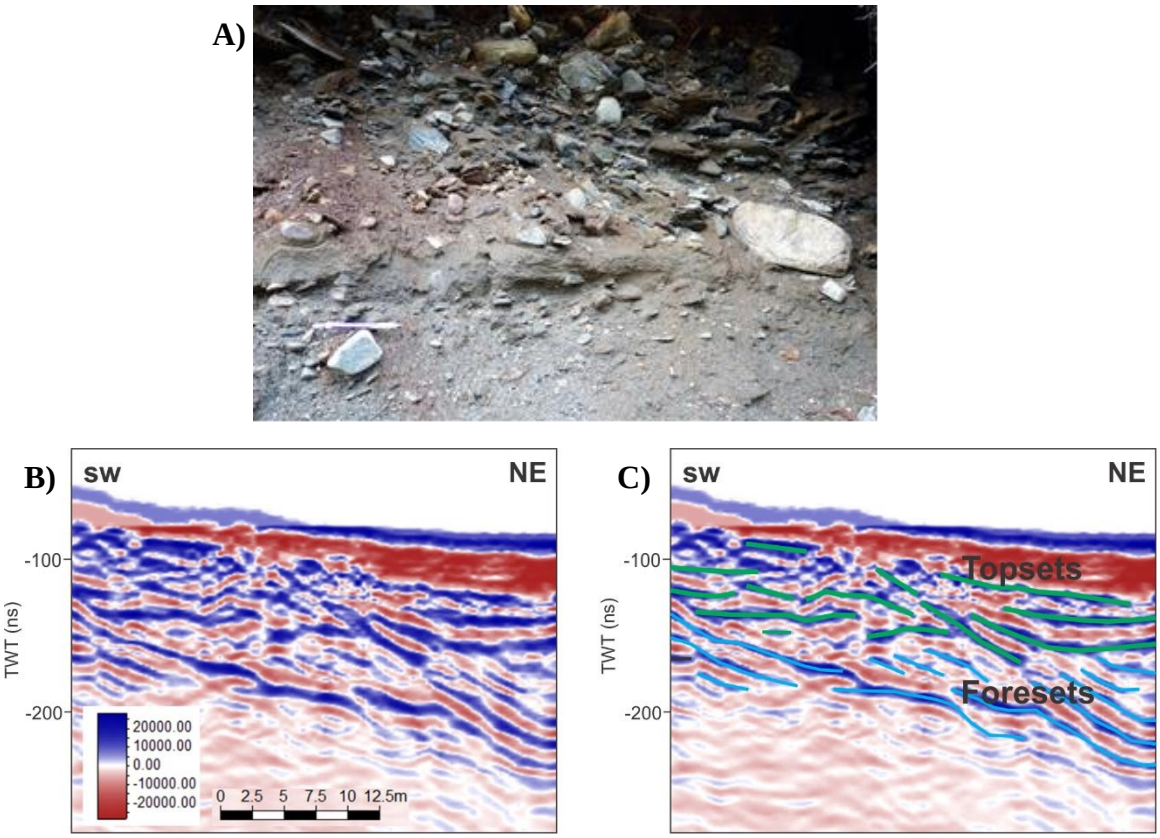

Figure 108: A) Fluvial topset sediment exposed within the gravel pit. The sediment is composed of massive, sub-rounded cobbly sandy gravel. B) Uninterpreted GPR profile Russ10. C) Interpreted GPR profile Russ10. A topset unit (green) and foreset unit (blue) have been identified. The location of the profile is shown in Figure 107.

4.3.3.2.2 Foresets

Two vertical sedimentary sections with deltaic foreset sediment are located within the abandoned gravel pit (Figure 107). The sedimentary section located on the eastern side of the gravel pit (Figure 109) shows lateral variations in grainsize, bed thickness and dip angle. In the southeast, the foreset sediment consists of interbedded sand- and gravel-dominated beds that dip at 25° (Figure 109 and Figure 110). A prominent 5.5 m long sand-dominated foreset bed occurs in the centre of the exposure (Figure 109). The dip of this sand bed decreases from 25° at the top to 22° at the bottom and the foreset beds above downlap onto this bed (Figure 109). The northwest section of the exposure is dominated by cobbly gravel foreset beds, which have a very steep gradient in the upper part of the bed (35°) that decreases towards the bottom of the bed. These observations are recorded in the graphical log presented in Figure 111.

A graphical log of the alternating sand- and gravel-dominated foreset beds is shown in Figure 110. This log shows that the bedding types include: massive laminations, imbrication and deformed bedding. Imbrication occurs when the long-axis of the gravel clasts is aligned with the dip of the bed. Soft sediment deformation structures were observed within a sand bed located between 23.55 m and 23.6 m (Figure 110B). A thick (40 cm) gravel-to-cobble-dominated bed occurs immediately above the soft sediment deformation structures. Therefore, these deformation structures could have been created due to the rapid deposition of the coarse-grained sediment on top of the sand causing liquification of the sand. Alternatively, they could be created by sediment creep on the delta slope.

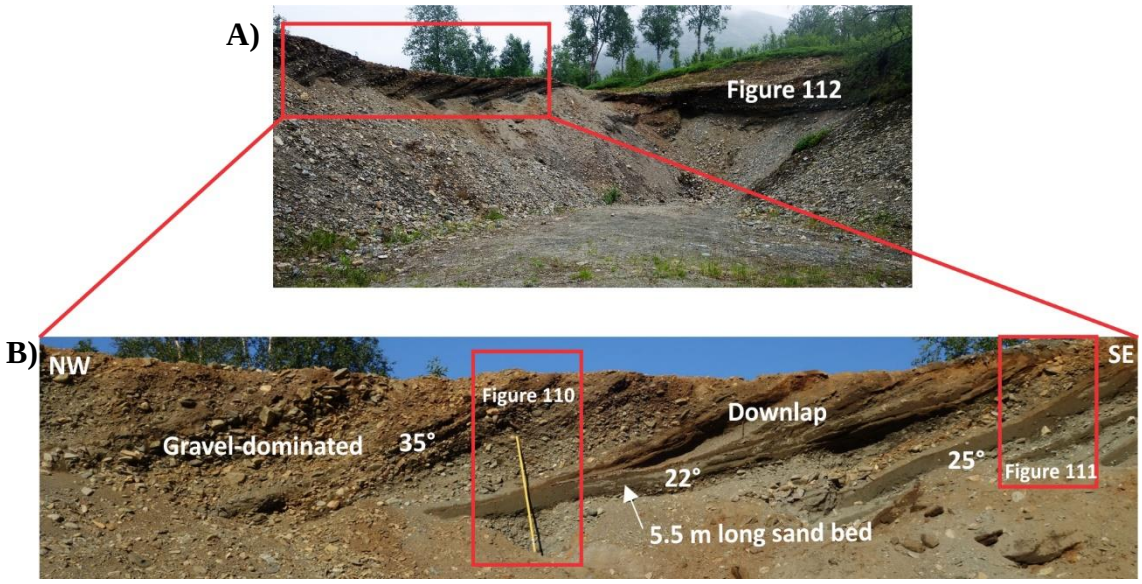

Figure 109: A) Photograph of the gravel pit showing the location of the two sedimentary sections. B) Photograph of the foreset beds located on the eastern side of the gravel pit showing lateral changes in grainsize and bed orientation. The dip of the foreset beds varies between 22° and 35°.

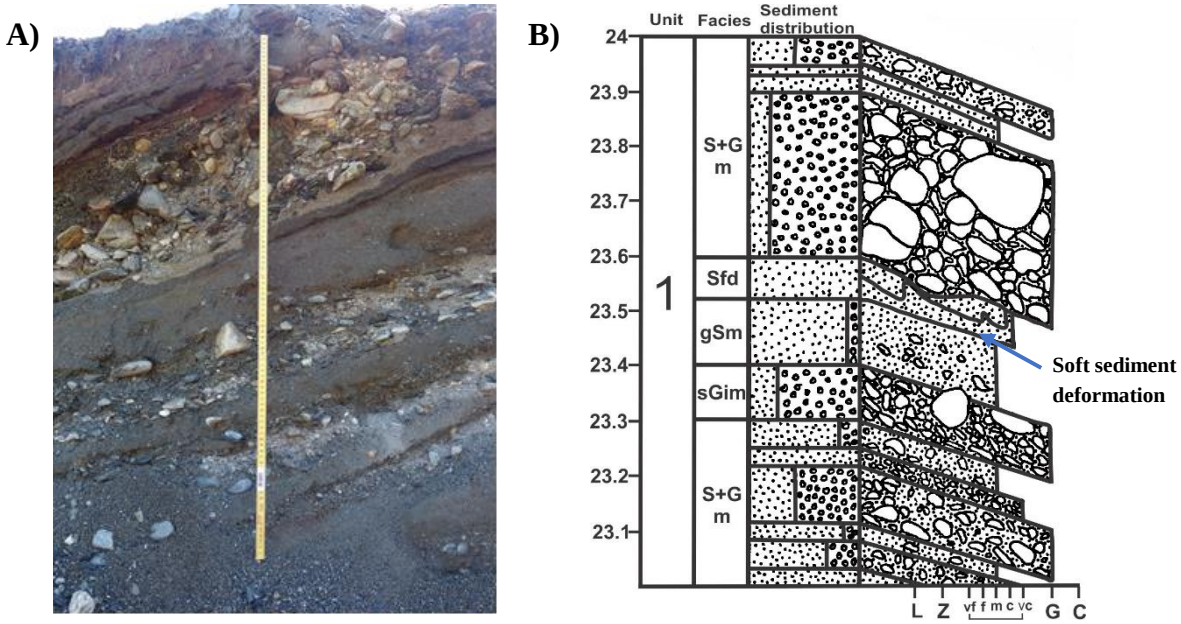

Figure 110: A) Photograph of the sand- and gravel-dominated delta foresets beds located on the south-eastern side of the gravel pit. B) Graphical log of the foreset beds showing changes in sediment grainsize and facies. Location of the log is shown in Figure 109.

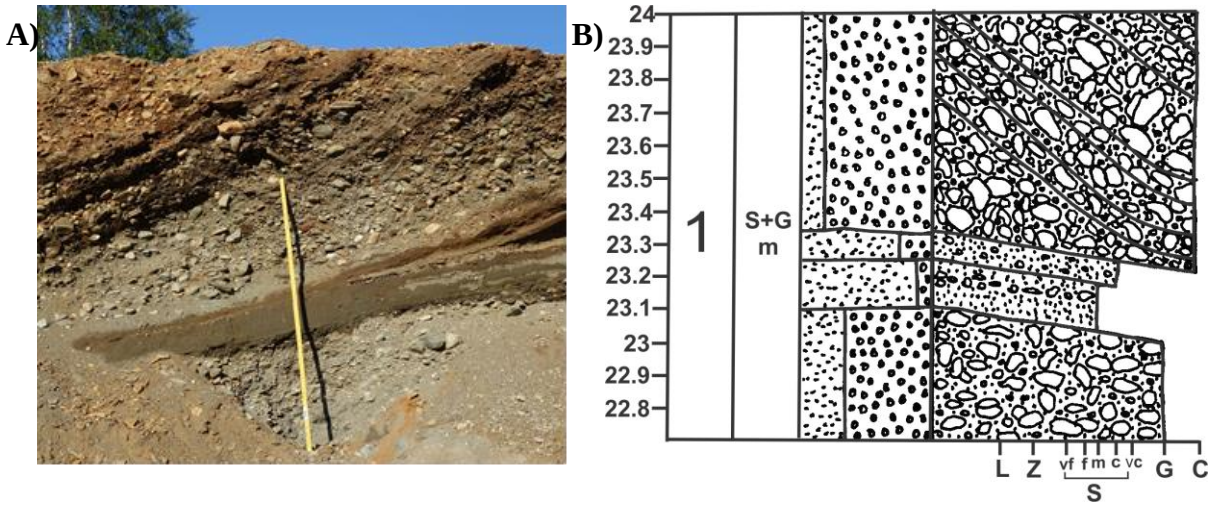

Figure 111: A) Photograph of the gravel-dominated delta foreset beds located on the north-western side of the gravel pit. B) Graphical log of these foreset beds showing changes in sediment grainsize and facies. Location of the section is shown in Figure 109.

Another sedimentary section is located at the back of the gravel pit (southern wall; Figure 107) and two different foreset units have been identified within the section (Figure 112). Unit 1 consists of thin (5 to 10 cm) sandy gravel beds that are dipping at 20° towards the northeast. The long-axis of most of the gravel clasts are preferentially aligned with the dip of the beds. Unit 1 is interpreted as delta foreset beds and they are located stratigraphically below the foreset beds on the eastern side of the gravel pit. The top of Unit 1 is truncated by Unit 2 and therefore, an unconformity occurs between these units. Unit 2 consists of laterally continuous sub-horizontal beds that alternate between gravel and sand. The gravel-dominated beds have a grainsize mode of 1 cm and a maximum grainsize of 9 cm. Some of the gravel clasts are oblate and imbricated. Unit 2 is also interpreted as delta foreset beds, whereby, the sedimentary section occurs perpendicular to the foreset dip direction. These foreset beds belong to the same unit that is exposed on the eastern side of the gravel pit.

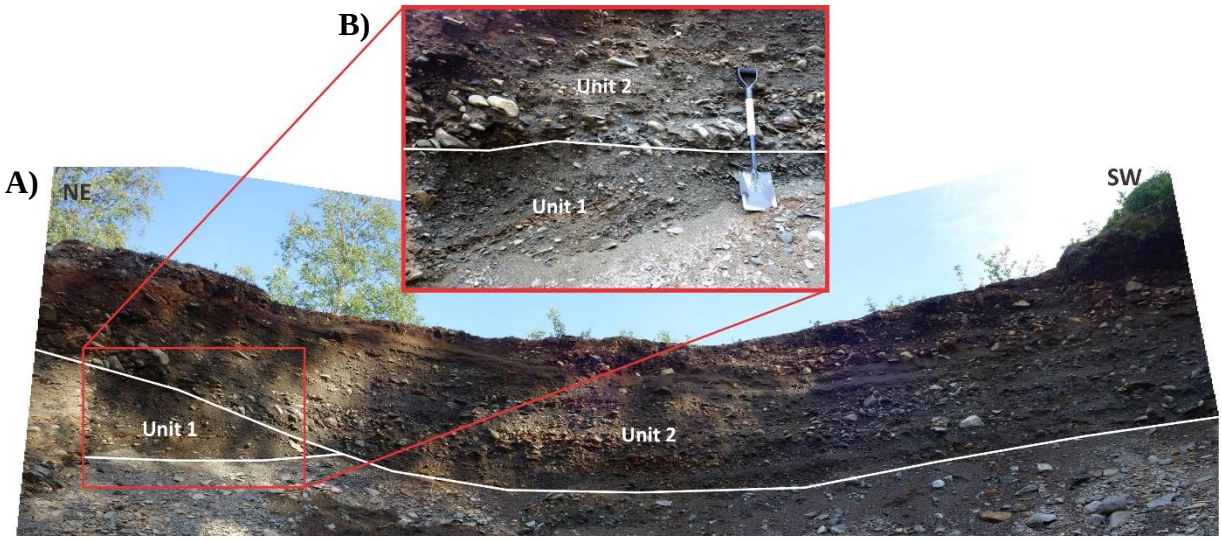

Figure 112: A) Photograph of the vertical sedimentary section located at the back of the gravel pit (Figure 107). The two different foreset units are shown. B) Photograph of the boundary between Unit 1 and 2. Unit 1 contains dipping foreset beds that are truncated by Unit 2. The location of the photograph is shown by the red box in A.

4.3.3.2.3 Large-scale architecture

The GPR profiles that were collected around the gravel pit can provide further information about the structure of the subsurface sediments and they can be used to place the detailed sedimentological information recorded in the gravel pit into a wider context (Figure 107).

GPR profile Russ8

GPR profile Russ8 is a 62 m long profile that was acquired in a north-south direction immediately adjacent to the gravel pit (Figure 107 and Figure 113). This GPR profile can be compared with the exposed vertical sedimentary section on the eastern side of the gravel pit (Figure 109). This GPR profile has been collected across an area with distinctive morphogenic features. The vegetation has been cleared along the first section of the profile and it is unclear if any sediment has been removed by gravel pit operations. There is an increase in the gradient of the slope at approximately 18 m (Figure 113). It is difficult to determine if the slope has been affected by anthropogenic activity. A shore notch has been identified at the bottom of this slope and a ridge occurs at the top (Figure 107B).

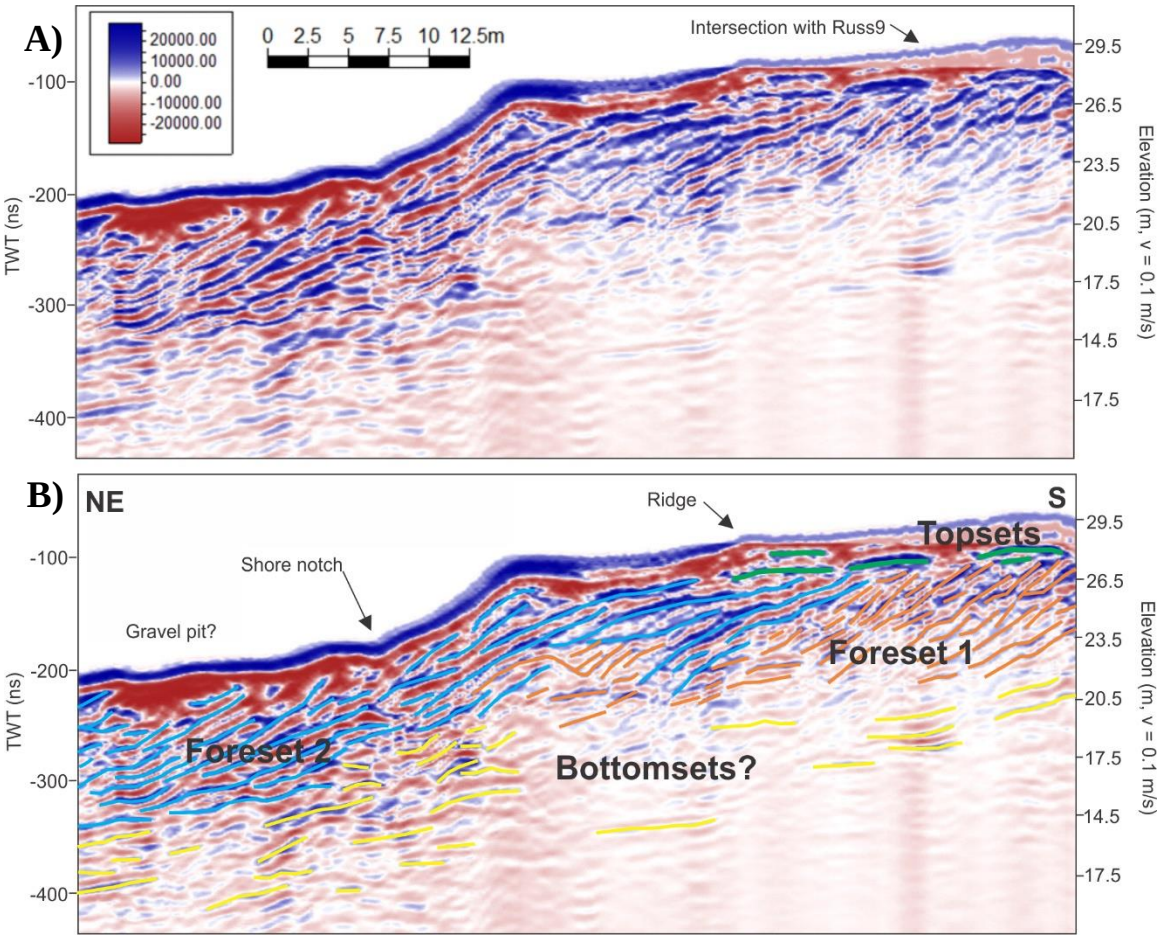

Figure 113: A) Uninterpreted GPR profile Russ 8. B) Interpreted GPR profile Russ 8. Delta bottomsets (yellow), foresets (blue and orange) and topsets (green) have been identified. The location of the profile is shown in Figure 107.

Most of the reflections in the top -300 ns of the GPR profile have a high amplitude and are steeply dipping, however, the continuity of the reflections varies along the profile. All three deltaic units (topsets, foresets and bottomsets) have been identified based on reflection geometry, amplitude

and frequency (Figure 113), although the bottomset unit is uncertain. The bottomset unit occurs at the base of the GPR profile and contains discontinuous low frequency reflections. A foreset unit overlies the bottomset unit and it has been divided into two units. Foreset unit 1 primarily occurs on the southern side of the GPR profile and consists of discontinuous dipping medium amplitude reflections, whilst foreset unit 2 occurs on the northeastern side of the profile and consists of continuous, high amplitude dipping reflections. These two foreset sub-units are interpreted to represent changes in the delta slope depositional environment or sediment supply. A thin topset unit erosively overlies the foreset unit on the south side of the profile and consists of sub-horizontal reflections. This unit is interpreted to be deposited unconformably over the foreset unit. The foreset unit within the GPR profile is interpreted to be equivalent to the delta foreset beds observed within the gravel pit, however, the continuity and length of the reflections is much greater (4 to 9 m) than that observed within the vertical sections in the gravel pit (1 m). This indicates that only a small section of the foreset beds is exposed within the gravel pit.

GPR profile Russ9

GPR profile Russ9 is an east-west profile located perpendicular to GPR profile Russ8 (Figure 107). These two GPR profiles intersect 10 m from the end of Russ8. All three deltaic units (topsets, foresets and bottomsets) have also been identified within this profile (Figure 114). Possible delta bottomset reflections occur at the base of the profile (below -170 ns) and these reflections have a medium amplitude and low frequency. The foreset reflections consist of high amplitude, semi-continuous, sub-horizontal reflections, which is interpreted to be equivalent to the delta foreset reflections identified in Russ8 (Figure 113). A thin topset unit defined by horizontal continuous reflections occurs at the top of the profile.

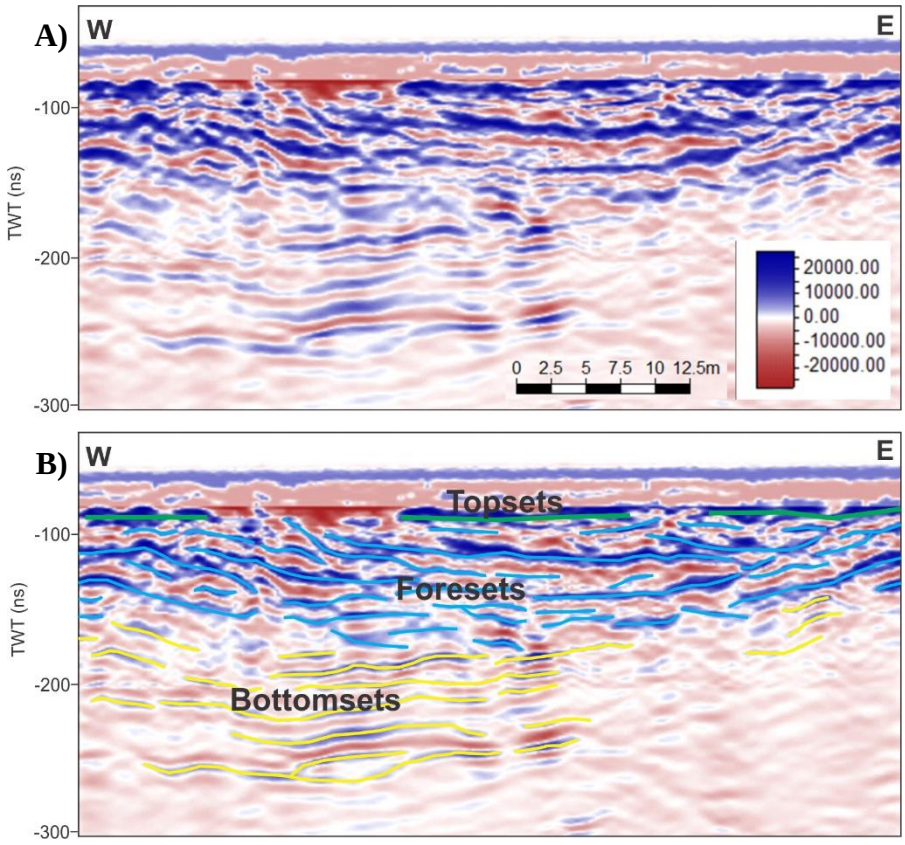

Figure 114: A) Uninterpreted GPR profile Russ9. B) Interpreted GPR profile Russ9. A bottomset unit (yellow), foreset unit (blue) and topset unit (green) have been identified. Location of the profile is shown in Figure 107.

4.3.3.3 Locality 2: River Bank

Deltaic bottomset and foreset sediment occurs within a sedimentary section that has been exposed by fluvial downcutting on the western side of the Buktelva river (Figure 114). The total height of the section is 3.9 m and variations in grainsize and lithology have been recorded in a graphical log that is presented in Figure 116.

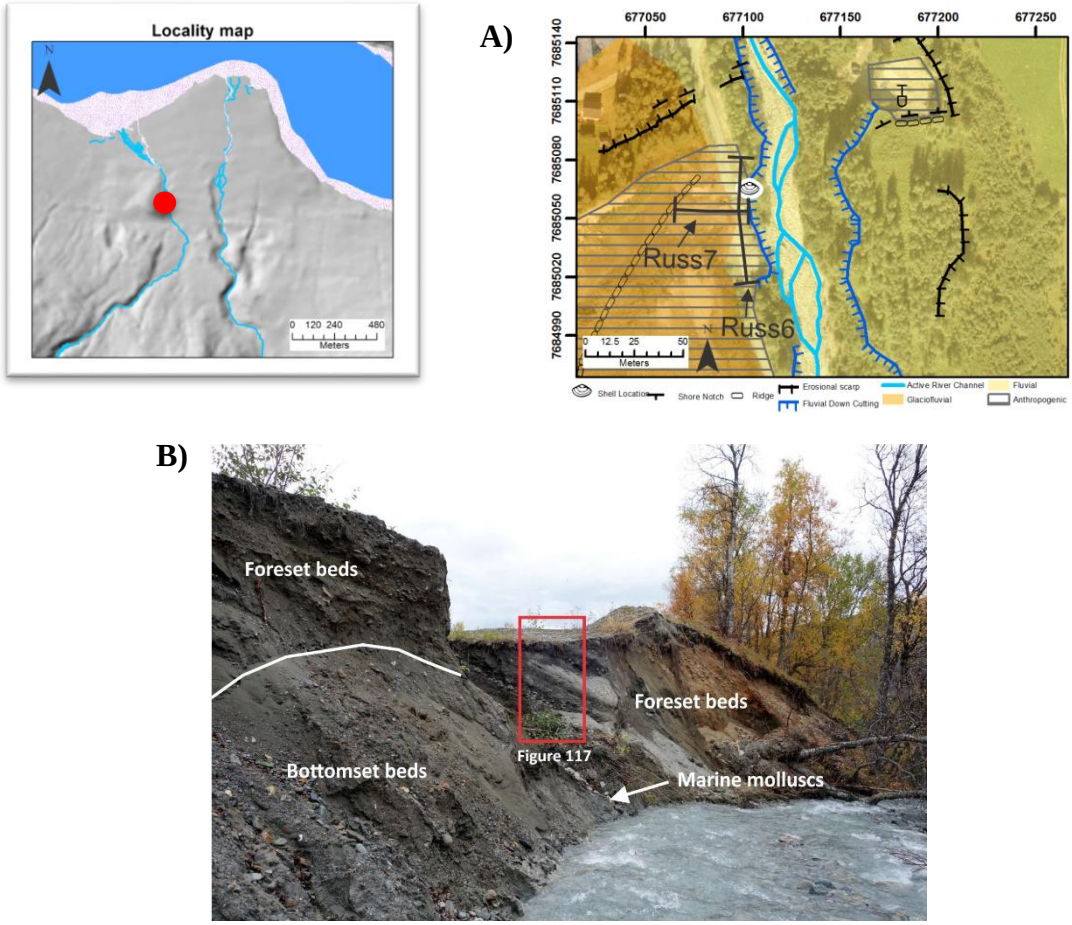

Figure 115: A) Aerial photograph Midt_troms_2013 showing the morphological and geological features mapped around the river cutting. The location of GPR profiles Russ6 and 7 is also shown. B) Photograph of the river cutting showing the location of the foreset and bottomset beds.

4.3.3.3.1 Bottomsets

The sedimentary section has been divided into two units. The bottom unit (Unit 1) consists of fine-grained clay silt and silty sand. Abundant paired molluscs have been found within this unit (Table 8), which indicates that the organisms are *in situ* and favourable conditions existed for the growth of molluscs. Therefore, the sediment was deposited in a calm environment with a low sedimentation rate. Most of Unit 1 is massive, however, thin wavy laminations (0.5 – 1 cm) were observed within the silty sand sediment located at the top of the unit (Figure 116C). Unit 1 is interpreted as prodelta bottomset beds and an erosional unconformity occurs at the top of Unit 1.

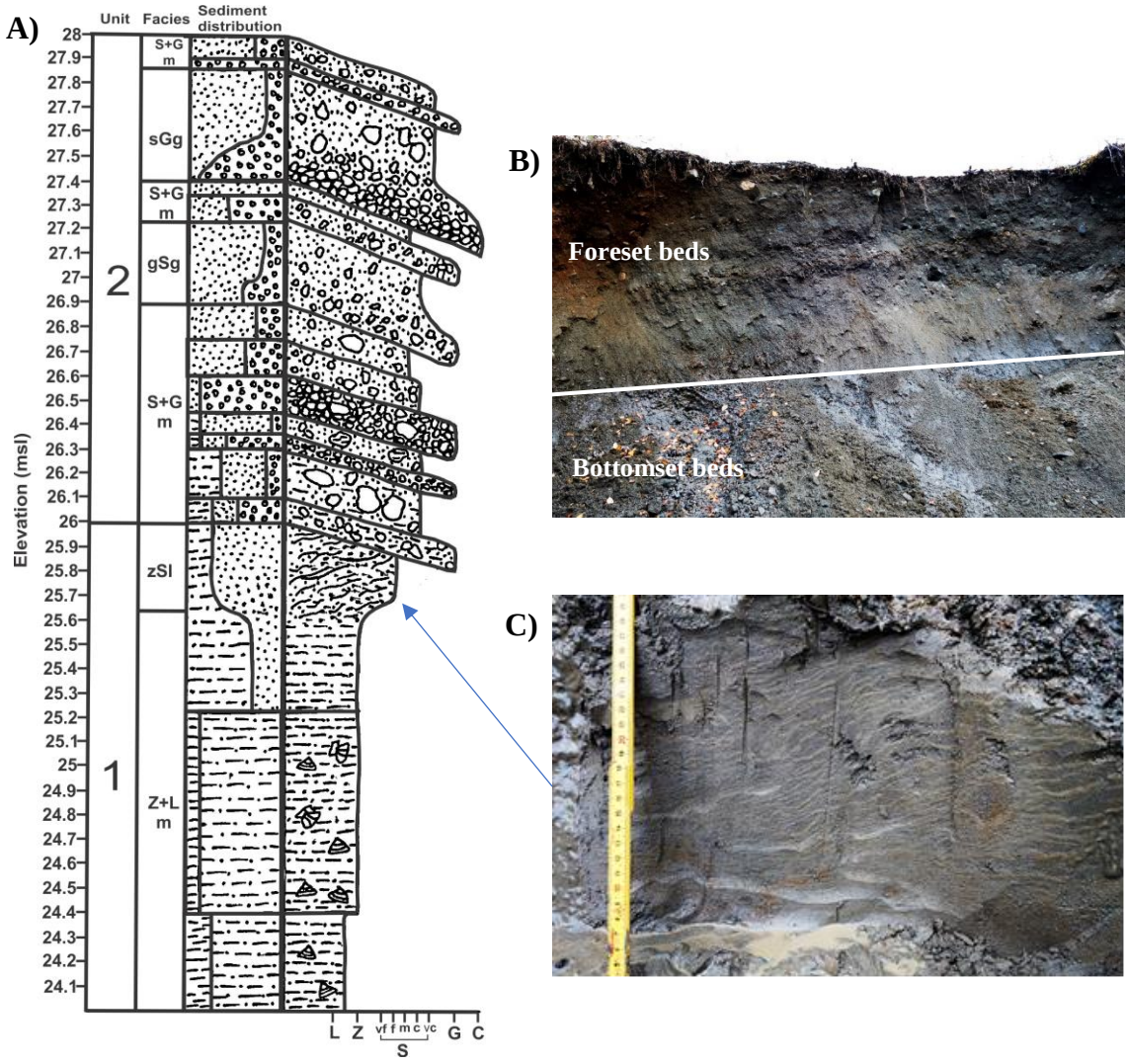

Figure 116: A) Graphical log of a sedimentary section located in the bank of the Buktelva river (Figure 115). The section has been divided into two units: Unit 1 is interpreted as prodelta bottomset sediment and Unit 2 is interpreted as prodelta foreset sediment. B) Photograph of part of the logged vertical section showing the deltaic foreset and bottomset sediment. C) Wavy laminations observed within silty sand in the upper section of Unit 1.

Four sediment samples were collected from this delta bottomset sediment and analysed in the laboratory. A list of the identified species is given in Table 8. Most of the identified species are suspension feeders and the only deposit feeder is *Macoma Calcarea* (Gmelin, 1791). Two of the mollusc samples were radiocarbon dated and the results are shown in Table 9. The radiocarbon date on the *Macoma Calcarea* sample gives the sediment an age between 10 472 and 10 234 cal. yr BP and the radiocarbon date from the *Mya Truncata* sample gives a similar age of 10 455 to 10 218 cal. yr BP.

4.3.3.3.2 Foresets

Unit 2 consists of inclined beds alternating between sandy gravel and gravelly sand. Bed thickness varies between 5 and 50 cm and normal grading occurs in the upper section of the unit. Figure 117 presents another graphical log that was produced at the river bank showing alternating gravel- and sand-dominated inclined beds. The majority of the beds are massive, however, one bed shows inverse grading. Unit 2 is interpreted as delta foreset beds that unconformably overly the bottomset sediment.

Table 8: List of the mollusca species identified in the study area. The environment information has been obtained from Oliver et al. (2016).

Species	Feeder type	Environment
Chlamys Islandica (Müller, 1776)	Suspension	Lives on hard substrates from the intertidal region to the shelf edge.
Macoma Calcarea (Gmelin, 1791)	Deposit	Lives on fine sand and mud from the intertidal zone down to 200 m.
Cerastoderma edule (Linnaeus, 1758b)	Suspension	Occurs in sandy mud, sand or fine gravel, from mid-tidal level to just below extreme low water spring tide level. Abundant in sheltered bays and estuaries.
***Astarte Sulcata* (de Costa, 1778)**	Suspension	Offshore in muddy sands to gravels. Depth range 5 to 250 m.
Hiatella Arctica (Linnaeus, 1767)	Suspension	Lives on hard substrates and can hide in holes and crevices or borrow into soft rocks. Occurs from lower shore to the edge of the continental shelf.
Thyasira Flexuosa (Montagu, 1803)	Suspension	Lives offshore to the edge of the continental shelf in muddy sand.
Heteranomia squamula?	Suspension	Occurs on hard substrates with algae.
***Mya Truncata* (Linnaeus, 1758a)**	Suspension	Lives in mixed sandy material from the lower shore to approximately 70 m. Burrower.

Table 9: Radiocarbon dates obtained from shells within the bottomset sediment during this study. The ages are given in yr BP and calibrated yr BP. Ages have been calibrated with 2013 INTCAL using the MARINE13 database (Ramsey, 2009, Reimer et al., 2013).

Laboratory no.	Elevation (m)	Material dated	^{14}C age (yr BP)	Calibrated age (yr BP, 2σ interval)	Weighted mean calendar age (± 1σ) (cal. yr BP)*
Beta - 463114	25	*Macoma Calcarea*	9570 ± 30	10472 – 10234	10 345 ± 84
Beta - 463115	25	*Mya Truncata*	9550 ± 30	10455 – 10218	

**Weighted mean calculated using inverse variance weighting*

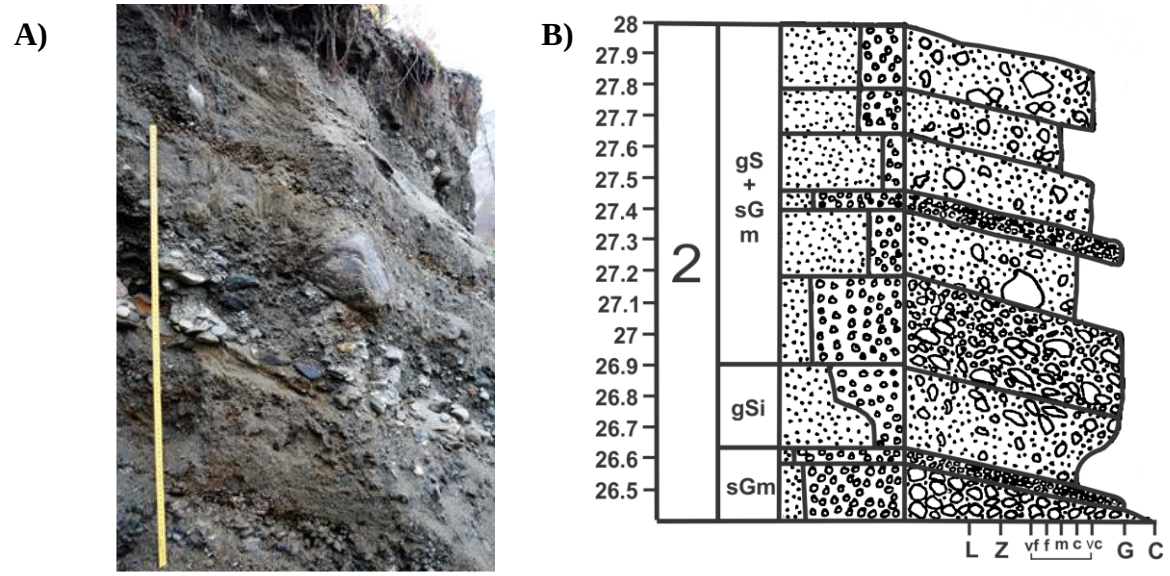

Figure 117: A) Photograph of part of the foreset sediment identified within the river cutting. The location is shown in Figure 115. B) Graphical log of the foreset beds showing changes in grainsize and facies.

4.3.3.3.3 Large-scale architecture

GPR profile Russ7 is an east-west profile that was collected perpendicular to the present-day Buktelva river (Figure 118 and Figure 114). This GPR profile has a few distinctive reflection packages that are identified as different units. A high amplitude continuous reflection with a high relief occurs on the eastern side of the GPR profile (purple) and this reflection is interpreted as a large erosional channel. This prominent reflection separates two different foreset units. Foreset unit 1 infills the channel and primarily consists of discontinuous high amplitude reflections. The top most reflections of this unit are dipping to the east and correspond to the foreset beds identified within the river bank (Figure 116). Therefore, the erosive channel is interpreted as a submarine channel that was formed on the delta slope. Submarine channels have not been identified on the present-day delta slope. However, they are common features in other deltas (Eilertsen et al., 2011). Foreset unit 2 consist of high amplitude semi-continuous dipping reflections, which are interpreted as extensive foreset beds. The bottomset sediment observed within the river bank cannot be identified within the GPR profile.

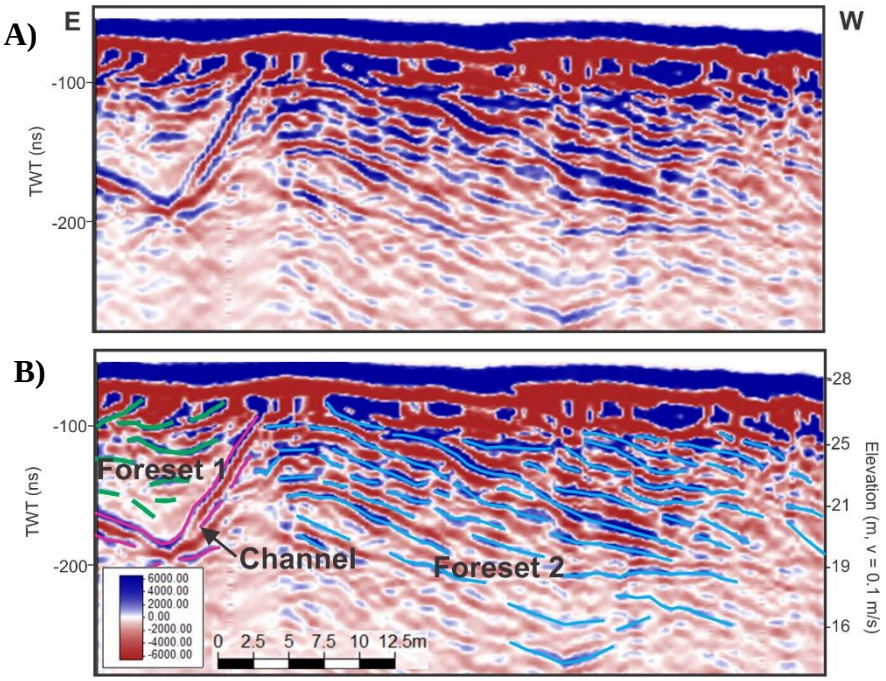

Figure 118: A) Uninterpreted GPR profile Russ 7. B) Interpreted of GPR profile Russ 7. A channel and two different foreset units have been identified. Location shown in

.

4.3.3.4 Interpretation

Interpretation of the depositional environment of the deltaic bottomset, foreset and topset units is given below. Table 10 provides information about the lithofacies observed within the study area.

4.3.3.4.1 Bottomsets

The bottomset sediment is interpreted to be deposited in the prodelta region of the fan delta. The bottomset sediment is dominated by massive bedding, which indicates that it has primarily been deposited from suspension settling of silt and fine sand. Additionally, the abundant macrafossils indicate a quiescent depositional environment. In other deltas in northern Norway, it is common for

bottomset sediment be dominated by rhythmic bedding, however, this lithofacies was not observed in the study area (Eilertsen et al., 2011).

Table 10: Summary of the lithofacies observed within the deltaic subsurface sediment. Table adapted from Eilertsen et al. (2011)

Lithofacies	Description	Frequency	Depositional component	Interpretation
Massive beds (m)	Silt, sand and gravel beds; sharp boundaries; 10 to 60 cm thick.	Abundant	Bottomsets, foresets, topsets	Massive silt beds deposited by suspension settling. Massive sand and gravel beds deposited by cohesionless debris flows
Normal graded beds (g)	Gravel to medium sand. Sharp boundaries. 20 to 40 cm thick.	Common	Foresets	Turbidity currents; debris flows waning current
Inverse graded beds (i)	Medium sand to fine gravel. Sharp boundaries. 25 cm thick	Rare	Foresets	Cohesionless grain flows
Deformed beds (d)	Medium to fine sand beds. < 10 cm thick. Erosional upper boundary. Folds and flame structures	Rare	Foresets	Liquification, slumping and sliding
Imbrication (im)	Preferential alignment of the long-axis of gravel clasts	Common	Foresets	Gravity flows, such as turbidity currents and grainflows
Laminated beds (l)	Thin (0.5 to 1 cm) beds of sand and silt.	Rare	Topsets	Planar bed flow

4.3.3.4.2 Foresets

The foreset sediment is interpreted to be deposited on the delta slope by mass movement processes and consequently, the foreset sediment consists of steeply dipping (22 to 35°) gravel- and sand-dominated beds. The lateral changes in grainsize reflect changes in the sediment supplied to the delta slope. The changes in the dip of the foreset beds can be correlated to the modern delta slope, whereby the dip of the bed decreases with increasing depth. The lithofacies observed include massive, deformed, normal graded and inverse graded beds, which indicate that sediment gravity flows are the dominant depositional process on the delta slope, such as turbitity currents, cohesionless grain flows and cohesionless debris flows. This is consistent with other Gilbert-type deltas (Prior and Borhold, 1989, Prior and Borhold, 1990, Eilertsen et al., 2011). However, massive beds are the most frequent lithofacies observed within the delta foreset sediment, which suggests cohesionless debris flows are the most comment depositional processes. This is consistent with the morphology of the present-day delta slope, which is reasonably smooth and featureless, indicating that it has been subjected to repeated unconfined flows (Prior and Borhold, 1990, Hansen et al., 2016). The delta foreset beds range in height from 4 to 9 m, which is similar to the height of the modern delta slope.

4.3.3.4.3 Topsets

Topset sediment is observed in two exposed sedimentary sections within the study area (Figure 78 and Figure 108) and the dominant lithofacies are massive and laminated beds. The maximum thickness of the delta topset sediment is 2.5 m and an erosional basal contact is often observed. The topset sediment does not contain beach sediment. The thickness of the topset unit and the erosive basal boundary indicate that the topset sediment has been deposited by a bedload dominated river as a result of aggradation and fluvial incision.

5 Discussion

5.1 Implications of the Ice-Contact Deglacial Landforms

This study of the postglacial Russenes fjord-side fan delta and associated deglacial landforms has uncovered a complex depositional history. It is the first time that the ice-contact deglacial landforms have been identified and mapped at Russenes and the presence of these landforms has implications for the deglacial history of Balsfjord.

5.1.1 Halt in the Retreat of the Balsfjord Glacier

A halt in the retreat of the Balfjord glacier in the location of the Russenes fjord-side fan delta has been recognised by the presences of two distinct landforms: (1) an submarine ice-contact fan; and (2) an ice-contact delta and rock-avalanche complex. Figure 119 shows a schematic model of the interpreted depositional environment of these landforms. The model shows that the submarine ice-contact fan and adjacent ice-contact delta were deposited by subglacial and englacial streams into an open marine environment during a halt in the retreat of the Balsfjord glacier.

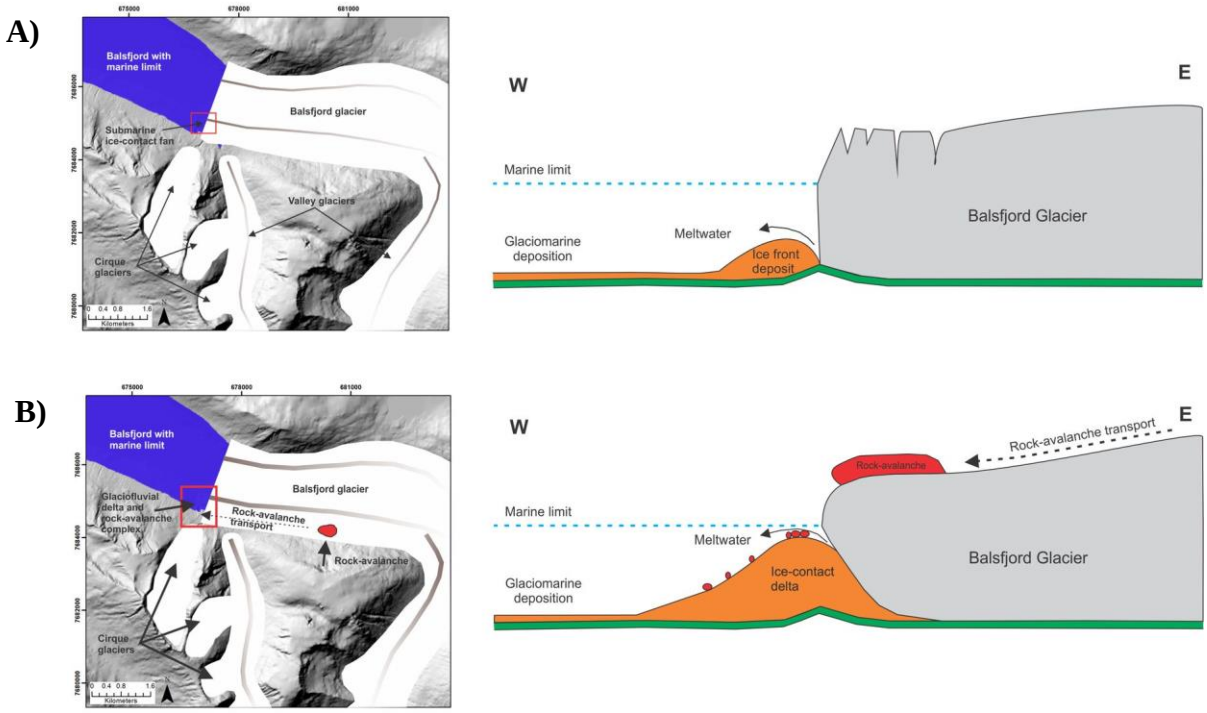

Figure 119: Schematic model of the deposition of the submarine ice-contact landforms during a halt in the retreat of the Balsfjord glacier. A) A submarine ice-contact fan is deposited from subglacial and englacial streams into an open marine environment. B) Simultaniously, an adjacent ice-contact delta that is graded to the marine limit is deposited. Rock-avalanche sediment is transported on the glacier to the site of the ice-contact delta and subsequently deposited.

During this study, it has been determined that the lower section of the rock-avalanche complex has been transported on the Balsfjord glacier and subsequently deposited onto the ice-contact delta (Section 0; Figure 119B). Recently, the effects of rock-avalanches on alpine glaciers in currently glaciated areas, such as New Zealand, Alaska and the Himalaya, has been an active area of research

(Deline, 2009, Hewitt, 2009, Reznichenko et al., 2011). It has been found that the presence of supraglacial rock-avalanche debris can modify the mass balance of a glacier because rock-avalanche debris can protect the glacier from solar radiation, which causes a reduction in surface ablation (Reznichenko et al., 2011). This can lead to thickening of the glacier ice and result in a glacier advance or surge (Reznichenko et al., 2011). For example, glacier surges following the deposition of rock-avalanches have been observed in the Himalaya (Hewitt, 2009). Reznichenko et al. (2011) have developed a depositional model for rock-avalanche debris that has been deposited onto the ablation zone of an alpine glacier and this model is shown in (Figure 120).

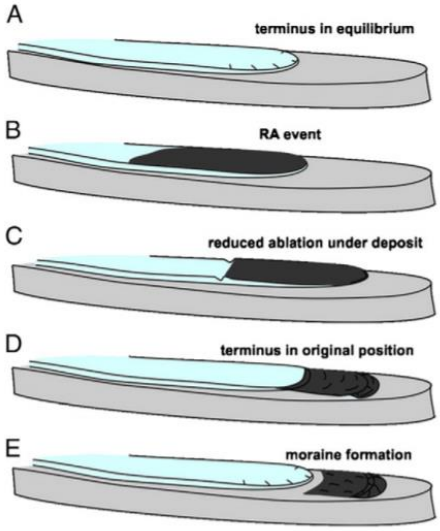

Figure 120: Schematic model showing the response of a glacier to rock-avalanche debris covering the ablation zone. A) the glacier is in equilibrium before the deposition of the rock-avalanche. B) Deposition of the rock-avalanche. Ablation is reduced by 70% C) Ice thickens and glacier advances. D and E) Glacier separates from debris-covered ice and retreats. Debris-covered ice continues to flow and the ice slowly melts forming a moraine. Adapted from Reznichenko et al. (2011).

Therefore, it is possible that the deposition of the rock-avalanche material onto the Balsfjord glacier could have affected the mass balance of the glacier resulting in a halt or a small glacier advance. Consequently, the ice-front landforms that were deposited during a halt in the retreating Balsfjord glacier could have been deposited due to the presence of rock-avalanche debris on the glacier. However, the effect of rock-avalanches on glacier dynamics has been primarily studied on small alpine glaciers, and therefore, it is difficult to determine whether the presence of rock-avalanche debris on the Balsfjord glacier would significantly reduce ablation. Regardless of whether the halt in the retreat of the glacier was caused by the rock-avalanche or other external factors, the rock-avalanche debris was transported to the front of the glacier and deposited as a mix of glacier ice and rock-avalanche boulders. The ice slowly melted and eventually deposited the rock-avalanche debris on top of the ice-contact delta.

5.1.2 Revised Deglacial History of Balsfjord

Ice front accumulations are deposited during a halt or readvance in the glacier retreat (Hambrey, 1994, Benn and Evans, 1998, Corner, 2006) and therefore, the identification of ice front accumulations within a fjord environment provides information about the glacier retreat chronology. The deglacial history of Balsfjord has been determined by the identification and mapping of subaerial and subaqueous deglacial landforms (Andersen, 1968, Forwick and Vorren, 2002). A summary of the previously published deglaciation history of Balsfjord is give in Section 1.2.3.1, which shows that a

Preboreal moraine has been identified in Balsfjord and radiocarbon dated to 11.4 ± 0.2 ka cal. yr BP (Forwick and Vorren, 2002) and two younger minor end moraines were also deposited into Balsfjord (Figure 8). However, previous authors have not recognised the submarine ice-contact fan and ice-contact delta located above the present-day fan delta at Russenes. Therefore, some authors have interpreted the growth of *Balanus* shells on the rock-avalanche boulders at Russenes to indicate the whole fjord was deglaciated by the time the rock-avalanche was deposited (Forwick and Vorren, 2002, Blikra et al., 2006, Fenton et al., 2011). Consequently, the radiocarbon date obtained from the *balanus* shells have been interpreted to give a minimum age for the deglaciation of Balsfjord at 10.9 ± 0.77 cal. Ka BP (Forwick and Vorren, 2002, Fenton et al., 2011).

However, the identification of the ice-contact delta and rock-avalanche complex and submarine ice-contact fan indicate that there was an additional halt in the retreat of the Balsfjord glacier at the location of the present-day Russenes fjord-side fan delta that was previously undocumented. Additionally, the detailed mapping of the ice-contact delta and rock-avalanche complex indicates that the front-most rock-avalanche boulders were deposited into the fjord as part of the ice-contact delta and the *balanus* shells grew on the boulders following deposition. Therefore, the radiocarbon dated rock-avalanche boulders give a minimum age for the halt in the retreat of the Balsfjord glacier and subsequent deposition of the ice-contact deglacial landforms (10 884 ± 96 cal. yr BP; weighted mean age calculated during this study) rather than a minimum age for the deglaciation of Balsfjord (Forwick and Vorren, 2002).

Recently there has been a lot of interest in the retreat chronology of the marine-terminating outlet glaciers that drained the Fennoscandian Ice Sheet following the Last Glacial Maximum (Winsborrow et al., 2010, Rydningen et al., 2013, Stokes et al., 2014) because the response of these outlet glaciers can be used as an analogue for the present-day retreat of the marine terminating glaciers in Greenland and Antarctica (Dowdeswell et al., 2005, Ó Cofaigh et al., 2005). A study by Stokes et al. (2014) investigates the deglaciation chronology of eight major outlet glaciers within the Fennoscandian Ice Sheet and concludes that fjord topography (e.g. bathymetry and width) exerts an important control on the rate of glacier retreat. The location of the ice-contact deglacial landforms within the study area supports this theory because the fjord narrows and shallows at Russenes, which could be responsible for a halt in the glacier retreat.

However, the minimum age of these deglacial ice-contact landforms is similar to the age of a large moraine deposited in the Lyngen-Storfjord area, which is radiocarbon dated to 10.8 ± 0.2 cal. Ka BP. This moraine was deposited during a climatically induced cooling event, known as the Skibotn event (Corner, 1980, Stokes et al., 2014). Therefore, the ice-contact deglacial landforms at Russenes could have been deposited during the Skibotn event. Some large ice-contact deglacial landforms are also located at Storesteinnes and Stromo-Høgmo in inner Balsfjord. However, these ice-contact landforms are younger than the ice-contact deposits that are located at Russenes (approximately 9190 ± 160 BP; radiocarbon date obtained from shells located immediately in front of the ice-contact delta at Stromo-Høgmo) and therefore, they were not deposited during the Skibotn event.

5.2 Implications of the Origin and Age of the Rock-Avalanche Complex

Mass movement processes in Norway have been widely studied over the last 20 years and remain a very active area of research because they pose a significant threat to Norwegian communities (Blikra, 1998, Forwick and Vorren, 2002, Braathen et al., 2004, Blikra et al., 2006, Sletten et al., 2006, Romstad et al., 2009, Dahl et al., 2010, Sandersen, 2011, Blikra and Christiansen, 2014, Eidsvåg and Øystein, 2016). Studying mass movement deposits can provide critical information about the depositional processes, such as source area, trigger, run-out distance and timing (Blikra et al., 2006). Determining the spatial and temporal pattern of rock-avalanche events is important for evaluating background hazard levels.

The rock-avalanche deposit at Russenes has been studied by a few different researches (Blikra et al., 2006, Sletten et al., 2006, Fenton et al., 2011). These researches have constrained the timing of the rock-avalanche deposit using the radiocarbon dates obtained from the *Balanus* shells that were attached to the rock-avalanche boulders and found that the rock-avalanche was deposited into an open marine environment during the deglacial period or shortly after deglaciation.

However, this study provides the first detailed map of the surficial morphology of the rock-avalanche complex at Russenes and mapping has determined that there were multiple rock-avalanche events that originated in different locations. This new information has implications for the timing of the rock-avalanche events and present-day hazard mapping and modelling in inner Balsfjord. For example, field mapping indicates that the lower section of the rock-avalanche deposit was sourced from outside the catchment area of the rock-avalanche complex and it was partially transported on a glacier. Therefore, identifying the source area of the rock-avalanche could provide important information about the risk of further mass movement processes at this location.

Additionally, the identification of multiple rock-avalanche events at Russenes has implications for the timing of the rock-avalanche events. The radiocarbon dated *Balanus* shells can still constrain the timing of the event by providing a minimum radiocarbon age for the rock-avalanche of 10 884 ± 96 cal. yr BP (σ). However, the recognition of a second rock-avalanche deposit indicates that there was another rock-avalanche event during the deglacial or postglacial period and the timing of this event is unconstrained. Most of the rock-avalanches mapped in Troms county where deposited during the period between 11,000 to 10,5000 cal. yr BP (Blikra et al., 2006), and therefore, it is likely that the upper rock-avalanche event occurred during this period. However, further fieldwork and dating would be useful to constrain the age of the upper rock-avalanche deposit.

5.3 Evolution of the Postglacial Fjord-Side Fan Delta

The postglacial Russenes fjord-side fan delta has prograded into Balsfjord under regressive depositional regime. The fjord-side fan delta has two different depositional environments: (1) a subaerial alluvial fan; and (2) a subaqueous Gilbert-type delta (Section 4.3). These components have developed through aggradational and progradational processes respectively. In both environments sediment transport is dominated by bedload processes during infrequent large flooding events and the relationship between fan delta aggradation and progradation is very dynamic because aggradation of sediment on the alluvial fan reduces sediment supply to the delta front. Therefore, the depositional regime varies between periods of net aggradation on the alluvial fan and periods of fluvial downcutting and sediment deposition at the delta front. The information that has been presented on the morphology and structure of the Russenes fjord-side fan delta will be used to determine the aggradational and progradational history of the fan delta.

5.3.1 Fan Delta Aggradation

5.3.1.1 Streamflow and Sheetflow Processes

The major defining feature of a fan delta is the steep subaerial alluvial fan. This feature separates fan deltas from other types of deltaic environments, such as fjord-head deltas. The postglacial alluvial fan of the Russenes fjord-side fan delta is dominated by streamflow and sheetflow processes and therefore, most of the aggradation on the postglacial alluvial fan has occurred through the deposition of fluvial sediment. Streamflow dominated aggradation occurs by channel infilling and avulsion (Galloway and Hobday, 1996, Field, 2001) and aggradation usually occurs when there is an excess in sediment supply. However, aggradation can also be effected by changes in sea level and climate (Blikra and Nemec, 1998). The alluvial fan on the Russenes fjord-side fan delta is composed of fluvial sediment that is deposited by two separate perennial river systems with adjacent catchment areas (Section 4.3). Therefore, the alluvial fan is composed of sediment that has been deposited by both rivers and this sediment interfingers laterally. The two river systems are subjected to the same sea level and climate regime; however, they have different catchment areas and therefore, the processes occurring within the two perennial river channels may differ depending on their independent supply of sediment.

Field (2001) determined that streamflow dominated alluvial fan aggradation involves five different stages of channel downcutting, backfilling and abandonment and the morphology of the river channels can be used to determine the present-day stage of the channel avulsion processes (Figure 121B). The Buktelva river is characterised by high and steep vertical banks and a wide bankfall area, which indicates that river is in the adjusted channel phase of the channel avulsion processes (Figure 121). Therefore, during flooding erosion occurs along the edges of the river channel and sediment is transported by bedload processes and deposited near the river mouth where the bank height decreases. Figure 123A shows the position of the present-day active depositional lobe at the end of the Buktelva river. However, the Buktelva river also has a large amount of sediment located within river channels and bars (Figure 123), and therefore, it is possible that the river has recently commenced an aggrading phase. Field (2001) suggests that large floods will continue to transport sediment to the active depositional lobe, whilst, small floods will lead to the deposition of sediment within the river channel, which will cause the channel to backfill and channel avulsion will eventually occur.

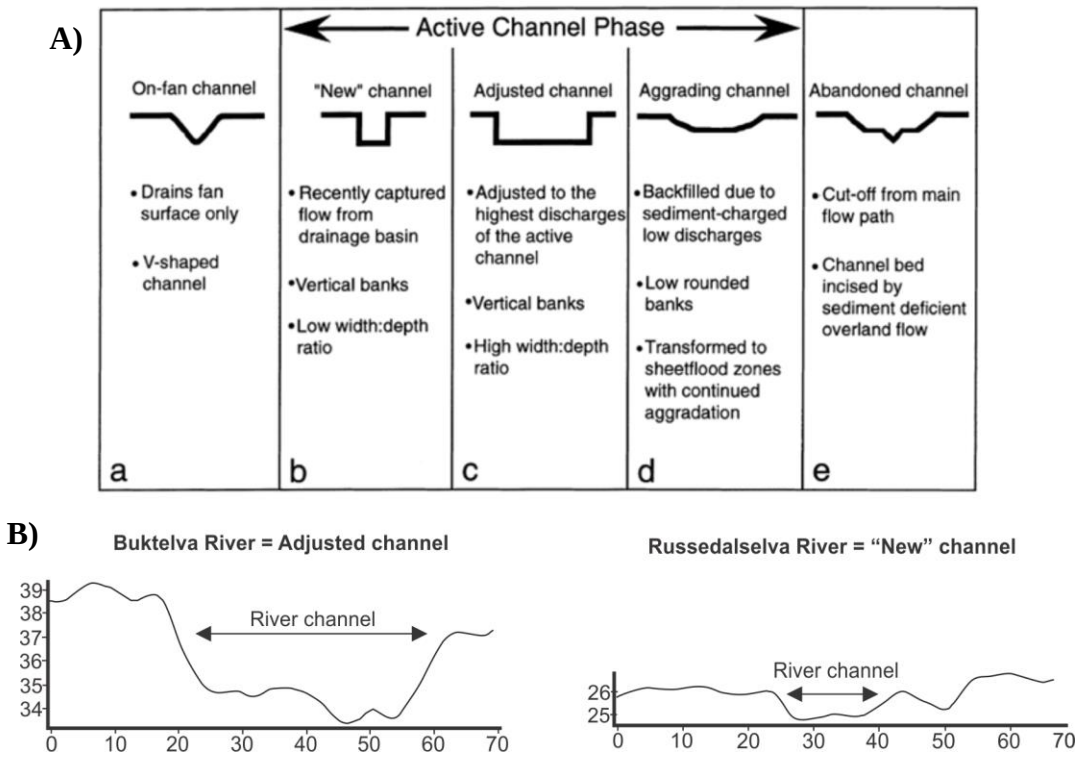

Figure 121: A) Five distinct channel morphologies observed on alluvial fans related to different stages of the channel avulsion processes. Reproduced from Field (2001). B) Channel profiles of the rivers within the Russedalselva alluvial fan. The Buktelva river has an adjusted channel profile and the Russedalselva river has a new channel profile. The profiles have been created using the Lidar-derived DTM avalaible from Statens Kartverk (https://hoydedata.no/LaserInnsyn/) and the location of the profiles is shown in Figure 123.

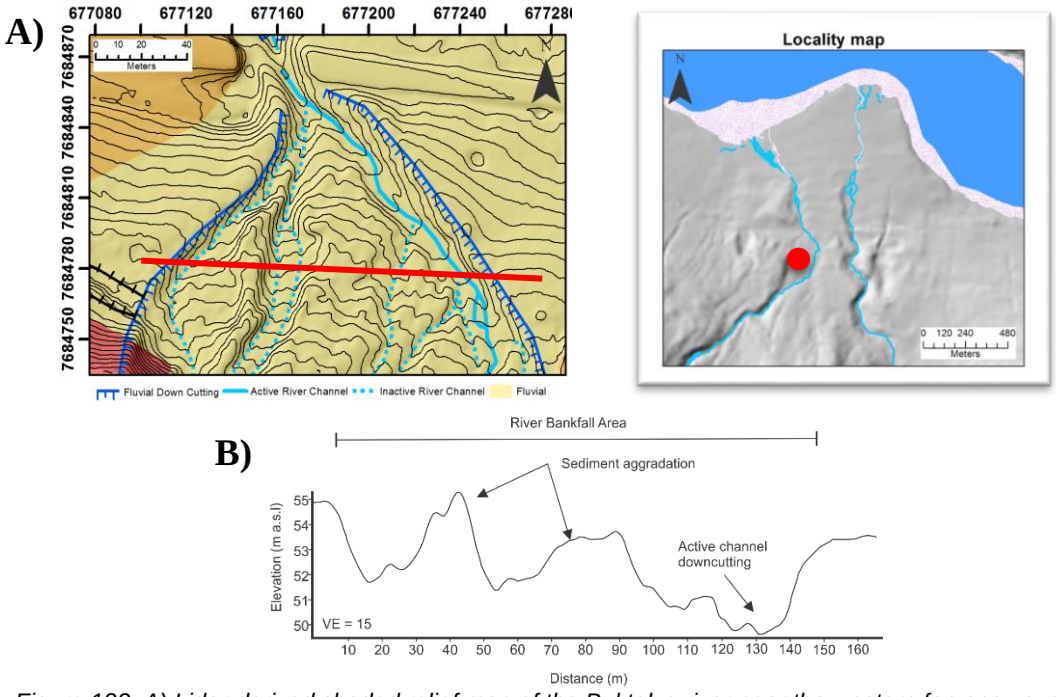

Figure 122: A) Lidar-derived shaded relief map of the Buktelva river near the western fan apex overlaied with the Quaternary Geological Map (sun azurmith = 315° and sun elevation = 45°). The lidar data is avalaible from Statens Kartverk (https://hoydedata.no/LaserInnsyn/). B) Elevation profile across the upper Buktelva river produced using the lidar-derived DTM. The profile shows a lot of sediment has accumulated within the bankfall area of the river. The location of the profile is shown by the red line in A.

The morphology of the Russedalselva river is different to that of the Buktelva river, which primarily reflects differences in the sediment supply and lithology. The upper section of the Russedalselva river is steeply downcutting through existing sediment, however, below the Tapes shoreline the banks of the Russedalselva river are low (<1 m) and vertical. This channel morphology indicates that the lower section of the Russedalselva is in the “new” channel phase of the channel avulsion processes (Figure 121) and therefore, channel avulsion has recently occurred below the Tapes shoreline. As the river bank height is low, this section of the Russedalselva river is also susceptible to sheetflow processes during flooding.

5.3.1.2 History

It is difficult to determine the depositional history of the alluvial fan as many landforms have been destroyed by fluvial erosional and depositional processes. For example, in other fluvial deltaic environments, distinct fluvial and deltaic terraces occur as steps down to the present-day river or sea level respectively, however, fluvial and deltaic terraces are uncommon on the Russenes alluvial fan. The morphology of both present-day rivers within the postglacial alluvial fan indicates that they are primarily downcutting through existing fluvial deltaic sediment. The final section of both rivers is interpreted to be aggradation and consequently two active depositional lobes occur near the head of each river.

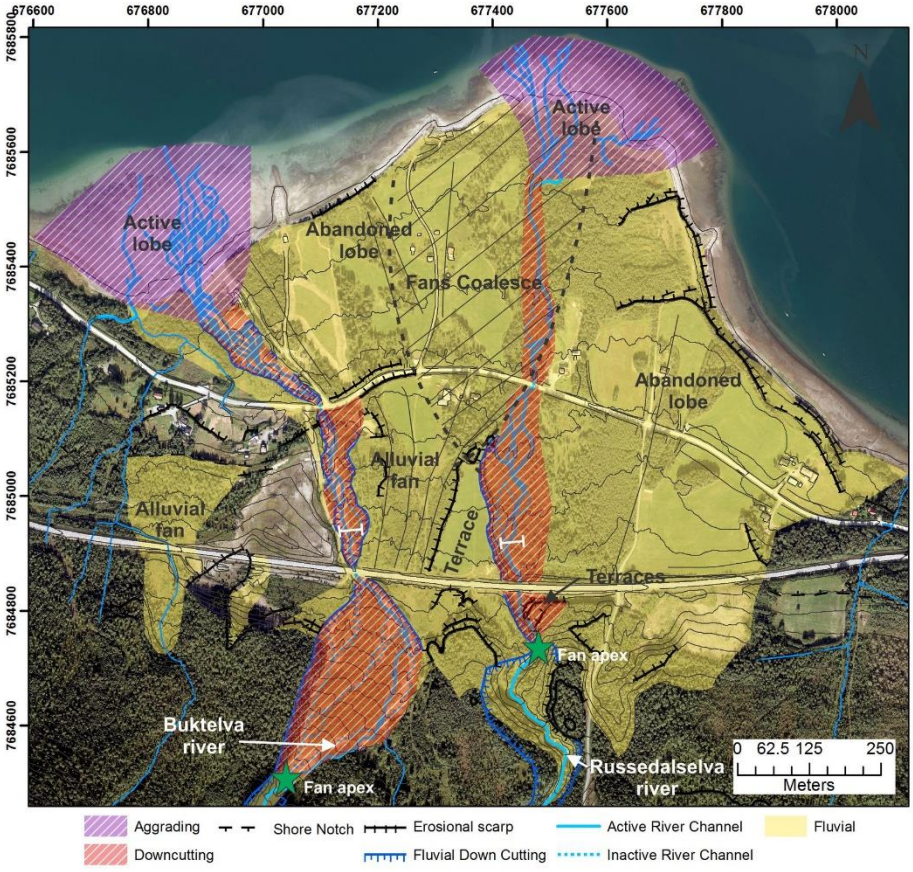

Figure 123: Map showing the morphology of the subaerial alluvial fan of the Russenes fjord-side fan delta. The fan is dominated by fluvial sediment and the areas that are actively downcutting and aggrading are shown. The distribution of the present-day active and abandoned lobes is also indicated. The location of the profiles from Figure 121B is shown by the white lines.

This indicates that the present-day active areas occur at the transition between the subaqueous and subaerial environment and consequently, the fan delta is currently dominated by subaqueous progradation and aggradation of sediment at the front of the alluvial fan where the river channels bifurcate and shallow. Figure 123 shows the present-day distribution of the active and abandoned depositional lobes of the Russenes fjord-side fan delta. The abandoned lobes are raised above the present-day mean sea level and some of the sediment within the abandoned lobes has been eroded by wave and tidal processes, creating erosional scarps at the back of the beach area. The abandoned lobe located on the east side of the fan delta is the oldest.

5.3.2 Fan Delta Progradation

5.3.2.1 Processes

Fan deltas prograd through the deposition of sediment on the subaqueous delta slope (Figure 19) and major delta progradation occurs during large high-magnitude low-frequency events, when coarse sediment (e.g. gravel and sand) is ejected from a flooded river mouth and transported to the delta slope (Prior and Borhold, 1989, Nemec, 1990a, Prior and Borhold, 1990). Sediment can be transported down the delta slope by a number of different processes including debris flows, inertia flows, turbidity currents and hypopycnal plumes. The raised foreset beds observed within the study area are dominated by interbedded sand and gravel and these size fractions are usually transported down the delta slope by debris flows and turbidity currents (Prior and Borhold, 1990). The multibeam bathymetry data collected over the present-day delta slope does not show evidence of slides, slumps or channels and therefore, unconfined debris flows are the dominant sediment transport mechanism on the present-day delta slope (Prior and Borhold, 1990, Hansen et al., 2016). The raised delta forest beds documented within the study area confirm that unconfined that debris flows dominate sediment transport (Section 4.3.3), however, they also indicate that other modes of sediment transport have occurred, such as sliding and turbidity flows. For example, the channel feature observed in GPR profile Russ7 (Figure 118) was probably created by turbidity currents. Turbidity currents are often a common method for sediment transport on the fan delta slope because high-energy hyperpycnal flows ejected from the river mouths during floods can reach the slope and subsequently transform into turbidity currents due to the relatively narrow intertidal delta platform region (100 to 200 m wide) (Prior and Borhold, 1989, Blikra and Nemec, 1998).

5.3.2.2 History

As a delta progrades under a regressive sea level regime old delta terraces are raised above the present-day mean sea level with the highest delta terraces corresponding to the oldest position of the delta front (Eilertsen et al., 2006). Therefore, it is possible to determine the progradational history of a delta through the radiocarbon dating of deltaic sediment and correlation of the deltaic terraces to sea level curves (Corner et al., 1990, Eilertsen et al., 2006). Unfortunately, the delta terraces within the Russenes fjord-side fan delta are not well defined and many of the terraces have been destroyed by the fluvial aggradation or erosion. Table 11 presents a summary of the radiocarbon dates that are available for the study area. Only two sediment packages have been radiocarbon dated: (1) radiocarbon dates have been obtained from the rock-avalanche boulders located on a paleo-deltaic slope (10 884 ± 96 cal. yr BP; Section 4.2.4); and (2) radiocarbon dates have been obtained from bottomset sediment (10,345 ± 84 cal. yr BP; Section 4.3.3.3.1). Nonetheless, the progradation history of the Russenes fjord-side fan delta has been reconstructed

based on these radiocarbon dates and correlation of a few identified deltaic terraces with the shoreline emergence curve shown in Figure 10.

Table 11: Summary of the radiocarbon dates that are avaliable for the study area. Calibration has been done using the INTCAL13 program and the MARINE13 database.

Lab number	Dated material	Location	Conventional Age (^{14}C BP)	Calibrated age (yr BP; 2σ)	Weighted mean calendar age (± 1σ) (cal. yr BP)*	Reference
T-13805	*Mya truncata*	Rock-avalanche boulder	9995 ± 75	10 674 – 11 108	10 884 ± 96	(Forwick and Vorren, 2002)
T-13806	*Balanus sp.*	Rock-avalanche boulder	10 050 ± 80	10 719 – 11 155		(Forwick and Vorren, 2002)
T-13807	*Balanus sp.*	Rock-avalanche boulder	10 055 ± 70	10 738 – 11 148		(Forwick and Vorren, 2002)
Beta - 463116	*Balanus sp.*	Rock-avalanche boulder	9930 ± 30	10 664 – 10 974		This study
Beta - 463114	*Macoma Calcarea*	Bottomset sediment	9570 ± 30	10 234 – 10 472	10 345 ± 84	This study
Beta - 463115	*Mya Truncata*	Bottomset sediment	9550 ± 30	10 218 – 10 455		This study

**Weighted mean calculated using inverse variance weighting*

The progradation history of the Russenes fjord-side fan delta is shown in Figure 124 and the rate of fan delta progradation corresponds well with changes in the rate of sea level fall. Delta progradation was initially very rapid in the early parts of the Holocene (0.26 m/year) when the rate of sea level fall was the greatest and there was a large supply of glaciofluvial and fluvial sediment. This initial rapid rate of delta progradation is well constrained by the two sediment packages that have been radiocarbon dated (Table 11). During the early part of the Holocene the morphology of the delta slope was different to the present-day delta with heights of 30 m and 12 m respectively (Figure 124). This indicates that there was a larger subaqueous accommodation space at the start of the Holocene.

The rate of delta progradation was the lowest between 10,200 cal. BP and approximately 5,100 cal. BP (0.02 to 0.09 m/year), which corresponds to the period known as the Tapes transgression, whereby sea level fall ceased in the inner fjord areas and sea level rose in the outer fjord areas (Figure 10). Following the Tapes transgression sea level started to fall again but at a slower rate than during the early Holocene and delta progradation continued at a rate of 0.17 to 0.1 m/year. These progradation rates correspond well with changes in relative sea level. However, this correlation could be effected by one of the methods used to determine the progradation rates, which correlates the deltaic terraces with the local sea level emergence curve. Therefore, the relationship between delta progradation and relative sea level could be better constrained by further radiocarbon dating of deltaic sediment.

The reconstruction of delta progradation rates indicates that there were two different styles of delta progradation during the evolution of the Russenes fjord-side fan delta (Figure 125). The initial progradation style is similar to conventional river deltas whereby sea level regression caused new delta terraces to form at lower elevations, which resulted in delta progradation. The second style of delta progradation occurred after the Tapes transgression and was characterised by extensive forward progradation of the fjord-side fan delta into the fjord (Figure 125B) and simultaneous subaerial aggradation.

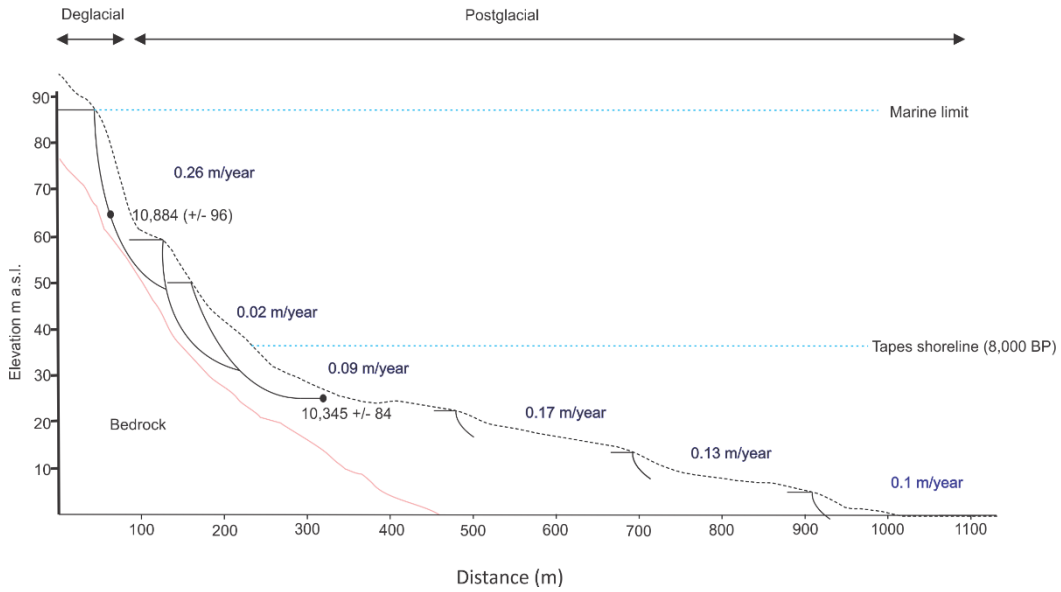

Figure 124: Reconstruction of fan delta progradation based on radiocarbon dated foreset and bottomset sediment, and the reconstruction of delta rim positions from deltaic terraces and foreset beds. The delta terraces have been correlated with the shoreline emergence curve (Figure 10) and subsequently, the delta progradation rates have been calculated.

The initial rapid progradation rate of the Russenes fjord-side fan delta is very similar to the early response of fjord-head deltas in northern Norway, which also underwent rapid progradation at the start of the Holocene (Eilertsen et al., 2006). Initial rapid progradation can be attributed to the rapid sea level fall and a large sediment supply of glaciofluvial and fluvial sand and gravel created rapid river incision (Eilertsen et al., 2006). Additionally, basin morphology has also had a major control on the progradation rates of many fjord-head deltas with shallow water promoting rapid progradation (Corner et al., 1990, Corner, 2006, Eilertsen et al., 2006). Therefore, it is possible that the change in delta progradation style could have been caused by a decrease in accommodation space created by a shallowing basin morphology.

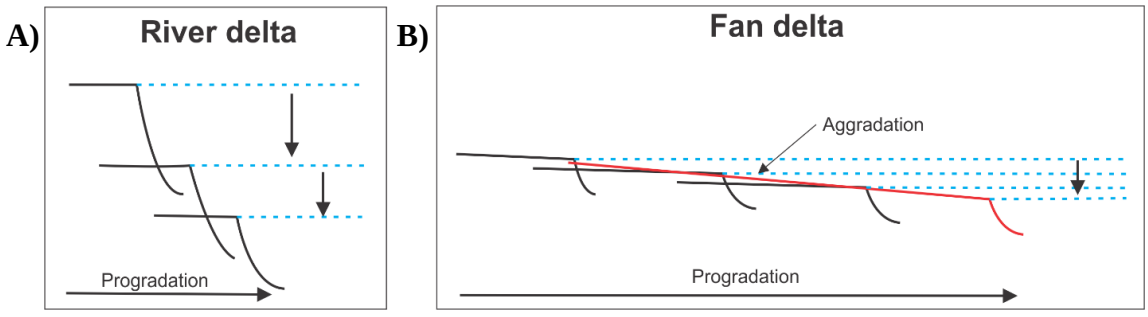

Figure 125: Schematic diagram showing the different styles of delta progradation that have occured during the evolution of the Russenes fjord-side fan delta. A) The initial style of delta progradation was similar to conventional river deltas that form under a regressive sea level regime. B) The second style of delta progradation resulted in extensive progradation of the fan delta into Balsfjord. This extensive progradation was accompanied by subaerial aggradation.

5.3.3 Russenes Fjord-Side Fan Delta Depositional Model

5.3.3.1 Initial Valley-Side Delta Progradation (before 8, 000 cal. Yr BP)

Following the retreat of the Balsfjord glacier, valley-side river deltas were formed where the Buktelva and Russedalselva rivers entered the sea. These deltas were initially fed by glaciofluvial sediment and meltwater from the valley glaciers. Delta progradation continued after the valley glaciers retreated into the mountain cirques through the deposition of fluvial sediment. Figure 126 shows a schematic model of the first stage of delta progradation at Russenes. Sea level fall was initially very rapid following deglaciation and there was a reasonably large accommodation space within the fjord. Therefore, the style of valley-side delta progradation was similar to common river deltas during this period and deltaic terraces were built out to contemporaneous sea level as the sea level continually fell. Most of these deltaic terraces were later destroyed by fluvial, wave and tidal processes.

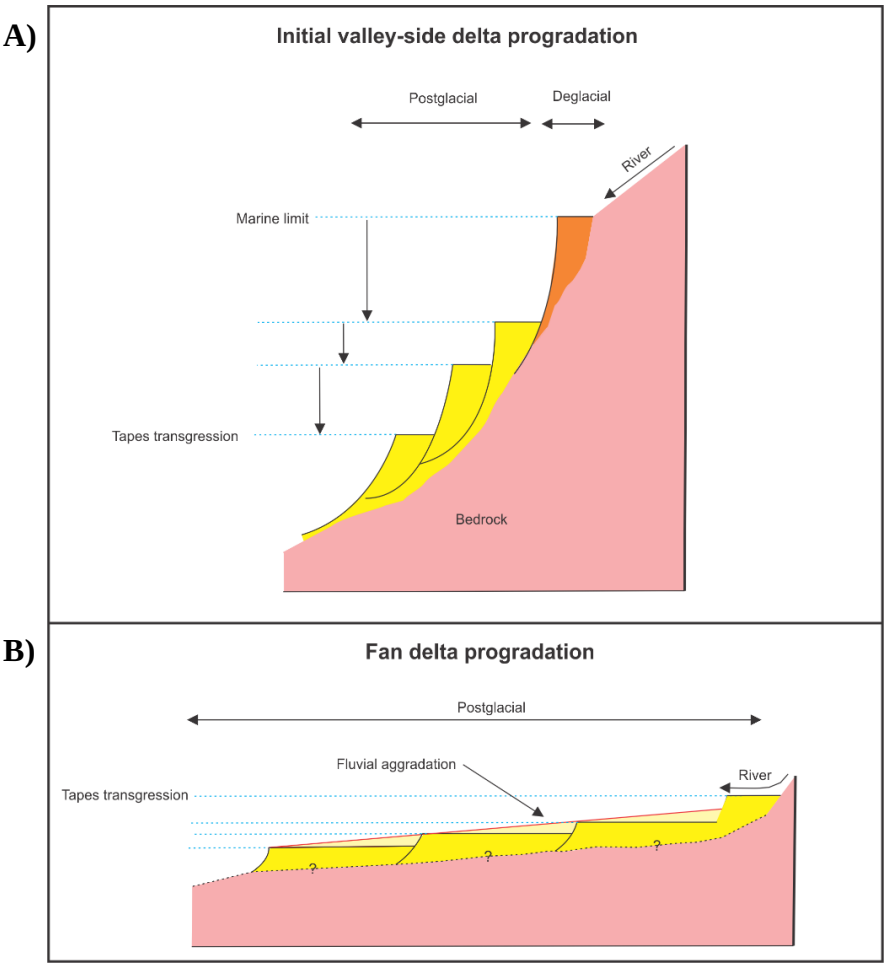

Figure 126: Schematic model of the two different stages of delta progradation under a regressive sea level regime. A) Model of the initial valley-side delta progradation style, which occured under a rapidly falling sea level B) Model of the progradation of the fjord-side fan delta after the Tapes transgression. Delta progradation was accompanied by fluvial aggradation forming a subaerial alluvial fan.

5.3.3.2 Progradation of the Fjord-Side Fan Delta (after 8,000 cal. Yr BP)

The style of delta progradation changed after the Tapes transgression to form a fjord-side fan delta. During fan delta progradation the position of the delta rim prograded a long way into the fjord compared with the rate of sea level fall. Therefore, the deltaic terraces that formed during progradation had long horizontal surfaces (Figure 125). This change in delta progradation style was accompanied by aggradation of the subaerial component of the delta, producing an alluvial fan. The extensive forward progradation of the fan delta into the fjord could have created shallow river gradients and resulted in the subaerial aggradation of fluvial material to restore river equilibrium. This second style of delta progradation created a true fjord-side fan delta.

5.4 Reflections on the Factors Controlling Fan Delta Deposition

5.4.1 Is Russenes a true fan delta?

Fan deltas were first recognised as distinct sedimentary systems by Holmes (1965) and defined as an alluvial fan that progrades into a standing body of water from an adjacent highland. However, during the 1980s and 1990s the definition of the term “fan delta” was very controversial and there were many attempts at modifying or improving the fan delta concept (McPherson et al., 1987, McPherson et al., 1988, Nemec and Steel, 1988, Nemec, 1990b). In the original definition, a fan delta is defined by the alluvial fan feeder system (Holmes, 1965). Consequently, the definition is directly related to the definition of an alluvial fan (Nemec and Steel, 1988).

Both the terms “fan” and “delta” are derived from geometric shapes; however, using geometric shapes to define fan deltas is not effective since the morphology of both alluvial fans or deltas does not necessarily fit into this geometric definition. For example, the morphology may be confined by topographic features (Nemec and Steel, 1988). Conversely, there are also many fan-shaped common river deltas that have been miss-identified as fan deltas because they are fan-shaped. Some researchers have applied the term fan delta to any coarse-grained bedload-dominated river delta, which has been formed by the progradation of braided alluvial plain systems into a standing body of water (McPherson et al., 1988). These types of deltas have also been incorrectly identified as they do not have an alluvial fan feeder system and therefore, they should be classified as braidplain deltas instead (McPherson et al., 1987, McPherson et al., 1988, Nemec and Steel, 1988).

McPherson et al. (1988) and McPherson et al. (1987) also argue that streamflow dominated alluvial fan deltas should be classified as braid deltas because their sedimentary characteristics are similar to a braided alluvial plains. Therefore, according to this definition, the Russenes fjord-side fan delta, which contains a streamflow-dominated alluvial fan with two perennial river systems, should be classified as a braidplain delta. However, Nemec and Steel (1988) disagree with this definition and argue that the term fan delta should apply to all types of alluvial fans regardless of grainsize, size, tectonic regime or depositional process (streamflow- or massflow-dominated).

A three-dimensional view of the subaqueous and subaerial components of the Russenes fjord-side fan delta is shown in Figure 127 and it demonstrates that the morphology of the delta fits well with the original definition of a fan delta because it consists of a 1 km wide, steep, streamflow-dominated alluvial fan that is prograding directly into Balsfjord beneath tall mountains. The fan shape is slightly

restricted on the western side due to the presence of the rock-avalanche and ice-contact fan deposits. Therefore, we conclude that the delta at Russenes is a true fjord-side fan delta.

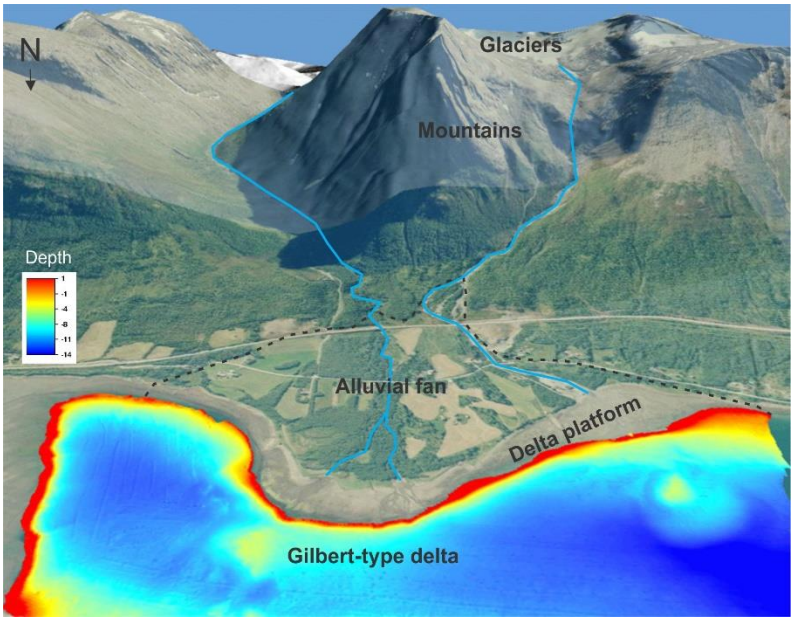

Figure 127: 3D oblique aerial view of the Russenes fjord-side fan delta showing the the delta contains the distinctive geomorphological elements of a fan delta. The image has been produced in ArcGlobe using the following datasets: 10 m DTM (avaliable at www.data.kartverket.no), aerial photographs Midt_Troms_2013 and TROMS_2006 (Table 1) and multibeam bathymetry (0.5 m resolution) (Corner and Eilertsen, 2013). Bathymetry map datum = lowest astronomical tide.

5.4.2 Other Examples of Holocene Fan Deltas

This study describes a postglacial fjord-side fan delta in Troms county, northern Norway. Investigation of the coastline of Troms county indicates that fjord-side deltas are common landforms, however, most of these deltas are common coarse-grained river deltas rather than fan deltas (G. Corner, per. Comm., 2017). For example, Figure 128C shows a small fjord-side fan-shaped delta with a glacier meltwater source in Lyngenfjord, however, the feeder system of this delta is a braided alluvial plain rather than an alluvial fan. Fan-shaped river deltas in Storfjord have been previously identified as cobbly, gravelly fan deltas (Corner, 1977). However, they are not true fan deltas because they do not have a subaerial alluvial fan (G. Corner, pers. comm., 2017). This raises some very important questions, such as: What are the favourable conditions for fan delta progradation? And what is the difference between the location of the Russenes fjord-side fan delta and other fjord-side river deltas in northern Norway?

A few deglacial and postglacial fjord-side fan deltas have been described at other locations across Norway, such as Svalbard, Finnmark and western Norway. However, not all of these deltas can be considered true fan deltas according to the definition of Holmes (1965). For example, a deglacial glaciofluvial, fjord-side fan delta has been described in Varangerfjord in Finnmark, northern Norway by Postma and Cruickshank (1988). This fjord-side delta consists of steeply dipping delta foreset beds overlaid by a topset unit composed of beach sediment. However, an alluvial fan does not occur above the deltaic sediment and therefore, this fjord-side delta cannot be considered a true fan delta.

The physiographic setting of western Norway is similar to that of Troms county because steep mountains rise directly from the fjords. Consequently, mass movement processes have resulted in the redistributed of a lot of sediment in western Norway and some of this sediment has been deposited as debris-flow dominated colluvial and alluvial fans and fan deltas (Blikra and Longva, 1995, Blikra and Nemec, 1998). For example, an array of debrisflow-dominated colluvial fan deltas are located along the western margin of Tomrefjord, in western Norway (Blikra and Longva, 1995, Blikra and Nemec, 1998) and several small alluvial and colluvial fan deltas have been deposited around Lovatnet lake, in western Norway (Hansen et al., 2016). These deglacial and postglacial fan deltas have a similar morphology to the Russenes fjord-side fan delta. For example, the alluvial or colluvial fans have a slope of 15 to 20° and display one main active channel. The present-day delta shoreline is located close to the delta slope (i.e. the intertidal region is narrow) and the delta slope is between 20 and 35° (Hansen et al., 2016). Therefore, the morphology of the fan deltas surrounding the Lovatnet lake indicate that the depositional processes are similar to the depositional processes of the Russenes fjord-side fan delta.

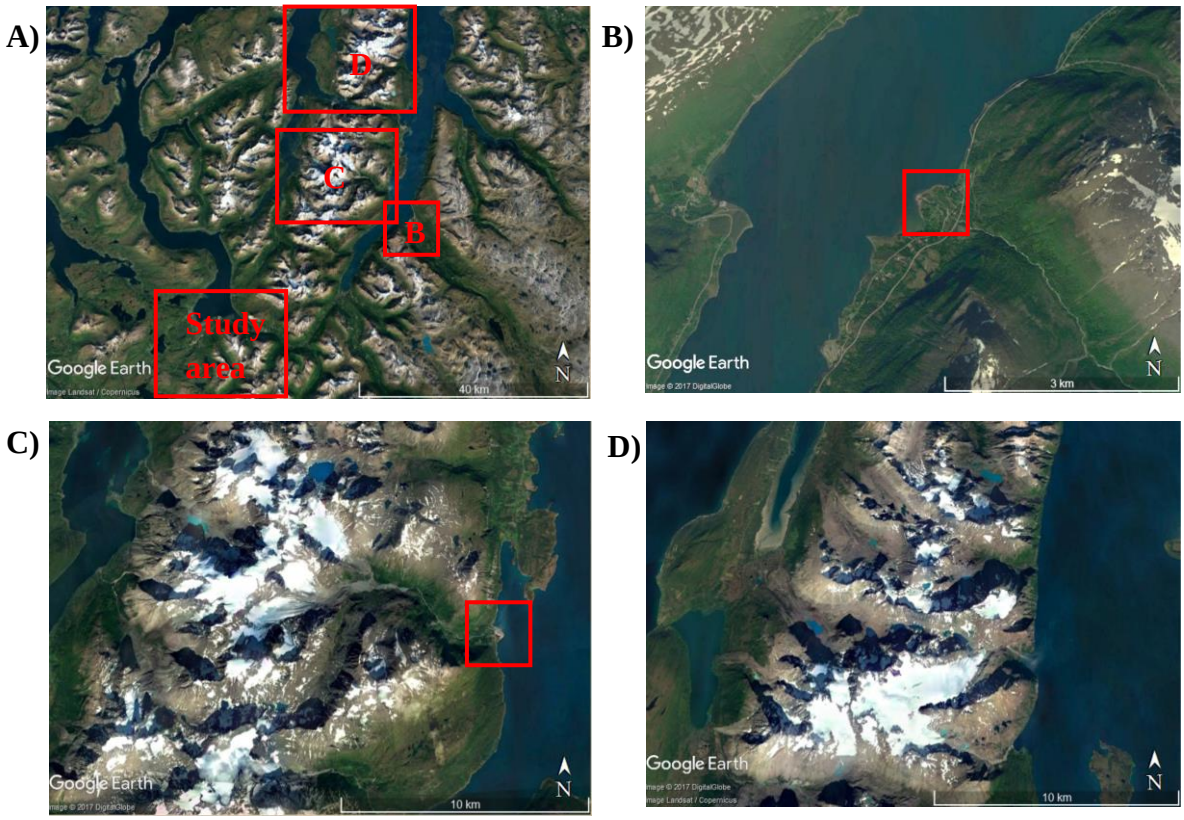

Figure 128: A) Aerial photograph showing a large section of Troms county. The locations of photographs B, C and D are shown. B) Aerial photograph of a small fjord-side fan delta at Elsnes in Storfjord. C) Aerial photograph of the southern Lyngen alps. This area contains many cirque glaciers and a fan-shaped braided delta is shown within the red box. D) Aerial photograph of the northern Lyngen alps. No fjord-side deltas exist. All aerial photographs are from Google Earth™.

5.4.3 Comparison with Fjord-Head Deltas

While fjord-side fan deltas are rare in northern Norway, fjord-head deltas are very common and have been widely studied. The Russenes fjord-side fan delta has many similarities with fjord-head deltas in Norway (Corner et al., 1990, Corner, 1998, Eilertsen et al., 2006, Eilertsen et al., 2011). For example, the delta rim, delta slope and prodelta morphogenic elements of the Russenes fjord-side fan delta are similar to the modern morphology of fjord-head deltas (Figure 129) (Corner et al., 1990, Corner,

1998, Eilertsen et al., 2011). Both types of deltas have a steep slope with a concave profile that decreases from 40 to 35° at the top of the slope to 3 or 4° at the bottom. This steep delta slope causes both types of deltas to have a Glilbert-type tripartite structure composed of topset, foreset and bottomset beds and therefore, the same types of subaqueous depositional processes occur within both deltas (Corner et al., 1990, Corner, 1998, Eilertsen et al., 2006, Eilertsen et al., 2011).

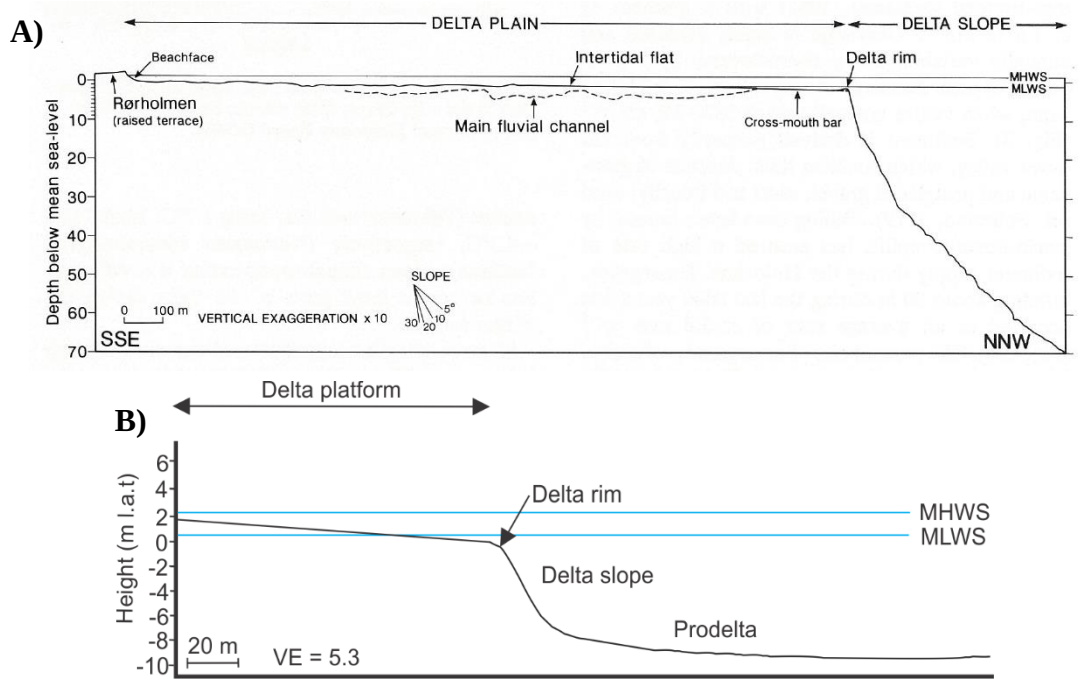

Figure 129: Profiles across (A) the Alta delta and (B) the Russenes fjord-side fan delta, which allow the morphology of the subaqueous components of the deltas to be compared. Mean high and low water spring tide levels (MHWS and MLWS) are indicated on both profiles. The diagrams have different vertical exaggerations. (A) is reproduced from Corner et al. (1990).

The main difference between a fjord-side fan delta and a fjord-head delta is the subaerial component of the deltas. Fjord-side fan deltas contain a steeply dipping subaerial alluvial fan, whilst fjord-head deltas contain a subaerial flatly lying alluvial plain. Additionally, the intertidal region of fjord-head deltas in northern Norway is an order of magnitude wider than the intertidal region of the Russenes fjord-side fan delta, which are 1.8 km and 200 m respectively.

The progradational history of the Russenes fjord-side fan delta is also similar the history of many fjord-head deltas in northern Norway, such as the fjord-head deltas located at Målselv and Alta (Corner et al., 1990, Eilertsen et al., 2006, Eilertsen et al., 2011). For example, falling sea level created by glacio-isostatic uplift has supplied a high rate of sediment to the deltas during the Holocene. During the deglacial phase the progradation rate of both types of deltas was very high due to an abundant supply of sediment created by a high rate of glacio-isostatic uplift that caused extensive fluvial incision. Both types of deltas experienced lower rates of sediment supply and subsequent delta progradation during the postglacial period because the rate of sea level fall and fluvial incision decreased (Corner et al., 1990, Corner, 2006, Eilertsen et al., 2006, Eilertsen et al., 2011). However, the progradation rate of fjord-head deltas is two orders of magnitude higher than the progradation rate for the Russenes fjord-side delta. For example, the maximum progradation rate of the Målselv fjord-head delta is 44 m/year (Eilertsen et al., 2006) whilst with the maximum rate at Russenes is just 0.26 m/year. The difference in the magnitude of delta progradation can be attributed to differences in the delta catchment size.

5.4.4 Sea level, climate and sediment supply

It has been determined that the Russenes fjord-side fan delta is an unusual prograding coastal landform in Troms county because fjord-side fan deltas are uncommon. Deltas prograde in response to changes in sea level, climate and sediment supply, and therefore, these factors will be investigated to determine why the Russenes fjord-side fan delta has prograded into inner Balsfjord during the Holocene.

5.4.4.1 Sea level fall

Sea level has fallen during the progradation of the postglacial fjord-side fan delta due to glacio-isostatic uplift. Sea level fall has resulted in fluvial incision to restore channel equilibrium and this process has had a large effect on the progradation rate of the Russenes fjord-side fan delta (Section 5.3.2). The rate of sea level fall varies between the inner and outer fjord areas (Section 1.2.3.2), with the largest rate of sea level fall occurring in the inner fjord areas. Therefore, it is more likely that fjord-side fan deltas will be deposited in the inner fjord areas due to higher rates of fluvial incision.

5.4.4.2 Climate

The progradation of the Russenes fjord-side fan-delta could be related to the presence of the three cirque glaciers located within the catchment area because they have provided the fan delta with a source of water and sediment throughout the Holocene (Figure 2). Studies of the nearby cirque glaciers located in the Lyngen Alps show that they fluctuated during the Holocene and there was a period where the glaciers disappeared entirely in the mid-Holocene due to a warming known as the Holocene Thermal Optimum (Ballantyne, 1990, Bakke et al., 2005). The only Holocene cirque glacier moraines that have been identified above the study area are the Little Ice Age moraines, which show that the glaciers have retreated by approximately 600 m since the Little Ice Age.

The effect that these glaciers had on fan delta progradation is examined through considering the primary methods of sediment transport and deposition within the fan delta. For example, there is a fjord-side fan delta located in Adventfjord, Svalbard, which was also located beneath tall mountains that hosted a cirque glacier during the early Holocene (Lønne and Nemec, 2004). It has been determined that progradation of the fan delta was directly related to the supply of seasonal meltwater and sediment from the cirque glacier because fan delta progradation ceased when the cirque glacier disappeared (Lønne and Nemec, 2004). However, the climate of Svalbard is very different to that of Troms county and consequently, the processes resulting to fan delta progradation are different. For example, rainfall is sparse in Svalbard and most of the flowing water is produced by meltwater during the summer months. Therefore, sediment transport within the fan delta in Adventfjord, Svalbard, occurred through meltwater induced alluvial and colluvial processes and the cirque glacier exerted a large control on fan delta progradation.

However, the maritime sub-arctic climate of Troms county is a very different to the polar climate of Svalbard and the morphology of the present-day Russenes alluvial fan indicates that most of the sediment transport occurs during periods of flooding induced by intense rainfall (Section 4.1). It follows that although the cirque glaciers within the study area have provided the fjord-side fan delta with a large sediment supply, episodic floods have been the primary control on fan delta development. This conclusion is supported by an investigation into the effects of glacier variations on a Late Holocene alluvial fan in southern Norway by McEwen et al. (2011), which found that although

glacier variation was a major control on sediment supply, episodic floods were the primary control on alluvial fan development.

5.4.4.3 Geographical location

The inner fjord location of the Russenes fjord-side fan delta in Balsfjord has had a large effect of fan delta progradation. The present-day fjord-side fan delta is located 500 m from the fjord-head delta at Nordkjosbotn and consequently, the fjord is extremely shallow in this location with a maximum depth of 14 m. Therefore, there is a restricted accommodation space within the fjord, which has caused extensive progradation of the fan delta during the Holocene (Section 5.3). The inner fjord location of the Russenes fjord-side fan delta also provides a sheltered subaqueous depositional environment with low wave energy. This is confirmed by the formation of sea ice surrounding the delta during winter because sea ice only forms in the sheltered parts of the fjords in Troms county. This sheltered inner fjord environment causes the fan delta to be dominated by fluvial processes rather than wave and tidal processes.

5.4.4.4 Summary

The Russenes fjord-side fan delta has received a large sediment supply during the Holocene due to three factors: (1) rapid fluvial incision created by a falling relative sea level; (2) the presence of three small cirque glaciers within the catchment area; and (3) sediment supply from two different river catchments. The Russenes fjord-side fan delta also has a favourable climate for sediment transport because the fan delta has been subjected to infrequent intense rainfall events during the Holocene allowing for sediment transport by bedload processes. However, a lot of the fjord areas in Troms county were subjected to the same climate regime and sediment supply processes during the Holocene. Therefore, the main control on the progradation of the Russenes fjord-side fan delta compared with other fjord-side deltas in Troms county is the geographical location of the fan delta. The sheltered and shallow inner fjord setting in Balsfjord has resulted in the extensive forward progradation of the Russenes fjord-side fan delta, which has been accompanied by alluvial fan aggradation.

6 Conclusions

A Quaternary Geological Map of the postglacial Russenes fjord-side fan delta and associated deglacial landforms has been produced during this study. Detailed mapping of the deglacial landforms has uncovered two previously undocumented deglacial ice-contact deposits located above the present-day fan delta: (1) a submarine ice-contact fan; and (2) an ice-contact delta and rock-avalanche complex. These landforms were deposited simultaneously during a halt in retreat of the Balsfjord glacier at Russenes. The minimum age of the ice-contact landforms is 10 884 ± 96 cal. yr BP (1σ), which has been determined from radiocarbon dating of *Balanus* shells attached to rock-avalanche boulders within the ice-contact delta and rock-avalanche complex.

Detailed mapping of a distinctive rock-avalanche complex located above the postglacial fjord-side fan delta indicates that it has been deposited by at least two different rock-avalanche events. The biotite garnet gneiss boulders that are located at the bottom of the rock-avalanche complex have been sourced from outside the catchment area and were transported on the Balsfjord glacier. These rock-avalanche boulders were subsequently deposited as part of the ice-contact glaciofluvial delta. The gabbro and metagabbro boulders identified in the upper section of the rock-avalanche complex were deposited by a separate rock-avalanche event that originated in the mountains directly above the deposit. The timing of this event is unconstrained.

Investigation of the present-day morphology of the postglacial Russenes fjord-side fan delta indicates that there are two distinctive depositional environments: (1) a subaerial alluvial fan; and (2) a subaqueous Gilbert-type delta. The steep present-day subaerial alluvial fan contains two perennial river channels that both have a braided character. Aggradation of the alluvial fan occurs by channel backfilling and avulsion. However, both rivers are currently predominantly downcutting through the alluvial fan and aggradation is restricted to two small active lobes at the river mouths. The present-day subaqueous delta has three major environments: (1) a flatly lying intertidal delta platform; (2) steeply dipping subaqueous delta slope (40 to 20°); and (3) deep, subaqueous, gently dipping prodelta region. Sediment transport on the delta slope is dominated by cohesionless debris flows.

Investigation of the subsurface structure the Russenes fjord-side fan delta shows that it has Gilbert-type structure that is composed of three main elements: (1) bottomset sediment composed of massive and laminated silt and fine sand; (2) foreset sediment composed of steeply dipping beds of sand- and gravel-dominated sediment (35 - 20°); and (3) topset sediment that erosively overlies the foreset unit and is dominated by massive cobbly gravel.

The progradation rate of the postglacial Russenes fjord-side fan delta corresponds with the rate of sea level fall and three different rates of delta progradation were observed: (1) fan delta progradation was initially very rapid in the early Holocene (0.26 m/year); (2) delta progradation was the slowest during the Tapes transgression; and (3) during the late Holocene the rate of delta progradation was between 0.1 and 0.17 m/year. Additionally, the morphology of the postglacial fan delta indicates that there were two different styles of delta progradation: (1) an initial valley-side delta progradation stage; and (2) a fan delta progradation stage following the Tapes transgression.

Three factors have affected the development of the Russenes fjord-side fan delta are: (1) abundant sediment supply from the catchment area; (2) a favourable climate for periodic high-energy flooding; and (3) a shallow accommodation space. However, the main control on the formation of a fjord-side fan delta at Russenes is the sheltered and shallow inner fjord depositional setting that has promoted extensive delta progradation after the Tapes transgression.

7 References

ALM, T. 1993. Øvre Æråsvatnet - palynostratigraphy of a 22,000 to 10,000 BP lacustrine record on Andøya, northern Norway. *Boreas,* 22**,** 177-188.

ANDERSEN, B. G. 1968. Glacial geology of western Troms, North Norway. *Norges Geologiske undersøkelse nør,* 256.

ANDERSEN, B. G. 1980. The deglaciation of Norway after 10 000 BP. *Boreas,* 9**,** 211-216.

ANDERSEN, B. G. 1988. Caledonian terranes of northern Norway and their characterisitics. *Trabajos De Geologia,* 17**,** 103-117.

ANDERSEN, B. G., MANGERUD, J., SØRENSEN, R., REITE, A., SVEIAN, H., THORESEN, M. & BERGSTRÖM, B. 1995. Younger Dryas ice-marginal deposits in Norway. *Quaternary International,* 28**,** 147-169.

ANDERSON, R. S. & ANDERSON, S. P. 2010. *Geomorphology. The mechanics and chemistry of landscapes,* United Kingdom, Cambridge University Press.

ANDREASSEN, L. M., WINSVOLD, S. H., PAUL, F. & HAUSBERG, J. E. 2012. Inventory of Norwegian Glaciers. Norwegian Water Resources and Energy Directorate.

ANNAN, A. P. 2009. Electromagnetic principles of ground penetrating radar. *In:* HARRY, M. (ed.) *Ground Penetrating Radar Theory and Applications.* The Neatherlands: Elsevier, Ltd.

BAKKE, J., DAHL, S. O., PAASCHE, Ø., LØVLIE, R. & NESJE, A. 2005. Glacier fluctuations, equilibrium-line altitudes and palaeoclimate in Lyngen, northern Norway, during the Lateglacial and Holocene. *The Holocene,* 15**,** 518-540.

BAKKE, J., DAHL, S. O., PAASCHE, Ø., SIMONSEN, J. R., BJØRN, K., BAKKE, K. & NESJE, A. 2010. A complete record of Holocene glacier variability at Austre Okstindbreen, northern Norway: an integrated approach. *Quaternary Science Reviews,* 29**,** 1246-1262.

BALLANTYNE, C. K. 1990. The Holocene glacial history of Lyngshalvöya, northern Norway: chronology and climatic implications. *Boreas,* 19**,** 93-117.

BALLANTYNE, C. K. 2007. Paraglacial geomorphology. *In:* ELIAS, S. A. (ed.) *Encyclopedia of Quaternary Science.* Elsevier Ltd.

BENN, D. I. & EVANS, D. J. A. 1998. *Glaciers and glaciation,* Great Britian, Hoddler Headline Group.

BERGH, S. G. & ANDRESEN, A. 1985. Tectonometamorphic evolution of the Allochthonous Caledonian Rocks between Malangen and Balsfjord, Troms, North Norway. *Geologiske Undersøkelse Bulletin,* 401**,** 1-34.

BHATTACHARYA, J. P. 2010. Deltas. *In:* JAMES, N. P. & DALRYMPLE, R. W. (eds.) *Facies models 4.* Newfoundland, Canada: Geological Association of Canada.

BJUNE, A. E., BIRKS, H. J. B. & SEPPÄ, H. 2004. Holocene vegetation and climate history on a continental-oceanic transect in nothern Fennoscandia based on pollen and plant macrofossils. *Boreas,* 33**,** 211-223.

BLAIR, T. C. & MCPHERSON, J. G. 2009. Processes and Forms of Alluvial Fans. *In:* PARSONS, A. J. & ABRAHAMS, A. D. (eds.) *Geomorphology of Desert Environments, 2nd ed.*: Springer Science + Business Media.

BLIKRA, L. H. 1998. Rock avalanches, gravidational faulting and its potential palaeoseismic cause. *In:* DEHLS, J. & OLESEN, O. (eds.) *Neotectonics in Norway, Annual Technical Report 1998.* Trondheim Geological Survey of Norway.

BLIKRA, L. H., ANDA, E., DEHLS, J. & STALSBERG, K. 2006. Rock slope failures in Norwegian fjord areas: Examples, spatial distribution and temporal pattern. *In:* EVANS, S. G., MUGNOZZA, G. S., STROM, A. & HERMANNS, R. L. (eds.) *Landslides from Massive Rock Slope Faliures.* The Neatherlands: Springer.

BLIKRA, L. H. & CHRISTIANSEN, H. H. 2014. A field-based model of permafrost-controlled rockslide deformation in northern Norway. *Geomorphology,* 208**,** 34-49.

BLIKRA, L. H. & LONGVA, O. 1995. Frost-shattered debris facies of Younger Dryas age in the coastal sedimentary successions in western Norway: palaeoenvironmental implications. *Palaeogeography, palaeoclimatology, Palaeoecology,* 118**,** 89-110.

BLIKRA, L. H. & LONGVA, O. 1999. Gravitational-slope failures in Troms: indications of palaeoseismic activity? *In:* DEHLS, J. & OLESEN, O. (eds.) *Neotectonics in Norway, Annual Technical Report 1999.* Trondheim Geological Suvery of Norway.

BLIKRA, L. H., LONGVA, O., BRAATHEN, A., ANDA, E. & STALSBERG, K. 2014. Rock slope failures in Norwegian fjord areas: examples, spatial distribution and temporal pattern. *In:* EVANS, S. G., MUGNOZZA, G. S., STROM, A. & HERMANNS, R. L. (eds.) *Landslides from massive rock slope failure.* The Netherlands: Springer.

BLIKRA, L. H. & NEMEC, W. 1998. Postglacial colluvium in western Norway: depositional processes, facies and palaeoclimatic record. *Sedimentology,* 45**,** 909-959.

BRAATHEN, A., BLIKRA, L. H., BERG, S. S. & KARLSEN, F. 2004. Rock-slope failures in Norway; type, geometry, deformation mechanisms and stability. *Norwegian Journal of Geology,* 84**,** 67-88.

BRADLEY, R. S. 2015. *Paleoclimatology (third edition) Reconstructing Climates of the Quaternary,* Oxford, United Kingdom, Elsevier Inc.

CORFU, F., ANDERSEN, T. B. & GASSER, D. 2014. The Scandinavian Caledonides: main features, conceptual advances and critical questions. *In:* CORFU, F., GASSER, D. & CHEW, D. M. (eds.) *New Perspectives on the Caledonides of Scandinavia and Related Areas.* United Kingdom: The Geolocial Society of London.

CORNER, G. D. 1977. *Deglaciation history and sediments of the Lyngen-Storfjord area, Troms, Norway.* The University of Tromsø.

CORNER, G. D. 1978. Deglaciation of Fugløy, Troms, North Norway. *Norsk Geologisk Tidsskrift,* 32**,** 137-142.

CORNER, G. D. 1980. Preboreal deglaciation chronology and marine limits of the Lyngen - Storfjord area, Troms, north Norway. *Boreas,* 9**,** 239-249.

CORNER, G. D. 1998. Recent natural and anthropogenic changes in a regulated river delta: Elvegård, nothern Norway. *Norsk Geologisk Tidsskrift,* 52**,** 135-150.

CORNER, G. D. 2005a. Atlantic coast and fjords. *In:* SEPPÄLÄ, M. (ed.) *The Physical Geography of Fennoscandia.* Oxford, United Kingdom: Oxford University Press.

CORNER, G. D. 2005b. Scandes Mountains. *In:* SEPPÄLÄ, M. (ed.) *The Physical Geography of Fennoscandia.* Oxford, United Kingdom: Oxford University Press.

CORNER, G. D. 2006. A transgressive-regressive model of fjord-valley fill; stratigraphy, facies and depositional controls. *Special Publication Society for Sedimentary Geology,* 85**,** 161-178.

CORNER, G. D. & EILERTSEN, R. S. 2013. Marine geological cruise with RV Hyas in inner Balsfjorden (Nordkjosbotn and Russenes deltas), Troms, nothern Norway, 9-10 September 2013. Tromsø, Norway: University of Tromsø.

CORNER, G. D. & HAUGANE, E. 1993. Marine-lacustrine stratigraphy of raised coastal basins and postglacial sea-level change at Lyngen and Vanna, Troms, northern Norway. *Norsk Geologisk Tidsskrift,* 73**,** 175-197.

CORNER, G. D., KOLKA, V. V., YEVZEROV, V. Y. & MØLLER, J. J. 2001. Postglacial relative sea-level change and stratigraphy of raised coastal basins on Kola Peninsula, northwest Russia. *Global and Planetary Change,* 31**,** 155-177.

CORNER, G. D., NORDAHL, E., MUNCH-ELLINGSEN, K. & ROBERTSEN, K. R. 1990. Morphology and sedimentology of an emergent fjord-head Gilbert-type delta: Alta delta, Norway. *In:* COLELLA, A. & PRIOR, D. B. (eds.) *Coarse-Grained Deltas.* Great Britaon: Blackwell Scientific Publications.

CORNER, G. D., STEINSUND, P. I. & ASPELI, R. 1996. Distribution of recent benthic foraminifera in a subarctic fjord-delta: Tana, Norway. *Marine Geology,* 134**,** 113-125.

DAHL, S. O., LINGE, H., FABEL, D., MURRAY, A. & BAKKE, J. 2010. Middle to late Weichselian glacier fluctuations and rock-glacier activity related to the sea-level history of northern Andøya, Arctic Norway. *Abstracts with Programs Geological Society of America,* 42**,** 243-244.

DAHL, S. O. & NESJE, A. 1992. Palaeoclimatic implications based on equilibrium-line altitude depressions of reconstructed Younger Dryas and Holocene cirque glaciers in Inner Nordfjord, Western Norway. *Palaeogeography, palaeoclimatology, Palaeoecology,* 94**,** 87-97.

DAHL, S. O. & NESJE, A. 1996. A new approach to calculating Holocene winter precipitation by combining glacier eqilibrium-line altitudes and pine-tree limits: a case study from Hardangerjokulen, central southern Norway. *The Holocene,* 6**,** 381-398.
DE COSTA, E. M. 1778. *Historia Naturalis Testaceorum Britanniae,* London, Millan, White, Elmsley & Robson.
DELINE, P. 2009. Interactions between rock avalanches and glaciers in the Mont Blanc massif during the late Holoene. *Quaternary Science Reviews,* 28**,** 1070-1083.
DONNER, J., ERONEN, M. & JUNGNER, H. 1977. The dating of the Holocene relative sea-level changes in Finnmark, North Norway. *Norsk Geologisk Tidsskrift,* 31**,** 103-128.
DOWDESWELL, J. A., OTTESEN, D., EVANS, J., Ó COFAIGH, C. & ANDERSON, J. B. 2005. Submarine glacial landforms and rates of ice-stream collapse. *Geology,* 36**,** 819-822.
EIDSVÅG, E. & ØYSTEIN, S. L. 2016. Skredfarekartlegging i Balsfjord kommune. Oslo: The Norwegian Water Resources and Energy Directorate.
EILERTSEN, R. S., CORNER, G. D. & AASHEIM, O. 2005. Deglaciation chronology and glacimarine successions in the Malangen-Målselv area, northern Norway. *Boreas,* 34**,** 233-251.
EILERTSEN, R. S., CORNER, G. D., AASHEIM, O., ANDREASSEN, K., KRISTOFFERSEN, Y. & YSTBORG, H. 2006. Valley-fill stratigraphy and evolution of the Målselv fjord valley, Northern Norway. *In:* DALRYMPLE, R. W., LECKIE, D. A. & TILLMAN, R. W. (eds.) *Incised valleys in time and space.*
EILERTSEN, R. S., CORNER, G. D., AASHEIM, O. & HANSEN, L. 2011. Facies characteristics and architecture related to palaeodepth of Holocene fjord-delta sediments. *Sedimentology,* 58**,** 1784-1809.
ERONEN, M. 2005. Land Uplift: Virgin Land from the Sea. *In:* SEPPÄLÄ, M. (ed.) *The physical geography of Fennoscandia.* Oxford, United Kingdom: Oxford University Press.
EVANS, S. G., MUGNOZZA, G. S., STROM, A. & HERMANNS, R. L. 2006. *Lanslides from Massive Rock Slope Failure,* The Neatherlands, Springer.
FENTON, C. R., HERMANNS, R. L., BLIKRA, L. H., KUBIK, P. W., BRYANT, C., NIEDERMANN, S., MEIXNER, A. & GOETHALS, M. M. 2011. Regional 10Be production rate calibration for the past 12 ka deduced from radiocarbon-dated Grøtlandsura and Russenes rock avalanches at 69°N, Norway. *Quaternary Geochronology,* 6**,** 437-452.
FIELD, J. 2001. Channel avulsion on alluvial fans in southern Arizona. *Geomorphology,* 37**,** 93-104.
FIMREITE, S., VORREN, K.-D. & VORREN, T. O. 2001. Vegetation, climate and ice-front oscillations in the Tromsø area, northern Norway during the Allerød and Younger Dryas. *Boreas,* 30**,** 89-100.
FORWICK, M. 2001. *Development of the sedimentary environment in Balsfjord (nothern Norway).* Masters of Geology Masters, UiT the Arctic University of Norway.
FORWICK, M. & VORREN, T. O. 2002. Deglaciation history and post-glacial mass movements in Balsfjord, nothern Norway. *Polar Research,* 21**,** 259-266.
FOSSEN, H., PEDERSEN, R.-B., BERGH, S. & ANDRESEN, A. 2008. Creation of a mountain chain. *In:* RAMBERG, I. B., BRYHNI, I., NØTTVEDT, A. & RANGNES, K. (eds.) *The making of a Land. Geology of Norway.* Trondheim, Norway: Norsk Geologisk Forening.
GABRIELSEN, R. H., BRAATHEN, A., DEHLS, J. & ROBERTS, D. 2002. Tectonic lineaments of Norway. *Norsk Geologisk Tidsskrift,* 82**,** 153-174.
GALLOWAY, W. E. 1975. Process framework for describing the morphologic and stratigraphic evolution of deltaic depositional systems. *In:* BROUSSARD, M. L. (ed.) *Deltas: Models for Exploration.* Houston, Texas, USA: Houston Geological Society.
GALLOWAY, W. E. & HOBDAY, D. K. 1996. *Terrigenous clastic depositional systems. Applications to fossil fuel and groundwater resources,* Italy, Springer - Verlag Berlin Heidelberg New York.
GILBERT, G. K. 1885. The topographic features of lake shores. *U.S. Geological Survey 5th Annual Report.*
GIOSAN, L. & GOODBRED JR, S. L. 2007. Deltaic Environments. *In:* ELIAS, S. A. (ed.) *Encyclopedia of Quaternary Science.* Elsevier Ltd.

GMELIN, J. F. 1791. Carli Linnaei systema Naturae per regna tria naturae. Editio decimatertia, aucta, reformata, Vermes Testacea. *Lipsiae,* 1 (6)**,** 3021-3910.
GRØNLIE, O. T. 1914. Kvartærgeologiske undersøkelser i Tromsø amt. III. Strandlinjer i amtet. *Tromsø Museum. Årsh.,* 35 -36**,** 221 - 240.
GRØNLIE, O. T. 1940. On the traces of the ice ages in Nord-land, Troms, and the south-western part of Finnmark in Northern Norway. *Norges Geologiske undersøkelse,* 20**,** 1 - 70.
GRØNLIE, O. T. 1951. On the rise of sea and land and the forming of strandflats on the west coast of Fennoscandia. *Norsk Geologisk Tidsskrift,* 29**,** 26 - 63.
GUTSELL, J. E., CLAGUE, J. J., BEST, M. E., BOBROWSKY, P. T. & HUTCHINSON, I. 2004. Architecture and evolution of a fjord-head delta, western Vancouver Island, British Columbia. *Journal of Quaternary Science,* 19**,** 497-511.
GUZZETTI, F., MONDINI, A. C., CARDINALI, M., FIORUCCI, F., SANTANGELO, M. & CHANG, K.-T. 2012. Landslide inventory maps: New tools for an old problem. *Earth Science Reviews,* 112**,** 42-66.
HALD, M., HUSUM, K., VORREN, T. O., GRØSFJELD, K., JENSEN, H. B. & SHARAPOVA, A. 2003. Holocene climate in the subarctic fjord Malangen, nothern Norway: a multi-proxy study. *Boreas,* 32**,** 543-559.
HALD, M. & VORREN, T. O. 1983. A shore displacement curve from the Tromsø district, North Norway. *Norsk Geologisk Tidsskrift,* 63**,** 103-110.
HAMBREY, M. 1994. *Glacial environments,* CRC Press.
HANSEN, L., WALDMANN, N., STORMS, J. E. A., EILERTSEN, R. S., ARIZTEGUI, D., CHAPRON, E. & NESJE, A. 2016. Morphological signatures of mass wasting and delta processes in a fjord-lake system: insights from Lovatnet, western Norway. *Norwegian Journal of Geology,* 96**,** 1-21.
HELLAND, A. 1899. Strandliniernes fald. *Norges Geologiske undersøkelse,* 28**,** 1 - 28.
HERMANNS, R. L. & LONGVA, O. 2012. Rapid rock-slope failures. *In:* CLAGUE, J. J. & STEEL, R. J. (eds.) *Landslides: Types, Mechanisms and Modelling.* Cambridge, United Kingdom: Cambridge University Press.
HEWITT, K. 2009. Rock avalanches that travel onto glaciers and related developments, Karakoram Himalaya, Inner Asia. *Geomorphology,* 103**,** 66-79.
HOLMES, A. 1965. *Principles of physical geology,* London, England, Thomas Nelson and Sons, Ltd.
HOWE, J. A., AUSTIN, W. E. N., FORWICK, M., PAETZEL, M., HARLAND, R. & CAGE, A. G. 2016. *Fjord systems and archives: a review,* London, Geological Society.
HUBBARD, B. & GLASSER, N. 2005. *Field techniques in glaciology and glacial geomorphology,* England, United Kingdom, John Wiley & Sons, Ltd.
INDREVÆR, K., BERGH, S., KOEHL, J.-B., HANSEN, J.-A., SCHERMER, E. R. & INGEBRIGTSEN, A. 2013. Post-Caledonian brittle fault zones on the hyperextended SW Barents Sea margin: New insights into onshore and offshore margin architecture. *Norwegian Journal of Geology,* 93**,** 167-188.
JONES, D. K. C. & LEE, E. M. 1994. Landsliding in Great Britain. London: HMSO, Department of the Environment.
KARTVERKET 2016. Tidevannstabeller den Norske kyst med Svalbard samt Drover, England 2017. Stravanger: Kartverket sjødivisjonen.
KNIGHT, J., MITCHELL, W. A. & ROSE, J. 2011. Geological field mapping. *In:* SMITH, M. J., PARON, P. & GRIFFITHS, J. S. (eds.) *Developments in Earth Surface Processes. Geomorphological mapping methods and application.* Great Britain: Elsevier.
KORHOLA, A., VASKO, K., TOIVONEN, T. T. & OLANDER, H. 2002. Holocene temperature changes in northern Fennoscandia reconstructed from chironomids using Bayesian modelling. *Quaternary Science Reviews,* 21**,** 1841-1860.
KRUMBEIN, W. C. 1934. Size frequency distributions of sediments. *Journal of Sedimentary Petrology,* 4**,** 65 - 77.
KVERNDAL, A.-I. & SOLLID, J. L. 1993. Late Weichselian glaciation and deglaciation in northeastern Troms, northern Norway. *Norsk Geologisk Tidsskrift,* 47**,** 163-177.
LEEDER, M. 1999. *Sedimentology and Sedimentary Basins. From turbulence to tectonics,* United Kingdom, Blackwell Science Ltd.

LIBBY, W. F. 1955. *Radiocarbon Dating,* Chicago, University of Chicago Press.
LILLEØREN, K. S., ETZELMÜLLER, B., SCHULER, T. V., GISNÅS, K. & HUMLUM, O. 2012. The relative age of mountain permafrost - estimation of Holocene permafrost limits in Norway. *Global and Planetary Change,* 92-93**,** 209-223.
LINNAEUS, C. 1758a. System Naturae. Editio decima. 1. Regnaum Animale. . *Holmiae, Laurentii Salvii***,** 824.
LINNAEUS, C. 1758b. Systema Naturae. Editio decima. 1. Regnum Animalle. *Holmiae, Laurentii Salvii***,** 824.
LINNAEUS, C. 1767. Systema Naturae. Editi decima. 1. Regnum Animalle. *Holmiae, Laurentii Salvii***,** 824.
LØNNE, I. 1995. Sedimentary facies and depositional architecture of ice-contact glaciomarine systems. *Sedimentary Geology,* 98**,** 13-43.
LØNNE, I. & NEMEC, W. 2004. High-arctic fan delta recording deglaciation and environment disequilibrium. *Sedimentology,* 51**,** 553-589.
LOWE, J. & WALKER, M. 2015. *Reconstructing Quaternary Environments,* New York, Routledge.
LYSÅ, A. & CORNER, G. D. 1994. Late Pleistocene glacial-deglacial facies successions and geologic histroy at Vuogamasjåkka, Finnmarksvidda, Norway. *Norsk Geologisk Tidsskrift,* 74**,** 9-23.
MANGERUD, J., BONDEVIK, S., GULLIKSEN, S., HUFTHAMMER, A. K. & HØISÆTER, T. 2006. Marine 14C reservoir ages for 19th century whales and molluscs from the North Atlantic. *Quaternary Science Reviews,* 25.
MANGERUD, J., GOEHRING, B. M., LOHNE, Ø. S. & SVENDSEN, J. I. 2013. Collapse of marine-based outlet glaciers from the Scandinavian Ice Sheet. *Quaternary Science Reviews,* 67**,** 8-16.
MARTHINUSSEN, M. 1960. Coast-and fjord area of Finnmark, with remarks on some other districts. *In:* HOLTEDAHL, O. (ed.) *Geology of Norway.* Norges Geologiske undersøkelse.
MARTHINUSSEN, M. 1962. C14-datings referring to shore lines, transgressions and glacial substages in Nothern Norway. *Norges Geologiske undersøkelse,* 215**,** 37-67.
MAURING, E., KOZIEL, J., LAURITSEN, T., RØNNING, J. S. & TØNNESEN, J. F. 1994. Målinger med georadar. Teori, anvedelse, teknikker og eksempler på opptak. Trondehim.
MCEWEN, L. J., OWEN, G., MATHEWS, J. A. & HIEMSTRA, J. F. 2011. Late Holocene development of a Norwegian apline alluvial fan affected by proximal glacier variations, episodic distal undercutting, and colluvial activity. *Geomorphology,* 127**,** 198-215.
MCPHERSON, J. G., SHANMUGAM, G. & MOIOLA, R. J. 1987. Fan-deltas and braid deltas: varieties of coarse-grained deltas. *Geological Society of America Bulletin,* 99**,** 331-340.
MCPHERSON, J. G., SHANMUGAM, G. & MOIOLA, R. J. 1988. Fan deltas and braid deltas: conceptual problems. *In:* NEMEC, W. & STEEL, R. J. (eds.) *Fan Deltas: Sedimentology and Tectonic Settings.* Glasgow: Blackie and Son Ltd.
MILSOM, J. & ASGER, E. 2011. Ground Penetrating Radar. *Field Geophysics, Fourth Edition.* Chichester, United Kingdom: John Wiley & Sons, Ltd.
MØLLER, J. J. 1989. Geometric simulation and mapping of Holocene relative sea-level changes in northern Norway. *Journal of Coastal Research,* 5**,** 403-417.
MØLLER, J. J., YEVZEROV, V. Y., KOLKA, V. V. & CORNER, G. D. 2002. Holocene raised-beach ridges and sea-ice-pushed boulders on the Kola Peninsula, northwest Russia: indicators of climate change. *The Holocene,* 12**,** 169-176.
MONTAGU, C. 1803. *Testacea Britannica, or natural history of British shells, marine, land and the fresh-water including the most minute: a systematically arranged and embellished with figures. ,* London.
MÜLLER, O. F. 1776. Zoologiae Danicae Prodromus, seu Animalium Daniae et Norvegiae Indigenarum, characteres, nomina, et synonyma imprimis popularum. *Havniae (Copenhagen): Typis Hallageriis***,** 281.
NEMEC, W. 1990a. Aspects of sediment movement of steep delta slopes. *In:* COLELLA, A. & PRIOR, D. B. (eds.) *Coarse-Grained Deltas.* Oxford, United Kingdom: Blackwell Scientific Publications.
NEMEC, W. 1990b. Deltas - remarks on terminology and classification. *In:* COLELLA, A. & PRIOR, D. B. (eds.) *Coarse-Grained Deltas.* Oxford, United Kingdom: Blackwell Scientific Publications.

NEMEC, W. & STEEL, R. J. 1988. What is a fan delta and how do we recognize it? *In:* NEMEC, W. & STEEL, R. J. (eds.) *Fan deltas: Sedimentology and Tectonic Settings.* Glasgow, United Kingdom: Blackie and Son Ltd.
NGU 2015a. Berggrunn N50 (1:50 000). https://www.ngu.no/en/topic/datasets.
NGU 2015b. Løsmasser N50/N250 dataset. https://www.ngu.no/en/topic/datasets.
Ó COFAIGH, C., DOWDESWELL, J. A., ALLEN, C. S., HIEMSTRA, J. F., PUDSEY, C. J., EVANS, J. & EVANS, D. J. A. 2005. Flow dynamics and till genesis associated with a marine-based Antarctic palaeo-ice stream. *Quaternary Science Reviews,* 24**,** 709-740.
OLESEN, O., BUNGUM, H., DEHLS, J., LINDHOLM, C., PASCAL, C. & ROBERTS, D. 2013. Neotectonics, seismicity and contemporary stress field in Norway - mechanisms and implications. *In:* OLSEN, L., FREDIN, O. & OLESEN, O. (eds.) *Quaternary Geology of Norway*. Trondheim.
OLESEN, O., DEHLS, J., BUNGUM, H., RIIS, F., HICKS, E., LINDHOLM, C., BLIKRA, L. H., FJELDSKAAR, W., OLSEN, L., LONGVA, O., FALEIDE, J. I., BROCKMANN, L., RISE, L., ROBERTS, D., BRAATHEN, A. & BREKKE, H. 2000. Neotectonics in Norway, Final Report. *NGU Report 2000.01*. Trondheim: Norges geologiske undersøkelse.
OLIVER, P. G., HOLMES, A. M., KILLEEN, I. J. & TURNER, J. A. 2016. *Marine Bivalve Shells of the British Isles* [Online]. Avalaible at http://naturalhistory.museumwales.ac.uk/BritishBivalves/home.php. [Accessed 2017].
OLSEN, L., SVEIAN, H., BERGSTRØM, B., OTTESEN, D. & RISE, L. 2013. Quaternary glaciations and their variations in Norway and on the Norwegian continental shelf. *In:* OLSEN, L., FREDIN, O. & OLSEN, O. (eds.) *Quaternary Geology of Norway.* Norway: Geological Survey of Norway.
OSMUNDSEN, P. T., REDFIELD, T. F., HENDRIKS, B. H. W., BERGH, S., HANSEN, J.-A., HENDERSON, I. H. C., DEHLS, J., LAUKNES, T. R., LARSEN, Y., ANDA, E. & DAVIDSEN, B. 2010. Fault-controlled alpine topography in Norway. *Journal of the Geological Society, London,* 167**,** 83-98.
PETTERSEN, K. 1880. Terrasser og gamle strandlinjer. *Tromsø Museum. Årsh.,* 3**,** 1 - 52.
PETTERSEN, K. 1884. Det nordlige Norge under den glaciale og postglaciale tid. *Tromsø Museum. Årsh.,* 7**,** 1 - 46.
POSTMA, G. & CRUICKSHANK, C. 1988. Sedimentology of a late Weichselian to Holocene terraced fan delta, Varangerfjord, nothern Norway. *In:* NEMEC, W. & STEEL, R. J. (eds.) *Fan deltas: Sedimentology and Tectonic Settings.* Glasgow: Blackie and Son Ltd.
POWELL, R. D. 1990. Glacimarine processes at grounding-line fans and their growth to ice-contact deltas. *In:* DOWDESWELL, J. A. & SCOURSE, J. D. (eds.) *Glaciomarine Environments: Processes and Sediments.*
POWERS, M. C. 1953. A new roundness scale for sedimentary particles. *Journal of Sedimentary Petrology,* 23.
PRIOR, D. B. & BORHOLD, B. D. 1989. Submarine sedimentation on a developing Holocene fan delta. *Sedimentology,* 36**,** 1053-1076.
PRIOR, D. B. & BORHOLD, B. D. 1990. The underwater development of Holocene fan deltas. *In:* COLELLA, A. & PRIOR, D. B. (eds.) *Coarse-Grained Deltas.* Oxford, United Kingdom: Blackwell Scientific Publications.
RAMSEY, B. C. 2009. Bayesain analysis of radiocarbon dates. *Radiocarbon,* 51**,** 337-360.
REIMER, P. J., BARD, E., BAYLISS, A. & BECK, J. W. 2013. IntCal13 and Marine13 Radiocarbon Age Calibration Curves 0-50,000 Years cal BP. *Radiocarbon,* 55**,** 1869-1887.
REZNICHENKO, N. V., DAVIES, T. R. H. & ALEXANDER, D. J. 2011. Effects of rock avalanches on glacier behaviour and moraine formation. *Geomorphology,* 132**,** 327-338.
ROMSTAD, B., HARBITZ, C. B. & DOMAAS, U. 2009. A GIS method for assessment of rock slide tsunami hazard in all Norwegian lakes and reservoirs. *Natural hazards and earth system sciences,* 9**,** 353-364.
ROMUNDSET, A., ØYSTEIN, S. L., MANGERUD, J. & SVENDSEN, J. I. 2010. The first Holocene relative sea-level curve from the middle part of Hardangerfjorden, western Norway. *Boreas,* 39**,** 87-104.

ROSE, J. & SYNGE, F. M. 1979. Glaciation and shoreline development between Nydal and Haukdal, south Varangerfjorden, nothern Norway. *Quaestiones Geographicae,* 5**,** 125-151.
RYDNINGEN, T. A., VORREN, T. O., LABERG, J. S. & KOLSTAD, V. 2013. The marine-based NW Fennoscandian ice sheet: glacial and deglacial dynamics as reconstructed from submarine landforms. *Quaternary Science Reviews,* 68**,** 126-141.
SANDERSEN, F. 2011. Kartlegging av skredfare Nordkjosbotn, Balsfjord. Oslo: Norwegian Geotechnical Institute.
SEPPÄ, H., BIRKS, H. H. & BIRKS, H. J. B. 2002a. Rapid climatic changes during the Greenland stadial 1 (Younger Dryas) to early Holocene transiton on the Norwegian Barents Sea coast. *Boreas,* 31**,** 215-225.
SEPPÄ, H. & BIRKS, H. J. B. 2001. July mean temperature and annual precipitation trends during the Holocene in the Fennoscandian tree-line area: pollen-based climate reconstructions. *The Holocene,* 11**,** 527-539.
SEPPÄ, H. & BIRKS, H. J. B. 2002. Holocene Climate Reconstructions from the Fennoscandian Tree-Line Area Based on Pollen Data from Toskaljavri. *Quaternary Research,* 57**,** 191-199.
SEPPÄ, H., NYMAN, M., KORHOLA, A. & WECKSTRÖM 2002b. Changes of treelines and alpine vegetation in relation to post-glacial climate dynamics in northern Fennoscandia based on pollen and chironomid records. *Journal of Quaternary Science,* 17**,** 287-301.
SHANMUGAM, G. 2016. Submarine fans: A critical retrospective (1950-2015). *Journal of Paleogeography,* 5**,** 110-184.
SKEI, J. M. 1983. Why sedimentologists are interested in fjords. *Sedimentary Geology,* 36**,** 75-80.
SLETTEN, K., BLIKRA, L. H., HANSEN, L., BARGEL, T. H. & OLSEN, L. 2006. Skredkartlegging i deler av Balsfjord kommune, Troms. *In:* UNDERSØKELSE, N. G. (ed.). Trondheim, Norway.
SOLLID, J. L., ANDERSEN, S., HAMRE, N., KJELDSEN, O., SALVIGSEN, O., STURØD, S., TVEITÅ, T. & WILHELMSEN, A. 1973. Deglaciation of Finnmark, North Norway. *Norsk Geologisk Tidsskrift,* 27**,** 233-323.
STOKES, C. R., CORNER, G. D., WINSBORROW, M. C. M., HUSUM, K. & ANDREASSEN, K. 2014. Asynchronous response of marine-terminating outlet glaciers during deglaciation of the Fennoscandian ice sheet. *Geology Boulder,* 42**,** 455-458.
SVEIAN, H., RIIBER, K., BERGSTRØM, B. & REITE, A. J. 2005. TROMS FYLKE, løsmassekart M: 1:310000. Norges geologiske undersøkelse.
SYVITSKI, J. P. M., BURRELL, D. C. & SKEI, J. M. 1987. *Fjords: Processes and Products,* New York, Springer-Verlag.
SYVITSKI, J. P. M. & SHAW, J. 1995. Sedimentology and geomorphology of fjords. *In:* PERILLO, G. M. E. (ed.) *Geomorphology and sedimentology of Estuaries.* Amsterdam, The Netherlands: Elsevier Science Publishers B.V.
UDDEN, J. A. 1914. Mechanical composition of clastic sediments. *Bulletin of the Geological Society of America,* 25**,** 655 - 744.
VAN HETEREN, S. 2014. Barrier systems. *In:* MASSELINK, G. & GEHRELS, R. (eds.) *Coastal environments and globle change.* West Sussex, United Kingdom: John Wiley & Sons, Ltd.
VORREN, K.-D. & ALM, T. 1999. Late Weichselian and Holocene environments of lake Endletvatn, Andøya, northern Norway: as evidence primarily by chemostratigraphical data *Boreas,* 28**,** 505-520.
VORREN, T. O. & ELVSBORG, A. 1979. Late Weishselian deglaciation and paleoenvironment of the shelf and coastal areas of Troms, noth Norway - a review. *Boreas,* 8**,** 247-253.
VORREN, T. O. & MANGERUD, J. 2008. Glaciations come and go. Quaternary to Holocene (Pleistocene); 2.6 million - 11,500 years ago. *In:* RAMBERG, I. B., BRYHNI, I., NØTTVEDT, A. & RANGNES, K. (eds.) *The Making of a Land - Geology of Norway.* Trondheim: Norsk Geologisk Gorening (Norwegian Geological Association).
VORREN, T. O., MANGERUD, J., BLIKRA, L. H., NESJE, A. & SVEIAN, H. 2008. The emergence of modern Norway. The last 11,500 years - The Holocene. *In:* RAMBERG, I. B., BRYHNI, I., NØTTVEDT, A. & RANGNES, K. (eds.) *The Making of a Land - Geology of Noway.* Trondheim: Norsk Geologisk Gorening (Norwegian Geological Association).

VORREN, T. O. & PLASSEN, L. 2002. Deglaciation and palaeoclimate of the Andfjord-Vågsfjord area, North Norway. *Boreas,* 31**,** 97-125.
WASSMANN, P., SVENDSEN, H., KECK, A. & REIGSTAD, M. 1996. Selected aspects of the physical oceanography and particle fluxes in fjords of northern Norway. *Journal of Marine Systems,* 8**,** 53-71.
WENTWORTH, C. K. 1922. A scale of grade and class terms for clastic sediments. *Journal of Geology,* 30**,** 377 - 392.
WESCOTT, W. A. & ETHRIDGE, F. G. 1990. Fan Deltas - Alluvial Fans in Coastal Settings. *In:* RACHOCKI, A. H. & M, C. (eds.) *Alluvial Fans: A Field Approrach.* England: John Wiley & Sons LTD.
WINSBORROW, M. C. M., ANDREASSEN, K., CORNER, G. D. & LABERG, J. S. 2010. Deglaciation of a marine-based ice sheet; late Weichselian palaeo-ice dynamics and retreat in the southern Barents Sea reconstructed from onshore and offshore glacial geomorphology. *Quaternary Science Reviews,* 29**,** 424-442.

Appendix 1: ArcGIS Methodology

The ArcGIS 10.4.1 software was used extensively during the study. This is a very useful software package for displaying, analyzing and interpreting spatial datasets. Some of the different methods employed in ArcGIS to view and interpret the data used in this study are outlined below.

Georeferencing field photographs

A hand-held GPS was used during fieldwork to record the path or track taken each day. This GPS track records information about the time, location (coordinates) and elevation at each point along the track. Simultaneously, the time that each photograph was taken in the field is recorded in the photo's metadata. Therefore, the field photos can be georeferenced by matching the time each photo was taken with the GPS track log. The Garmin BaseCamp™ was used to georeferenced the photos as follows:

1) Load GPS tracks into Garmin BaseCamp
2) Right click on the GPS track > select the Geotag Photos using Track… > browse to the photo location

Once the field photos have been geotagged with location information they can be imported into ArcMap as points using the "Geo Tagged Photos to Points" tool. This tool creates a point feature class in a geodatabase with each point representing a photo location and the photos can be attached to each point. The method is as follows:

1) In ArcMap find the Geo Tagged Photos to Points tool. Go to Toolbox > Data Management Tools > Photos > Geo Tagged Photos to Points tool.
2) Fill in the dialog box shown below by browsing to the location of the geotagged photos.

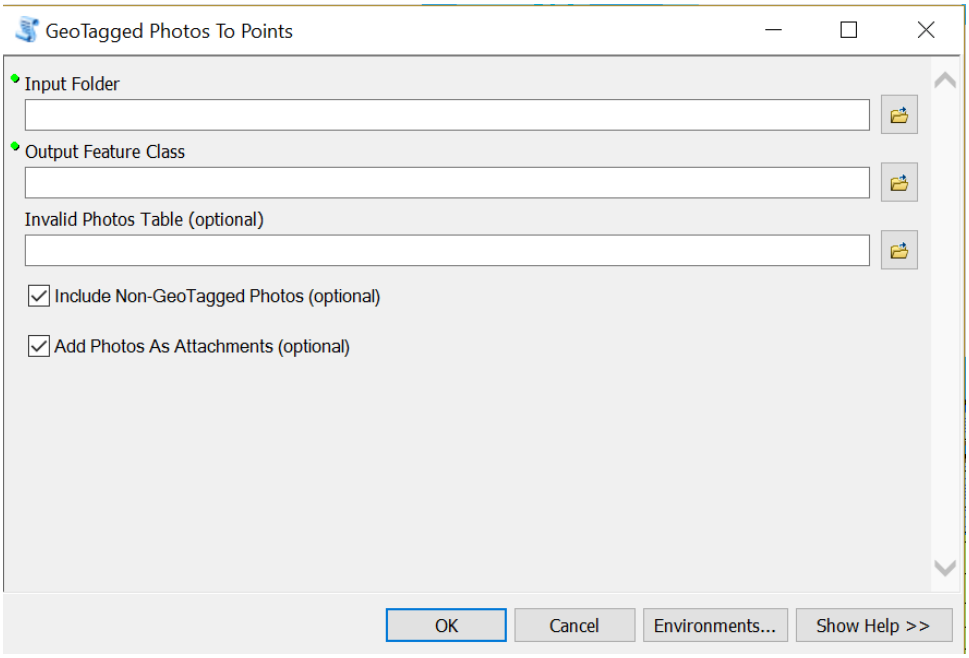

3) When the process is complete the new point feature class will be added to your map.

4) The photos can be viewed by clicking on the points with the HTML Popup tool as shown in the figure below.

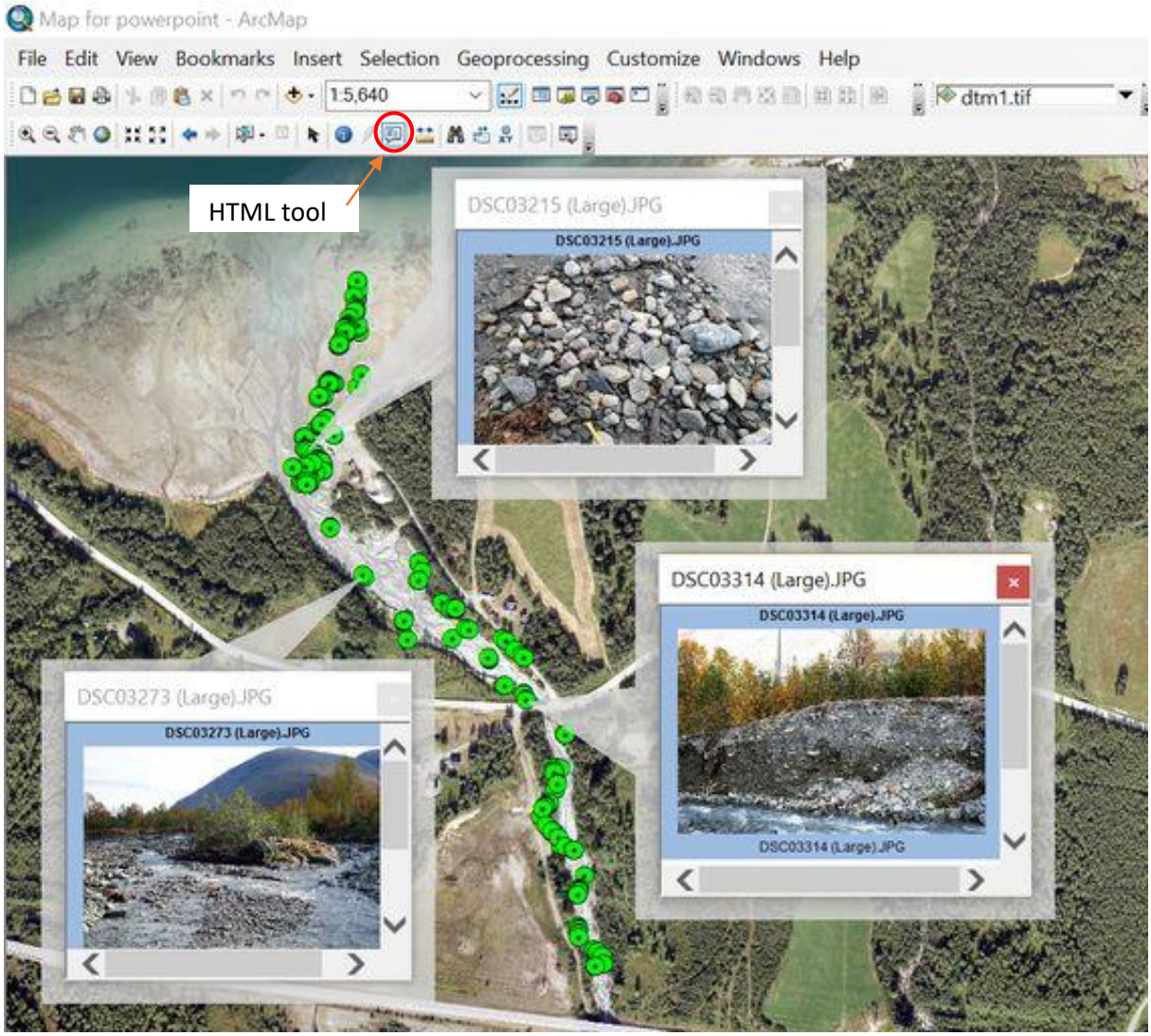

Adding field photos to your ArcMap project is a very powerful tool at assist with digitizing your map.

DTM visualization and interpretation

The Raster Surface Toolbox can be used to quantify and display different information about the terrain using a digital terrain model (DTM). To use the toolbox the raster elevation surface (DTM) needs to be used as the input, therefore, add the DTM to the ArcMap project.

Hillshade creates a shaded relief image of the DTM. To view the DTM using the hillshade function:

1) Windows > image analysis. The image analysis window will open.
2) Fill in the following parameters (shown in the image below):

- Highlight the DTM at the top of the window.
- Check the DRA box
- Choose a greyscale colour bar

- Click the shaded relief button shown in the picture below.

This will create the hillshade raster surface and add it to the ArcMap project.

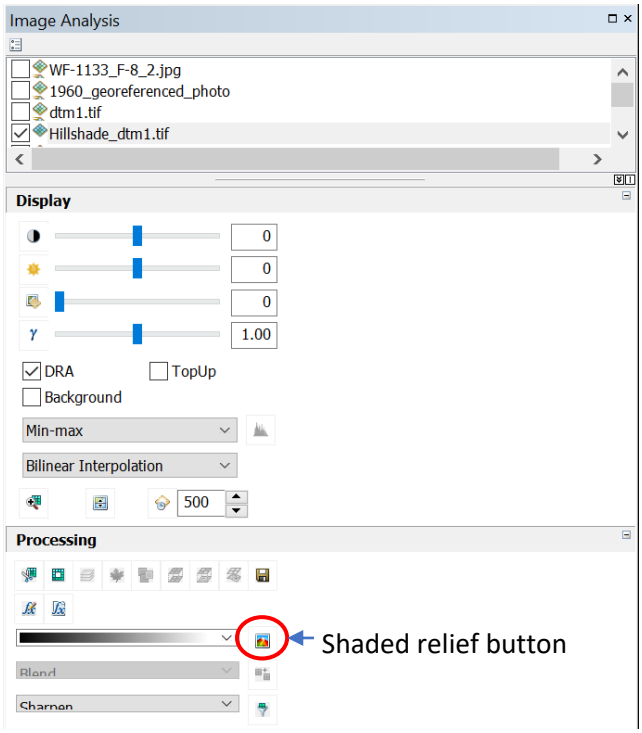

Alternatively, the hillshade tool can be used as follows Arc Toolbox > 3D analyst tools > Raster Surface > Hillshade.

3) The azimuth and elevation of the light can be changed as follows:
   Right click on the hillshade layer > properties > functions > hillshade function (double click) > change the azimuth and elevation as required.

The raster surface toolbox contains other useful tools including the “contour tool”, which produces a line feature class of contours based on the DTM and “slope tool”, which measures the gradient for each cell in the raster surface.

The 3D analysis toolbar can be used to visualize the DTM in 3D through creating profile graphs and this data can be exported. The process is outlined below:

1) View > toolbars > 3D analyst
2) Select the digital terrain model from the drop down menu.
3) Create a profile line using the interpolate line tool.
4) Display the profile by clicking profile graph in the dropdown menu.
5) To export the graph or data right click on the graph > export.

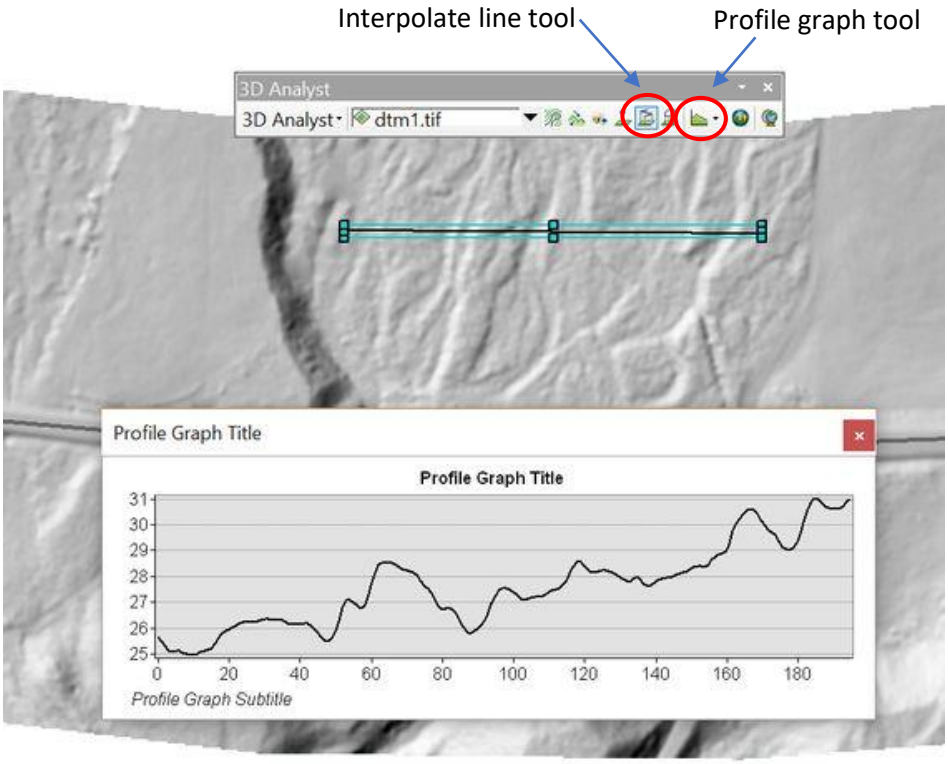

The image above shows the 3D analyst tool bar and an example profile graph created using the DTM.

Georeferencing maps in ArcMap

Some of maps and aerial photographs used in this study did not contain special information. Therefore, this data needs to be manually georeferenced in order to be viewed and interpreted in ArcMap. The process is outlined below:

1) Add the map or photograph to the ArcMap project. You will receive a warning that the data does not contain special information. Click OK.
2) Add the georeferencing tool bar. View > toolbars > georeferencing.
3) Select the dataset from the dropdown menu in the georeferencing tool bar.
4) Click georeferencing > fit to display. This will make the dataset appear.
5) Now you need to find points in the dataset that match points in a reference dataset/s that is already specially located (e.g. a different aerial photograph or map). These points could include buildings, roads, coastline etc.
6) Use the “add control points” tool to mark these matching points. First click the point on the dataset with known spatial information. This will place a cross mark at the location. Then click on the same location in the undefined map or photograph. Repeat this step for different control points across the image. For best results the first four points should be located in the outer corners of the dataset.
7) To check the accuracy of the georeferenced image click on the “view link table” button. The residual column shows how well the fit is between the true locations and the transformed location. Points with large residual values can be deleted from the table using the “delete link” tool to produce more accurate results.

Appendix 2: GPR Profiles

10 GPR profiles were collected across the study area and the locations of the GPR profiles are shown in the figure below. This appendix contains the uninterpreted GPR profiles and associated field notes.

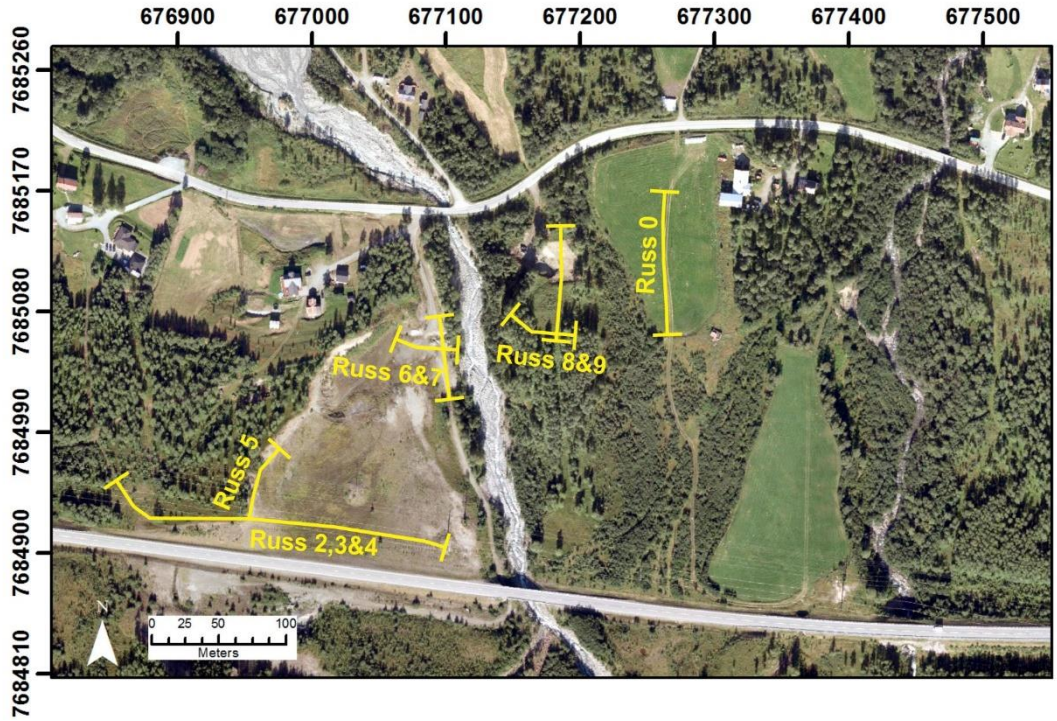

17 September 2016

GPR profile Test 5 was acquired in the paddock to the east of the gravel pit. This profile has been relabelled to Russ 0. The location of the GPR line is shown below. It started at the gate at the top of the paddock and followed the track. It passed one power line post and ended at the second power line post.

The elevation change along the profile was 695 cm and the GPR profile needs to be corrected. A second profile was taken perpendicular to Russ 0 and commencing at the first pole however, the computer battery died during acquisition and therefore the line failed.

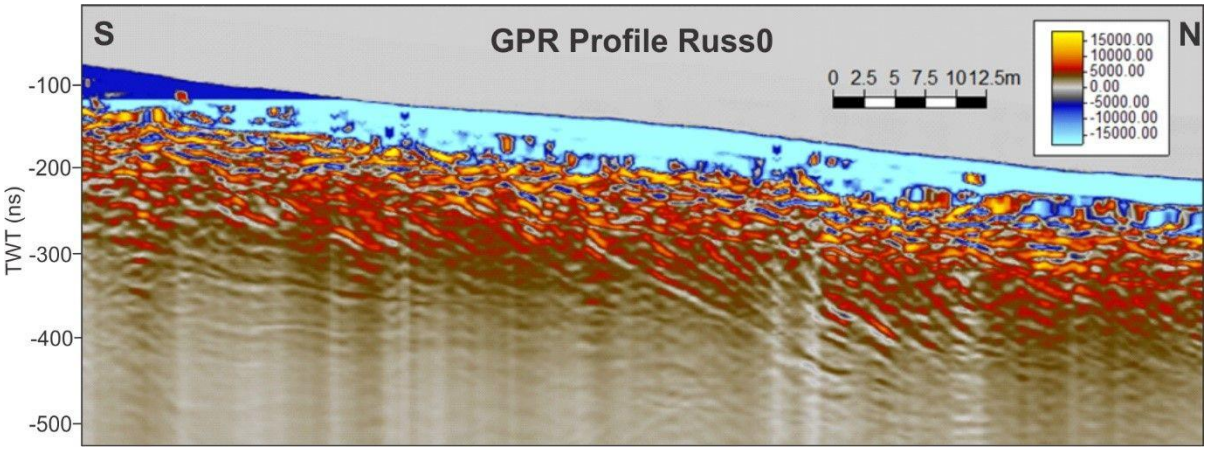

5 October 2016

GPR line Russ1 was collected above the gravel pit. The line started at the power pole and ended at the top of the rise when a battery stopped working and we lost the signal. The first section of the line was collected on flat terrain, whilst the slope increased towards the end as shown in the picture below.

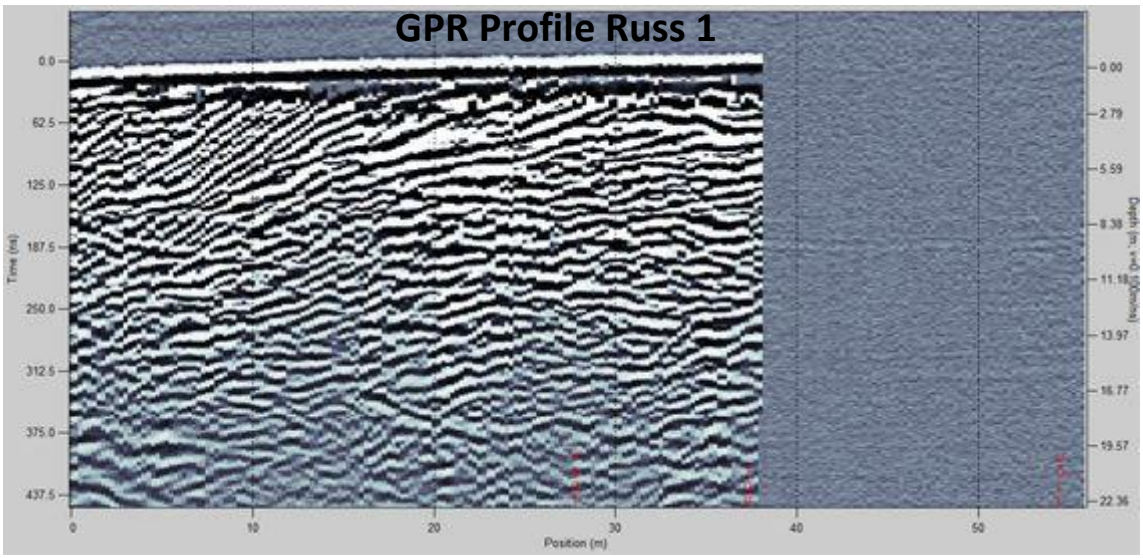

14 October 2016

Collected 8 GPR profiles were collected. The GPS tracks and line locations are shown below.

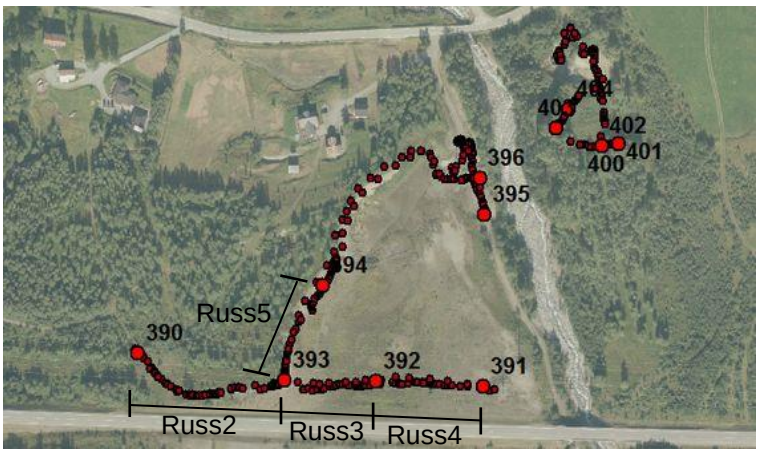

GPR Profile Russ2

The first three profiles (Russ2, 3 and 4) were collected in a continuous line and will be merged together during processing. Russ2 commenced on the alluvial fan and transitioned into the ice front deposit. It was stopped at the top of the mound just after the electricity poles. This part of the line is believed to be undisturbed by anthropogenic activities due to the thick vegetation cover.

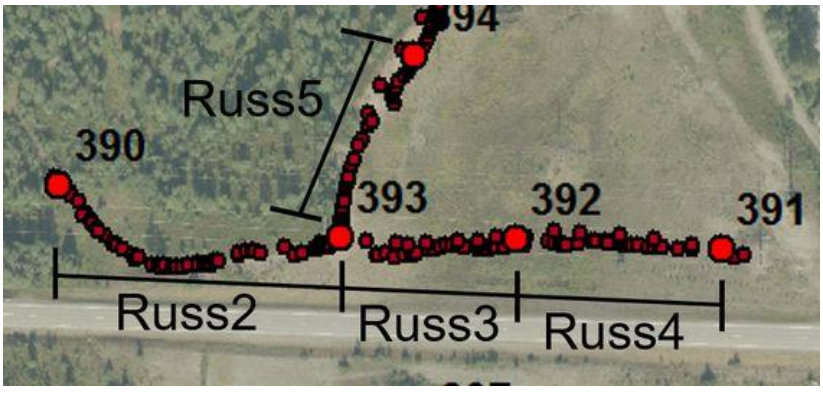

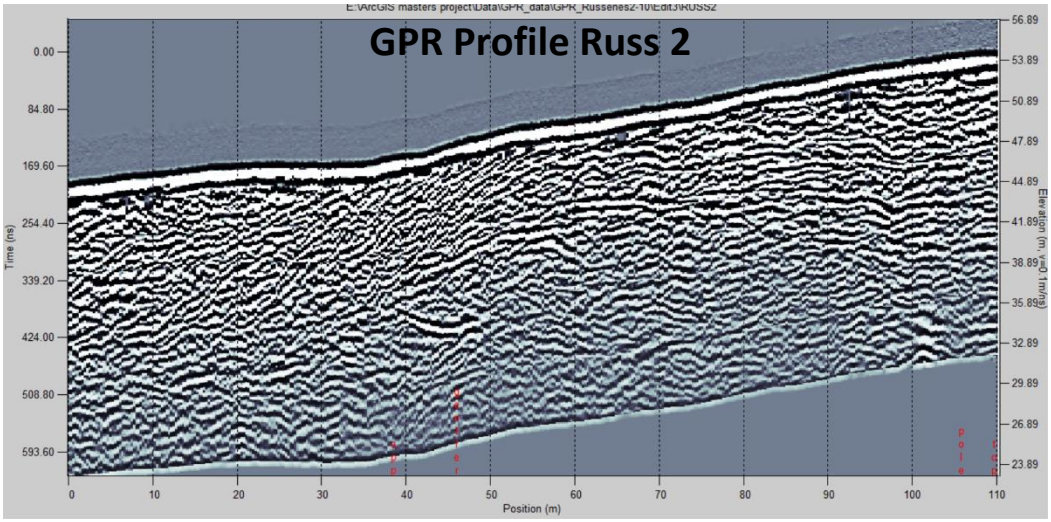

Line Russ3

This line continued from Russ2 at the top of the ice front deposit and ended in the middle of the boggy section marked by GPS waypoint. This part of the line has clearly been disturbed by anthropogenic activity. It contains minimal vegetation and its appearance suggests material has been removed (i.e. it forms part of a gravel pit). From 30 m to 60 m the line is quite boggy/wet.

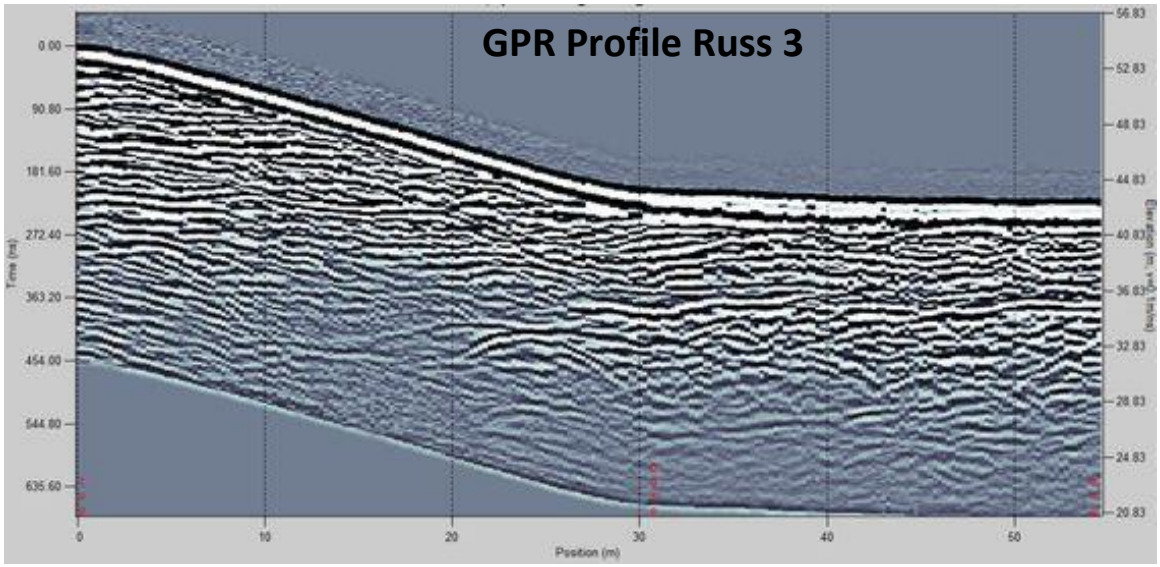

Line Russ4

This line continues from Russ3 to the top of a small mound beneath electricity poles. The material in the mound could be in its original position.

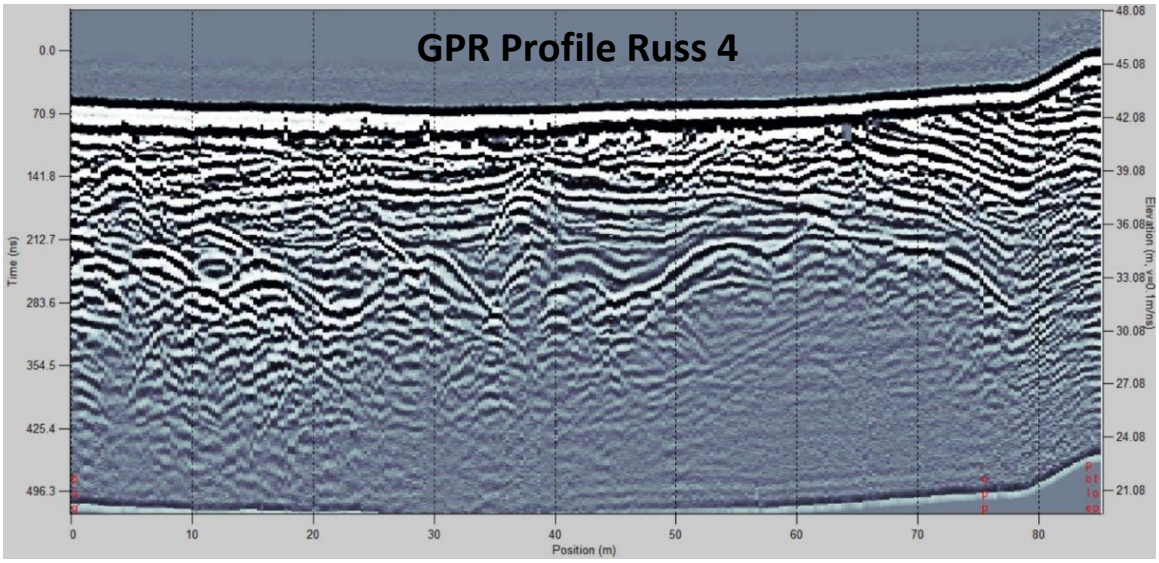

These three GPR profiles have been combined together to form one line shown below.

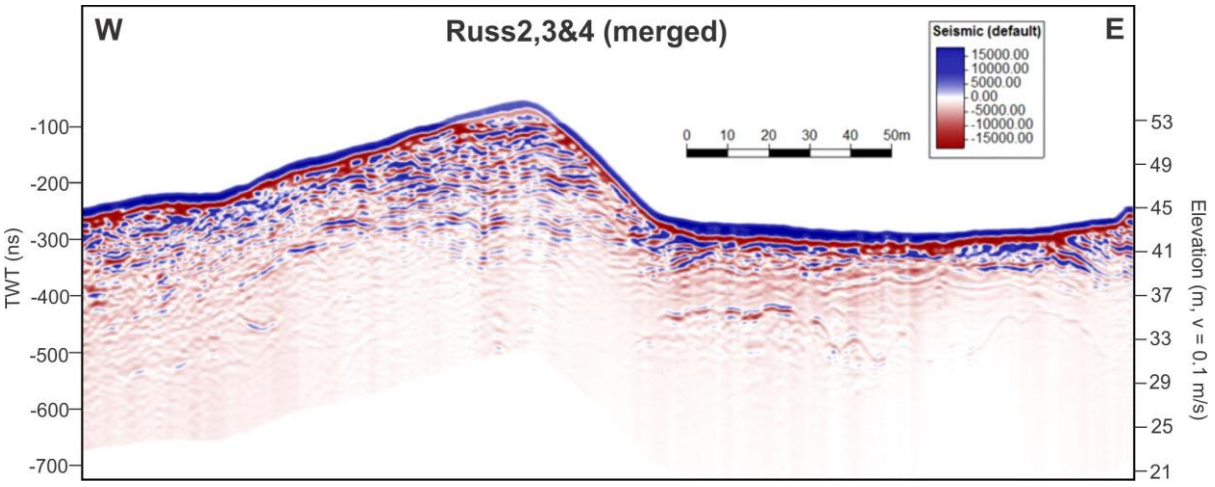

GPR Profile Russ5

This profile started at the top of the ridge beneath the power lines and followed the ridge down. It ended at the bottom of the second rise before the large boulders.

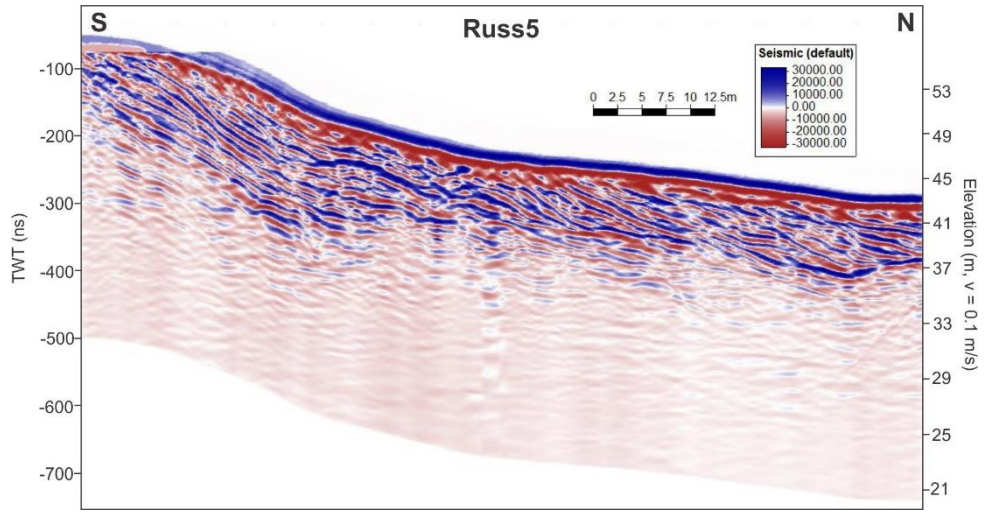

GPR profiles Russ 6 and 7

The next two lines were taken to assist with interpretation of the delta section observed in the river bed.

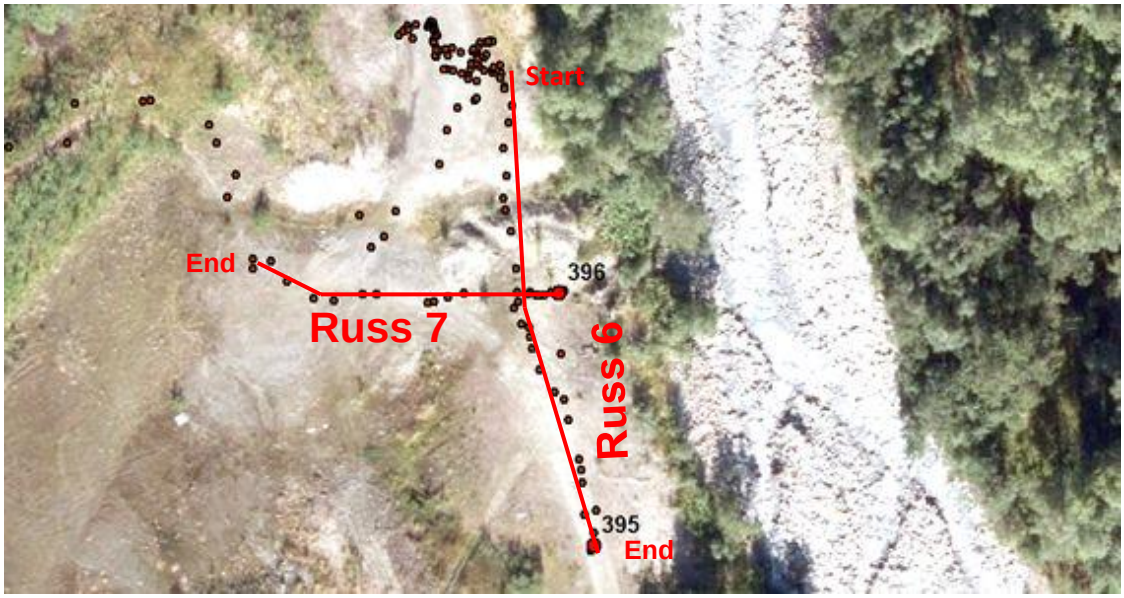

GPR profile Russ 6 occurs parallel to the river. It started where the car was parked and ended where a ditch started to form on the east side of the line. The line is shown below.

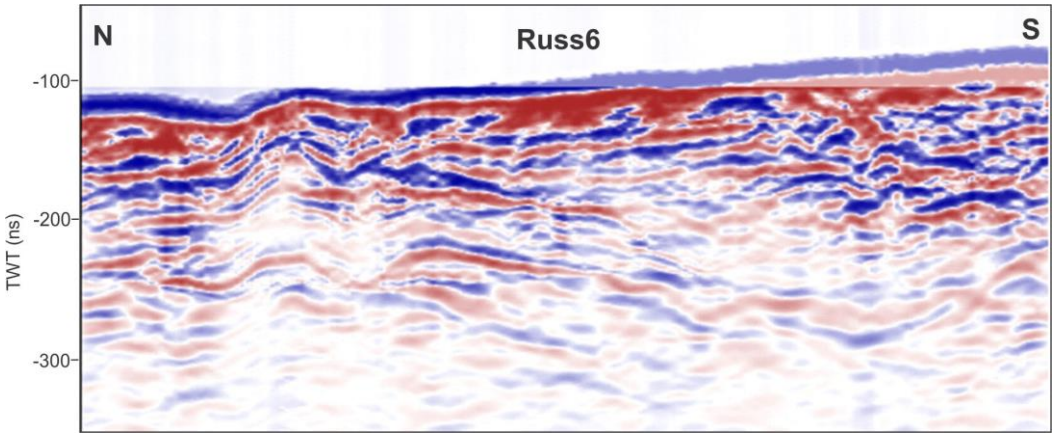

Russ 7 occurs perpendicular to Russ 6. And the start of Russ 7 is approximately 8 m south of Russ 6. Russ 7 changed direction slightly during the profile to end at the 3 orange markers.

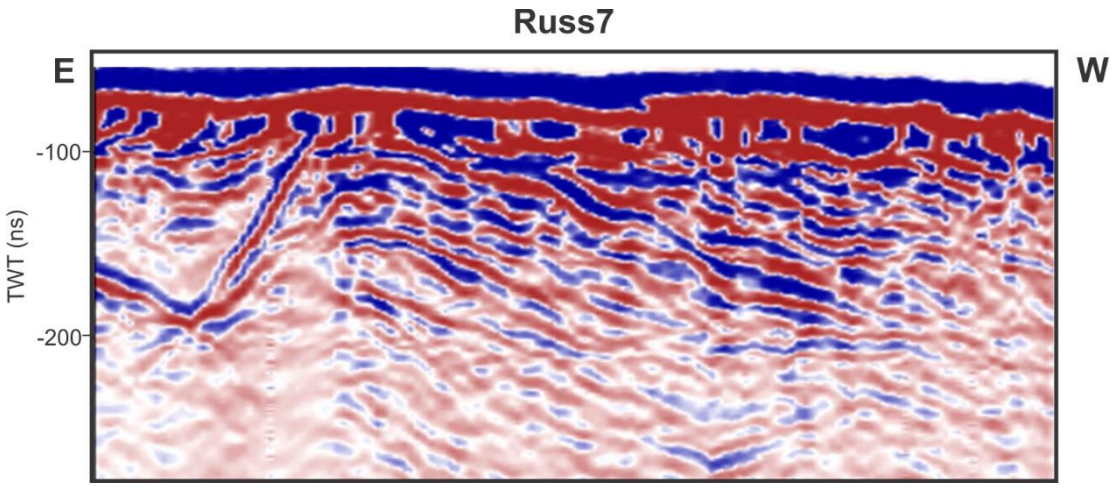

GPR profiles Russ 8, 9 and 10

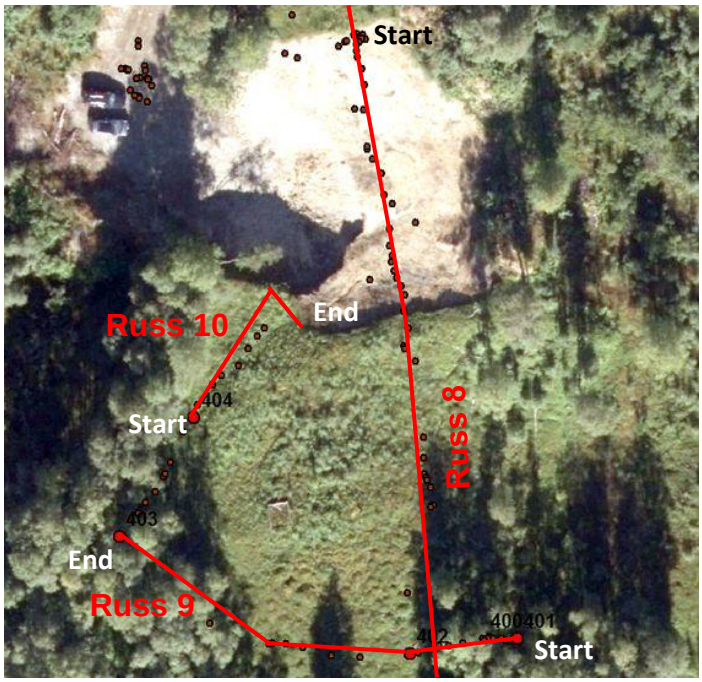

These lines were collected near the gravel pit to finish the work that was started with Russ 1. Three lines were collected. The first line, Russ 8, started to the east of Russ 1. It travelled over the cleared area above the gravel pit, up the shore notch and south across the vegetated area.

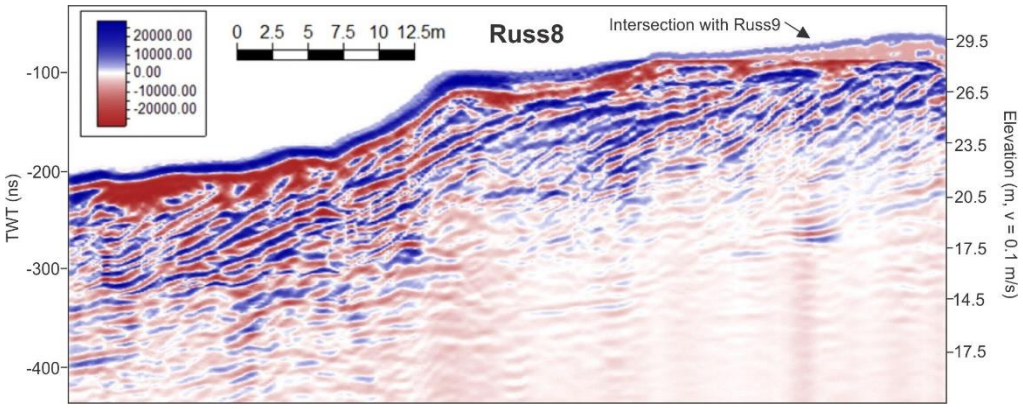

Russ 9 was taken perpendicular to Russ 8 from and the topography stepped down twice just before the end of the line.

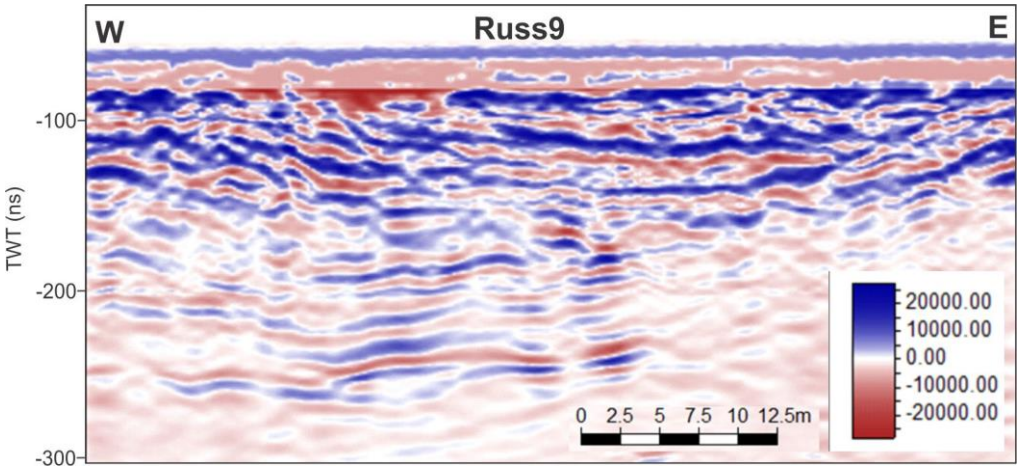

Russ 10 was taken over the fluvial terrace beside the gravel pit. It started from Stop 404 and went to the edge of the pit before the direction changed 90 degrees for the final 5 m of the line. All the lines are shown below.

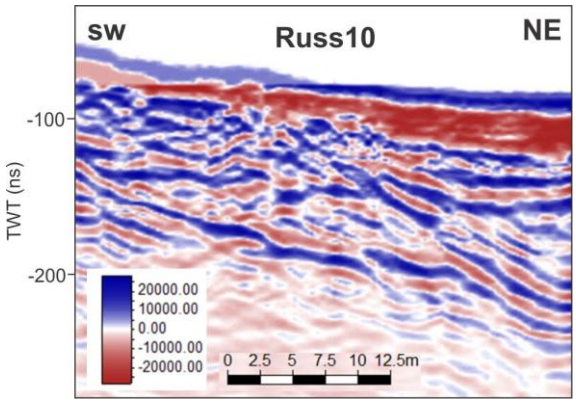

Appendix 3: Grainsize Data

The table below contains the grainsize information that was recorded for different sediment samples during fieldwork. The location of each grainsize sample was recorded as a waypoint using the hand-held GPS (accurate to 3 m). The methodology for recording grainsize information is outlined in section Section 3.1.3. The faces codes are as follows: clay = L; silt = z; sand = s; gravel = g; cobbles = c; and boulders = b.

Longitude	Latitude	Grainsize Mode (cm)	Maximum grainsize (cm)	Composition	Description	Location description
19.488113	69.214668		7	60ms/10cs/5L/15g/10c	Cobbly gravelly sand	Terrace slope
19.48622	69.213656		20	100fs	Sand	Terrace
19.485767	69.213452	1.5	6.5	60fs/40c	Fine sand with cobbles	Terrace
19.487149	69.213836		9	70cs/15g/15c	Cobbly gravelly sand	Terrace slope
19.487149	69.213836		9	70z/30c	Silt with cobbles	Terrace slope
19.489037	69.213952		5	70cs/15g/15c	Cobbly gravelly sand	Gravel pit
19.489037	69.213952		5	80z/20g	Silt with gravel	Gravel pit
19.478127	69.217641	1	9	25cs/25vcs/25g/25c	Cobbly gravelly sand	Gravel pit
19.498464	69.217167		50	80cs/20c	Cobbly sand	Terrace slope
19.49495	69.218546	3	8	60cs/20g/20c	Cobbly gravelly sand	Beach
19.489987	69.220809	1		30cs/20vcs/50g	Sandy cobbly gravel	Terrace
19.506145	69.214633		15	30cs/50g/20c	Sandy cobbly gravel	Terrace slope
19.475835	69.217144	1.5	6.5	50cs/30vcs/20c	Gravelly sand	River bank
19.474398	69.214786		6	50ms/20cs/15g/15c	Cobbly gravelly sand	Gravel pit
19.472802	69.214719	2	15	50cs/25g/15c	Cobbly gravelly sand	Gravel pit
19.47039	69.214603	5	25	20ms/30cs/20vcs/30g	Gravelly sand	Rockslide
19.470824	69.214944		7	10ms/40cs/20vcs/30g	Gravelly sand	Gravel pit
19.47394	69.213112		10	30z/30fs/20cs/30g	Gravelly silty sand	River bank
19.461336	69.211212		6	20L/50z/20fs/20c	Cobbly sandy silt	Rockslide
19.467127	69.214871		20	100fs	Fine sand with boulders	Terrace
19.464539	69.215162		14	50fs/30z/20L	Gravelly silty sand	Terrace slope
19.470379	69.213894			80z/20fs	Sandy cobbly silt	Rockslide
19.471757	69.214276			70fs/20z/10g	Silty cobbly sand	Rockslide
19.470281	69.220123	1.5	19	20ms/30cs/20vcs/30g	Gravelly sand	beach

19.467603	69.219929		4	40ms/30cs/20vcs/10g	Gravelly sand	beach
19.465211	69.219518		5	70vfs/20L/10c	Cobbly sand	
19.464529	69.218888		4	70vfs/20L/10c	Cobbly sand	
19.461539	69.218678	1.5	4	50L/40z/10fs	Silty gravelly sand	
19.460544	69.218293	2	22	40vfs/10fs/40z/10c	Silty gravelly sand	
19.456929	69.217571	1.5	5	30ms/30cs/30g	Gravelly cobbly sand	Terrace
19.454789	69.216917		5	20fs/50z/30L	Silty gravelly sand	
19.455657	69.217854		16	20fs/50z/30L	Cobbly sandy silt	Terrace
19.45691	69.219951	1.5	13	20clay/20silt/30fs/30ms/10g	Silty gravelly sand	
19.481629	69.214918	11	2	50ms/20cs/10vcs/20g	Gravelly cobbly sand	Terrace slope
19.48139	69.214353	2		80fs/10cs/10g	Gravelly sand	Terrace
19.480264	69.212355			20L/50z/30fs	Sandy silt	
19.482409	69.210091		7	30L/40z/20fs/10c	Sandy silt	
19.483754	69.211954			100fs	Sand	
19.482509	69.212788		8	10L/10z/50fs/10cs/20g	Gravelly silty sand	
19.480321	69.213536			60z/30vfs/10g	Sandy gravelly silt	
19.488037	69.215783			20z/30ms/20cs/30g	Gravelly silty sand	Ridge
19.49184	69.214393	2	11	20fs/50ms/10cs/20g	Gravelly sand	Gravel pit
19.490979	69.213973			100ms	Sand	Gravel pit
19.490979	69.213973		8	30ms/30cs/20g/10c	Gravelly cobbly sand	Gravel pit
19.490248	69.213173			20L/50z/30fs	Silty sand	
19.49015	69.212502			80ms/30g	Gravelly sand	
19.490647	69.211956			100ms	Sand	
19.49211	69.211606			10L/20z/70fs	Silty sand	Terrace
19.495816	69.213315			20L/50z/30fs	Sandy gravelly silt	
19.470275	69.215406	1	14	30ms/20cs/20vcs/30g	Gravelly sand	Gravel pit
19.469522	69.2155			20L/50fs/20cs/10g/10c	Cobbly gravelly sand	Gravel pit
19.469001	69.214774			20z/30fs/20ms/15g/15c	Cobbly gravelly sand	Rockslide
19.468516	69.214547	2	18	20L/50z/30fs	Sandy cobbly silt	Valley
19.468504	69.214262			20L/40z/40g	Gravelly sandy silt	Rockslide
19.467869	69.214317		15	50fs/20z/30g	Gravelly silty sand	
19.46958	69.212585			20L/80z	Silty gravelly sand	Rockslide
19.47222	69.216194	2		10L/70fs/20c	Cobbly sand	
19.473788	69.217244		7	20ms/20cs/20vcs/40g	Gravelly cobbly sand	
19.472922	69.218887		200	B		River bar

19.472425	69.221615			60z/20fs/20L	Sandy silt	Delta bar
19.472425	69.221615			100L	Clay	Delta bar
19.472425	69.221615		4	60cs/40g	Gravelly sand	Delta bar
19.472365	69.22138	2	6		Clay with gravel	Delta channel
19.472198	69.221326	0.75		100ms	Sand	Delta bar
19.472198	69.221326			50fs/50z	Silty sand	Delta bar
19.472198	69.221326	1		60cs/40g	Gravelly sand	Delta bar
19.472009	69.221184			80fs/20L	Sandy clay	Delta bar
19.472009	69.221184	1.5	4	60g/30vcs/10cs	Sandy gravel	Delta bar
19.47165	69.220844	1	3	100g	Gravel	Delta bar
19.471673	69.220817	2	8	100g	Gravel	Delta bar
19.471381	69.220713	3	11	100g	Gravel	Delta bar
19.470997	69.220406	3	7	70g/30ms	Sandy gravel	Delta bar
19.471042	69.22031	5	25	100g	Cobbly gravel	Delta bar
19.47132	69.220204	0.5	2	50vcs/50g	Sandy gravel	River bank
19.47132	69.220204		7	10L/60cs/30c	Cobbly stily sand	River bank
19.47098	69.220252	1	5	70g/30cs	Sandy gravel	Delta bar
19.471017	69.220166	3	5	100g	Gravel	Delta bar
19.470734	69.220178	5	10	50g/30c/20cs	Sandy cobbly gravel	Delta bar
19.47101	69.220039	8	30		cobbles with fine sand matrix	River bar
19.471433	69.219696	11	15		boulders with medium sand matrix	River bar
19.472339	69.219143	4	14	70cs/30g	Gravelly sand	River bar
19.473401	69.219362	6	10	20cs/40g/40c	Cobbly sandy gravel	River bank
19.473402	69.219238	7	40		Boulder with fine sand matrix	River bar
19.473856	69.219001	4	12	50g/50cs	Sandy gravel	River bar
19.474141	69.218958	4	30	50g/20cs/30vcs	Sandy gravel	River bank
19.474311	69.218797	6	20		Boulders with a coarse sand martix	River bar
19.475086	69.218323	10	30	60cs/40g	Sandy gravel	River bar
19.476093	69.217639	10	50		Boulders with very coarse sand matrix	River bar
19.476073	69.217586			40fs/40ms/20c	Cobbly sand	River bank
19.475904	69.217353	4	10	50ms/30cs/20c	Cobbly sand	River bank
19.476092	69.217069	14	35		Boulders with coarse sand matrix	River bar
19.476378	69.216968		20		Boulders with coarse sand matrix	River bar

19.476403	69.216612	2	30		Boulders with very coarse sand matrix	River bar
19.476341	69.216271		50	50g/50vcs	Sandy gravel	River bank
19.476729	69.216143	20	40			River bar
19.47685	69.216041	10	15		Boulders with coarse sand matrix	River bar
19.476325	69.221059	2	8	60g/40cs	Sandy gravel	Terrace slope
19.476325	69.221059			60z/40fs	Sandy silt	Terrace slope
19.477584	69.2213	4	14	50ms/30c/20g	Cobbly gravelly sand	Terrace slope
19.481306	69.222223	2	4	20cs/80g	Sandy gravel	Beach
19.483437	69.222755	4	15	100g	Gravel	Delta channel
19.483806	69.222772	2	9	70g/30cs	Sandy gravel	Delta bar
19.485113	69.222725	4	15	80g/20vcs	Sandy gravel	Delta channel
19.486377	69.22219	5	20		Cobbles with coarse sand matrix	River bar
19.486592	69.221829	5	30		Cobbles with medium sand matrix	River bar
19.486159	69.221547	15	17		Boulders with find sand matrix	River bank
19.485804	69.221118	4	50			River bank
19.4859	69.220011	5	30		Boulders with medium sand matrix	River bar
19.485906	69.219789	10	25		Boulders with fine sand matrix	Tributary channel
19.486449	69.219309	4	15	60cs/40g	Gravelly sand	River bar
19.48516	69.218842	5	30		Boulders with fine sand matrix	Tributary channel
19.485296	69.218744	10	20			River bank
19.484989	69.218148	15	25		Boulders with medium sand	River bank
19.484233	69.217665	2	7	20cs/70g	Sandy gravel	Tributary channel
19.484233	69.217665	10	60		Coarse sand	Tributary channel
19.483446	69.217371	3	20	60cs/30c	Cobbly sand	River bank
19.483446	69.217371	5	20		Boulders with medium sand	River bed
19.483258	69.217258		7	100ms	Sand	River bank
19.483258	69.217258		3	70vcs/30g	Gravelly sand	River bank

19.483841	69.217112	8	20			River bar
19.48447	69.216523	6	25			River bar
19.484173	69.216369	15	30		Boulders with fine sand matrix	Tributary channel
19.483542	69.21586	20	15			River bar
19.473262	69.216977	1	7	60cs/40g	Gravelly sand	Gravel pit
19.472186	69.216978	1	10	60cs/40g	Gravelly sand	Gravel pit
19.468709	69.213604	15	70			Rockslide
19.474704	69.213963		200		Boulders with coarse sand matrix	River bed
19.474633	69.213409		55		Boulders with gravel matrix	River bed
19.473763	69.212877	6	10		Boulders with fine sand matrix	River bank
19.473453	69.212545			30g/50cs/30z	Gravelly silty sand	River bank
19.504177	69.215881	20	75			Beach
19.504177	69.215881	3	12	60vcs/40g	Gravelly sand	Beach
19.502757	69.21618	50	135			Beach
19.502757	69.21618	1.5	12	80cs/20g	Gravelly sand	Beach
19.501957	69.21636	1.5	65	70g/30cs	Sandy gravel	Beach
19.501288	69.216566	60	100			Beach
19.501288	69.216566	1	10		coarse sand	Beach
19.500425	69.216733	20	105			Beach
19.500425	69.216733	2	20		Cobbles with coarse sand matrix	Beach
19.49868	69.216922	6	40		Cobbles with gravel matrix	Beach
19.498637	69.216959	1	20	70g/30c	Cobbly gravel	Beach
19.498637	69.216959	3	20	80g/20cs	Sandy gravel	Beach
19.498157	69.217249	8	40			Beach
19.498157	69.217249	3	8		Cobbles with coarse sand matrix	Beach
19.497051	69.217704	3	15	70vcs/30g	Gravelly sand	Beach
19.496171	69.218001	8	20		Boulders with gravel matrix	Beach
19.496171	69.218001	3	15		Boulders with gravel matrix	Beach
19.495189	69.218351	25	35		Boulders with gravel matrix	Beach
19.495189	69.218351	2	10		Cobbles with coarse sand matrix	Beach
19.494245	69.218823	3	10	70g/30cs	Sandy gravel	Beach

19.493683	69.219327	2	14	50cs/50g	Sandy gravel	Beach
19.49295	69.220497	5	15		Gravelly sand	Beach
19.492353	69.220917		3	80cs/30c	Cobbly sand	Terrace slope
19.492353	69.220917	4	30	50vcs/50g	Sandy gravel	Terrace slope
19.492474	69.221066	4	15		Gravelly sand	Beach
19.492237	69.221523	1	5			Beach
19.492237	69.221523	2	15			Beach
19.491797	69.221831	1	3		Sandy gravel	Beach
19.49105	69.22188	1.5	4	70g/30cs	Sandy gravel	Delta channel
19.490788	69.221902	0.5	5	80g/20cs	Sandy gravel	Delta bar
19.490986	69.222053			70cs/30g	Sandy gravel	Delta bar
19.491149	69.222084	3	6	50g/50cs	Sandy gravel	Delta bar
19.490007	69.221915	2	3	30cs/70g	Sandy gravel	Beach
19.490053	69.222128		3	80cs/20g	Gravelly sand	Beach
19.48986	69.222434	3	10	70g/30cs	Sandy gravel	Beach
19.487995	69.222601	4	27		Cobbles with fine sand matrix	Delta channel
19.487485	69.222596	3	15		Gravelly sand	Beach
19.486697	69.222667	3	5		Gravel	Delta bar
19.486413	69.222574	7	20		Boulders with coarse sand matrix	Delta bar
19.486987	69.223134	2	10		Cobbles with coarse sand martrix	Delta bar
19.486993	69.223589	3	10		Cobbles with medium sand	Delta bar
19.485433	69.223383	4	15			Delta bar
19.484574	69.223316	3	15			Delta bar
19.471834	69.220486	2	15	50g/50cs	Gravelly sand	Beach
19.47197	69.220655	1	4			Delta channel
19.47352	69.220897	3	6		Cobbles	Beach
19.473637	69.220836	1	4		Gravelly sand	Beach
19.473704	69.220791	2	7			Beach
19.475822	69.221075	20	30		Gravel	Beach
19.47751	69.221303	3	15	60ms/40g	Gravelly sand	Terrace slope
19.478455	69.221526	4	20		Cobbles with gravel matrix	Beach
19.478851	69.22154	3	10		Conglomerate	Terrace slope
19.479319	69.221748	2	12		Gravel	beach
19.48105	69.222278	1	4		Sandy gravel	Beach
19.483502	69.22247	2	12			Beach
19.483625	69.222443	1	8		Gravel	Beach